Developing proxies in secondary carbonates with application to ENSO variability and basin-wide paleo-hydrology

Christopher M. Theaker
St Cross College
University of Oxford

Thesis submitted to the University of Oxford
for the degree of Doctor of Philosophy

April 2022

Supervised by Dr. Christopher Day, Dr. Stacy Carolin
and Professor Samar Khatiwala

"I'm old, Gandalf. I know I don't look it but I'm beginning to feel it in my heart. I feel thin... sort of stretched, like butter scraped over too much bread. I need a holiday. A very long holiday. And I don't expect I shall return. In fact I mean not to."

- Bilbo Baggins, Lord of the Rings: The Fellowship of the Ring

Declaration

I hereby declare that the thesis submitted is entirely my own work and has not been submitted to any other university for any degree, diploma or other qualifications. All direct or indirect sources used are acknowledged as references.

Abstract

This thesis develops new, and expands existing, methods of reconstructing paleoclimate from geochemical proxies hosted in secondary carbonate precipitates. This is done by: i) Developing a new multi-proxy approach for using lacustrine cave carbonates (LCCs) to reconstruct past shifts in precipitation-evaporation (P-E) over lake drainage basins, and ii) Investigating the suitability of speleothems as paleo-ENSO archives. Chapters 2 and 3 use modelled and measured values from LCC samples to generate a framework for understanding how Mg/Ca, U/Ca and $\delta^{\frac{44}{42}}Ca$ in LCCs can be used as a combined multi-proxy approach to reconstruct past shifts in P-E. This multi-proxy approach is subsequently used to generate a novel reconstruction of P-E over the Bonneville Basin (a terminal basin in the Great Basin region of the southwestern United States), during Heinrich Stadial 1. Results suggest that moisture supply to the Great Basin region was impacted by a southwards shift of the ITCZ and variations in the elevation of North American ice sheets during Heinrich Stadial 1. Chapter 4 investigates the suitability of applying speleothem BA03 as a paleo-ENSO archive. Firstly, the impacts of age model and $\delta^{18}O$ uncertainties on speleothem ENSO variability reconstructions are quantified. A total of eight high resolution ($>$ 2 samples per year) $\delta^{18}O$ time-series are then used to reconstruct shifts in ENSO variability over the Holocene. This new ENSO variability reconstruction suggests a reduction in ENSO variability during the mid-Holocene (5.68 kyr BP – 3.78 kyr BP), the termination of which coincides with the end of the so called "4.2 Kyr Event". This thesis advances the paleoclimate application of numerous geochemical proxies, expanding the use of precisely dated, high-resolution secondary carbonate archives.

Extended Abstract

The modelled impact of anthropogenically forced climate change on major areas of human population is still debated. This is the case for the El Niño-Southern Oscillation (ENSO) and moisture supply to the already arid southwestern United States. Understanding the impact of future climate change on these climate systems is crucial in order to plan for, and mitigate, the impacts on human populations. Paleo-climate archives provide estimates of how climate systems varied under a variety of natural forcing scenarios. This allows them to provide insights into the underlying controls on climate systems and test the ability of climate models to accurately reconstruct climate under different forcing scenarios. The goals of this thesis are to provide new constraints on: i) shifts in moisture supply to the Great Basin region of the southwestern United States during the last deglaciation, and ii) shifts in ENSO variability over the duration of the Holocene epoch. This is achieved by developing a new multi-proxy approach for reconstructing past shifts in precipitation-evaporation (P-E) over lake drainage basins and investigating the suitability of speleothems as paleo-ENSO archives.

Chapters 2 and 3, further develop the existing use of lacustrine cave carbonates (LCCs) to reconstruct basin wide shifts in P-E using a more robust multi-proxy approach. LCCs can provide continuous records of lake chemistry during periods of growth and can be dated with high precision U-Th chronology. Here I use a combination of modelled and measured results to generate a framework for understanding how Mg/Ca, U/Ca and $\delta^{\frac{44}{42}}Ca$ in LCCs can be used as a combined multi-proxy approach for reconstructing past shifts in P-E.

Firstly, Chapter 2 seeks to define how lake chemistry, specifically Mg/Ca, U/Ca and $\delta^{\frac{44}{42}}Ca$, responds to shifts in basin wide P-E and whether these chemical and isotopic changes are sufficiently large to be measurable in precipitated lacustrine cave carbonates (LCCs). This chapter defines a new software tool, LakeCalc, a single box model designed to reconstruct the volume and chemical composition of Lake Bonneville over its rise and fall during the last glaciation, between 30 kyr (BP) and 13 kyr (BP). Using

LakeCalc, I define the required shifts in the balance between river inflow and evaporation that are necessary to produce measurable shifts in LCC Mg/Ca, U/Ca and $\delta^{\frac{44}{42}}Ca$. In specific situations (e.g. without major changes to the configuration of the drainage basin) these LCC proxies can be used to contribute to P-E reconstructions over the Bonneville Basin.

In Chapter 3, Mg/Ca, U/Ca and $\delta^{\frac{44}{42}}Ca$ values were measured from LCC samples CC3 and CC5, which precipitated between 25.3 kyr (BP) and 13.6 kyr (BP) in the Bonneville Basin, situated in the Great Basin region of the southwestern United States. Measured LCC values are combined with LakeCalc model outputs to test whether Mg/Ca, U/Ca and $\delta^{\frac{44}{42}}Ca$ can be used as a robust new multi-proxy approach to reconstructing shifts in basin-wide P-E. Close agreement between modelled and measured values during the rise of Lake Bonneville (25 kyr BP - 18.8 kyr BP), where Lake Bonneville is a closed basin lake and P-E is well constrained by paleo-shoreline reconstructions, indicates that this new multi-proxy approach is robustly recording shifts in basin-wide P-E. This multi-proxy approach is then used to reconstruct shifts in P-E during the overflowing period of Lake Bonneville's history ($\sim$18.0 kyr BP - $\sim$14.7 kyr BP), for which P-E reconstructions were previously hindered by the open basin nature of the system. Here a link between moisture supply to the Great Basin region and Heinrich Stadial 1 is identified, with moisture supply suggested to be impacted by a southwards shift of the ITCZ and variations in the elevation of North American ice sheets.

Chapter 4 tests the suitability of BA03, a Western Pacific Warm Pool speleothem, to be used a paleo-ENSO archive. The El Niño-Southern Oscillation (ENSO) is a major source of inter-annual climate variability, impacting a large portion of the world's population. However, the frequency and magnitude of ENSO events before the existence of instrumental and historical records are still poorly constrained. This study investigates the impact of age model and $\delta^{18}O$ analytical uncertainty on speleothem based paleo-ENSO reconstructions; and expands the number of century length ENSO variability

records generated from speleothem BA03. Here, I present two new centennial length, sub-annual ($>$ 2 samples per year) resolution $\delta^{18}O$ time-series from stalagmite BA03 covering 3830 Yr. (BP) – 3730 Yr. (BP) and 4150 Yr. (BP) – 4010 Yr. (BP). Together with six existing high resolution BA03 $\delta^{18}O$ time-series (Chen et al., 2016) these are used to generate eight centennial length records of ENSO variability throughout the Holocene. A new methodology is developed to propagate age model and $\delta^{18}O$ uncertainties onto speleothem ENSO variability proxy values. While age model and $\delta^{18}O$ analytical uncertainty were found to introduce large uncertainties to the speleothem ENSO variability proxy, they do not preclude speleothems as paleo-ENSO archives once accounted for. ENSO variability records generated from BA03 show a reduction in ENSO variability during the mid-Holocene (5.68 kyr BP – 3.78 kyr BP) compared to the early and late Holocene. This supports the findings of existing coral, mollusc and foraminiferal paleo-ENSO records from the central and eastern tropical Pacific. The period of reduced ENSO variability inferred in the mid-Holocene coincides with a maximum in western Pacific warm pool convective activity (3500 Yr. BP – 5500 Yr. BP; Partin et al., 2007a), suggesting that increased WPWP convection could be related to suppressed ENSO variability in this period. Finally the termination of the mid-Holocene reduction in ENSO variability is observed to coincide with the end of the so called "4.2 Kyr Event" suggesting a link between the increase in ENSO variability and the end of this centennial scale climate perturbation.

Acknowledgments

Firstly, I would like to thank NERC and St Cross College for funding my DTP placement. The radiocarbon analysis in this work was funded by NEIF Radiocarbon NRCF010001 (allocation number 2226.032).

I would also like to thank the many people who helped and guided me throughout my DPhil. Whilst many people deserve a mention here, for brevities sake I am forced to focus on a specific few. Firstly, I would like to thank my supervisors Chris Day, Stacy Carolin and Samar Khatiwala for their many hours of invaluable help and guidance throughout the DPhil. Thanks are also due to Andrew Mason and Alan Hsieh for putting up with my constant questions about P2; Jane Barling, for her help, advice, and tireless efforts to maintain the clean labs; and finally, Phil Holdship for my trace element measurements.

During my time in Oxford I have met many lifelong friends and I appreciate all the good times they have given me over the last 4 years. Special thanks goes to Hamish for keeping me going through long nights in the lab with double strength hot chocolates and many (maybe too many) office test matches and other office entertainments; Frankie, for putting up with mine and Hamish's office antics; Andrew for always being around for a hot chocolate/coffee, a walk, or even a row, whenever writing got too much; Ollie, Marcus and Jimmy for their constant friendship; and finally, Sean for being an excellent housemate, training buddy and cartoon/vine enthusiast.

I would also like to thank my parents, Mike and Anne, and my sister Holly, for their constant support and belief that helped make the last few years of COVID and the DPhil much easier than they otherwise would have been, it was and still is greatly appreciated.

Finally, I would like to thank Laura for all of her patience during my many late nights, especially during the write up, and always being there to cheer me up after a hard day's work with a message, a call or a visit!

Contents

1 Introduction **1**

1.1 Overview 3

1.2 Secondary carbonates as paleo-climate archives 4

1.2.1 Speleothems 4

1.2.2 Lake systems 7

1.3 Geochemical proxies in secondary carbonates 9

1.3.1 Oxygen isotopes 9

1.3.2 Trace elements 10

1.3.3 Calcium isotopes 12

1.4 Southwestern USA climate 15

1.5 The tropical Pacific and the El Niño Southern Oscillation 21

2 Developing the LakeCalc model to assess the combined use of Ca-isotopes and trace elements to reconstruct basin wide Precipitation-Evaporation **26**

2.1 Introduction 30

2.2 Lake Bonneville overview 33

2.2.1 Geology of the Bonneville catchment area 36

2.3 Lacustrine Cave Carbonates (LCCs) as a multi-proxy archive for reconstructing P-E 38

2.3.1 LCCs as archives of lake water chemistry 38

2.3.2 Calcium carbonate precipitation as a function of regional P-E over the Bonneville Basin . . . 38
2.3.3 Calcium isotopes as proxy for reconstructing past shifts in $CaCO_3$ precipitation in Lake Bonneville . . . 41
2.3.4 Developing a multi-proxy approach to reconstructing changes in P-E over the Bonneville Basin . . . 43
2.4 LakeCalc description . . . 45
2.4.1 LakeCalc assumptions . . . 45
2.4.2 Reconstructed LakeCalc inputs . . . 49
2.4.3 Reconstructed LakeCalc outputs . . . 51
2.4.4 Model equations . . . 54
2.4.4.1 Lake Volume . . . 54
2.4.4.2 Mass of elements in the lake . . . 55
2.4.4.3 Calcium isotope composition . . . 57
2.5 Modelled controls on the Mg/Ca, U/Ca and $\delta^{\frac{44}{42}}Ca$ composition of LCCs 59
2.5.1 PICP control on LCC composition . . . 59
2.5.2 Sensitivity testing . . . 64
2.5.3 Other controls on LCC composition . . . 69
2.6 The potential for LCCs to reconstruct shifts in P-E over the Bonneville Basin . . . 70
2.7 Summary . . . 73

3 A multi-proxy approach to reconstructing P-E in the Bonneville Basin from Lacustrine Cave Carbonates 74

3.1 Introduction . . . 78
3.2 Study site and methodology . . . 80
3.2.1 Lake level change in Lake Bonneville . . . 80
3.2.2 Cathedral Cave . . . 82
3.2.3 Sample description . . . 84

3.2.4 Sampling . . . 86
3.2.5 U-Th chronology . . . 86
3.2.6 Age depth models . . . 87
3.2.7 Calcium isotope analysis . . . 88
3.2.8 Trace element analysis . . . 89
3.2.9 LakeCalc . . . 89
3.3 Results . . . 91
3.3.1 U-Th ages . . . 91
3.3.2 Age depth models . . . 93
3.3.3 Ca isotopes . . . 95
3.3.4 Trace elements . . . 96
3.4 Discussion . . . 99
3.4.1 Comparing the measured and modelled composition of LCC deposits during well constrained shifts in P-E over the Bonneville Basin (25 kyr BP - 18.8 kyr BP) . . . 99
3.4.2 Insights into basin structural changes using LCCs: Constraining the timing of the Bonneville Flood . . . 102
3.4.3 New insights into the period of overflow of Lake Bonneville from LCC deposits (∼18.0 kyr BP - ∼14.7 kyr BP) . . . 106
3.4.3.1 Identifying shifts in P-E . . . 106
3.4.3.2 Potential mechanisms causing identified shifts in P-E . 110
3.5 Future work and outlook . . . 112
3.6 Conclusion . . . 113

4 Reconstructing Holocene paleo-ENSO variability using $\delta^{18}O$ from a Bornean stalagmite 114

4.1 Introduction . . . 118
4.2 Northern Borneo intra-seasonal to inter-annual hydro-climate . . . 121
4.3 Stalagmite $\delta^{18}O$ used as a paleo-ENSO archive . . . 122

4.4 Methodology . . . 127
4.4.1 Speleothem sub-sampling . . . 127
4.4.2 U-Th disequilibrium dating . . . 127
4.4.3 Radiocarbon dating . . . 128
4.4.4 OxCal age v. depth model . . . 129
4.4.5 Trace element analysis . . . 130
4.4.6 Stable isotope analysis . . . 131
4.4.7 Spectral analysis . . . 132
4.4.8 Generating a speleothem-hosted ENSO variability proxy . . . 132
4.4.8.1 Propagating age model uncertainty onto the ENSO variability proxy . . . 133
4.4.8.2 Investigating the impact of differing analytical $\delta^{18}O$ uncertainties . . . 134
4.5 Results . . . 136
4.5.1 Uranium-Thorium ages . . . 136
4.5.2 Radiocarbon ages . . . 144
4.5.3 OxCal age model . . . 147
4.5.4 Trace element time-series . . . 149
4.5.5 High resolution $\delta^{18}O$ ENSO variability windows . . . 151
4.5.5.1 3780 Yr. (BP) Window . . . 152
4.5.5.2 4080 Yr. (BP) Window . . . 152
4.5.6 Spectral analysis . . . 154
4.5.7 ENSO variability proxy . . . 155
4.5.7.1 Mean OxCal age model ENSO variability . . . 155
4.5.7.2 Propagating age model uncertainty onto the ENSO variability proxy . . . 159
4.5.7.3 $\delta^{18}O$ analytical uncertainty propagation . . . 163
4.6 Discussion . . . 164

4.6.1 Stalagmite BA03 as a paleo-ENSO archive 164
4.6.2 Evolution of reconstructed ENSO variability through the Holocene 166
4.6.3 A minimum in ENSO variability coeval with the "4.2 kyr event" 170
4.6.4 Study Limitations 172
4.7 Conclusion 174

5 Concluding remarks and future outlook 175

A Chapter 2 Appendix 197
A.1 LakeCalc Matlab script 198

B Chapter 3 Appendix 215
B.1 LakeCalc model output 216

C Chapter 4 Appendix 217
C.1 Radiocarbon Data 218
C.2 Trace Element Cross Plots 218

List of Figures

1.1 An overview of speleothem precipitation 6
1.2 Global distribution of major endoheric basins 8
1.3 Diagram of North American climate during the modern day and LGM . 17
1.4 Maximum extents and timings of Great Basin terminal lake highstands 19
1.5 The global distribution and seasonality of teleconnections during: A) El Niño events; and B) La Niña events. 24

2.1 A regional map showing: the maximum extent of Lake Bonneville . . . 34
2.2 A comparison between the lake level reconstruction of Oviatt (2015) and the simplified lake level history used by this study 36
2.3 A diagram showing the sources and sinks in Lake Bonneville reconstructed in LakeCalc 47
2.4 A schematic of a LakeCalc model timestep 48
2.5 Modelled PICP vs proxy relationship in Lake Bonneville LCCs. 63
2.6 The LakeCalc model output for testing the sensitivity of LakeCalc to changing riverine inflow compositions 66
2.7 The LakeCalc model output for testing the sensitivity of LakeCalc to changing volumes of groundwater outflow 68
2.8 The LakeCalc model output for the rise and fall of Lake Bonneville . . 72

3.1 Lake level reconstruction of Lake Bonneville over its highstand period . 82
3.2 A diagram of the relative stratigraphy of LCC Growth Phases 84

3.3 Annotated images of samples CC3 and CC5 85
3.4 Age v. depth models for samples CC3 and CC5 94
3.5 $\delta^{\frac{44}{42}}$Ca timeseries from both: A) Sample CC5 and B) Sample CC3 . . . 96
3.6 Trace element (Mg/Ca and U/Ca) timeseries for samples CC5 and CC3 98
3.7 Comparison of modelled LakeCalc outputs and measured LCC proxy data during the aragonite portion of Growth Phase I 101
3.8 A comparison of modelled and measured LCC composition at the time of the Bonneville Flood 105
3.9 Comparison of Lake Bonneville and regional and global paleo-climate records 109

4.1 Global correlation between interannual (2-7 year band) rainfall and the Niño 3.4 index (1979-2014) 122
4.2 Caves of Gunung Buda and Gunung Mulu National Parks 125
4.3 Annotated image of speleothem BA03 126
4.4 Depth vs age plots for BA03 U-Th ages 137
4.5 Radiocarbon measurements from BA03 146
4.6 Test OxCal age models plots for BA03 148
4.7 OxCal age v. depth model for BA03 149
4.8 BA03 trace element time-series 151
4.9 The BA03 high resolution stable isotope time-series centered on 3780 Yr. (BP) 153
4.10 The BA03 high resolution stable isotope time-series centered on 4080 Yr. (BP) 154
4.11 Power spectra of high resolution BA03 δ^{18}O time-series 155
4.12 Raw and interpolated high resolution BA03 δ^{18}O time-series 157
4.13 Bandpass (2-7 year) filtered δ^{18}O time-series of the interpolated high resolution BA03 δ^{18}O time-series 158
4.14 Mean and 30-year sliding window mean OxCal ENSO variability values 159

4.15 The distribution of ENSO variably values generated from the 1000 ensemble age models for all high resolution BA03 $\delta^{18}O$ time-series 162
4.16 A comparison of mean OxCal ENSO variability values and ensemble mean ENSO variability values 163
4.17 Comparison of ensemble mean ENSO variability values and propagated analytical instrument uncertainty 164
4.18 Comparison of tropical Pacific paleo-ENSO archives and western warm pool convective activity over the Holocene 169

List of Tables

2.1 Estimated lake parameters used in LakeCalc for well defined Lake Bonneville shorelines. 50
2.2 Chemical composition of the riverine inflow to Lake Bonneville used by LakeCalc. 51
2.3 Fractionation factors and partition coefficients used in LakeCalc 53
2.4 A summary of LakeCalc modelled outputs for different types of lake evolution 61

3.1 Bounding ages and heights of Growth Phase II and III in sample CC5 . 88
3.2 U-Th ages calculated from samples CC3 and CC5 92

4.1 Data for all ages measured on BA03. 143
4.2 ENSO variability values of the high resolution BA03 $\delta^{18}O$ time-series . 160

List of Abbreviations

General

GCM General circulation model

GSL Great Salt Lake

MC-ICP-MS Multi-collector Inductively Coupled Plasma Mass Spectrometer

NEIF National Environmental Isotope Facility

P-E Precipitation-Evaporation

PCP Prior calcite precipitation

PICP Proportion of inflowing Ca removed by $CaCO_3$ precipitation

U-Th Uranium-Thorium

Climate Terms

AMOC Atlantic Meridional Overturning Circulation

ENSO El Niño-Southern Oscillation

ITCZ Intertropical Convergence Zone

LGM Last Glacial Maximum

SON insolation September-October-November insolation

WPWP Western Pacific Warm Pool

Samples

BA03 Speleothem from Bukit Assam cave, northern Borneo

CC3 LCC sample from Cathedral Cave, situated in the Bonneville Basin

CC5 LCC sample from Cathedral Cave, situated in the Bonneville Basin

LCC Lacustrine Cave Carbonate

Standards

V-PDB Vienna Pee Dee Belemnite; oxygen isotope reference material

NBS-18 Oxygen and carbon isotope standard

NBS-19 Oxygen and carbon isotope standard

NIST SRM 915a Ca isotope reference material

NIST SRM 915b Ca isotope standard

NOCZ Oxygen and carbon isotope standard

Units

BP (Before the year 1950)

C.E. Common Era

g Gram

km Kilometre

kyr Thousands of years

masl Metres above sea level

ml Millilitre

mol Mole

ppb Parts per billion

ppm Parts per million

Yr. Year

m Milli (10^{-3})

μ Micro (10^{-6})

n Nano (10^{-9})

Chapter 1

Introduction

Contents

1.1 Overview 3

1.2 Secondary carbonates as paleo-climate archives 4

1.2.1 Speleothems 4

1.2.2 Lake systems 7

1.3 Geochemical proxies in secondary carbonates 9

1.3.1 Oxygen isotopes 9

1.3.2 Trace elements 10

1.3.3 Calcium isotopes 12

1.4 Southwestern USA climate 15

1.5 The tropical Pacific and the El Niño Southern Oscillation 21

1.1 Overview

Secondary calcium carbonate precipitates have the potential to provide excellent paleoclimate archives as they can be absolutely dated with high precision U-Th chronology, store multiple geochemical proxies and form globally, in a wide variety of environmental systems and climate regimes. This thesis aims to further expand the use of secondary calcium carbonate precipitates as paleoclimate archives by developing new and critically analysing existing proxy methods of reconstructing past environmental change from secondary carbonates.

This thesis specifically focuses on evaluating the suitability of Western Pacific Warm Pool speleothems to reconstruct past changes in the El Niño Southern Oscillation, and developing a multi-proxy approach to reconstruct changes in precipitation-evaporation from lacustrine cave carbonates in the Bonneville Basin, western United States.

This chapter introduces the paleoclimate archives (speleothems and lacustrine cave carbonates) and major climate systems studied in this thesis. Section 1.2 details the benefits of using secondary carbonates as paleoclimate archives, before summarising speleothems and lake systems as paleoclimate archives. Section 1.2 describes the geochemical proxies used in this thesis, and how they are able to reconstruct shifts in paleo-climate. Section 1.3 introduces the climate of the western United States, and the present state of knowledge as to how it has shifted since the last glacial maximum (LGM). Finally section 1.4 introduces the El Niño Southern Oscillation (ENSO), how it impacts global climate, and the present understanding of its behaviour throughout the Holocene.

1.2 Secondary carbonates as paleo-climate archives

Paleo-climate archives are useful tools for not only reconstructing shifts in past climate, but also testing the ability of climate models to reconstruct climate under variable forcings (Schmidt, 2010; Emile-Geay et al., 2016; McGee et al., 2018). Many different archives have been used to reconstruct paleo-climate including ice cores (e.g Rasmussen et al., 2006), speleothems (e.g. Chen et al., 2016), corals (e.g. Cobb et al., 2013), tree rings (e.g. D'Arrigo et al., 1993), peat bogs (e.g. Roland et al., 2014), sediment cores (e.g. Koutavas and Joanides, 2012), and lake paleo-shoreline deposits (e.g. Oviatt, 2015). Paleoclimate reconstructions from proxy records can be limited by low resolution sampling, large age uncertainties, or multiple controls on proxy values. Secondary carbonate precipitates can overcome some of these difficulties providing archives with the potential to host multiple geochemical proxies (e.g. Weber et al., 2018), be sampled up to sub-annually (e.g. Cobb et al., 2013; Chen et al., 2016) and be absolutely dated using high precision U-Th chronology (Edwards et al., 1987b). This thesis therefore focuses on using speleothems, and speleothem-like inorganic secondary carbonate precipitates from lake systems to generate and better constrain novel methods of paleo-climate reconstruction.

1.2.1 Speleothems

Speleothems are secondary mineral precipitates that form within caves. They are most commonly formed of calcium carbonate, occurring as either the calcite or aragonite polymorph. Speleothems precipitate from water infiltrating the undersaturated zone and either dripping into or flowing through caves. Most speleothems form by a common process (Figure 1.1). Meteoric waters infiltrate the soil zone and equilibrate with the high partial pressure of CO_2 (P_{CO_2}) in the soil zone, produced by the decomposition of organic matter and respiration of plants and microbes. (Eq. 1.1). The dissolved CO_2 forms carbonic acid (H_2CO_3) which dissolves carbonate minerals in the soil and epikarst (Eq. 1.2). Cave voids commonly have a much lower P_{CO_2} than the soil zone,

consequently when groundwater percolates into the cave CO_2 degassing occurs, resulting in the over-saturation and precipitation of $CaCO_3$ forming speleothems (reverse of Eq. 1.2) (e.g. Fairchild and Baker, 2012).

$$CH_2O + O_2 \rightarrow CO_2 + H_2O \tag{1.1}$$

$$CO_2 + CaCO_3 + H_2O \rightarrow Ca^{2+} + 2HCO_3^- \tag{1.2}$$

Speleothems provide advantageous paleoclimate archives for a number of reasons. Firstly, they have the potential to be absolutely dated with high precision U-Th chronology (e.g. McDermott et al., 2011). Secondly, during periods of growth, speleothems grow continuously which, when coupled with high growth rates and increasingly high resolution analysis techniques, allows speleothems to provide continuous high resolution paleo-climate records, with up to sub-annual resolution (e.g. Chen et al., 2016; Baldini et al., 2019; Lu et al., 2021). Speleothems also have a wide spatial distribution, being found in karstic environments throughout the globe, only requiring the presence of carbonate minerals to dissolve, void spaces to precipitate in, liquid water and vegetation to form. This has allowed them to provide terrestrial paleo-climate archives in the mid-latitudes outside the range of other commonly used paleoclimate archives such as marine sediment cores or ice cores. Finally, as speleothems record the chemical signature of solutions they precipitated from, multiple geochemical proxies can be measured from the same aliquot of sample, including oxygen isotopes (e.g. Chen et al., 2016), carbon isotopes (e.g. Lechleitner et al., 2021), calcium isotopes (e.g. Owen et al., 2016), strontium isotopes (e.g. Verheyden et al., 2000) and trace element-to-calcium ratios (e.g. Fairchild and Treble, 2009). This allows the combined use of multiple proxies to robustly reconstruct shifts in paleoclimate from speleothem archives.

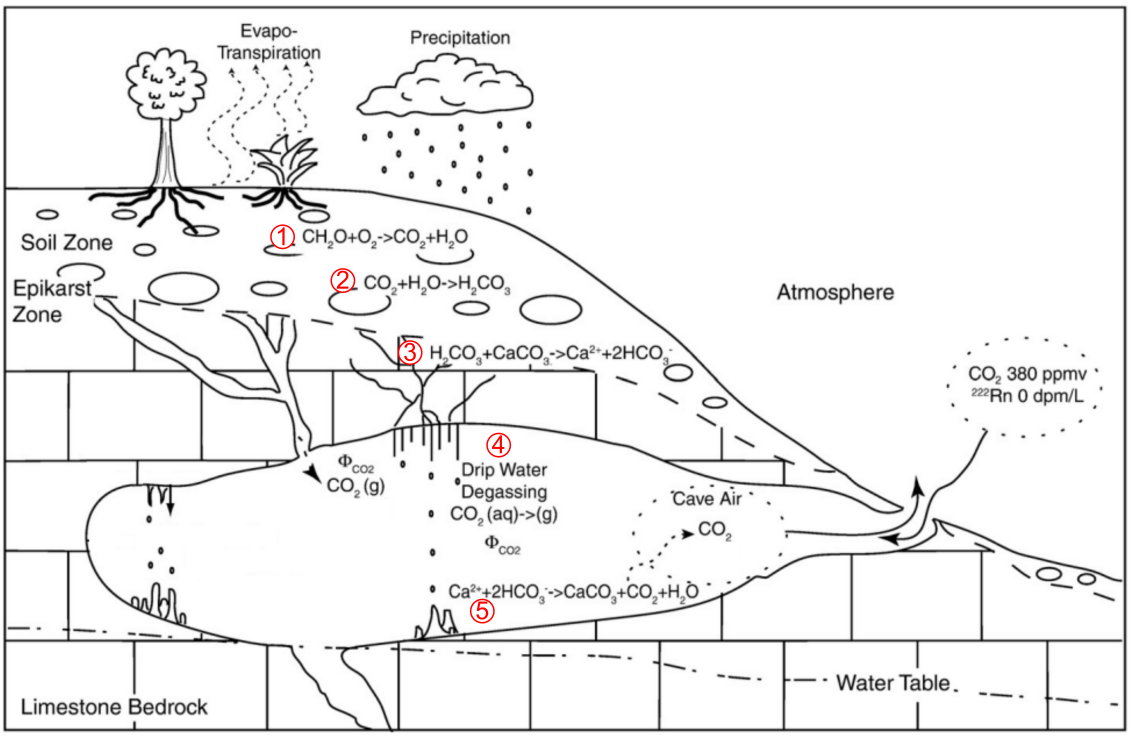


Figure 1.1: An overview of speleothem precipitation. Chemical equations describe the major processes resulting in speleothem formation: 1) Decay of organic matter; 2) Formation of carbonic acid; 3) Dissolution of carbonate minerals; 4) CO_2 degassing; and 5) $CaCO_3$ precipitation. Figure altered from Kowalczk and Froelich (2010).

1.2.2 Lake systems

The hydrological balance of a lake is set by the balance of rainfall and evaporation over a lake's drainage basin, consequently making lake systems a common target for studies attempting to reconstruct shifts in regional precipitation-evaporation (P-E) (e.g. Broecker et al., 2009; Broecker and Putnam, 2012). This is particularly the case for terminal lakes (Gilbert, 1890; Oviatt, 2015; Santi et al., 2019), which have no riverine outflow, and as such, all solution which enters the lake has to be removed by evaporation (Oviatt, 2015). Consequently, both the volume (Oviatt, 2015) and chemistry (McGee et al., 2012) of terminal lakes are sensitive to shifts in P-E. A given lake system provides regional (i.e drainage basin) scale information on P-E. The global distribution of endoheric basins (drainage basins that allows no outflow to other water bodies), suggests terminal basins could be used throughout the globe to reconstruct past changes in terrestrial P-E (Figure 1.2). P-E is commonly reconstructed from terminal lake systems using the dating of paleo-shoreline deposits (Gilbert, 1890; Oviatt, 2015) or the composition and lithology of sedimentary cores (Spencer et al., 1984; Benson et al., 2011). However, while these methods offer valuable information on shifts in P-E they are commonly low resolution and have large age uncertainties (McGee et al., 2012).

The precipitation of calcium carbonate is common in terminal lake systems. However, secondary carbonates precipitated in the water column are commonly deposited with detrital carbonates, and as fine particles prone to post depositional alteration, limiting the ability of studies to reconstruct the original composition of precipitated carbonates (e.g. Chen et al., 2020). Recently, a new form of lacustrine secondary carbonate has been discovered, lacustrine cave carbonates (LCCs). LCCs, are dense layered calcium carbonate deposits which precipitated in protected spaces with still water and low detrital input in Lake Bonneville (McGee et al., 2012). The low detrital content and continuous growth histories of LCCs allows them, in some cases, to be treated like speleothems, being dateable using U-Th chronology and recording the chemical signature of precipitating solutions (McGee et al., 2012). The abundant presence of la-

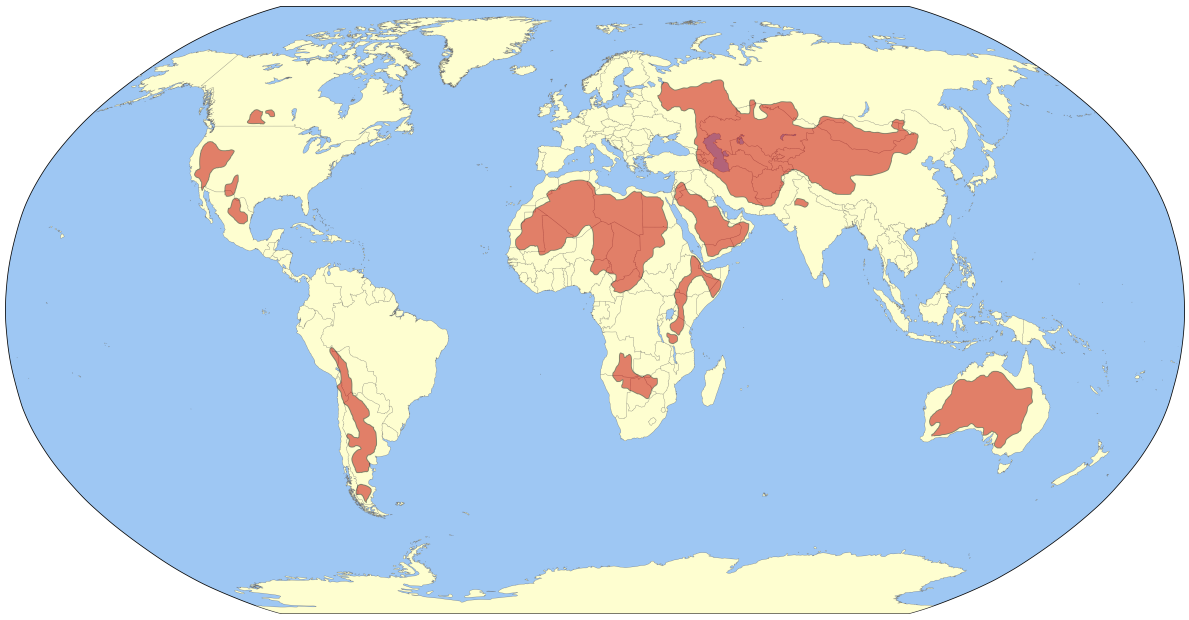


Figure 1.2: Global distribution of major endoheric basins, shaded in red. Data from Wang et al. (2018).

custrine cave carbonates in Lake Bonneville, found in more than 40 locations, suggests that they should be present in other terminal lake systems, creating the potential for a new globally extensive archive for reconstructing P-E (McGee et al., 2012). Chapters 2 and 3 develop a new multi-proxy approach using the trace element and calcium isotope composition of LCCs to reconstruct basin wide P-E.

1.3 Geochemical proxies in secondary carbonates

This thesis focuses on reconstructing past shifts in climate using chemical proxies stored in secondary carbonates. The ability of secondary carbonates to record a snapshot of solution composition at the time of precipitation allows them to contain multiple proxy systems. In this thesis, I focus on oxygen isotopes, calcium isotopes and trace element to calcium ratios.

1.3.1 Oxygen isotopes

Oxygen isotope composition is one of the most extensively used proxies in secondary carbonates. The precipitation of $CaCO_3$ fractionates oxygen isotopes with heavier isotopes included in the solid phase, and lighter isotopes remaining in solution (e.g. Kim and O'Neil, 1997; Day and Henderson, 2011). Oxygen isotope composition is recorded using delta notation as $\delta^{18}O$, which is defined as:

$$\delta^{18}O = \left(\frac{\left(\frac{^{18}O}{^{16}O}\right)_{Sample}}{\left(\frac{^{18}O}{^{16}O}\right)_{Standard}} - 1 \right) \times 1000‰ \tag{1.3}$$

The fractionation of oxygen isotopes between solution and $CaCO_3$ is now relatively well understood, due to to multiple laboratory based studies empirically calculating the fractionation factor in thin-film (speleothem-like) (e.g. Day and Henderson, 2011; Dreybrodt, 2012) and beaker (ocean and lake like) (e.g. Kim and O'Neil, 1997; Kim et al., 2007) experiments, over a range of temperatures and growth rates. The fractionation of oxygen isotopes into $CaCO_3$ is temperature dependent, with greater fractionation at lower temperatures (Kim et al., 2007; Day and Henderson, 2011). Assuming near-equilibrium conditions, the $\delta^{18}O$ of precipitated $CaCO_3$ should be controlled by the $\delta^{18}O$ of the precipitating solution and the precipitation temperature via:

$$\delta^{18}O_{CaCO_3} = \left(\left(\delta^{18}O_{Solution} + 1000\right) \times \alpha_{CaCO_3-Solution}\right) - 1000 \tag{1.4}$$

Where $\alpha_{CaCO_3-Solution}$ is the temperature dependent fractionation factor between solution and precipitated $CaCO_3$.

The $\delta^{18}O$ composition of secondary carbonates has therefore been used to reconstruct shifts in the $\delta^{18}O$ of precipitating solutions and the temperature of precipitation in differing environments. In speleothems, $\delta^{18}O$ is most commonly used to reconstruct changes in past rainfall $\delta^{18}O$, which can be caused by multiple processes including shifts in rainfall amount (Ayalon et al., 1998; Bowen, 2008), rainfall source (LeGrande and Schmidt, 2006) or the condensation temperature of the rainfall (Dansgaard, 1964). This is complicated by potential site specific issues, including disequilibrium fractionation of $\delta^{18}O$ into $CaCO_3$ (Deininger et al., 2012) or karst processing of the rainfall $\delta^{18}O$ signal (Ellis et al., 2020; Treble et al., 2022). In lake systems, lake water $\delta^{18}O$ is controlled by both the $\delta^{18}O$ of rainfall falling over the basin, but also fractionation of $\delta^{18}O$ by evaporation which preferentially removes lighter oxygen isotopes (Talbot, 1990; McGee et al., 2012).

Whilst $\delta^{18}O$ has the potential to provide crucial information about many aspects of the climate system, understanding the cause of shifts in $\delta^{18}O$ in secondary carbonates can be difficult. Cave monitoring, and the use of multiple speleothems to discount site specific effects are crucial in cave settings. The same is true in lakes, where comparing shifts in $\delta^{18}O$ with other nearby records is key to understanding whether lake waters are responding to shifts in rainfall $\delta^{18}O$, evaporation, or other processes.

1.3.2 Trace elements

Trace elements can be incorporated into secondary carbonates through a variety of mechanisms, either substituted directly into the crystal lattice or transported with organic or colloidal matter (Fairchild and Treble, 2009). In this thesis, I only consider trace elements which form divalent cations in solution and can substitute for Ca^{2+} in the crystal lattice (e.g. Magnesium, Barium, Strontium, Uranium etc). For elements substituting into the crystal lattice the relationship between the trace element to cal-

cium ratio (X/Ca) in the precipitating solution and $CaCO_3$ can be related by a simple equation defining the partition co-efficient (Morse and Bender, 1990):

$$\left(\frac{X}{Ca}\right)_{CaCO_3} = \left(\frac{X}{Ca}\right)_{Solution} \times D\left(X\right)_{CaCO_3-Solution} \tag{1.5}$$

where $D\left(X\right)_{CaCO_3-Solution}$ is the partition co-efficient of element X between solution and $CaCO_3$.

Many studies have constrained the partitioning of elements into both aragonite and calcite in both laboratory and field experiments, showing partition coefficients to be dependent on temperature (e.g. Gascoyne, 1983; Huang and Fairchild, 2001; Day and Henderson, 2013), growth rate (e.g. Gabitov et al., 2014; Riechelmann et al., 2014) and solution composition (e.g. Borsato et al., 2007).

In speleothems, changes in X/Ca are commonly used to reconstruct shifts in the amount of $CaCO_3$ precipitated in the karst system prior to the drip waters reaching the speleothem, a process termed prior carbonate precipitation (PCP) (Fairchild et al., 2000). Elements which are incompatible in the $CaCO_3$ lattice $\left(D\left(X\right)_{CaCO_3-Solution} < 1\right)$ will be concentrated in solution with respect to Ca if the amount of PCP increases. Conversely, compatible elements $\left(D\left(X\right)_{CaCO_3-Solution} > 1\right)$ will be depleted in solution with respect to Ca as PCP increases. Increasing PCP is commonly considered a signal of increasing aridity, with less rainfall introducing more gas filled voids into the karst system and hence more opportunities for CO_2 degassing and $CaCO_3$ precipitation (e.g Fairchild et al., 2000; Fairchild and Treble, 2009; Owen et al., 2016). However, identifying a PCP signal from a single element can be challenging. In addition to PCP, the X/Ca of drip waters can also be altered by multiple factors including: changes in dust supply above the cave (Carolin et al., 2019); or changes in residence time of drip waters in the overlying karst (Fairchild and Treble, 2009). In addition, the partition co-efficient between drip waters and precipitated $CaCO_3$ can also be altered by multiple factors including: precipitation temperature (Day and Henderson, 2013), growth rate (Gabitov et al., 2014; Riechelmann et al., 2014) or competition for lattice sites with other ions

(Borsato et al., 2007). The impact of the large number of controls on speleothem X/Ca can be mitigated in PCP reconstructions by considering multiple trace elements simultaneously. If multiple elements are behaving as expected for a PCP control, then PCP can be robustly inferred to be the controlling mechanism. However, if multiple elements display behavior inconsistent with a PCP control, then it is likely another mechanism is controlling drip water X/Ca. This highlights the benefits of secondary carbonate precipitates as multi-proxy archives.

In lakes, X/Ca is set by the balance between the magnitude and X/Ca composition of inputs and outputs from the lake. In lake systems, $CaCO_3$ precipitation will alter the X/Ca composition of lake waters in a similar way to PCP in caves, concentrating or depleting elements in solution relative to Ca depending on their partition co-efficient (McGee et al., 2012). However, shifts in X/Ca in lake waters will be muted by the constant supply of new solution to the lake. Much like cave drip waters, multiple controls exist on the X/Ca of lake waters. However this thesis aims to test whether a multi-proxy approach allows the magnitude of $CaCO_3$ precipitation to be reconstructed from the X/Ca of lacustrine carbonates.

1.3.3 Calcium isotopes

Calcium is one of three major elements in $CaCO_3$. Despite much research into the controls on oxygen and carbon isotopes in secondary carbonates, calcium isotopes have been relatively understudied in terrestrial environments. This is due to the relatively small range of calcium isotopes in the terrestrial world, resulting in analytical techniques struggling to resolve changes in calcium isotope composition. Advances in modern calcium isotope analysis has led to a large increase in the number of studies attempting to understand and use Ca isotope fractionation. In this thesis I exclusively consider the ratio between ^{44}Ca and ^{42}Ca which is expressed using delta notation as $\delta^{\frac{44}{42}}Ca$:

$$\delta^{\frac{44}{42}}Ca = \left(\frac{\left(\frac{^{44}Ca}{^{42}Ca}\right)_{Sample}}{\left(\frac{^{44}Ca}{^{42}Ca}\right)_{Standard}} - 1 \right) \times 1000‰ \quad (1.6)$$

Throughout this thesis I express $\delta^{\frac{44}{42}}Ca$ relative to NIST SRM 915a.

Many studies have observed the Ca isotope composition of precipitated $CaCO_3$ to be isotopically lighter than the precipitating solution (Gussone et al., 2005; Tang et al., 2008; Reynard et al., 2011), with the magnitude of the fractionation dependent on both the temperature and growth rate during precipitation (Tang et al., 2008). The growth rate control, coupled with the preference for light isotopes in the solid phase, suggest that that the observed Ca isotope fractionation is kinetic in origin (DePaolo, 2011). This is supported by a number of studies which have investigated the precipitation of $CaCO_3$ at ultra-slow precipitation rates and calculated near zero equilibrium fractionation factors (Steuber and Buhl, 2006; Fantle and DePaolo, 2007; Jacobson and Holmden, 2008). Despite this, many studies have worked to constrain the magnitude of the kinetic fractionation of Ca isotopes during the precipitation of $CaCO_3$ for beaker experiments (Gussone et al., 2003; Tang et al., 2008) and thin-film environments (Reynard et al., 2011; Owen et al., 2016).

Most calcium isotopes studies in secondary carbonates have been focused on the marine environment where calcium isotopes are used to reconstruct shifts in magnitude and isotopic composition of calcium inputs and outputs from the ocean (Fantle and DePaolo, 2007; Fantle, 2010; Blättler et al., 2011; Fantle and Tipper, 2014). More recently, Ca isotopes have been applied to cave environments and speleothems, where, if the calcium isotope composition of bedrock is known, they can be used to give quantitive reconstructions of PCP through time (Owen et al., 2016).

Closed lake basins should be similar in concept to the marine environment, with $\delta^{\frac{44}{42}}Ca$ responding to shifts in the balance of both the magnitude and isotopic composition of calcium inputs and outputs from the lake. As such, much like trace elements, changes in the magnitude of $CaCO_3$ precipitation in lake systems will alter the enrich-

ment of heavy calcium isotopes in lake waters (Nielsen and DePaolo, 2013).

1.4 Southwestern USA climate

In the modern day, the climate of the Great Basin region of the United States is characterised by aridity and low precipitation (Santi et al., 2019). Climate models predict that rainfall will be further reduced in this region under anthropogenically forced climate change, although there are disagreements as to the magnitude of this change (Seager and Vecchi, 2010; Scheff and Frierson, 2012). Understanding the climate controls on moisture supply to the southwestern United States is therefore very important in order to mitigate the impacts of anthropogenic climate change on large human populations in this region, such as Los Angeles. During the last glaciation, there is abundant evidence from the expansion of terminal lakes in the Great Basin region that the climate of the southwestern United States was markedly wetter (Gilbert, 1890; Oviatt, 1997; Santi et al., 2019). Understanding the causes of shifts in moisture supply to this region in the past could provide greater insights into the underlying controls of modern rainfall, which in turn can help with future climate predictions.

Modern climate

In the modern day, rainfall in the southwestern United States is dominated by westerly moisture sources from the Pacific Ocean. With the exception of the North Pacific coast, western North America is semi-arid, with aridity increasing away from the coast (Redmond and Koch, 1991). Much of the southwestern United States receives precipitation carried from the north and central Pacific by winter cyclones. These originate south of the Aleutian low and are transported over North America by the westerly winter storm track (Figure 1.3) (Cayan et al., 1999). Moisture from these cyclones can be carried deep into North America, and while the bulk of rainfall falls below the winter storm track, the southern extent of storms provides the dominate source of modern precipitation to the Great Basin (Oster et al., 2019).

The most intense rainfall events occurring on the west coast of the United States are linked to extra-tropical cyclones carrying moisture from the central and eastern tropical

Pacific (Oster et al., 2019). These develop narrow corridors of moisture transport known as "atmospheric rivers", causing the warmest and wettest storms to reach the coast of the western United States (Zhu and Newell, 1998; Dettinger, 2011; Ralph and Dettinger, 2011). The majority of modern "atmospheric river" rainfall is concentrated in the northwestern United States (Figure 1.3) (Oster et al., 2019).

Last glacial maximum and deglaciation

There is abundant evidence that the southwestern United States were dramatically wetter during the last glaciation, primarily provided by the expansion of terminal lakes in the Great Basin region (Gilbert, 1890; Oviatt, 2015; Santi et al., 2019; McGee et al., 2018). The development of extensive North American ice sheets deflected westerly winds and the winter storm track along a northwest to southeast trend increasing moisture supply to the southwestern United States (Figure 1.3) (Oster et al., 2015b). In addition, the strengthening of the Aleutian low and weakening of the North Pacific high during the last glacial maximum induced a southward shift in the mean latitude of "atmospheric river" landfall, further increasing moisture supply to the south-western United States (Figure 1.3) (Lora et al., 2017).

Paleo-climate reconstructions show the wettest conditions in the southwestern United States occurring during Heinrich Stadial 1 (Munroe and Laabs, 2013; McGee et al., 2018). The mechanism linking Heinrich Stadial 1 and increased southwestern United States rainfall remains elusive, with studies suggesting a further southward shift of the North American storm track (Asmerom et al., 2010), or increased moisture supply from south westerly "atmospheric river" events (McGee et al., 2018; Oster et al., 2019). Determining the correct causal mechanism is complicated by the large age uncertainties and low temporal resolutions of paleo-lake level reconstructions from Great Basin terminal lakes (McGee et al., 2012), reducing the ability to observe the temporal and spatial characteristics of increased rainfall during Heinrich Stadial 1 (Santi et al., 2019).

In this thesis (Chapters 2 and 3), I aim to generate a new multi-proxy approach

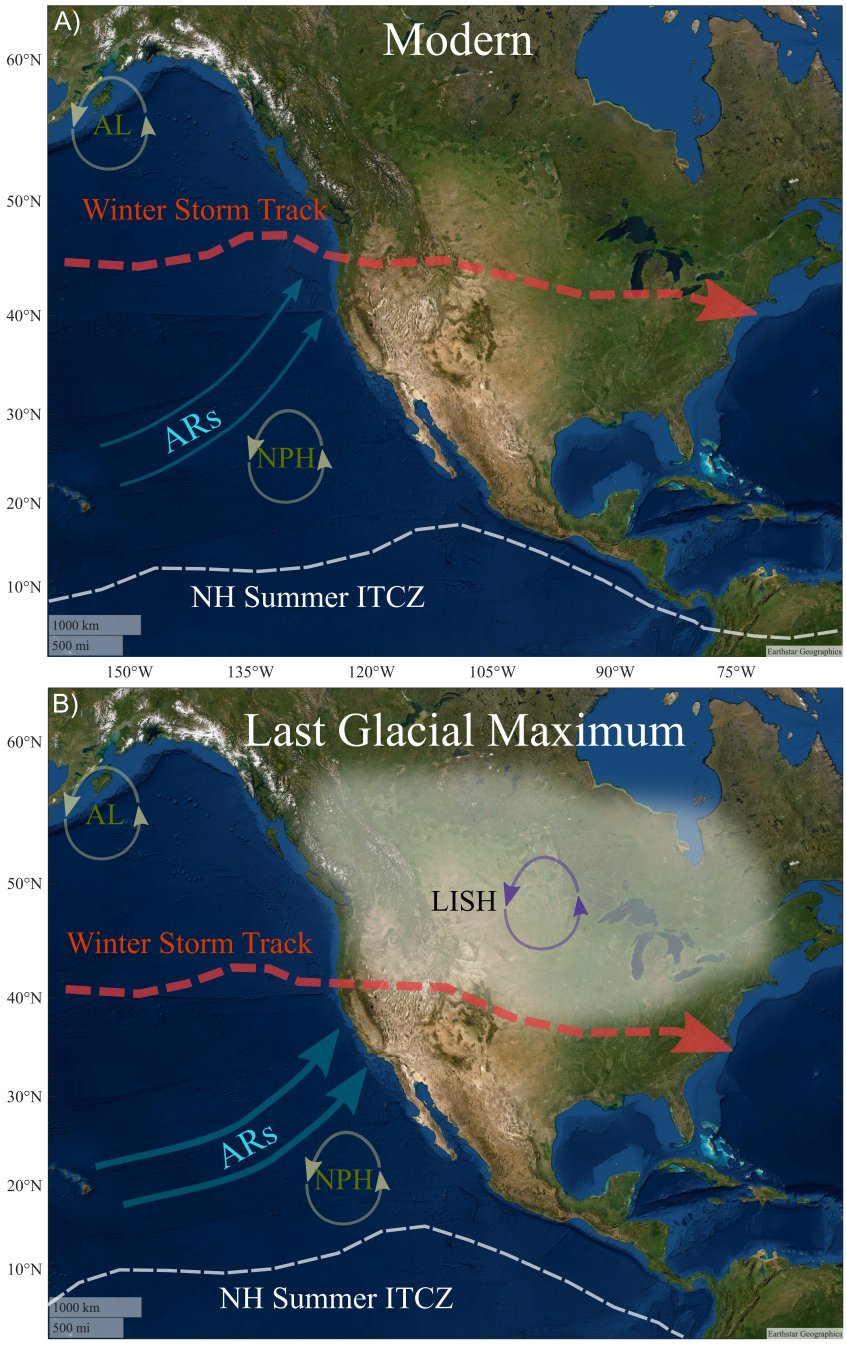


Figure 1.3: Diagram of North American climate during the modern day and LGM. White shading indicates the maximum of extent of North American ice sheets during the LGM. AL is the Aleutian low; NPH is the north Pacific high; and LISH the high pressure system over the Laurentide ice sheet. The position of the ITCZ in northern hemisphere summer is marked with a white dashed line. The red dashed arrow shows the North American winter storm track; and blue solid arrows the trajectory of atmospheric river (ARs) events. Data taken from Oster et al. (2019).

from LCCs to reconstruct precipitation-evaporation over the Bonneville Basin during the last deglaciation. As lacustrine cave carbonates can be dated with high precision U-Th ages this will help constrain the timings of increased moisture supply to the Bonneville Basin during Heinrich Stadial 1.

Terminal Great Basin lakes as paleo-hydrology archives

The expansion and contraction of Great Basin terminal lakes have been used extensively to reconstruct shifts in moisture supply to the Great Basin region (e.g. Oviatt et al., 1994; McGee et al., 2018; Santi et al., 2019). While lakes located near each other display similar timings of rise and fall during the last glaciation, the timings of lake highstands vary across the Great Basin suggesting a spatially heterogeneous moisture supply (Santi et al., 2019). Multiple studies have attempted to utilise numerous paleo-lake level reconstructions to constrain spatial and temporal shifts in moisture supply to the Great Basin, and hence the climate mechanism responsible for shifting hydrology (McGee et al., 2018; Santi et al., 2019). Despite the large age uncertainties and low resolutions of paleo-lake level reconstructions, a north-west progression of lake highstands through time has been identified, with lakes occurring on a line parallel to Panamint-Bonneville line appearing to display concurrent lake highstands (Figure 1.4) (McGee et al., 2018; Santi et al., 2019). The usefulness of Lake Bonneville in constraining shifts in Great Basin paleo-hydrology is complicated by a period of overflow from Lake Bonneville which decoupled lake level from regional hydrology. This thesis aims to supplement the current literature by generating paleo-hydrology records from Lake Bonneville with lower age uncertainties capable of reconstructing shifts in paleo-hydrology during the period of overflow.

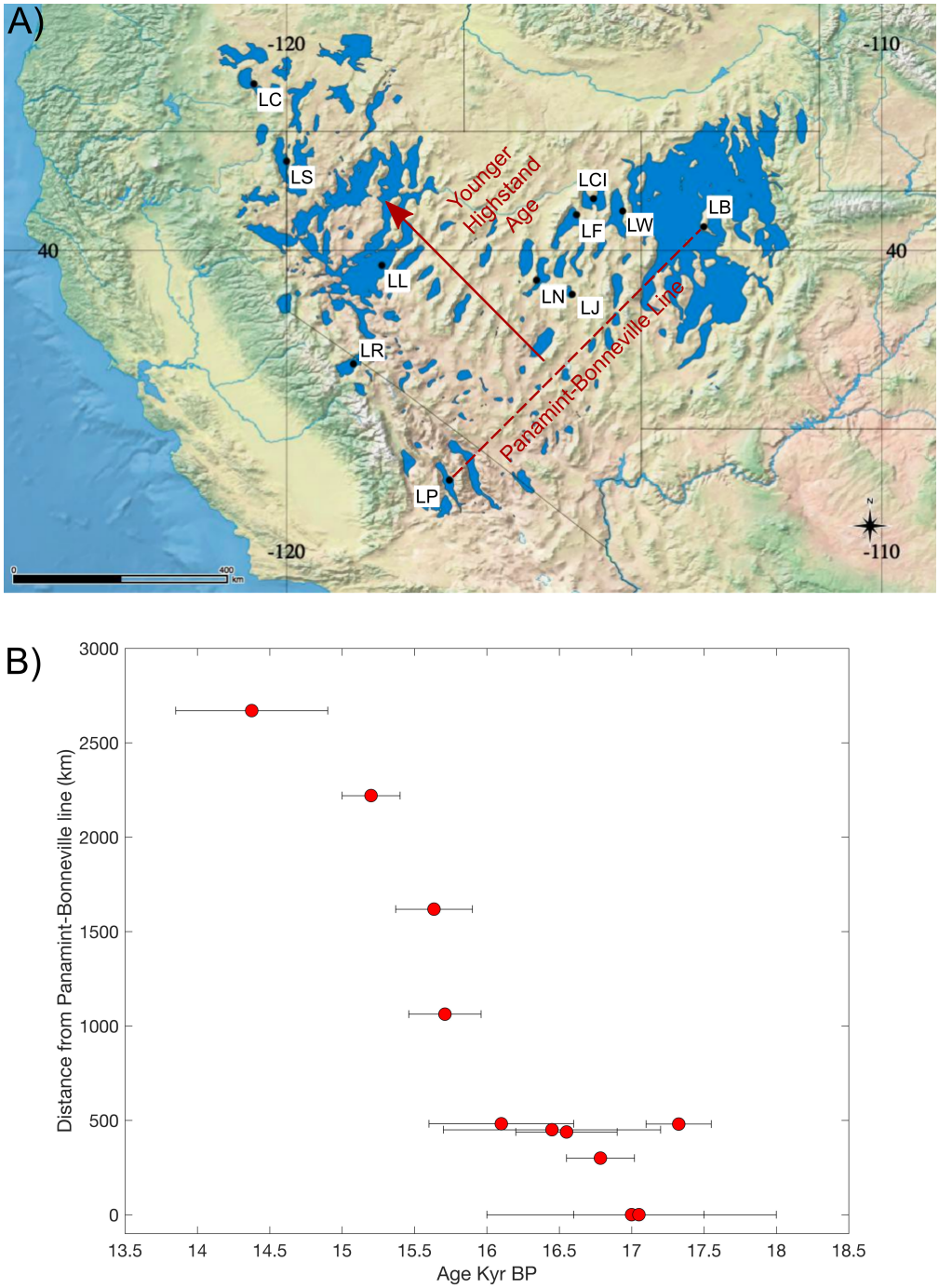


Figure 1.4: A) A map showing the greatest extents of Great Basin terminal lakes during the last glacial cycle. Terminal lakes in the Great Basin region where paleo-lake level reconstructions have been attempted are labelled: LB - Lake Bonneville; LC - Chewaucan; LCl - Lake Clover; LF - Lake Franklin; LJ - Lake Jakes; LL - Lake Lahontan; LN - Lake Newark; LP - Lake Panamint; LR - Lake Russel; LS - Lake Surprise; LW - Lake Waring. Figure altered from Santi et al. (2019). B) Age estimates with 95% confidence intervals for lake highstands during the last deglaciation plotted against distance from a line connecting Lakes Panamint and Lake Bonneville (Dashed line in A) for lakes labelled in A. Data from McGee et al. (2018); Santi et al. (2019).

1.5 The tropical Pacific and the El Niño Southern Oscillation

The El Niño Southern Oscillation

The tropical Pacific is perturbed from its mean state quasi-periodically by ENSO events which form due to coupled ocean-atmosphere interactions (Bjerknes, 1969). ENSO events are the primary source of inter-annual climate variability in the tropics (Cane, 2005; Vecchi and Wittenberg, 2010) and have the capacity to dramatically impact major areas of human population through droughts, flooding or failure of fisheries (McPhaden et al., 2006). As such, understanding how the ENSO system will evolve in the future, under increasing anthropogenic climate change, is crucial in order to mitigate the impact on human populations. Whilst some modeling studies predict an increase in ENSO intensity under future greenhouse warming (Cai et al., 2015, 2018), the future evolution of the ENSO system remains uncertain due to the lack of inter-model agreement (Cai et al., 2018) and incomplete characterization of ENSO processes in general circulation models (Bellenger et al., 2014).

Tropical Pacific mean state and Walker Circulation

Atmospheric circulation over the tropical Pacific is controlled by the Pacific Walker Cell (Bjerknes, 1969). In the mean state, trade winds (tropical easterlies) blow from east to west across the tropical pacific, causing warm equatorial water to pool in the west of the tropical Pacific, forming the western Pacific warm pool (WPWP). The WPWP is defined as an area of sea surface temperature (SST) $> 28\,^{\circ}\mathrm{C}$ between approximately 20°N - 20°S and 100°E - 135°W. The westward flow of warm surface waters results in upwelling of cooler deep waters and a shallowing of the thermocline off the west coast of South America. The warm SST of the WPWP cause deep convection of moisture laden air which rises and cools causing low pressure and large amounts of precipitation over the WPWP. The rising air then reaches neutral buoyancy, returns eastward, before

descending over the cool waters of the western South American margin, forming a region of high pressure and low precipitation. The pressure gradient over the tropical Pacific caused by the upwelling and downwelling limbs of the Walker Cell further strengthens the trade winds.

ENSO events

The mean state of the tropical Pacific is inherently unstable and coupled ocean-atmosphere interactions lead to the development of ENSO events, in the form of El Niño or La Niña events (Bjerknes, 1969; McPhaden et al., 2006). During El Niño events, trade winds over the tropical Pacific weaken, and can even reverse direction, resulting in the WPWP being pulled to the east and a subsequent reduction in upwelling off the western South American margin (McPhaden et al., 2006). Consequently, a warm SST anomaly develops in the eastern tropical Pacific, and a cold SST anomaly in the western tropical Pacific. The rising limb of the Walker Cell follows the eastward migration of the WPWP, reducing rainfall over the western tropical Pacific. Conversely during La Niña events, the trade winds strengthen, further warming waters in the western tropical Pacific, generating a warm SST anomaly (McPhaden et al., 2006). The strengthened trade winds drive increased upwelling off the the western South American margin, cooling SST here and generating a negative SST anomaly in the eastern tropical Pacific. This results in a strengthening of the Pacific Walker cell, increasing rainfall over the WPWP and decreasing rainfall over western South America.

Sea surface temperature anomalies in the Niño 3.4 region of the equatorial Pacific (5°N - 5°S, 170°W - 120°W) statistically capture the state of the ENSO system (Trenberth, 1997; Bamston et al., 1997; Kaplan et al., 1998). Warm (cold) SST anomalies greater than 0.5 °C in the Niño 3.4 region are indicative of El Niño (La Niña) conditions. The NOAA Climate Prediction Center officially characterises an ENSO event when the 3-month running mean SST anomaly in the Niño 3.4 region exceeds ±0.5 °C for five consecutive months.

Global impact of ENSO events

The impact of ENSO events extends well beyond the tropical Pacific (Figure 1.5) through both atmospheric (e.g. Bjerknes, 1969; McPhaden et al., 2006; Stan et al., 2017) and oceanic teleconnections (e.g. Gordon and Fine, 1996; Frischknecht et al., 2015; Vergara et al., 2017), influencing the pattern of seasonal winds, temperature and precipitation globally (Davey et al., 2014). The term "teleconnection" here refers to a statistically significant remote response concurrent or time lagged to an ENSO event in the tropical Pacific (Yeh et al., 2018). Global teleconnections are not constant for every ENSO event, and are thought to be impacted by the spatial pattern of the individual ENSO event, the mean state of oceans outside the tropical Pacific and the extent of terrestrial and sea ice (Yeh et al., 2018). However, the controls on ENSO teleconnections are hard to assess due to the short length of instrumental records. As such, the understanding of how both the ENSO system and the global response to ENSO events will change under global warming is currently limited.

Reconstructing the ENSO system through the Holocene

The small number of ENSO events captured in decadal length instrumental record makes it difficult to detect robust responses of the ENSO system to changing climatic forcings (Grothe et al., 2019). Reconstructions of the frequency and magnitude of ENSO events from paleo-climate archives provide estimates of how the ENSO system has varied under a variety of natural forcing scenarios (e.g. Koutavas and Joanides, 2012; Cobb et al., 2013; McGregor et al., 2013; Carré et al., 2014; Chen et al., 2016; Grothe et al., 2019). Paleo-ENSO archives can therefore provide an estimate of the natural range of decadal scale ENSO variability (Cobb et al., 2013; Chen et al., 2016) and test the ability of climate models to reconstruct ENSO under differing climate forcings (Schmidt, 2010; Emile-Geay et al., 2016).

However, many paleo-ENSO archives do not have sufficient resolution to resolve individual ENSO events (Koutavas and Joanides, 2012) and many coral reconstructions,

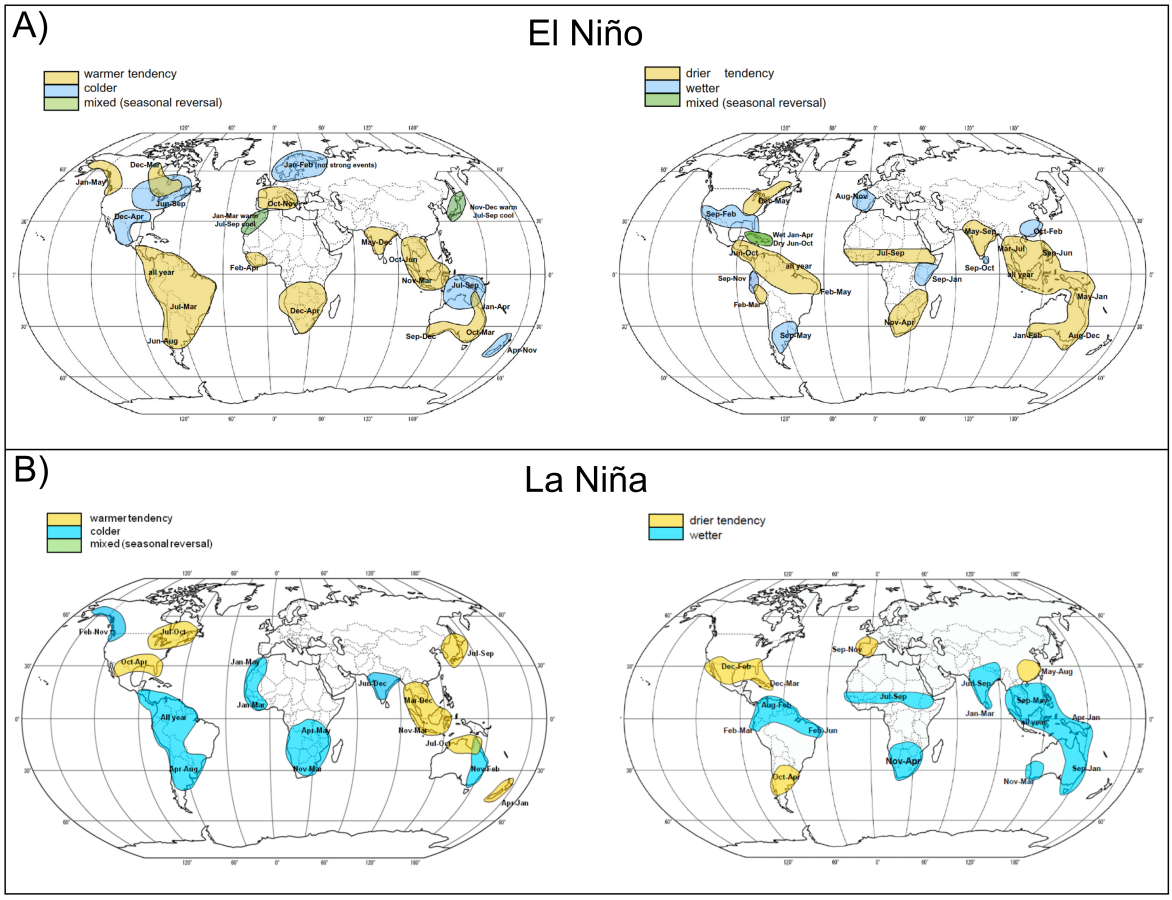


Figure 1.5: The global distribution and seasonality of teleconnections during: A) El Niño events; and B) La Niña events. The left hand maps show temperature anomalies during ENSO events and the right hand maps precipitation anomalies. Figure adapted from Davey et al. (2014).

while seasonal in resolution, are too short to resolve centennial scale shifts in the ENSO system from high decadal scale variability (Cobb et al., 2013; Grothe et al., 2019). Despite these limitation, a review of available paleo-ENSO reconstructions across the tropical pacific suggests a broad reduction in ENSO between 5000 Yr. (BP) - 3000 Yr. (BP) (Emile-Geay et al., 2016).

Speleothems, due to their long periods of continuous growth and ability to be sampled at sub-annual resolution, provide a promising target for future paleo-ENSO reconstructions. In this thesis (Chapter 4), I test the suitability of speleothems to reconstruct past shifts in the magnitude and frequency of ENSO events, and increase the number of windows of paleo-ENSO reconstruction from a Northern Borneo speleothem from the heart of the WPWP.

Chapter 2

Developing the LakeCalc model to assess the combined use of Ca-isotopes and trace elements to reconstruct basin wide Precipitation-Evaporation

Abstract

Lake hydrology and chemistry respond significantly to changes in precipitation-evaporation (P-E) over their drainage basins. This chapter seeks to define how lake chemistry, specifically Mg/Ca, U/Ca and $\delta^{\frac{44}{42}}Ca$, responds to shifts in basin wide P-E, and whether these chemical and isotopic changes are sufficiently large to be measurable in precipitated lacustrine cave carbonates (LCCs). I am looking to further develop the existing use of LCCs to reconstruct basin wide shifts in P-E using a more robust multi-proxy approach. This chapter defines a new software tool LakeCalc, a single box model designed to reconstruct the volume and chemical composition of Lake Bonneville over its rise and fall during the last glaciation 30 kyr (BP) - 13 kyr (BP). Using LakeCalc, I define the required shifts in the balance between river inflow and evaporation that are necessary to produce measurable shifts in LCC Mg/Ca, U/Ca and $\delta^{\frac{44}{42}}Ca$. In specific situations (e.g. without major changes to the configuration of the drainage basin) these LCC proxies can be used to contribute to P-E reconstructions over the Bonneville Basin.

Contents

2.1 Introduction 30

2.2 Lake Bonneville overview 33

2.2.1 Geology of the Bonneville catchment area 36

2.3 Lacustrine Cave Carbonates (LCCs) as a multi-proxy archive for reconstructing P-E 38

2.3.1 LCCs as archives of lake water chemistry 38

2.3.2 Calcium carbonate precipitation as a function of regional P-E over the Bonneville Basin 38

2.3.3 Calcium isotopes as proxy for reconstructing past shifts in $CaCO_3$ precipitation in Lake Bonneville 41

2.3.4 Developing a multi-proxy approach to reconstructing changes in P-E over the Bonneville Basin 43

2.4 LakeCalc description 45

2.4.1 LakeCalc assumptions 45

2.4.2 Reconstructed LakeCalc inputs 49

2.4.3 Reconstructed LakeCalc outputs 51

2.4.4 Model equations 54

2.5 Modelled controls on the Mg/Ca, U/Ca and $\delta^{\frac{44}{42}}Ca$ composition of LCCs 59

2.5.1 PICP control on LCC composition 59

2.5.2 Sensitivity testing 64

2.5.3 Other controls on LCC composition 69

2.6 The potential for LCCs to reconstruct shifts in P-E over the Bonneville Basin 70

2.7 Summary 73

2.1 Introduction

The last glaciation has been identified as a period of dramatic expansions in the size of multiple terminal lakes in the Great Basin region of the southwestern United States (e.g. Oviatt, 1997, 2015; Santi et al., 2019). The presence of large freshwater lakes in this currently arid region suggests a dramatic shift in regional climate. The largest of these, Lake Bonneville, occupied a series of connecting basins in the eastern Great Basin region. Between 30 kyr before 1950 (BP) and 13 kyr (BP), Lake Bonneville expanded from an ephemeral lake to its maximum size covering over 41,000 km^2, before dramatically shrinking to 4200 km^2 forming the modern Great Salt Lake (Spencer et al., 1985). Much effort has been put into reconstructing the lake-level history of Lake Bonneville over its rise and fall between 30 kyr (BP) and 14 kyr (BP) as it provides a valuable archive of shifting precipitation - evaporation (P-E) over the Great Basin region.

Multiple methods have been used to reconstruct changes in P-E over the Bonneville Basin, with the most common being: the mapping and dating of paleo-shorelines (e.g. Oviatt, 2015); and reconstructing changes in lake water chemistry (e.g. Hart et al., 2004; McGee et al., 2012).

The value of paleo-shoreline reconstructions is well recognised with many studies utilising terminal lake systems to track changes in regional P-E (e.g. Oviatt, 1997; Armitage et al., 2015). The lack of an outflow makes lake level in terminal lakes highly dependent on P-E over their drainage basin, as all solution which enters the lake has to be removed by evaporation (Oster et al., 2015a). While paleo-shoreline records allow for accurate reconstructions of paleo-lake level, they often suffer from low resolution and large dating uncertainties (McGee et al., 2012). This makes reconstructing the timing and rates of lake level change, as well as their relationship with other paleoclimate records, difficult. Furthermore, lake level is only an indicator of regional P-E for terminal basins. During periods of riverine outflow, lake level will be controlled by the height of the riverine outflow as opposed to regional paleo-climate (Miller, 2016). While Lake

Bonneville is a terminal basin for most of its lake cycle, it overflows the Bonneville Basin for approximately 3500 years between 18.3 kyr (BP) - 14.8 kyr (BP) (Oviatt, 2015). Unfortunately, this precludes paleo-shoreline reconstructions from providing insights into Lake Bonneville's response to Great Basin climate during the "mystery interval" (Denton et al., 2006), a period where other Great Basin terminal lakes experienced shifts in lake level (Broecker et al., 2009; Broecker and Putnam, 2012).

In order to overcome the limitations of paleo-shoreline deposits, studies have started attempting to reconstruct past changes in Bonneville Basin hydrology from shifts in lake water chemistry (Hart et al., 2004; McGee et al., 2012). This has been aided by the identification of a new class of lacustrine calcium carbonate deposits in the Bonneville Basin, lacustrine cave carbonates (LCCs). LCCs form as dense layered carbonates which precipitated directly onto cave walls and other nucleation sites in protected spaces in Lake Bonneville (McGee et al., 2012). The ability for LCCs to record lake water chemistry at the time of precipitation, and be absolutely dated, allows high resolution records of Lake Bonneville chemistry to be generated (McGee et al., 2012). LCCs have already been used to generate high resolution records of the oxygen isotope composition of Lake Bonneville in an attempt to reconstruct shifts in basin wide P-E (McGee et al., 2012). As evaporation preferentially removes light oxygen isotopes and rainfall replenishes the lake with heavier oxygen isotopes shifts in regional P-E should alter the oxygen isotope composition of Lake Bonneville. However, controls on the oxygen isotope composition of waters flowing into a lake are complex, numerous and often non-local, including rainfall moisture source, rainfall amount or the atmospheric condensation temperature of rainfall (e.g. Dansgaard, 1964; Ayalon et al., 1998; LeGrande and Schmidt, 2006). As such, identifying a solely P-E signal is difficult.

In order to generate increasingly robust geochemical reconstructions of Bonneville Basin P-E, I investigate the ability of calcium isotopes and trace element to calcium ratios recorded in LCC deposits to form an additional multi-proxy tool. Shifts in P-E over Lake Bonneville, would alter the degree to which evaporation concentrates solutes

in lake waters and hence the amount of $CaCO_3$ precipitation. $CaCO_3$ precipitation preferentially incorporates lighter Ca isotopes (e.g. Gussone et al., 2003; Owen et al., 2016), and certain elements (e.g. Day and Henderson, 2013; Wassenburg et al., 2016; Jamieson et al., 2016), altering both the Ca isotope composition and trace element to calcium ratios of lake waters. Changes in the magnitude of $CaCO_3$ precipitation will alter the degree to which the Ca isotope and trace element composition of lake waters are altered. While there are multiple controls on Ca isotope and trace element composition in both lake waters and precipitated carbonates, using multiple proxies increases the confidence that a robust $CaCO_3$ precipitation signal can be reconstructed. However, in order for lake water trace element and Ca isotope compositions to be used to identify past shifts in P-E, the shifts in the proxy values must be sufficiently large that they can be reconstructed from LCC deposits and therefore greater than instrument uncertainty.

This chapter introduces a new geochemical box model (LakeCalc) designed to calculate the chemical evolution of trace element to calcium ratios (Mg/Ca and U/Ca) and calcium isotope composition of Lake Bonneville's waters and secondary lake carbonates over its highstand period. The LakeCalc model outputs are then used to investigate whether the modelled perturbations to calcium isotopes and trace element to calcium ratios are sufficiently large that they can contribute towards robust reconstructions of shifting $CaCO_3$ precipitation in Lake Bonneville and hence regional P-E.

2.2 Lake Bonneville overview

Lake Bonneville (41°N, 113°W) was a large freshwater to brackish lake in the Great Basin region of the Western United States, occupying the basin in which the modern Great Salt Lake resides (Figure 2.1). In this study, Lake Bonneville refers to the most recent cycle of lake transgression (an increase in lake volume) and regression (a decrease in lake volume) in this basin, corresponding to the period between 30 kyr (BP) and 13 kyr (BP) (Oviatt, 2015). During the last glaciation, Lake Bonneville rose from a ephemeral lake to a maximum size of over 40,000 km^2, before rapidly falling to the size of the modern Great Salt Lake, 4200 km^2 (Spencer et al., 1984, 1985; Oviatt, 2015).

Lake Bonneville is of particular interest to this study as extensive knowledge of its lake level history, and confirmed presence of LCC deposits, make it an ideal natural laboratory for testing whether shifts in basin wide P-E can be reconstructed from the calcium isotope and trace element composition of LCCs.

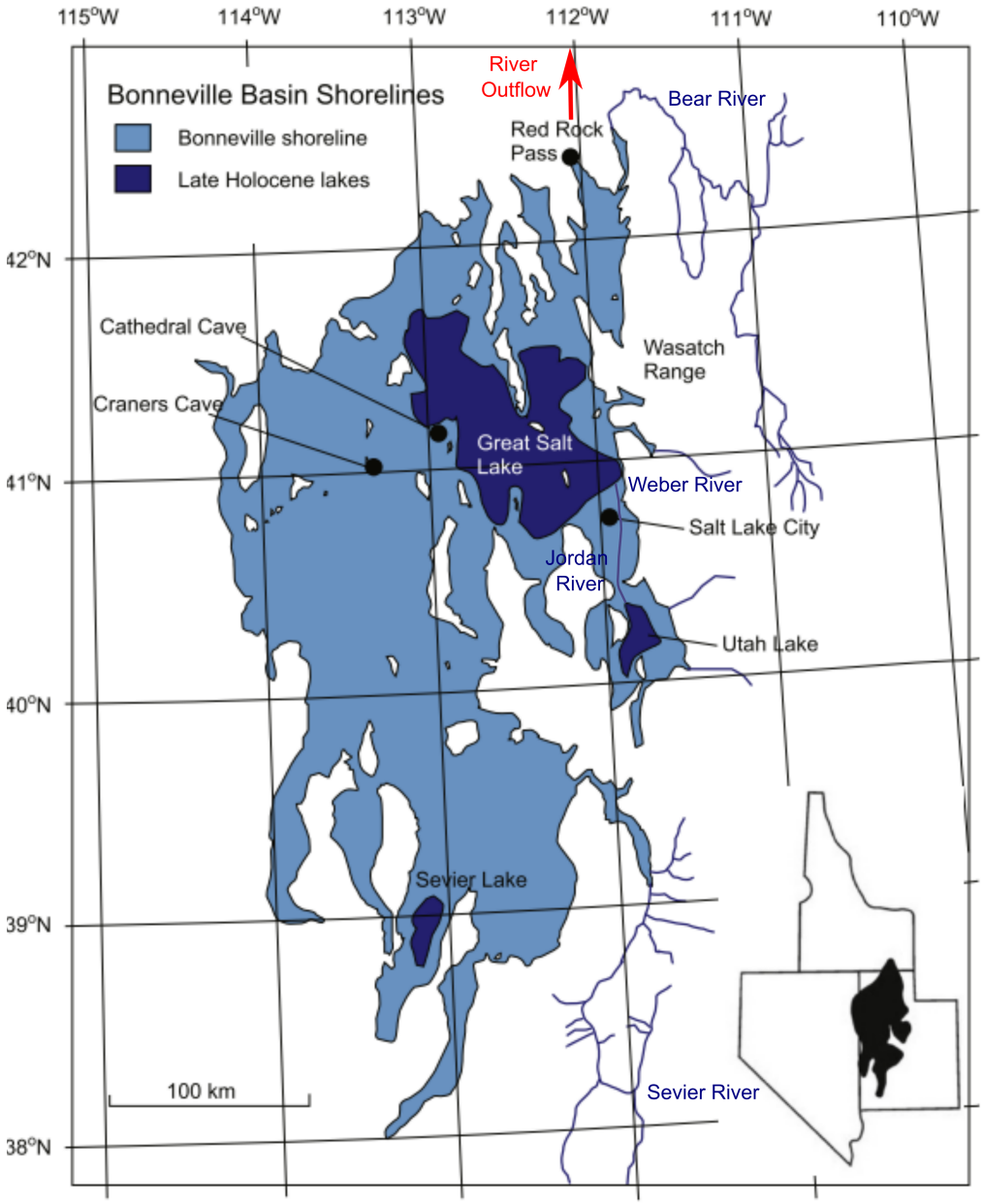


Figure 2.1: A regional map showing: the maximum extent of Lake Bonneville at the Bonneville shoreline; the major inflows into Lake Bonneville, annotated in blue; Lake Bonneville's outflow at Red Rock Pass, annotated in red; and the shorelines of the modern Great Salt Lake, Utah Lake and Sevier Lake. Figure altered from McGee et al. (2012).

Over 360 radiocarbon dates have been calculated from Lake Bonneville paleo-shoreline deposits to generate a near continuous record of lake level over its rise and fall, as summarised in Figure 2.2 (Oviatt, 2015). Between ~30 kyr (BP) and ~18.3 kyr (BP) lake level rose from 1280 metres above sea level (masl; corrected for isostatic rebound) to

the Bonneville shoreline at 1550 masl (Oviatt, 2015; Vennin et al., 2019). Lake level rise was not continuous and was punctuated by 3-5 small regressions (Oviatt et al., 1992; Oviatt, 1997; Patrickson et al., 2010). The largest and best documented of these is the Stansbury Oscillation, where lake level stalled and oscillated around the Stansbury shoreline (1370 masl) for approximately two thousand years (∼26.4 kyr BP - ∼24.5 kyr BP) (Patrickson et al., 2010).

At ∼18.3 kyr (BP) the collapse of the basin wall at Red Rock Pass (Figure 2.1) resulted in lake level falling almost instantaneously by approximately 130m (Gilbert, 1890; Currey, 1983; Miller et al., 2013; Oviatt, 2015). A new stable lake shoreline, the Provo shoreline, was then formed at the height of the outflow (1444 masl). During the period of overflow lake level was fixed by the height of the riverine outflow, and no longer responded to increases or decreases in basin-wide P-E (Miller, 2016).

Overflow continued until ∼14.8 kyr (BP), when lake level started to fall (Godsey et al., 2011; Miller, 2016). The regression of the lake was rapid with lake level falling to approximately that of the modern Great Salt Lake (1280 masl) by 13 kyr (BP) (Oviatt, 2015).

In order to model Lake Bonneville, I simplify the lake level reconstruction of Oviatt (2015) by considering five successive periods of lake evolution where lake level either rises, falls or remains constant between well preserved paleo-shorelines (Figure 2.2). The initial transgression (T1) where lake level rose from 1280 masl to 1370 masl between 30 kyr (BP) and 26.4 kyr (BP); a standstill period (S1) corresponding to the Stansbury Oscillation where the lake level remained constant at 1370 masl between 26.4 kyr (BP) and 24.5 kyr (BP); a second transgression (T2) where lake level rose from 1370 masl to 1550 masl between 24.5 kyr (BP) and 18.3 kyr (BP); a period of overflow (O1) at 1440 masl 18.3 kyr (BP) and 14.8 kyr (BP); and finally a period of regression (R1) where lake level fell from 1440 masl to 1280 masl 14.8 kyr (BP) and 13 kyr (BP) (Figure 2.2).

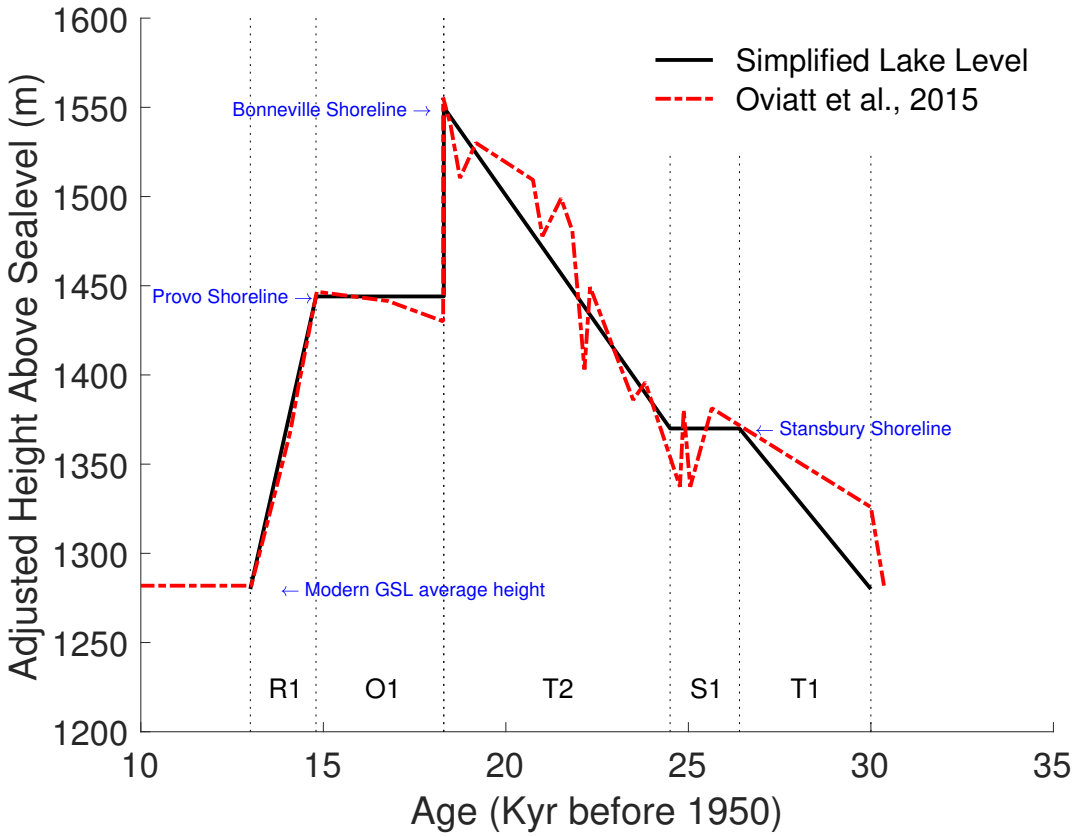


Figure 2.2: A comparison between the lake level reconstruction of Oviatt (2015) and the simplified lake level history used in this study. The simplified lake level history is split into 5 sections: T1: Transgression 1; S1: Standstill 1; T2: Transgression 2; O1: Overflow 1; and R1: Regression 1, as explained in the main text. In this figure the separate sections are divided by vertical dotted lines. Lake level is given in adjusted metres above sea-level accounting for isostatic rebound caused by the regression of Lake Bonneville. The major paleo-shorelines of Lake Bonneville: the Stansbury shoreline, the Bonneville shoreline, the Provo shoreline and the average lake height of the modern Great Salt Lake (GSL) are annotated in blue text.

2.2.1 Geology of the Bonneville catchment area

The large catchment area of the Bonneville basin contains many heterogeneous rock types. During the last glaciation, the hydrological budget of Lake Bonneville was dominated by three rivers, the Bear River, the Weber River and the Sevier River (Figure 2.1) (Jones et al., 2009). Due to differences in catchment geology the chemical composition of each river was distinct. The Bear River drained areas to the north and east of Lake Bonneville, predominately weathering volcanic silicate and carbonate rocks (Hart

et al., 2004) The Weber River drained areas immediately to the east of the modern Great Salt Lake in the Wasatch mountain range, predominately weathering volcanic silicates (Jones et al., 2009). The Sevier River drained areas south of Lake Bonneville primarily weathering sulphate rich sedimentary rocks, including halite (FETH, 1959; Hart et al., 2004).

The range of rock types weathered by different rivers draining into Lake Bonneville could result in a variety of differing Ca isotope compositions in riverine inflow. However, the range of $\delta^{\frac{44}{42}}Ca$ in terrestrial rocks is small with silicates measured to have a range of 0.4‰ - 0.7‰, evaporites 0‰ - 0.8‰ and carbonates 0.1‰ - 0.5‰ (Tipper et al., 2010). This suggests that the heterogeneous lithology of the Lake Bonneville catchment area is unlikely to result in large shifts in $\delta^{\frac{44}{42}}Ca$ between rivers flowing into Lake Bonneville. Furthermore, strontium isotopes from Lake Bonneville shoreline tufas remained constant between the Stansbury, Provo and Bonneville shorelines suggesting the ratio of solution supply from rivers flowing into Lake Bonneville remained approximately constant over the highstand of Lake Bonneville (Hart et al., 2004).

2.3 Lacustrine Cave Carbonates (LCCs) as a multi-proxy archive for reconstructing P-E

2.3.1 LCCs as archives of lake water chemistry

A new class of lacustrine carbonates, lacustrine cave carbonates (LCCs), have been identified in the Bonneville Basin (McGee et al., 2012). LCCs form as dense layered calcium carbonates deposits which precipitate directly from lake waters in protected spaces such as caves or crevices, which provide the nucleation sites, low detrital input and still water conditions they require to form (McGee et al., 2012). The protection from detrital input offered to LCCs by their host caves and crevices ensures clean $CaCO_3$ with the potential for high precision U-Th dating (McGee et al., 2012). In a similar way to cave secondary $CaCO_3$ precipitates (speleothems), LCCs provide a continuous record of the chemistry of solutions from which they precipitated. The close replication of isotope and trace element timeseries and synchronous cessations of growth in LCCs from cave sites 50 km apart, suggests LCCs are recording shifts in Lake Bonneville water composition as opposed to site specific processes (McGee et al., 2012). LCCs can therefore provide a continuous multi-proxy archive of lake water chemistry over the duration of growth.

In Lake Bonneville, LCC deposits precipitated between 25 kyr (BP) and 13.6 kyr (BP) (McGee et al., 2012) covering periods of significant hydrological change as the climate shifted from peak glacial conditions during the last deglaciation (Figure 2.2). It is the nature of these hydrological changes that I seek to reconstruct.

2.3.2 Calcium carbonate precipitation as a function of regional P-E over the Bonneville Basin

Mineral precipitation occurs when minerals reach a critical supersaturation in solution. In terminal lake systems, lake waters are concentrated by evaporation and diluted by

solution inflows (groundwater, riverine or rainfall). The balance between inflowing solution and evaporation in a lake is set by the regional P-E. If rainfall increases (decreases) relative to evaporation over a lake's drainage basin, solution inflows will increase (decrease) relative to evaporation, diluting (concentrating) lake waters. Assuming a critical level of supersaturation at which minerals precipitate, shifts in regional P-E, and hence the degree to which solutes are concentrated in lake waters, will alter the amount of mineral precipitation from a lake.

$CaCO_3$ is commonly the first element to precipitate upon the concentration of lake waters (Spencer et al., 1985; Jones et al., 2009). The saturation index of $CaCO_3$ (SI_{CaCO_3}) is controlled by both the concentration of Ca^{2+} and $CO3^{2-}$ and defined in Equation 2.1. A $SI_{CaCO_3} = 0$ indicates the solution is in thermodynamic equilibrium with the mineral phase. Whereas, a $SI_{CaCO_3} > 1$ and $SI_{CaCO_3} < 1$ suggest the solution is overstated and undersaturated respectively:

$$SI = log\left(\frac{\gamma_{Ca^{2+}}\,\gamma_{CO_3^{2-}}\,[Ca^{2+}]\,[CO_3^{2-}]}{K_{SP}}\right) \tag{2.1}$$

Where, K_{SP} = the solubility product of $CaCO_3$, $\gamma_{Ca^{2+}}$ = the activity coefficients of calcium ions, $\gamma_{CO_3^{2-}}$ = the activity coefficients of carbonate ions, $[Ca^{2+}]$ = the concentration of calcium ions, and $[CO_3^{2-}]$ = the concentration of carbonate ions (Equation from Renforth and Henderson, 2017).

Increases in $[Ca^{2+}]$ or $[CO_3^{2-}]$ will result in increases in SI_{CaCO_3}. Once a critical over-saturation is reached, $CaCO_3$ precipitation will occur. In theory this critical oversaturation will be a $SI_{CaCO_3} > 0$, however in practice the precipitation of $CaCO_3$ is inhibited in natural waters by a variety of factors including organics, magnesium, phosphates and sulphates so the critical SI_{CaCO_3} required to force $CaCO_3$ precipitation is commonly greater than 0 (e.g. Berner, 1975; Nielsen and DePaolo, 2013). The concentration of Ca^{2+} in lake waters is controlled by the Ca^{2+} concentration of solutions flowing into the lake, evaporation of lake waters and precipitation of $CaCO_3$. Controls on the concentration of CO_3^{2-} are, however, more complex. CO_3^{2-} concentration can be

increased by increasing alkalinity in lake waters, or changes in PH altering the balance of dissolved inorganic carbon species in the solution. In terminal lakes, large increases in salinity and hence dissolved cations such as Mg^{2+} and Na^{+} can result in a large increase in alkalinity and hence increases in the concentration of non-conservative anions, such as CO_3^{2-} and HCO_3^{-} in order to maintain charge balance. If this occurs, then CO_3^{2-} concentration and hence SI_{CaCO_3} will increase, and $CaCO_3$ precipitation can result. As the threshold SI_{CaCO_3} for precipitation of $CaCO_3$ should remain approximately constant, and the precipitation of $CaCO_3$removes Ca^{2+} and CO_3^{2-} in a 1:1 molar ratio, if precipitation is forced by increasing CO_3^{2-} concentration then the concentration of Ca^{2+}in lake waters must decrease. In alkali lakes this results in lake waters having very small Ca^{2+}: CO_3^{2-} ratios (e.g. in Mono Lake $a_{Ca^{2+}}$: $a_{CO_3^{2-}} = 0.0001$; Nielsen and DePaolo, 2013), as well as high Mg/Ca ratios (e.g. in Mono Lake Mg/Ca = 14.5 mol mol^{-1}; Nielsen and DePaolo, 2013). However, this appears to not have been the case during the rise of Lake Bonneville where the lake waters were thought to be fresh from ostracode assemblages (Jones et al., 2009) and with Mg/Ca ratios sufficiently low to even allow the precipitation of calcite instead of aragonite during the freshest portions of the lake's history (e.g. Spencer et al., 1985; McGee et al., 2012). A previous study modelling the chemical evolution of Lake Bonneville's waters indicated that despite large changes in the concentration of Mg and other cations, Ca concentration stayed approximated constant over the highstand of lake Bonneville, buffered by $CaCO_3$ precipitation. As such, it is assumed in this study that concentration of Ca in lake waters is the dominant mechanism by which $CaCO_3$ precipitation is forced, as opposed to shifts in alkalinity, and calcium concentration can be used to be approximate the critical SI_{CaCO_3} at which $CaCO_3$ precipitation occurs.

In Lake Bonneville there is evidence of both significant changes in P-E, from 270 m shifts in lake level (Figure 2.2); and $CaCO_3$ precipitation, from LCCs (McGee et al., 2012), shoreline tufas (Vennin et al., 2019) and sediment cores (Oviatt et al., 1994). In this chapter, I use LakeCalc to quantify whether shifts in regional P-E were large enough

to generate measurable shifts in LCC chemistry, and hence whether LCCs should be able to be used to reconstruct changes in regional P-E.

2.3.3 Calcium isotopes as proxy for reconstructing past shifts in $CaCO_3$ precipitation in Lake Bonneville

The precipitation of $CaCO_3$ fractionates Ca isotopes, with lighter isotopes preferentially included in the solid phase (e.g. Gussone et al., 2005; Tang et al., 2008; Reynard et al., 2011; Owen et al., 2016). This fractionation has been used by multiple studies in a variety of environments to reconstruct past shifts in the magnitude of $CaCO_3$ precipitation. In speleothems, variations in Ca isotope composition ($\delta^{\frac{44}{42}}Ca$) have been used to reconstruct the proportion of Ca removed from solution by the precipitation of secondary carbonate minerals in the overlying karst (Owen et al., 2016), a process termed prior calcite precipitation (PCP) (Fairchild and Treble, 2009). In marine environments, shifts in $\delta^{\frac{44}{42}}Ca$ have been used to reconstruct imbalances between Ca inputs and removal via $CaCO_3$ precipitation (Blättler et al., 2011), with the marine environment similar in concept to a closed basin lake.

Much like marine environments, the $\delta^{\frac{44}{42}}Ca$ of Lake Bonneville's waters will be set by the balance between the magnitude and isotopic composition of Ca inputs and outputs. In Lake Bonneville, the dominant Ca input was dissolved Ca in river inflow, with groundwater input negligible due to the high hydrostatic gradient of lake waters (Spencer et al., 1985). From measurements in sediments from multiple locations, the replication of isotopic and elemental analyses suggest the lake was well mixed (Hart et al., 2004; McGee et al., 2012). In a well mixed lake, riverine output would have a $\delta^{\frac{44}{42}}Ca$ equal to lake waters, and hence unable to alter the isotopic composition of lake waters (Equation 2.16). As such, the $\delta^{\frac{44}{42}}Ca$ of Lake Bonneville can be approximated to be set by the balance between riverine Ca input and $CaCO_3$ precipitation output, summarised by the following isotope balance equation:

$$N_{Ca}.\frac{d}{dt}(\delta^{\frac{44}{42}}Ca_{Lake}) = (\delta^{\frac{44}{42}}Ca_{River} - \delta^{\frac{44}{42}}Ca_{Lake}) \times F_{River} - (\delta^{\frac{44}{42}}Ca_{CaCO_3} - \delta^{\frac{44}{42}}Ca_{Lake}) \times F_{CaCO_3} \quad (2.2)$$

Where N_{Ca} = the total number of moles of Ca in Lake Bonneville (mole); F the number of moles added or lost from the lake by either riverine input or $CaCO_3$ precipitation (mole year^{-1}); and $\delta^{\frac{44}{42}}Ca$ the isotopic composition of either the lake waters, riverine inflow or precipitated $CaCO_3$ (‰). Equation adapted from Blättler et al. (2011).

For a given set of inputs and outputs, lake water $\delta^{\frac{44}{42}}Ca$ will evolve to a steady state value where $\frac{d}{dt}(\delta^{\frac{44}{42}}Ca_{lake}) = 0$. The difference between $\delta^{\frac{44}{42}}Ca$ in precipitated $CaCO_3$ and lake waters is fixed by well known fractionation factors (Equation 2.18) for both aragonite (Gussone et al., 2003) and calcite precipitation (Owen et al., 2016). Consequently, shifts in Ca isotope composition of lake waters can be caused by changes in $\delta^{\frac{44}{42}}Ca$ of riverine input; changes in the dominant polymorph of $CaCO_3$ precipitated from Lake Bonneville and hence $\delta^{\frac{44}{42}}Ca$ fractionation factor; or the relative magnitudes of riverine Ca input and $CaCO_3$ precipitation output (referred to in this chapter as the proportion of inflowing Ca removed by $CaCO_3$ precipitation (PICP) which is equal to $\frac{F_{Carb}}{F_{River}}$). As explained in Section 2.3.2, shifts in basin-wide P-E, will alter the magnitude of $CaCO_3$ precipitation from Lake Bonneville, and hence PICP.

In order to use Lake Bonneville $\delta^{\frac{44}{42}}Ca$ as a proxy for PICP, the impact of changing fractionation factors and riverine $\delta^{\frac{44}{42}}Ca$ must be discounted. Shifts in the dominant polymorph of $CaCO_3$ precipitated from Lake Bonneville can be reconstructed from the sedimentary record (McGee et al., 2012) and hence accounted for. However, shifts in the $\delta^{\frac{44}{42}}Ca$ of riverine input are difficult to identify. The $\delta^{\frac{44}{42}}Ca$ composition of river waters is set by the average $\delta^{\frac{44}{42}}Ca$ composition of material weathered by the river (Tipper et al., 2010). While the global range of river $\delta^{\frac{44}{42}}Ca$ is relatively small, <0.8‰ (Tipper et al., 2010), and the average $\delta^{\frac{44}{42}}Ca$ of weathered material unlikely to rapidly and dramatically change for a single river, shifts in the $\delta^{\frac{44}{42}}Ca$ of riverine inflow cannot be discounted as a potential cause of shifts in Lake Bonneville $\delta^{\frac{44}{42}}Ca$ composition using

Ca isotopes alone.

2.3.4 Developing a multi-proxy approach to reconstructing changes in P-E over the Bonneville Basin

Robust interpretations from a single proxy (e.g. $\delta^{\frac{44}{42}}Ca$) are impeded by not knowing which of the multiple controls are responsible for any measured variability. This study aims to quantify the behavior of multiple proxy systems in LCCs to generate a robust framework for reconstructing shifts in P-E over lake drainage basins.

In addition to fractionating $\delta^{\frac{44}{42}}Ca$, $CaCO_3$ precipitation alters the trace element to calcium ratio (X/Ca) of precipitating solutions. Trace element incorporation into $CaCO_3$ is controlled by well known partition co-efficients, $(D(X)_{CaCO_3\text{- Solution}})$ (e.g. Day and Henderson, 2013; Wassenburg et al., 2016; Jamieson et al., 2016) and the X/Ca of precipitating solutions (Equation 2.13). Elements with $D(X)_{CaCO_3\text{- Solution}} > 1$ are preferentially included in $CaCO_3$ over Ca, while elements with $D(X)_{CaCO_3\text{- Solution}} < 1$ are preferentially left in solution. The precipitation of $CaCO_3$ therefore increases (decreases) the X/Ca of elements in the remaining solution with a $D(X)_{CaCO_3\text{- Solution}}$ less (greater) than one. Similarly to $\delta^{\frac{44}{42}}Ca$, the X/Ca of lake waters are controlled by the magnitude and X/Ca of inputs and outputs from lake waters. While the global range of X/Ca in river waters is much larger (e.g. U concentrations vary between 4.2×10^{-12} mol kg^{-1} and 4.2×10^{-9} mol kg^{-1}; Gaillardet et al. 2003) than for $\delta^{\frac{44}{42}}Ca$ (Tipper et al., 2010), increases or decreases in PICP will also drive shifts in lake water X/Ca. As such, during periods where multiple X/Ca ratios and $\delta^{\frac{44}{42}}Ca$ are demonstrating a coherent signal of changing PICP, greater confidence can be attributed to PICP being the control of lake water chemistry. However, when multiple different proxies are not demonstrating the coherent behaviour expected for a shift in PICP then a different mechanism, such as shifting input compositions or local kinetic factors could be responsible.

In this chapter I consider $\delta^{\frac{44}{42}}Ca$, alongside the Mg/Ca and U/Ca ratios of lake waters to test for changes in PICP. Magnesium (Mg) was selected due to its almost

conservative behavior in lake waters (Jones et al., 2009) and partition coefficients into both calcite and aragonite much lower than one (Table 2.3) allowing preferential removal of Ca by $CaCO_3$ precipitation to have a large effect on lake water Mg/Ca ratios. Uranium (U) was selected as it has a partition coefficient greater than one in aragonite, allowing it to display a contrasting PICP signal to Mg in the aragonite sections of LCCs. Both elements were also chosen as they have sufficiently high concentrations in Lake Bonneville LCCs to be accurately measured. (McGee et al., 2012).

In order to use a multi-proxy approach to reconstruct PICP and hence basin wide P-E, shifts in proxy values in LCCs must be larger than analytical instrument error. To test for this, I develop and use a new lake chemistry model, LakeCalc, to understand the magnitude and direction of shifts of PICP, U/Ca, Mg/Ca and $\delta^{\frac{44}{42}}Ca$ over the rise and fall of Lake Bonneville.

2.4 LakeCalc description

This chapter introduces a single box model (LakeCalc) designed to investigate the impact of shifting P-E on PICP, Mg/Ca, U/Ca and $\delta^{\frac{44}{42}}Ca$ in Lake Bonneville. LakeCalc uses a simplified lake level reconstruction of Lake Bonneville (Figure 2.2) to model shifts in lake volume; lake inputs and outputs; transitions between open and closed basin conditions; and lake chemistry. LakeCalc converts the lake level reconstruction to lake volume by assuming a linear interpolation between discreet lake height and lake volume estimates for well developed Lake Bonneville paleo-shorelines (Table 2.1). I start by describing the assumptions behind LakeCalc (Section 2.4.1). Sections 2.4.2 and 2.4.3 describe the inputs and outputs reconstructed in LakeCalc respectively. Section 2.4.4 details the underlying equations used to build LakeCalc. The Matlab script for the LakeCalc model is presented in Appendix A.

2.4.1 LakeCalc assumptions

LakeCalc makes a series of assumptions to simplify the modelling of Lake Bonneville. These are listed below, with additional details explained in Sections 2.4.2 and 2.4.3.

LakeCalc inputs (c.f. Section 2.4.2)

- Inputs to Lake Bonneville are rainfall input and riverine input (Figure 2.3).
- The chemical and isotopic composition of lake inputs are constant over a model run (the magnitude of the inputs are able to change).
- No dissolution of $CaCO_3$ or other minerals occurs.

LakeCalc outputs (c.f. Section 2.4.3)

- Outputs from Lake Bonneville are evaporation, riverine output and $CaCO_3$ precipitation (Figure 2.3).
- Only $CaCO_3$ (one polymorph at a time) precipitates from lake waters.

General

- Lake waters are well mixed.
- Lake water composition is set to equal riverine input composition for the first model timestep.

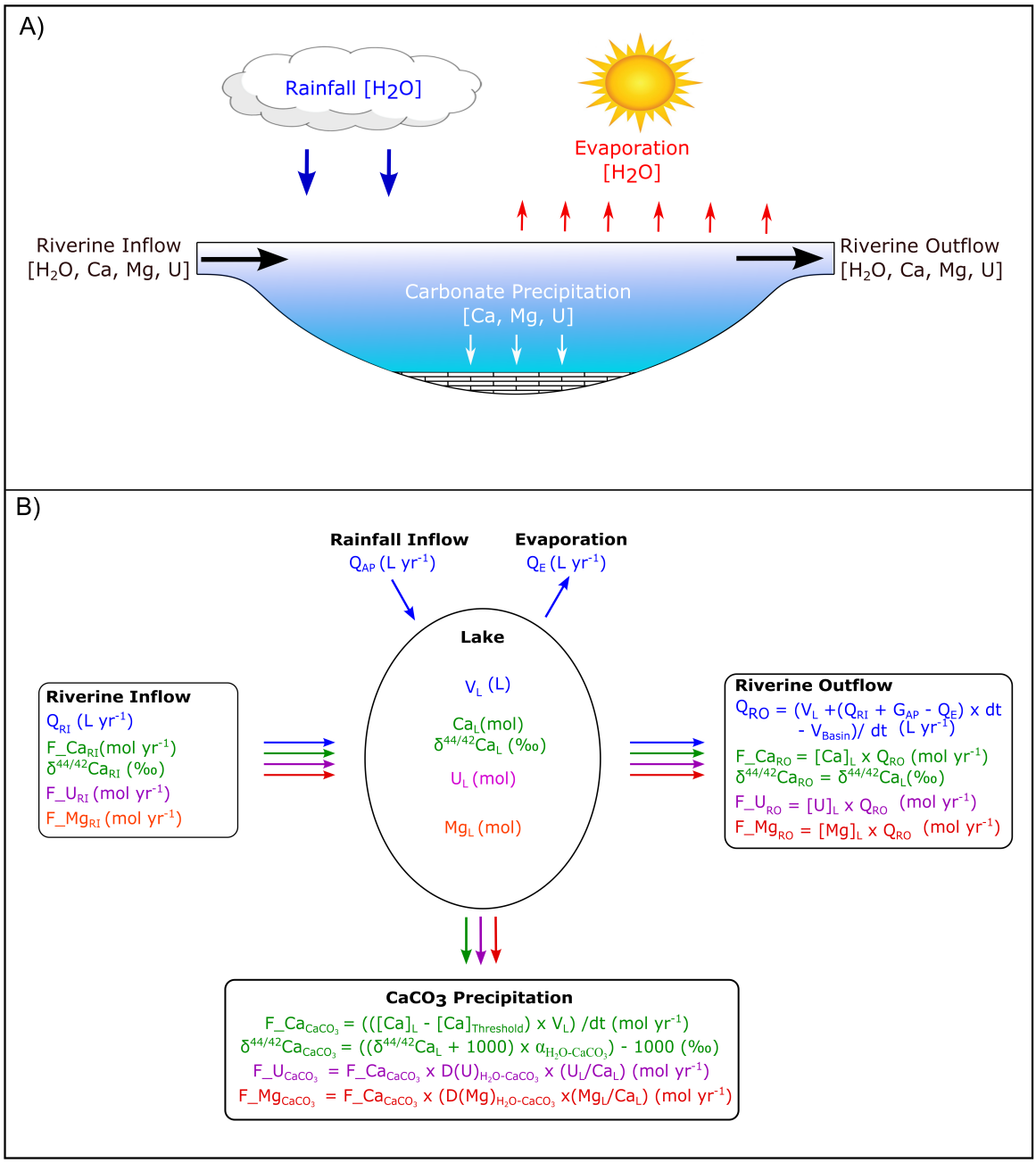


Figure 2.3: A) A cartoon showing the sources and sinks in Lake Bonneville reconstructed in LakeCalc. B) A schematic showing the sources and sinks of water (blue), calcium (green), uranium (purple) and magnesium (orange) in LakeCalc. The schematic also shows the equations used to calculate the magnitude and composition of outputs where they are dependent on lake conditions (Section 2.4.4).

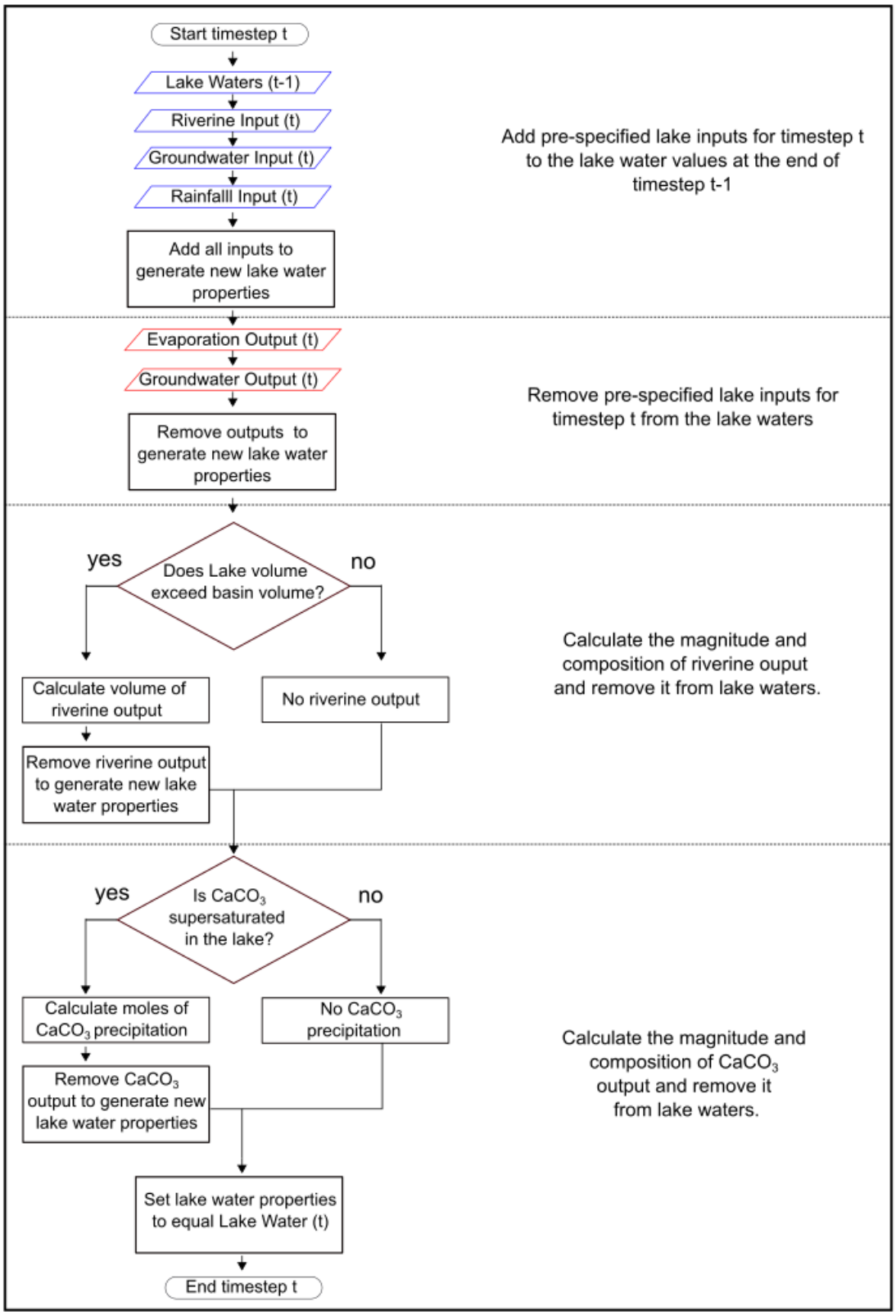


Figure 2.4: A flowchart showing the order LakeCalc deals with the various inputs and outputs to Lake Bonneville during a model timestep.

2.4.2 Reconstructed LakeCalc inputs

LakeCalc considers only two inputs to Lake Bonneville: riverine input and rainfall input. In order to accurately model Lake Bonneville, the volume and chemical composition of the individual inputs have to be accurately estimated.

Total solution input to Lake Bonneville is controlled by basin-wide P-E. Rainfall falling on the lake's surface will enter the lake as rainfall input. Rainfall which falls in the lake's drainage basin, but not on the lake, will enter the lake as riverine input. The proportion of solution supplied by riverine input and rainfall input is therefore controlled by the proportion of the drainage basin's surface area covered by the lake. Spencer et al. (1985) estimated lake volume, surface area, total solution inflow and the ratio of riverine to rainwater inflow; for well-defined Lake Bonneville paleo-shorelines (Table 2.1). LakeCalc uses linear interpolation between the discreet estimates of Spencer et al. (1985) to generate continuous relationships between lake volume, surface area, total water input and the ratio of riverine to rainwater inputs. LakeCalc then calculates the volume of riverine and rainwater inflow as a function of lake volume. The exception to this is during the period of overflow at the Provo shoreline. During overflow lake level is decoupled from lake height, so lake volume cannot be used to estimate total solution input. To overcome this, LakeCalc estimates the total solution input during overflow at the Provo shoreline to equal the estimated solution input for the Bonneville shoreline (Table 2.1). The solution input at the Bonneville shoreline was selected as this is the estimated solution input to Lake Bonneville immediately before basin collapse allowed the development of an outflow.

Shoreline	Volume (10^{15} L)	Surface Area (10^9 m^2)	Total Water Input (10^{13} $L\,yr^{-1}$)	Ratio of Riverine to Rainwater inflow ($L\,L^{-1}$)
Stansbury	1.1	24.5	1.3	1:4
Bonneville	6.5	41.2	2.2	1:10
Provo	3.0	33.1	1.7	1:10
Modern GSL	0.3	4.2	0.5	2:1

Table 2.1: Estimated lake parameters used in LakeCalc: volume; surface area; total inflow volume per year; and the ratio of riverine to rainwater inflow; from well developed paleo-shorelines and the modern GSL. Values from Spencer et al. (1985).

I consider rainwater to be sufficiently pure that it contributes only water and no solutes to lake waters.

The chemical composition of the riverine inflow to Lake Bonneville is set to equal to the amount weighted mean composition of the modern Bear, Weber and Jordan rivers (Figure 2.1), which supply 90% of the river input to the modern Great Salt Lake (Jones et al., 2009). Due to the lack of available data for the U concentration and Ca isotopic composition of these rivers the global riverine average for these parameters are used (Gaillardet et al., 2003; Tipper et al., 2010). The estimated chemical composition of the riverine input is summarised in Table 2.2.

LakeCalc assumes inputs by groundwater or the dissolution of $CaCO_3$ to Lake Bonneville to be negligible. A previous study modelling the chemical evolution of Lake Bonneville concluded the high hydraulic gradient imposed by Lake Bonneville waters resulted in negligible groundwater input (Spencer et al., 1985). Strontium isotopes have been used to show the recycling of $CaCO_3$ and other salts to be negligible in Lake Bonneville (Hart et al., 2004). This is supported by multiple sediment cores which contain $CaCO_3$ throughout the rise and fall of Lake Bonneville, suggesting large scale dissolution of lake floor $CaCO_3$ did not occur (Spencer et al., 1984; Jones et al., 2009).

Riverine Inflow Composition			
Elements	Concentration ($\mathrm{mol\,kg^{-1}}$)	X/Ca Ratio ($\mathrm{mol\,mol^{-1}}$)	Reference
Ca	1.35×10^{-3}	1	Jones et al. (2009)
Mg	1.11×10^{-3}	0.82	Jones et al. (2009)
U	1.56×10^{-9}	1.16×10^{-6}	Gaillardet et al. (2003)
Isotopes	Isotopic Ratio (‰, Relative to SRM 915a)		Reference
$\delta^{\frac{44}{42}}$ Ca	0.38		Tipper et al. (2010)

Table 2.2: Chemical composition of the riverine inflow to Lake Bonneville used by LakeCalc.

2.4.3 Reconstructed LakeCalc outputs

LakeCalc considers three processes which remove H_2O, Mg, U and Ca from Lake Bonneville: evaporation, riverine output and $CaCO_3$ precipitation. While groundwater output from lakes is highly variable and can represent a large portion of total solution output (contributing between 0.1% - 91% of total solution output; Rosenberry et al., 2015) due to the lack of available estimates of groundwater outflow from Lake Bonneville, groundwater outflow is assumed negligible in LakeCalc. This assumption would lead to LakeCalc overestimating PICP as a certain proportion of Ca will be removed from the lake by groundwater output (Section 2.5.2). This has to be taken into account when comparing LakeCalc outputs with measured proxy data.

LakeCalc calculates the composition of Lake Bonneville outputs using a single box model. In order to use a single box model, LakeCalc must assume the Lake Bonneville is well mixed on the scale of the yearly model timesteps. As 93% of modern lakes are vertically mixed on yearly timescales (Woolway and Merchant, 2019) and strontium isotopes from Lake Bonneville paleo-shoreline deposits suggest the lake was chemically well mixed on longer timescales (Hart et al., 2004), this assumption appears robust.

Riverine outflow Riverine outflow occurs in LakeCalc when the modelled lake volume exceeds the volume of the lake basin (c.f. Equation 2.5). As the lake is assumed to be well mixed the chemical composition of the riverine outflow is set to equal that

of the lake waters.

Evaporation Evaporation removes only H_2O from Lake Bonneville. Evaporation is used by LakeCalc to maintain the required change in volume specified by the simple lake level reconstruction (Figure 2.2). As the required change in volume of Lake Bonneville is specified, and total water input a function of lake volume, evaporation is set to equal the difference between total solution input to the lake and the required change in lake volume (Equation 2.4). The only exception to this is during the period of overflow at the Provo shoreline. As lake height is kept constant at the height of the overflow, changes between the balance of solution input and output cannot be reconstructed by changes in lake level. As such, evaporation is set to equal the estimate of evaporation calculated by Spencer et al. (1985) for the Provo shoreline, $1.7 \times 10^{13}\ \mathrm{L\,yr^{-1}}$.

Carbonate precipitation $CaCO_3$ precipitation removes Ca, Mg and U and alters the X/Ca and $\delta^{\frac{44}{42}}Ca$ of lake waters.

LakeCalc estimates $CaCO_3$ precipitation will occur when lake water Ca concentration exceeds a threshold concentration. When this occurs all excess Ca is removed by $CaCO_3$ precipitation (c.f. Equation 2.11). In the real world, $CaCO_3$ precipitation is controlled by the saturation index of $CaCO_3$ (SI_{CaCO_3}), which in turn is a function of the activities of Ca^{2+} and ${CO_3}^{2-}$ in solution. The modelling study of Spencer et al. (1985) reconstructed that Ca concentration in Lake Bonneville was buffered at a set concentration by the precipitation of $CaCO_3$. This suggests the assumption of a threshold Ca concentration for $CaCO_3$ precipitation is valid.

The threshold Ca concentrations required for $CaCO_3$ precipitation in LakeCalc are: $1.25 \times 10^{-3}\,\mathrm{mol\,L^{-1}}$ for calcite; and $1.53 \times 10^{-3}\,\mathrm{mol\,L^{-1}}$ for aragonite. The threshold Ca concentrations are calculated using the PHREEQC geochemically modelling software (Parkhurst and Appelo, 1999, 2013) for a solution with a $SI_{CaCO_3} = 1.05$ (the amount weighted mean SI_{CaCO_3} from the modern Bear, Weber and Jordan rivers); $\mathrm{T} = 15\,^{\circ}\mathrm{C}$; and in equilibrium with a 210 ppmV CO_2 atmosphere (the average atmospheric CO_2

concentration over the period of interest; Petit et al., 1999).

The X/Ca and $\delta^{\frac{44}{42}}$Ca of precipitated $CaCO_3$ is set by the composition of the lake waters and the trace element partition co-efficients and isotopic fractionation factors between solution and $CaCO_3$ (c.f. Table 2.3; and Equations 2.13 and 2.17).

LCC deposits comprise of only one $CaCO_3$ polymorph at a given time with the switch between the precipitated polymorph occurring simultaneous between differing cave sites (McGee et al., 2012). As such, LakeCalc assumes that only one $CaCO_3$ polymorph will precipitate at a given time. Shifts in the polymorph of $CaCO_3$ precipitated by LakeCalc are modelled to occur at the same time as well dated shifts in polymorph precipitation in LCC deposits (McGee et al., 2012).

LakeCalc only considers the precipitation of $CaCO_3$. This assumption is supported by multiple sediment cores from Lake Bonneville which contain only endogenic $CaCO_3$ over the period of interest (30 kyr BP - 13 kyr BP) (Spencer et al., 1984; Jones et al., 2009).

Partition Coefficients and Fractionation Factors			
Elements	$D(X)_{Aragonite-H_2O}$	$D(X)_{Calcite-H_2O}$	Reference
Ca	1	1	N.A
Mg	9.7×10^{-5}	0.0073	Wassenburg et al. (2016); Day and Henderson (2013)
U	3.74	0.0962	Jamieson et al. (2016); Day and Henderson (2013)
Isotope	$1000\ln(\alpha_{Aragonite-H_2O})$	$1000\ln(\alpha_{Calcite-H_2O})$	Reference
$\delta^{\frac{44}{42}}$ Ca	-0.86	-0.63	Gussone et al. 2003; Owen et al. 2016

Table 2.3: Fractionation factors and partition coefficients used in LakeCalc.

2.4.4 Model equations

LakeCalc is based on three core mass balance equations modelling: lake volume (Eq. 2.3); total mass of dissolved elements in the lake (Eq. 2.7); and Ca isotopic composition of lake waters (Eq. 2.14). These three equations allow lake volume; elemental concentrations for Ca, U and Mg; and calcium isotope composition to be modelled through time. Figure 2.4 presents a flow diagram showing the order in which inputs and outputs are added and removed from the model lake during each timestep of LakeCalc.

2.4.4.1 Lake Volume

The change in lake volume at time t equals the combined water input minus the combined water output. As specified previously (Sections 2.4.2 and 2.4.3) water only enters Lake Bonneville via riverine and rainwater inflow; and only leaves via riverine outflow and evaporation.

$$V_L\left(t+dt\right) = V_L\left(t\right) + \left(Q_{RI}\left(t\right) + Q_{AP}\left(t\right) - Q_{RO}\left(t\right) - Q_E\left(t\right)\right) \times dt \tag{2.3}$$

Where:

$V_L(t)$ = Lake Volume at time t (L).

$Q_y(t)$ = Flow of water at time t, for process y ($L\,yr^{-1}$). y can be riverine input: RI; rainfall input: AP; riverine output: RO; or evaporation output: E.

dt = Time step (yr).

The change of lake volume per timestep is specified by the simple lake level reconstruction used to force LakeCalc. As such, evaporation is set to equal the difference between total solution input and the required change in volume at time t:

$$Q_E\left(t\right) = Q_{RI}\left(t\right) + Q_{AP}\left(t\right) - \Delta V_L\left(t\right) \tag{2.4}$$

Where: $\Delta V_L\left(t\right)$ = The specified change in lake volume at time t.

The exception to this is during the overflowing portion of Lake Bonneville's history, where evaporation is set equal to the estimate of Spencer et al. (1985) for the Provo shoreline. During the period of overflow, riverine output is calculated by the model and occurs when the modelled lake volume exceeds the volume of the lake's basin:

$$Q_{RO}(t) = \begin{cases} (V(t) + Q_{Net}(t) \times dt) - V_{L\,Max} & if\ V(t) + Q_{Net}(t) \times dt > V_{L\,Max} \\ 0 & Otherwise \end{cases} \tag{2.5}$$

Where:

$V_{L\,Max}$ = Volume of lake basin (L).

$Q_{Net}(t)$ = The net input of water into the lake, excluding riverine output ($L\,yr^{-1}$):

$$Q_{Net}(t) = Q_{RI}(t) + Q_{AP}(t) - Q_E(t) \tag{2.6}$$

2.4.4.2 Mass of elements in the lake

The change in mass of element X (Mg, U or Ca) in the lake at time t, is set by the difference between the mass entering the lake and the mass leaving the lake. As specified in Sections 2.4.2 and 2.4.3, dissolved elements enter the lake via riverine input and are removed by calcium carbonate precipitation and riverine output.

$$X_L(t+1) = X_L(t) + (F_X_{RI}(t) - F_X_{RO}(t) - F_X_{CaCO_3}(t)) \times dt \tag{2.7}$$

Where:

$X_L(t)$ = Total amount of element X in lake at time t (mol_X).

$F_X_y(t)$ = The mass of element X transported by process y ($mol_X\ yr^{-1}$). y can be riverine input, RI; riverine output, RO; or calcium carbonate precipitation, $CaCO_3$.

The mass of X entering or leaving the lake via solution is controlled by the volume of the flow and the concentration of X in the solution. For riverine input, the concentration of X is specified at the start of the model run. The concentration of X in riverine output is assumed to equal that of lake waters (Sections 2.4.2 and 2.4.3).

$$F_X_{RI}(t) = Q_{Ri}(t) \times C_X_{RI} \tag{2.8}$$

$$F_X_{RO}(t) = Q_{RO}(t) \times C_X_{L}(t) \tag{2.9}$$

Where:

C_X_y = Constant concentration of element X in riverine input (mol_X L^{-1}).

C_X_L(t) = The concentration of X in lake waters at time t (mol_X L^{-1}).

The mass of element X removed from the modelled lake by calcium carbonate precipitation at each time step (F_X_{CaCO_3}(t) $mol_X yr^{-1}$), is controlled by the amount of $CaCO_3$ precipitation (M_{CaCO_3}(t) mol_{Ca} yr^{-1}) and the concentration of element X in the precipitated $CaCO_3$ ($\left(\frac{X}{Ca}\right)_{CaCO_3}(t)$, mol_X mol_{Ca}^{-1}):

$$F_X_{Carb}(t) = M_{CaCO_3}(t) \times \left(\frac{X}{Ca}\right)_{CaCO_3}(t) \tag{2.10}$$

$CaCO_3$ precipitation is modelled to occur when the concentration of Ca (mol_{Ca} L^{-1}) exceeds a threshold concentration:

$$M_{CaCO_3}(t) = \begin{cases} \frac{(Ca_L(t) + Ca_{Net}(t) \times dt) - [Ca]_{L\,Max} \times V_L(t)}{dt} & if\ Ca_L(t) + Ca_{Net}(t) \times dt > [Ca]_{L\,Max} \times V_L(t) \\ 0 & Otherwise \end{cases} \tag{2.11}$$

Where:

$[Ca]_L$Max = The threshold Ca concentration above which $CaCO_3$ precipitation occurs (mol_{Ca} L^{-1}).

$Ca_L(t)$ = The total number of moles of Ca in the lake (mol_{Ca} yr^{-1}).

$Ca_{Net}(t)$ = The net inflow of Ca into the lake, excluding calcium carbonate precipitation (mol_{Ca} yr^{-1}):

$$Ca_{Net}(t) = F_Ca_{RI}(t) - F_Ca_{RO}(t) \tag{2.12}$$

The $\frac{X}{Ca}$ molar ratio in precipitated calcium carbonate, at time t, is controlled by the partition coefficient ($D(X)_{CaCO_3-H_2O}$, c.f. 2.3) and the $\frac{X}{Ca}$ molar ratio of the lake waters:

$$\left(\frac{X}{Ca}\right)_{CaCO_3}(t) = \left(D(X)_{CaCO_3-Solution} \times \frac{X_L(t)}{Ca_L(t)}\right) \tag{2.13}$$

2.4.4.3 Calcium isotope composition

The change in Ca isotopic composition of lake waters is controlled by the addition of Ca to the lake by riverine input, and its removal by riverine output and calcium carbonate precipitation:

$$\delta^{\frac{44}{42}}Ca_L(t+1) = \delta^{\frac{44}{42}}Ca_L(t) + \frac{\left(M\delta^{\frac{44}{42}}Ca_{RI}(t) - M\delta^{\frac{44}{42}}Ca_{RO}(t) - M\delta^{\frac{44}{42}}Ca_{CaCO_3}(t)\right) \times dt}{Ca_L(t)} \tag{2.14}$$

Where:

$\delta^{\frac{44}{42}}Ca_L(t)$ = The calcium isotopic ratio of lake waters at time t (‰, relative to SRM915a).

$M\delta^{\frac{44}{42}}Ca_y(t)$ = The magnitude of process y on the lake's Ca isotopes (‰ mol_{Ca} yr^{-1}). y can be riverine input, RI; riverine output, RO; or calcium carbonate precipitation, $CaCO_3$.

The magnitude of each process ($M\delta^{\frac{44}{42}}Ca_y(t)$) is dependent on both the amount of Ca added or removed from the lake and the difference between the Ca isotope composition of lake waters and the Ca added or removed from the lake for each process.

A constant $\delta^{\frac{44}{42}}Ca_{RI}$ is specified at the start of the model run (Table 2.1):

$$M\delta^{\frac{44}{42}}Ca_{RI}(t) = \left(\delta^{\frac{44}{42}}Ca_{RI} - \delta^{\frac{44}{42}}Ca_L(t)\right) \times F_Ca_{RI}(t) \tag{2.15}$$

Riverine outflow has a Ca isotopic composition equal to that of the lake water, $\left(\delta^{\frac{44}{42}}Ca_{RO}(t) - \delta^{\frac{44}{42}}Ca_L(t) = 0\right)$ and as such has no direct effect on the Ca isotopic composition of the lake:

$$M\delta^{\frac{44}{42}}Ca_{RO}(t) = \left(\delta^{\frac{44}{42}}Ca_{RO}(t) - \delta^{\frac{44}{42}}Ca_L(t)\right) \times F_Ca_{RO}(t) = 0 \tag{2.16}$$

The Ca isotopic composition of precipitated calcium carbonates ($\delta^{\frac{44}{42}}Ca_{CaCO_3}$, ‰) is controlled by the Ca isotopic composition of the lake waters ($\delta^{\frac{44}{42}}Ca_L(t)$) and the fractionation factor of Ca during the precipitation of calcium carbonate ($\alpha_{CaCO_3-Solution}$, c.f. Table 2.3):

$$M\delta^{\frac{44}{42}}Ca_{CaCO_3}(t) = \left(\delta^{\frac{44}{42}}Ca_{CaCO_3}(t) - \delta^{\frac{44}{42}}Ca_L(t)\right) \times F_Ca_{CaCO_3}(t) \tag{2.17}$$

$$\delta^{\frac{44}{42}}Ca_{CaCO_3}(t) = \left(\left(\delta^{\frac{44}{42}}Ca_L(t) + 1000\right) \times \alpha_{CaCO_3-Solution}\right) - 1000 \tag{2.18}$$

2.5 Modelled controls on the Mg/Ca, U/Ca and $\delta^{\frac{44}{42}}Ca$ composition of LCCs

LakeCalc was used to reconstruct shifts in lake water and LCC composition over the rise and fall of Lake Bonneville between 30 kyr (BP) and 13 kyr (BP). The two major controls on LCC chemistry in LakeCalc were PICP and the precipitated polymorph of $CaCO_3$.

2.5.1 PICP control on LCC composition

PICP is defined as the proportion of Ca entering the lake which is removed by $CaCO_3$ precipitation. LakeCalc reconstructs PICP in Lake Bonneville to be controlled by the balance between solution input into the lake and evaporation output. When the volume of solution input equals the volume of evaporation, PICP = 1. When the volume of solution input is greater (less) than the volume of evaporation output, PICP is lower (greater) than one, with the greater the imbalance between solution input and evaporation output, the further PICP moves away from one. If evaporation output is sufficiently smaller than solution input lake waters will be diluted below the threshold Ca concentration required by LakeCalc for $CaCO_3$ precipitation and PICP = 0.

During the rise and fall of Lake Bonneville, lake evolution can be characterised by four distinct types: rising lake volume in a closed basin (CBR); constant lake volume in a closed basin (CBS); falling lake volume in a closed basin (CBF) and an open basin (OB) (Figure 2.8). In a closed basin of constant volume, evaporation equals solution input so PICP = 1. In a closed basin shifts in the balance between the volume of inputted solution and volume of evaporation result in changes in lake volume. The lake either increases of decreases in size until evaporation, proportional to the surface area of the lake, equals solution input and a steady state volume is reached. In closed basins, changes in the balance between inputted solution and evaporation result in transient shifts in PICP while the lake is changing in size, before PICP returns to one when a

new steady state volume is reached. In an open basin, as the volume of the lake is fixed by the height of the riverine outflow, shifts in balance between evaporation and solution inputs alter the volume of riverine outflow. As riverine outflow tends to zero, PICP tends to one, and as riverine outflow increases PICP will decrease until the lake is sufficiently fresh no $CaCO_3$ precipitation occurs and PICP = 0. Consequently, each type of lake evolution has a potential range of PICP values, which allow lake water and LCC composition to be related to riverine input composition (Table 2.4).

	Type of Lake Evolution	Closed Basin Stationary (CBS)	Closed Basin Rising (CBR)	Closed Basin Falling (CBF)	Open Basin (OB)
	Range of potential PICP values	$PICP = 1$	$0 \leq PICP < 1$	$PICP > 1$	$0 \leq PICP < 1$
Aragonite precipitating lake	$\Delta\delta^{\frac{44}{42}}$Ca (‰)	$\rightarrow$	$\downarrow$	$\uparrow$	$\downarrow$
	$\Delta\frac{Mg}{Ca}$ (mol mol^{-1})	$\rightarrow$	$\downarrow$	$\uparrow$	$\downarrow$
	$\Delta\frac{U}{Ca}$ (mol mol^{-1})	$\rightarrow$	$\downarrow$	$\uparrow$	$\downarrow$
Calcite precipitating lake	$\Delta\delta^{\frac{44}{42}}$Ca (‰)	$\rightarrow$	$\downarrow$	$\uparrow$	$\downarrow$
	$\Delta\frac{Mg}{Ca}$ (mol mol^{-1})	$\rightarrow$	$\downarrow$	$\uparrow$	$\downarrow$
	$\Delta\frac{U}{Ca}$ (mol mol^{-1})	$\rightarrow$	$\uparrow$	$\downarrow$	$\uparrow$

Table 2.4: A summary of LakeCalc modelled outputs for different types of lake evolution. This table shows the range of PICP values possible for each type of lake evolution and the response of proxy values, expressed relative to the value in the inflowing solution. $\Delta\delta^{\frac{44}{42}}Ca = \delta^{\frac{44}{42}}Ca_{CaCO_3} - \delta^{\frac{44}{42}}Ca_{RI}$ (‰); $\Delta\frac{Mg}{Ca} = \frac{Mg}{Ca}_{Carb} - \frac{Mg}{Ca}_{RI}$ (mol mol^{-1}); and $\Delta\frac{U}{Ca} = \frac{U}{Ca}_{CaCO_3} - \frac{U}{Ca}_{RI}$ (mol mol^{-1}). $\rightarrow$ indicates carbonate values will evolve towards the riverine values. $\uparrow$ ($\downarrow$) indicates the carbonate value will evolve towards values higher (lower) than the the riverine value.

A unique steady state LCC chemical and isotopic composition exists for each PICP value, which allows elemental and isotopic lake inputs to equal lake outputs (Figure 2.5). Once the PICP value of a lake shifts, LCC composition will evolve towards the new steady state composition, with the rate of change of proxy values dependent on both the size of the lake's proxy reservoir; and the difference between the steady state proxy value the system is evolving towards and the current proxy value. When PICP = 0, there is no $CaCO_3$ precipitation and the composition of lake water will evolve towards the riverine input. As PICP increases lake waters will become increasingly enriched in heavier calcium isotopes, and elements with a $D(X)_{CaCO_3\text{-Solution}} < 1$, and depleted with elements with a $D(X)_{CaCO_3\text{-Solution}} > 1$, compared to the composition of the riverine input (Figure 2.5). When PICP = 1, the composition of LCCs will evolve to equal that of the riverine input (Figure 2.5).

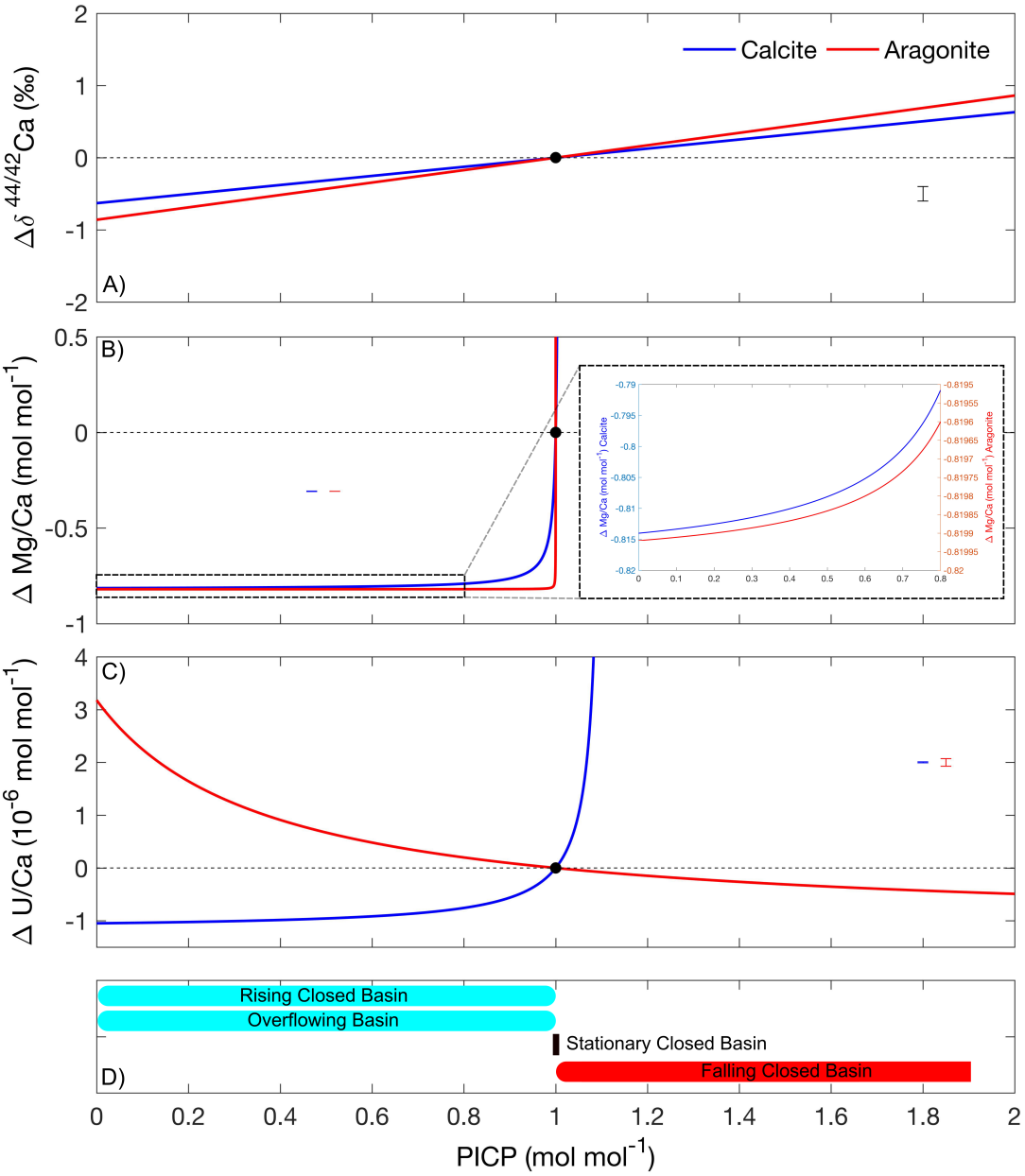


Figure 2.5: The steady state $\Delta_{\text{Carbonate -Riverine Inflow}}$ values for differing PICP values in Lake Bonneville. The values for both aragonite and calcite precipitating lakes are plotted with red and blue lines respectively. $\Delta\delta^{\frac{44}{42}}Ca = \delta^{\frac{44}{42}}Ca_{CaCO_3} - \delta^{\frac{44}{42}}Ca_{RI}$ (‰); $\Delta\frac{Mg}{Ca} = \frac{Mg}{Ca}_{CaCO_3} - \frac{Mg}{Ca}_{RI}$ (mol mol^{-1}); and $\Delta\frac{U}{Ca} = \frac{U}{Ca}_{CaCO_3} - \frac{U}{Ca}_{RI}$ (mol mol^{-1}). Error bars show the average 2σ uncertainties of analytical measurements of LCC proxy values (c.f. Chapter 3), blue are for calcite values, red for aragonite and black where they are the same for both polymorphs. The expected value for the stationary closed basin is plotted with a black circle. Elements with a $D(X)_{CaCO_3\text{-}H_2O} < 1$ have a threshold PICP where the steady state LCC concentration tends to infinity. This PICP threshold equals: $PICP_{Threshold} = \frac{-1}{\left(D(X)_{CaCO_3-H_2O}-1\right)}$, corresponding to a PICP of 1.001 for $\frac{Mg}{Ca}$ in calcite, 1.0001 for $\frac{Mg}{Ca}$ in aragonite and 1.11 for $\frac{U}{Ca}$ in calcite. Due to the large range of values, sub-plot B contains an insert showing the behaviour of Mg/Ca in aragonite and calcite between 0 - 0.7 PICP. The range of PICP values expected for each type of lake evolution are plotted in sub-figure D.

$\delta^{\frac{44}{42}}Ca$ increases linearly with PICP and, as such, is equally sensitive to changes in PICP across all PICP values. However, due to the large analytical uncertainties on $\delta^{\frac{44}{42}}Ca$, shifts in PICP > 0.1 in aragonite and 0.15 in calcite are required to exceed instrument uncertainty and be reconstructed from LCCs (Figure 2.5A).

Trace elements have smaller analytical uncertainties and therefore can detect smaller shifts in PICP, however a non-linear response to shifts in PICP makes trace elements more sensitive in certain PICP ranges (Figure 2.5). Elements with a $D(X)_{CaCO_3\text{-Solution}}$ < 1 have a threshold PICP value above which there is no steady state LCC composition that allows lake outputs to balance lake inputs (Figure 2.5). If PICP increases above this threshold then LCC and lake X/Ca would theoretically continue to increase in concentration indefinitely (Figure 2.5). Consequently, elements with a $D(X)_{CaCO_3\text{-Solution}}$ < 1 lose sensitivity to shifts in PICP above this threshold.

While all shifts in PICP result in shifts in the composition of lake waters, in order to reconstruct shifts in PICP from LCC deposits the impact on proxy values must be measurable (outside of analytical instrument error). This requires the shift in PICP to be sufficiently large to generate a measurable change in LCC composition, but also last sufficiently long to allow a measurable shift n LCC composition to be generated. In LakeCalc this typically takes 200 years, but is dependent on the proxy system and the size of the PICP perturbation.

2.5.2 Sensitivity testing

The sensitivity of LakeCalc to changes in riverine input composition and the volume of groundwater outflow from the lake were tested in a simple rising closed lake scenario for both an aragonite and calcite precipitating lake. The rising lake scenario models the rise in lake level from the Stansbury Shoreline to the Bonneville Shoreline (Figure 2.2) and assumes the starting lake water composition equals the riverine composition.

Riverine Composition

Three separate riverine inflow compositions were tested using the LakeCalc software, a low concentration where: Mg/Ca = 0.25 gg^{-1} , U/Ca = 50 ppm, and $\delta^{\frac{44}{42}}Ca$ = 0.3‰; a medium concentration where: Mg/Ca = 0.5 gg^{-1} , U/Ca = 69 ppm, and $\delta^{\frac{44}{42}}Ca$ = 0.38‰; and a high concentration where: Mg/Ca = 0.75 gg^{-1} , U/Ca = 90 ppm, and $\delta^{\frac{44}{42}}Ca$ = 0.5‰. The medium concentration scenario being the composition used in all other model runs specified in Table 2.2.

These tests showed that changes in the composition of the riverine Mg/Ca, U/Ca and $\delta^{\frac{44}{42}}Ca$ can have a large impact on the absolute composition of the lake water and hence precipitated $CaCO_3$(Figure 2.6). However, the trends in the proxy values remained constant, with a constant increase in $\delta^{\frac{44}{42}}Ca$ (Figure 2.6E), and a constant percentage increase in Mg/Ca and U/Ca (Figure 2.6C and D) in precipitated carbonates across all three scenarios. Therefore, while riverine inflow composition is modelled to have an impact on the absolute proxy values in precipitated $CaCO_3$it does not have an impact on the modelled trends of proxies during the growth of the lake.

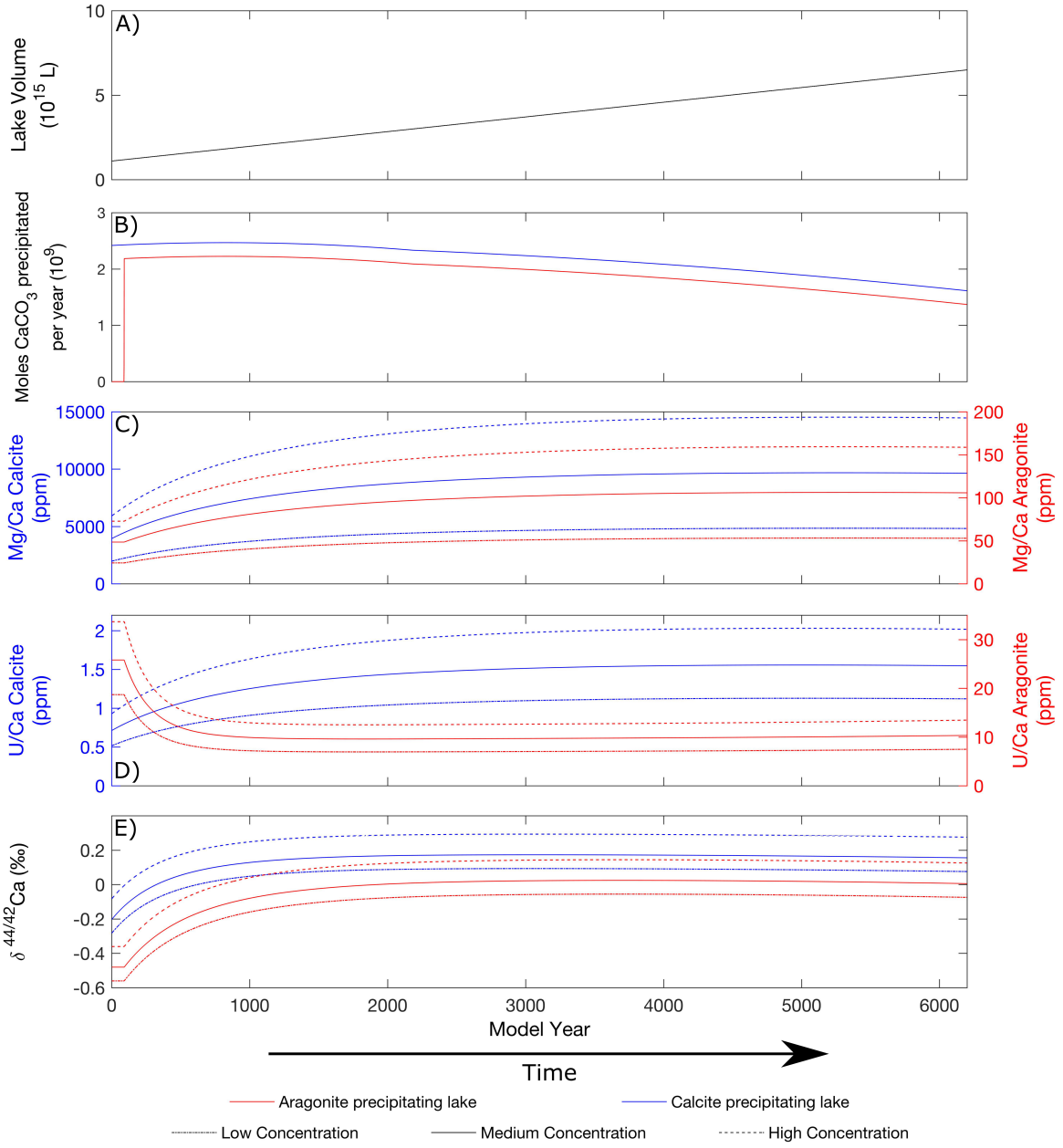


Figure 2.6: The LakeCalc model output for a rising closed basin under three riverine composition scenarios, a low concentration scenario: Mg/Ca = 0.25 gg^{-1} , U/Ca = 50 ppm, and $\delta^{\frac{44}{42}}Ca = 0.3‰$; medium concentration scenario: U/Ca = 69 ppm, and $\delta^{\frac{44}{42}}Ca = 0.38‰$; and high concentration scenario: Mg/Ca = 0.75 gg^{-1} , U/Ca = 90 ppm, and $\delta^{\frac{44}{42}}Ca = 0.5‰$. LakeCalc was run for 6200 model years simulating the rise from the Stansbury Shoreline to the Bonneville Shoreline. A) Modelled lake volume in litres. B) Precipitated $CaCO_3$ (mol per year). C) Mg/Ca in precipitated carbonate (ppm). D) U/Ca in precipitated carbonate (ppm). E) $\delta^{\frac{44}{42}}Ca$ in precipitated carbonate (‰). Red lines show carbonate values for an aragonite precipitating lake and blue lines for a calcite precipitating lake. . Dashed lines represent the low concentration scenario, solid lines the medium concentration scenario and dotted lines the high concentration scenario.

Groundwater Outflow

The impact of varying amounts of groundwater outflow on the LakeCalc model was tested for three groundwater outflow scenarios, 0% of total solution input removed via groundwater outflow, 2.5% of total solution input removed via groundwater outflow, and 5% of total solution input removed via groundwater outflow. As the lake system is assumed to be well mixed the composition of the groundwater output was approximated by lake water composition.

LakeCalc modelled that as the proportion of inflowing solution removed as groundwater increased, the amount of $CaCO_3$ precipitated per year from the lake decreased. This is because a smaller amount of evaporation is required to force shifts in lake volume. Consequently, for an equal shift in lake volume, the greater the volume of solution lost to groundwater outflow, the lower the value of PICP (Figure 2.7B). If groundwater outflow increases sufficiently, it will hit a threshold whereby evaporation is sufficiently reduced that PICP reduces to 0, and $CaCO_3$precipitation ceases. This is seen in the 5% groundwater outflow scenario for the aragonite precipitating lake where PICP reaches 0 approximately 5000 years into the model run (Figure 2.7B). The decrease in PICP with increasing groundwater outflow impacts all three modelled proxy values (Mg/Ca, U/Ca and $\delta^{\frac{44}{42}}Ca$) with smaller shifts in proxy values occurring with increasing groundwater outflow (Figure 2.7C, D and E). Consequently, groundwater outflow, if occurring during the highstand of Lake Bonneville, could have a large impact on lake chemistry, reducing the size of perturbations to proxy values caused by shifting P-E over the lake basin.

Due to the lack of available estimates of groundwater outflow from Lake Bonneville, groundwater outflow is assumed negligible in subsequent model runs. This could lead to LakeCalc overestimating PICP for shifts in lake volume, and this should be considered when analysing LakeCalc outputs.

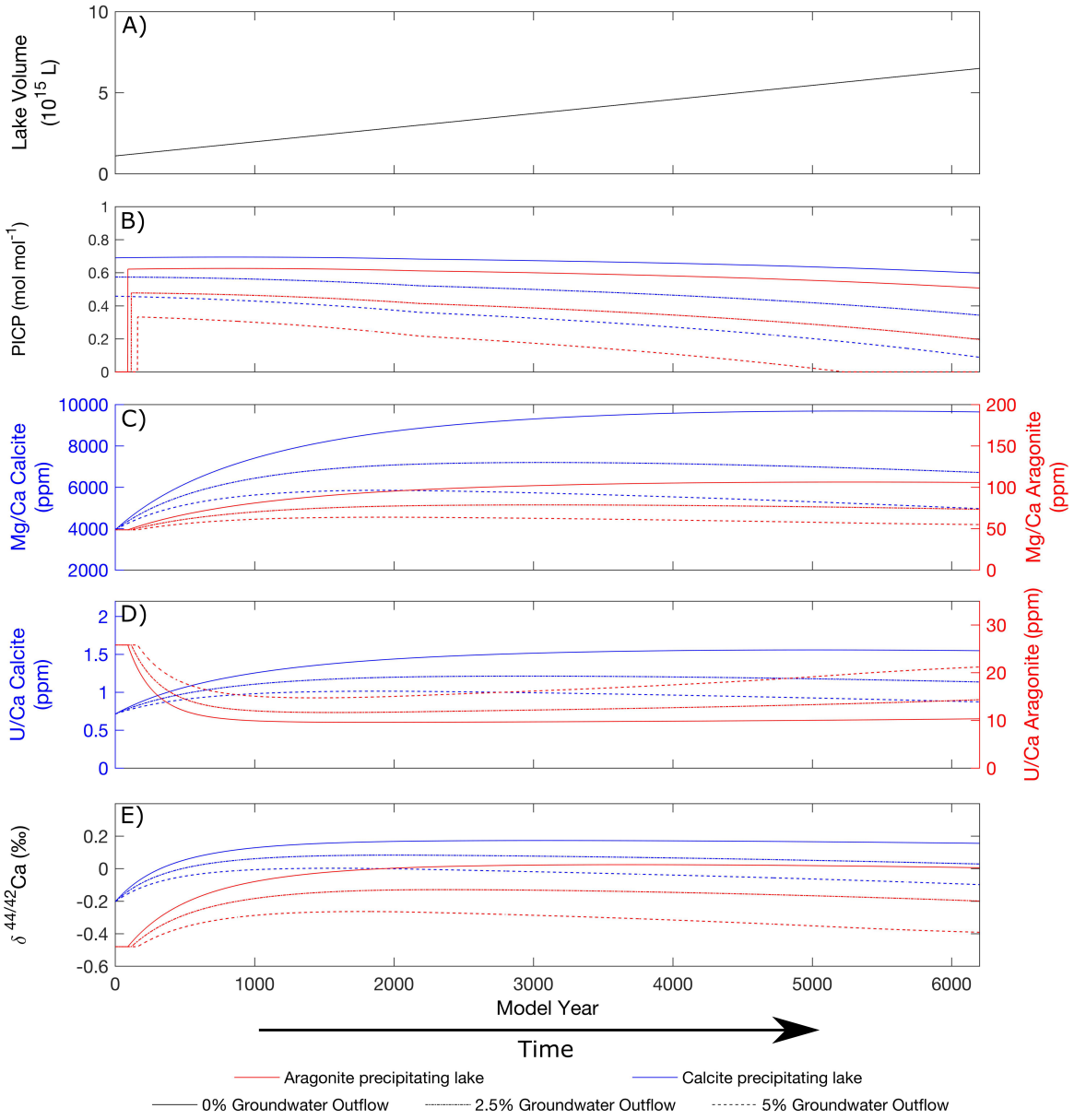


Figure 2.7: The LakeCalc model output for a rising closed lake for three groundwater outflow scenarios: 0% of total solution input removed via groundwater outflow, 2.5% of total solution input removed via groundwater outflow, and 5% of total solution input removed via groundwater outflow. LakeCalc was run for 6200 model years simulating the rise from the Stansbury Shoreline to the Bonneville Shoreline. A) Lake volume in litres. B) PICP (mol mol^{-1}). C) Mg/Ca in precipitated carbonate (ppm). D) U/Ca in precipitated carbonate (ppm). E) $\delta^{\frac{44}{42}}Ca$ in precipitated carbonate (‰). Red lines show carbonate values for an aragonite precipitating lake and blue lines for a calcite precipitating lake. Solid lines represent 0% of total solution input removed via groundwater outflow, dashed lines 2.5% and dotted lines 5%.

2.5.3 Other controls on LCC composition

In LakeCalc, LCC and lake water composition are affected by switches between aragonite and calcite precipitation (Figure 2.8). A shift between these $CaCO_3$ polymorph results firstly, in a step change in LCC composition due to differences in partition coefficients and fractionation factors between aragonite and calcite. Secondly, lake chemistry then starts to evolve to reach a steady state composition with the new fractionation factor and partition coefficients (Figure 2.5). However, changes in precipitated polymorph can be easily identified from precipitated LCC deposits (McGee et al., 2012) and hence shifts in LCC chemistry caused by shifting $CaCO_3$ polymorph easily accounted for.

In the real world, LCC composition could also be affected by changes in the composition of solution inputs, dust deposition to the lake surface, the precipitation of minerals other than $CaCO_3$ or disequilibrium affects impacting the fractionation of Ca isotopes into LCCs. This is particularly the case in scenarios where LakeCalc predicts very large concentrations of trace elements, such as magnesium in a stationary or falling lake. When the concentration of these elements exceeds normal lake values, other minerals such as Mg-silicates or magnesite will precipitate limiting their maximum concentration in lake waters (Jones et al., 2009). However, by taking a multi-proxy approach, shifts in proxy values in LCCs can be compared with the expected LakeCalc response to distinguish a PICP control from other mechanisms.

2.6 The potential for LCCs to reconstruct shifts in P-E over the Bonneville Basin

LakeCalc reconstructs large and long lived shifts in PICP over the rise and fall of Lake Bonneville, between $0\,\mathrm{mol\,mol^{-1}}$ and $2.2\,\mathrm{mol\,mol^{-1}}$, resulting in large changes in proxy values in both lake waters and LCCs (Figure 2.8). While changes in proxy values over the whole model run are much higher than analytical uncertainty, this is not the case for all shifts in lake evolution, specifically the transition between the original rise of Lake Bonneville (T1) and the period of constant lake volume (S1) (Figure 2.8).

The initial rise of Lake Bonneville (T1) occurs slowly with an average PICP = $0.91\,\mathrm{mol\,mol^{-1}}$ (Figure 2.8B). When the lake stops rising at the stationary period, PICP increases to $1\,\mathrm{mol\,mol^{-1}}$. While Mg/Ca is very sensitive to small changes in PICP when PICP is less than one, and starts rapidly increasing, the shift in PICP between T1 and S1 is not sufficiently large to generate a measurable signal in $\delta^{\frac{44}{42}}Ca$ or U/Ca (Figure 2.8). However, aside from this transition the rest of the modelled shifts in lake evolution generate much larger shifts in PICP and a measurable signal in all three proxies (Figure 2.8). This includes the shift between the stationary period (S1) and the second rise of Lake Bonneville (T2), a shift in PICP $\approx 0.4\,\mathrm{mol\,mol^{-1}}$; the second rise of Lake Bonneville (T2) and the period of overflow (O1), a shift in PICP $\approx 0.6\,\mathrm{mol\,mol^{-1}}$; and the period of overflow (O1) and the fall of Lake Bonneville (R1), a shift in PICP $\approx 2.2\,\mathrm{mol\,mol^{-1}}$.

The largest modelled shift in LCC chemistry is caused by the onset of riverine outflow, between the second rise of Lake Bonneville (T2) and the overflowing period (O1). The large instantaneous increase in riverine outflow, caused by the collapse of the basin wall, freshens the lake sufficiently that $CaCO_3$ precipitation ceases and PICP reduces to zero. This generates a large shift in proxy values in the lake waters as they evolve towards the riverine composition. However, LCC deposits would not record these shifts as they are no longer precipitating (Figure 2.8).

Therefore, LakeCalc reconstructed PICP shifts over the rise and fall of Lake Bonneville were sufficiently large to generate measurable shifts in U/Ca, Mg/Ca and $\delta^{\frac{44}{42}}Ca$ (Figure 2.8). While changes in lake volume and hence PICP over the rise and fall of Lake Bonneville are commonly ascribed to changes in P-E over the Great Basin region (e.g. Oviatt, 1997, 2015; Santi et al., 2019), one of the largest modelled shifts in PICP is caused by the onset of riverine outflow (Figure 2.8). The development of a riverine outflow was not a result of shifts in P-E, but a structural change in the Bonneville Basin, caused by the collapse of part of the basin wall at the Red Rock Pass (e.g. Gilbert, 1890; Currey, 1983; Miller et al., 2013; Oviatt, 2015). While this can easily be discounted as a shift in P-E in Lake Bonneville, due to the identification of this flood event in sedimentary records (Gilbert, 1890), in other less well studied lakes structural shifts in lake basins or regional drainage patterns could alter lake hydrology and hence PICP while regional P-E remains constant. When large structural changes can be discounted, LakeCalc suggests multiple proxy systems in LCC deposits will be able to reconstruct shifts in basin wide P-E.

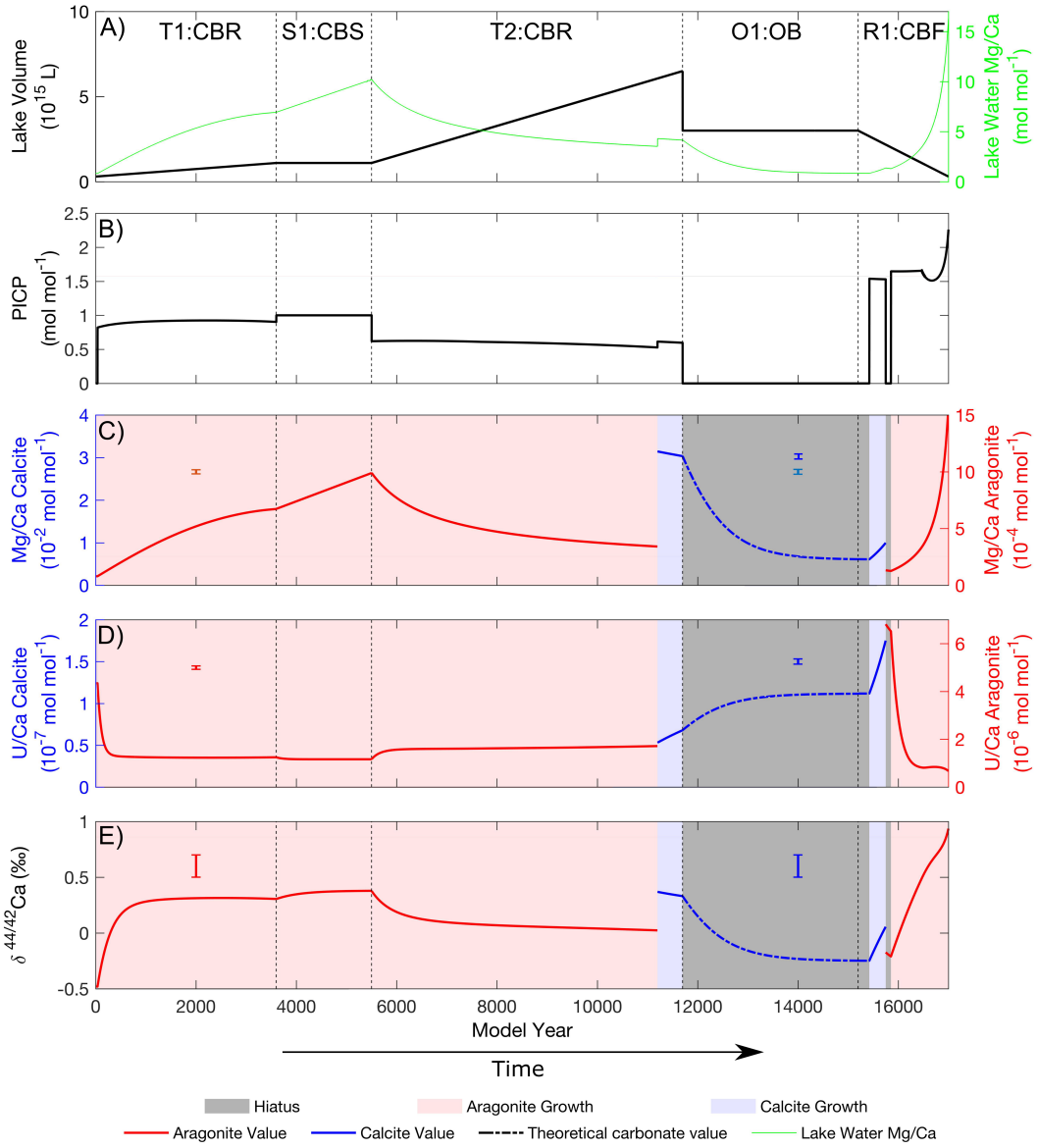


Figure 2.8: The LakeCalc model output for the rise and fall of Lake Bonneville. The output is 17,000 years long, covering the whole 30 kyr (BP) - 13 kyr (BP) of Lake Bonneville rise and fall, with model year = 0, corresponding to 30 kyr (BP). A) The simplified lake level reconstruction used by LakeCalc to reconstruct shifts in Lake Bonneville chemistry plotted with the LakeCalc modelled lake water Mg/Ca (mol mol^{-1}) timeseries. Model year = 0 corresponds to 30 kyr (BP) in Figure 2.2. The type of lake evolution: Closed Basin Stationary (CBS), Closed Basin Rising (CBR), Closed Basin Falling (CBF) and Overflowing Basin (OB) are annotated; B) PICP values (mol mol^{-1}); C) Mg/Ca ratios of precipitated carbonates (mol mol^{-1}); D) U/Ca ratios of precipitated carbonates (mol mol^{-1}); and E) $\delta^{\frac{44}{42}}$Ca of precipitated carbonates (‰). Error bars show the average 2σ uncertainties of analytical measurements of proxy values (c.f. Chapter 3), blue are for calcite values and red for aragonite. The precipitated polymorph of $CaCO_3$ is indicated in both the shading and color of lines in sub-plots C, D and E; with red corresponding to aragonite growth and blue calcite growth. Grey shading indicates periods where $CaCO_3$ precipitation is modelled to cease, and the theoretical LCC value which would be precipitated from lake waters at this time indicated with a dashed line.

2.7 Summary

The LakeCalc output suggests that changes in PICP over the rise and fall of Lake Bonneville produced sufficiently large chemical perturbations to lake waters that they should be resolvable in the Mg/Ca, U/Ca and $\delta^{\frac{44}{42}}Ca$ of LCC deposits. While reconstructed changes in P-E generate measurable shifts in proxy values, this work also demonstrates the significant impact of structural changes in lake basins on PICP. Authors need to be aware of this when interpreting chemical proxies from precipitated lacustrine carbonates. However, in lakes where structural shifts in lake basins have been identified from the sedimentary record, LCCs would be able to provide supporting evidence and high precision U-Th ages on these structural changes.

LakeCalc suggests modelled changes in P-E during the rise and fall of Lake Bonneville generate sufficiently large shifts in all three proxies that a multi-proxy approach using using LCCs would be able to robustly identify large and long lived shifts in basin wide P-E. LCCs, therefore, represent a valuable archive for investigating and reconstructing the complex past behavior of lake systems in which they precipitate.

While LakeCalc predicts a hiatus in LCC growth during the overflowing period of Lake Bonneville (approx. 18 kyr BP - 15 kyr BP) the observed precipitation of LCCs during portions of this period (McGee et al., 2012) are indicative of changes in P-E over the Bonneville Basin at this time. LCC deposits therefore provide an opportunity to investigate changes in P-E over the Bonneville Basin during the overflowing period where, due to the decoupling of lake level and regional P-E, paleo-shoreline deposits provide little information and shifts are still debated (Miller, 2016). This is tested in Chapter 3.

Chapter 3

A multi-proxy approach to reconstructing P-E in the Bonneville Basin from Lacustrine Cave Carbonates

Abstract

In this chapter I further develop lacustrine cave carbonates (LCCs) as archives for reconstructing past shifts in basin wide P-E. LCCs can provide continuous records of lake chemistry during periods of growth and can be dated with high precision U-Th chronology. Mg/Ca, U/Ca and $\delta^{\frac{44}{42}}Ca$ values were measured from LCC samples CC3 and CC5 which precipitated between 25.3 kyr (BP) and 13.6 kyr (BP) in the Bonneville Basin, in the Great Basin region of the southwestern United States. Measured values are combined with LakeCalc model outputs to test whether Mg/Ca, U/Ca and $\delta^{\frac{44}{42}}Ca$ can be used as a robust new multi-proxy approach to reconstructing shifts in basin-wide P-E. Close agreement between modelled and measured values during the rise of Lake Bonneville (25 kyr BP - 18.8 kyr BP), where Lake Bonneville is in a closed basin and P-E is well constrained by paleo-shoreline reconstructions, indicates that this new multi-proxy approach is robustly recording shifts in basin-wide P-E. This multi-proxy approach is then used to reconstruct shifts in P-E during the overflowing period of Lake Bonneville's history ($\sim$18.0 kyr BP - $\sim$14.7 kyr BP), for which P-E reconstructions were previously hindered by the open basin nature of the system. Here a link between moisture supply to the Great Basin region and Heinrich Stadial 1 is identified, with moisture supply suggested to be impacted by a southwards shift of the ITCZ and variations in the elevation of North American ice sheets.

Contents

3.1 Introduction 78

3.2 Study site and methodology 80

3.2.1 Lake level change in Lake Bonneville 80

3.2.2 Cathedral Cave 82

3.2.3 Sample description 84

3.2.4 Sampling 86

3.2.5 U-Th chronology 86

3.2.6 Age depth models 87

3.2.7 Calcium isotope analysis 88

3.2.8 Trace element analysis 89

3.2.9 LakeCalc 89

3.3 Results 91

3.3.1 U-Th ages 91

3.3.2 Age depth models 93

3.3.3 Ca isotopes 95

3.3.4 Trace elements 96

3.4 Discussion 99

3.4.1 Comparing the measured and modelled composition of LCC deposits during well constrained shifts in P-E over the Bonneville Basin (25 kyr BP - 18.8 kyr BP) 99

3.4.2 Insights into basin structural changes using LCCs: Constraining the timing of the Bonneville Flood 102

3.4.3 New insights into the period of overflow of Lake Bonneville from LCC deposits (∼18.0 kyr BP - ∼14.7 kyr BP) 106

3.5 Future work and outlook 112

3.6 Conclusion 113

3.1 Introduction

Paleo-shoreline reconstructions from the Great Basin region of the southwestern United States established that a dramatic rise in the level of terminal lakes occurred during the last glaciation (e.g. Gilbert, 1890; Patrickson et al., 2010; Santi et al., 2019; McGee et al., 2012; Oviatt, 2015). The largest and best studied of these, Lake Bonneville, expanded from a small ephemeral lake to a large freshwater body covering over 41,000 km^2, before reducing to form the 4200 km^2 Great Salt Lake in the modern day (e.g. Spencer et al., 1985; Oviatt, 2015).

The expansion of Great Basin terminal lakes during the last glaciation has been linked to increases in rainfall as a result of a southwards displacement of the winter storm track by large North American ice sheets (Hostetler and Benson, 1990), as well shifts in the magnitude of moisture supplied to the region by "North Pacific Atmospheric River" events (Lora et al., 2017; McGee et al., 2018).

Paleo-shoreline reconstructions provide crucial records of shifts in precipitation–evaporation (P-E) over lake drainage basins (Oviatt, 1997, 2015; Santi et al., 2019). However, while paleo-shoreline reconstructions are valuable for reconstructing shifts in P-E over the southwestern United States, they have two major limitations. Firstly, they are commonly low resolution and have large age uncertainties, make comparing shifts in P-E between lakes and other paleoclimate archives challenging (McGee et al., 2012). Secondly, during periods of overflow, lake level becomes decoupled from basin-wide P-E, with shifts in P-E resulting in changes in the volume of solution outflow as opposed to lake level (Miller, 2016). This has made understanding the response of Great Basin P-E to abrupt shifts in climate during the last deglaciation difficult, with studies even disagreeing as to the sign of the shift in P-E during Heinrich Stadials (Oviatt, 1997; Benson et al., 2011; McGee et al., 2012).

This is particularly true for Lake Bonneville, where a prolonged period of outflow lasting approximately 3500 years between 18.3 kyr (BP) and 14.8 kyr (BP) (Oviatt, 2015) prevents detailed P-E reconstructions from taking place during a key period of

the last deglaciation. Amongst others, this hinders understanding the impact of abrupt millennial scale events, such as Heinrich Stadial 1, on P-E over Lake Bonneville, and therefore regional hydrology.

To solve the limitations of paleo-shoreline reconstructions from Lake Bonneville McGee et al. (2012) used chemical proxies from lacustrine cave carbonates (LCC). LCCs are a new form of lacustrine carbonates, capable of recording shifts in lake chemistry and being absolutely dated using U-Th chronology, which can therefore generate continuous timeseries of lake water chemistry over periods of growth (McGee et al., 2012).

A pioneering study by McGee et al. (2012) applied $\delta^{18}O$ measurements of LCCs to the topic of reconstructing basin-wide P-E, bringing the advantage of absolute U-Th chronology, and sequential $\delta^{18}O$ measurements covering thousands of years. A difficulty with using lake water $\delta^{18}O$ to reconstruct changes in P-E are the multiple controls on the $\delta^{18}O$ composition of rainfall, including moisture source, rainfall amount or the atmospheric condensation temperature of rainfall (e.g. Dansgaard, 1964; Ayalon et al., 1998; LeGrande and Schmidt, 2006). These multiple controls hinder P-E reconstructions using $\delta^{18}O$.

This chapter makes use of Mg/Ca, U/Ca and $\delta^{\frac{44}{42}}Ca$ measurements on LCC samples to provide a multi-proxy approach to reconstructing P-E over Lake Bonneville. The LakeCalc model (Chapter 2) suggested that shifts in P-E over the Bonneville Basin should cause measurable shifts in the Mg/Ca, U/Ca and $\delta^{\frac{44}{42}}Ca$ compositions of LCCs, driven by increases or decreases in $CaCO_3$ precipitation. While multiple controls exist for each individual proxy, coherent shifts in all three would increase confidence that they are being controlled by changes in $CaCO_3$ precipitation and hence basin-wide P-E.

This chapter focuses on reconstructing P-E during two specific time periods in the history of Lake Bonneville: i) In the period 25 kyr (BP) - 18.8 kyr (BP) where P-E is well constrained by the closed basin nature of Lake Bonneville and the chronology of paleo-shoreline deposits. ii) In the overflowing period of Lake Bonneville's history (18.0 kyr BP - 14.7 kyr BP), for which P-E reconstructions are currently significantly challenged

by the open basin nature of the system. Period (i) allows me to test whether the LakeCalc modelled response of Mg/Ca, U/Ca and $\delta^{\frac{44}{42}}Ca$ agrees with measured shifts in LCCs during a period of well constrained P-E. Period (ii) allows the multi-proxy approach to P-E reconstruction to investigate the size, direction and potential causes of shifts in P-E during the poorly constrained overflowing period.

3.2 Study site and methodology

3.2.1 Lake level change in Lake Bonneville

Lake Bonneville refers to the most recent cycle of lake rise and fall in the Bonneville Basin, spanning the period 30 kyr (BP) - 13 kyr (BP), for which the lake level history is given in Figure 3.1. Over 360 radiocarbon dates of paleo-shoreline deposits contribute to this reconstruction of the lake level history of Lake Bonneville (Oviatt, 2015). From this rich collection of radiocarbon dates there are three stages of lake level evolution described below: a rising phase; an overflowing phase; and a falling phase (Figure 3.1).

The rising phase of Lake Bonneville occurred between ∼30 kyr (BP) and ∼18.3 kyr (BP) (Oviatt, 2015). During the rising phase, Lake Bonneville was a closed basin and increases in basin-wide P-E resulted in rapid increases in lake volume (Oviatt, 2015). At approximately 30 kyr (BP) lake level started to rise from 1280 metres above sea-level (masl; adjusted for isostatic rebound), which is approximately the height of the modern Great Salt Lake. This transgression continued until Lake Bonneville reached its maximum height of 1550 masl at the Bonneville shoreline (Figure 3.1). The transgression was punctuated by 3-5 small regressions, the largest and best documented of these being the Stansbury Oscillation when lake level stalled and oscillated around the Stansbury shoreline between ∼26.4 kyr (BP) and ∼24.5 kyr (BP) (Currey, 1990; Patrickson et al., 2010; Oviatt, 2015). Once the lake level reached the Bonneville shoreline the catastrophic failure of an alluvial fan, acting as a natural dam in the Red Rock pass, resulted in an almost instantaneous fall in lake level of 130m (Oviatt, 2015; Miller,

2016). This basin wall collapse is known as the "Bonneville Flood". The Bonneville Flood marked the end of the lake's rise, and lake level stabilised at the height (1440 masl) of a new bedrock outflow at the Red Rock pass (Oviatt, 2015; Miller, 2016). The timing of the Bonneville Flood is still debated, with various archives placing the date between 18.3 kyr (BP) and 17.1 kyr (BP) (e.g. Benson et al., 2011; McGee et al., 2012; Oviatt, 2015).

The overflowing phase lasted for approximately 3500 years between ∼18.3 kyr (BP) and ∼14.8 kyr (BP) (Oviatt, 2015). Lake level stabilised at the height of the outflow in the Red Rock pass, forming the prominent Provo shoreline (1440 masl) (Oviatt, 2015). The height of the Provo shoreline increased during the overflowing period as sediment deposition increased the height of the overflow threshold (Miller, 2016). When Lake Bonneville operated as an open basin system, lake level was fixed by the height of the riverine outflow, and no longer responded to increases or decreases in regional P-E (Miller, 2016). Therefore, shifts in P-E over the Bonneville Basin are poorly constrained during this period .

The falling phase started when lake level fell below the overflow threshold in the Red Rock Pass. The timing of the start of the falling phase, is still debated, with estimates ranging between 16.4 kyr (BP) (Godsey et al., 2011; Miller, 2016) and 14.8 kyr (BP) (McGee et al., 2012). The falling phase saw lake level fall from the height of the overflow at the Provo shoreline (1440 masl) to an altitude similar to the modern Great Salt Lake (1280 masl) by ∼13 kyr (BP) (Oviatt, 2015).

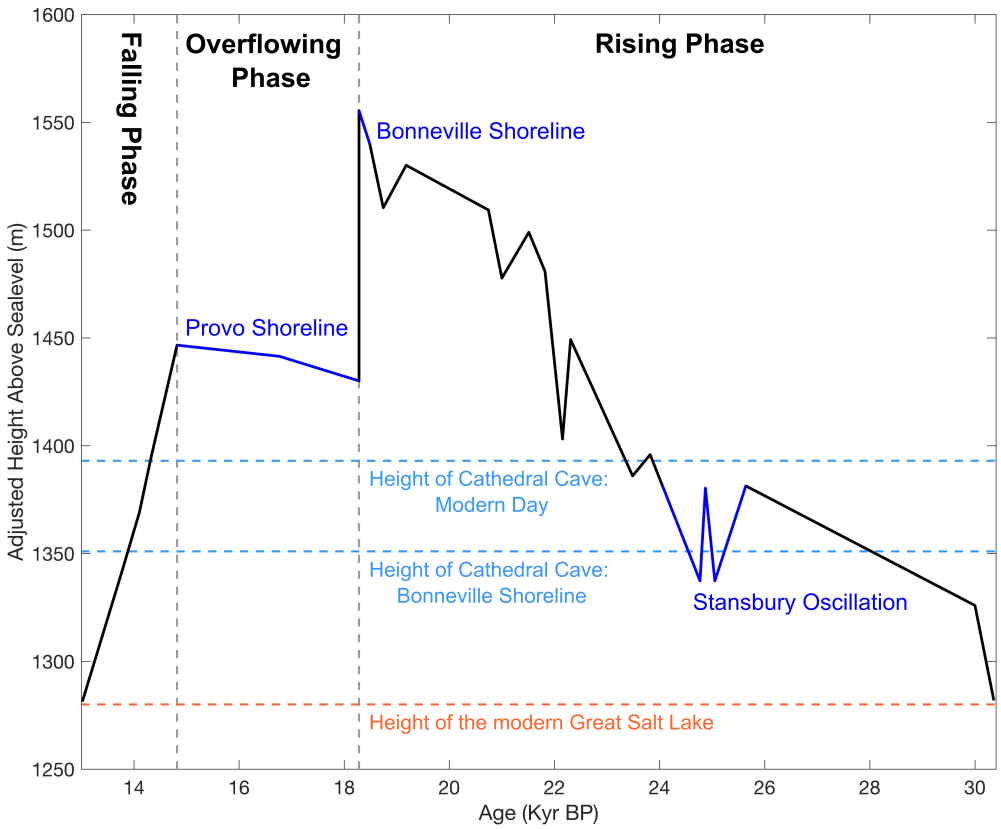


Figure 3.1: Lake level reconstruction of Lake Bonneville over its highstand period. Modified from the lake level record of Oviatt (2015) which is based on the dating of paleo-shoreline deposits. Major lake shorelines are identified and highlighted in blue on the lake level reconstruction: The Bonneville shoreline; The Provo shoreline and The Stansbury Oscillation. The modern height of the Great Salt Lake is plotted in orange. The modern height of Cathedral Cave and its height corrected for isostatic rebound during the Bonneville shoreline are plotted in light blue. The history of Lake Bonneville is divided into three broad sections by grey vertical dashed lines: the rising phase of the lake; the period of overflow; and the fall of the lake.

3.2.2 Cathedral Cave

LCCs studied in this chapter were collected by David McGee from Cathedral Cave in the Bonneville Basin, Utah (41.1653° N, 112.9358° W). A full description of Cathedral Cave is available in McGee et al. (2012) and a summary of information relevant to this chapter is provided here. Cathedral Cave is a karstic cave situated in the Permian Oquirruh Limestone in the Lakeside Range, Utah. Modern day climate above the cave

has a Köppen classification (Chen and Chen, 2013) of cold semi-arid climate with an annual average rainfall of 275 mm/year (Data sourced from climexp.knmi.nl; Trouet and Van Oldenborgh, 2013).

In the modern, Cathedral Cave has an elevation of 1393 masl, 110 m above the level of the Great Salt Lake. When corrected for isostatic rebound, Cathedral cave is estimated to have had an elevation of 1351 masl during the highstand of Lake Bonneville. As Cathedral Cave is within the perimeter and below the elevation of Lake Bonneville highstands, such as the Bonneville and Provo shorelines (Figure 3.1), when lake level exceeded the elevation of Cathedral Cave, the cave was flooded with lake waters. Calcium carbonate precipitated sub-aqueously onto the cave walls during intervals when Cathedral Cave was flooded by Lake Bonneville and lake waters were supersaturated with respect to calcite or aragonite. These lacustrine $CaCO_3$ precipitates are referred to in this chapter as lacustrine cave carbonates (LCCs).

The study of McGee et al. (2012) identified three distinct periods of calcium carbonate precipitation in Cathedral Cave LCCs (Figure 3.2):

Growth Phase I is comprised of 4 cm - 7 cm of aragonite overlain by 0.5 cm - 1 cm of calcite. Growth Phase I varies between fine sub-mm thick lamina and inter-grown mammillary forms.

Growth Phase II is exclusively made of discrete mammillary forms, up to 2 cm thick.

Growth Phase III is a discontinuous layer of aragonite 2 mm - 4 mm thick, which drapes over horizontal surfaces but does not appear on vertical or overhanging surfaces.

Cathedral Cave is currently dry, with no evidence of speleothem formation or dripping water (except at the cave entrance) (McGee et al., 2012). This suggests the lacustrine cave carbonates precipitated in Cathedral Cave have had no interaction with liquid water since the regression of Lake Bonneville.

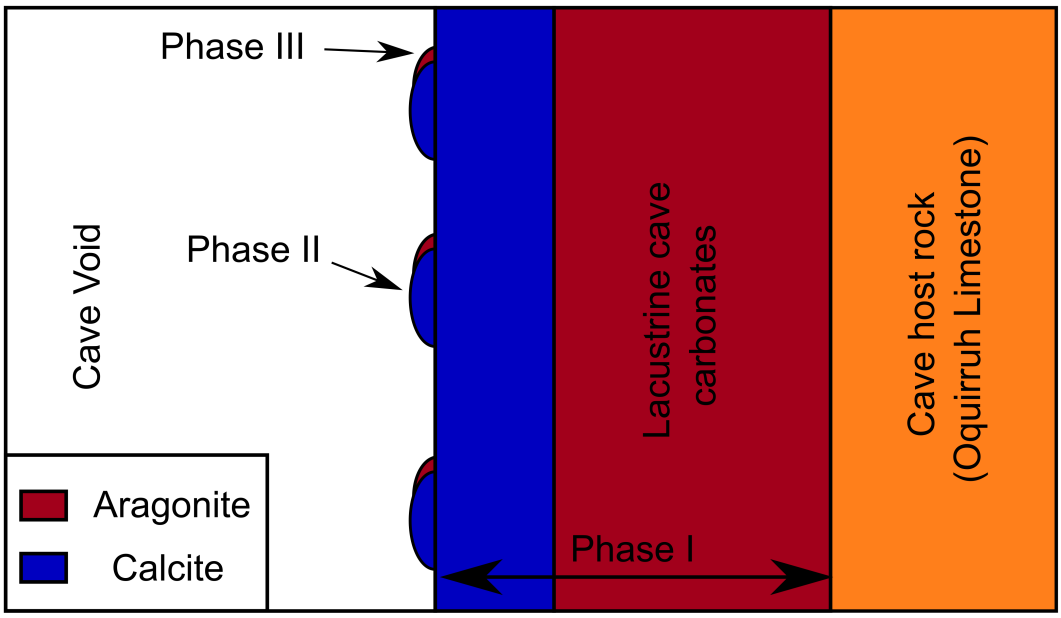


Figure 3.2: A diagram of the relative stratigraphy of LCC Growth Phases, showing difference in mineralogy and Growth Phase. d.

3.2.3 Sample description

This chapter analyses two samples of lacustrine cave carbonates which were collected from the cave walls approximately 60 m from the entrance to Cathedral Cave, samples CC3 and CC5 (Figure 3.3). Sample CC3 is comprised of only Growth Phase I, with ∼4 cm of aragonite overlain by ∼0.5 cm of calcite (Figure 3.3C). Sample CC5 comprises of Growth Phases I, II and III (Figure 3.3B). Growth Phase I contains ∼4 cm of aragonite overlain by ∼0.5 cm of calcite. Growth Phase II is on average 0.5 cm thick. Growth Phase III is a small nodule of aragonite precipitated on top of one of the Growth Phase II mammillary forms (Figure 3.3B).

The differing morphology of Growth Phase III, coupled with it only being identified in Cathedral Cave LCCs, led McGee et al. (2012) to assume a differing origin than Growth Phases I and II. As such, Growth Phase III is not used to reconstruct shifts in basin-wide P-E in this Chapter.

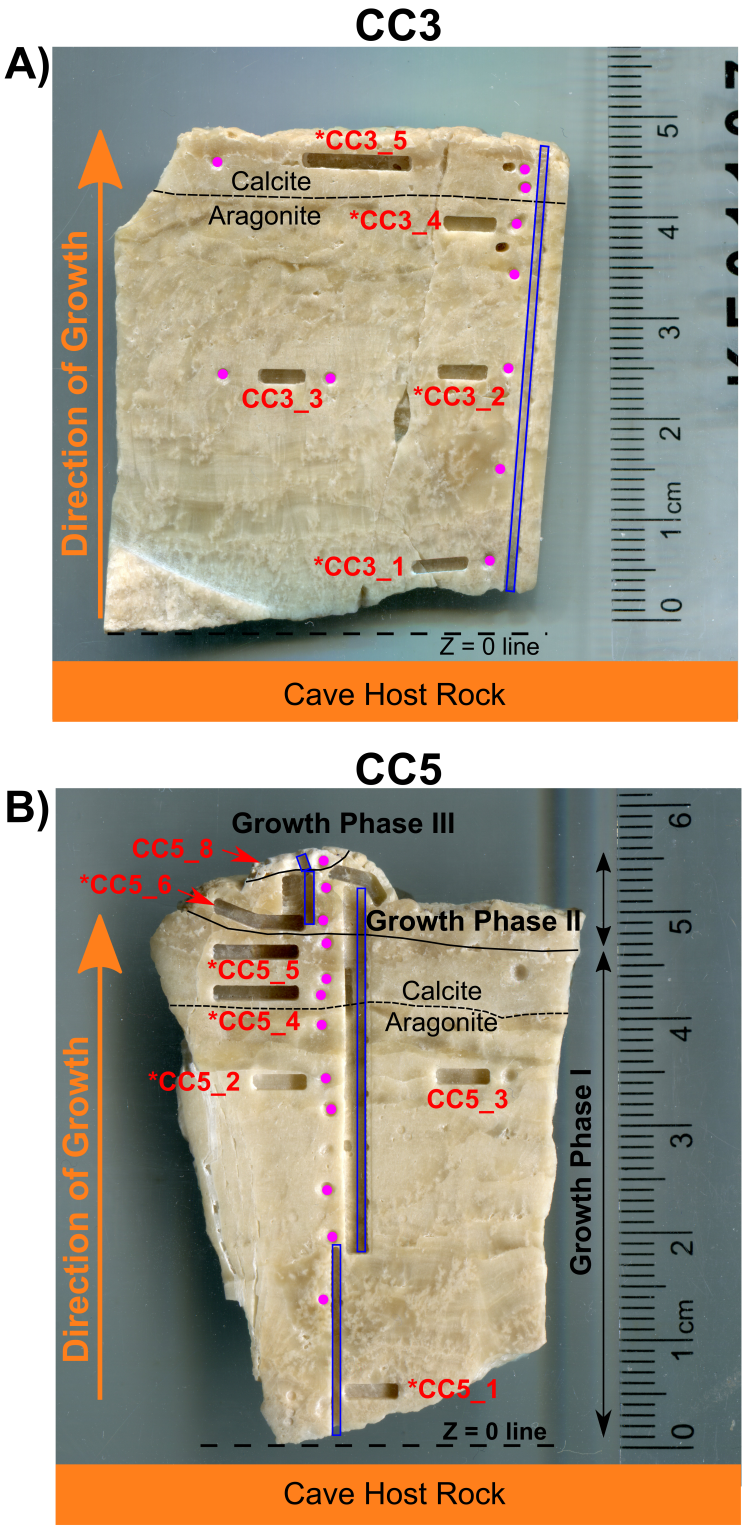


Figure 3.3: Annotated images of samples CC3 and CC5. A) Sample CC3 B) Sample CC5. Continuous black lines separate Growth Phases I, II and III. Annotated dashed lines show the boundary between aragonite and calcite growth in Growth Phase I. Pink dots indicate sampling pits for Ca isotope analysis. Blue rectangles indicate the sampling trenches for trace element analysis. U-Th pits are labelled in red, with * indicating ages used to generate OxCal age models. The direction of sample growth is annotated with an orange arrow, and the zero height (Z) line is annotated below each sample. The approximate relationship between samples and the cave host rock is also shown.

3.2.4 Sampling

After collection, samples CC3 and CC5 were cut to a thickness of < 2 cm and polished prior to sub-sampling. All sampling for U-Th, and trace elements was carried out using a New Wave Research micro-mill fitted with a 0.8 mm diameter tungsten carbide drill bit. Sampling for $\delta^{\frac{44}{42}}$Ca sub-samples was carried out using a hand operated Dremel drill fitted with a 0.85 mm diameter tungsten carbide drill bit. To remove any potential contamination, at least the top 100 μm of each sampled surface was milled and discarded.

Sub-samples for trace element analysis were milled continuously from trenches 0.8 mm wide and 1 mm deep perpendicular to growth laminar at a spatial resolution of 0.5 mm per sub-sample. For sample CC3 a single continuous trench covered the full vertical length of sample CC3 (Figure 3.3A). For sample CC5, the milled trench was shifted, to avoid U-Th and Ca isotope sample pits (Figure 3.3B).

Sub-samples for all analyses were stored in acid cleaned 2 ml sealed Eppendorf polypropylene centrifuge tubes. All centrifuge tubes were cleaned using standard procedure, leaching in 10% HNO_3 for 48 hours and then rinsed five times with 2M H_2O (Laxen and Harrison, 1981).

Sub-sample locations are reported as heights perpendicular to growth lamina above the lowest point in the sample (Figure 3.3). These heights were measured digitally using high resolution scans of CC3 and CC5.

3.2.5 U-Th chronology

Sub-samples of $CaCO_3$ powder for U-Th analyses were collected in the 80 mg - 87 mg mass range for calcite sub-samples, and 17.5 mg - 22.5 mg for aragonite sub-samples, due to varying uranium concentrations in the different polymorphs (Table 3.2).

The sub-samples were dissolved in distilled nitric acid, and uranium and thorium chemically separated following procedures adapted from Edwards et al. (1987a). Uranium and thorium isotopes were then measured on a Nu Plasma Multi-collector Induc-

tively Coupled Plasma Mass Spectrometer (MC-ICP-MS) at the Department of Earth Sciences, University of Oxford following the procedures described in Vaks et al. (2013). The ages were corrected for an initial $^{230}Th/\ ^{232}Th$ ratio of 8 ± 2 ppm, calculated for Cathedral Cave LCC samples by McGee et al. (2012). The raw data was processed using the in-house processing software (DONKEY) which solved the U-Th disequilibrium age equation using 10,000 monte-carlo simulations to generate absolute ages and uncertainties for each sub-sample, accounting for uncertainties in the measured isotope ratios and initial $^{230}Th/^{232}Th$ ratio.

3.2.6 Age depth models

Discrete U-Th ages were used to generate continuous age v. depth models for CC3 and CC5 using the OxCal (version 4.4) age modelling software's Poisson Process deposition model (Ramsey, 2008; Ramsey and Lee, 2013). OxCal is a bayesian deposition model which uses Markov Chain Monte Carlo (MCMC) sampling to generate an ensemble of possible age model solutions from which a mean age model and confidence intervals are calculated (Ramsey, 2008). OxCal parameters of $k_0 = 40$ and $\log_{10}(k/k_0) = U(-1,1)$ were used (Ramsey, 2008, 2009; Ramsey and Lee, 2013).

Due to the presence of well documented hiatuses between growth phases in Cathedral Cave LCCs (McGee et al., 2012), separate OxCal age models were generated for each growth phase (Figure 3.3 and Figure 3.4).

In Growth Phases II and III, less than two U-Th ages were generated in this chapter, precluding the generation of age v. depth models. The study of McGee et al. (2012) applied U-Th chronology to other LCC samples from Cathedral Cave covering all three Growth Phases. In order to allow the generation of age v. depth models for Growth Phases II and III, the start and end ages of these growth phases calculated by McGee et al. (2012) (Table 3.1) were used as constraints in the OxCal age model.

	Height (mm)	Age (Yr. BP)	2σ Error (Yr.)
Growth Phase II Start	47.1	16,400	200
Growth Phase II End	53.3	14,700	200
Growth Phase III Start	53.3	13,800	100
Growth Phase III End	55.5	13,600	100

Table 3.1: Bounding ages and heights of Growth Phase II and III in sample CC5. These discreet age depth constraints are used to constrain generated OxCal age models. The top and bottom heights of the Growth Phases II and III in sample CC5 were measured in this study. The start and end ages of Growth Phase II and III were reported in McGee et al. (2012).

3.2.7 Calcium isotope analysis

Sub-samples of $CaCO_3$ powder were prepared to 100 ppm – 300 ppm Ca in 2M distilled HNO_3. To avoid isobaric interferences during MC-ICP-MS an Elemental Scientific PrepFAST MC was used to separate Ca from Mg and Sr, following the method of Owen (2017). Sub-samples were then refluxed in 16M distilled HNO_3 for 24 hours to destroy any organic matter from the column or samples, dried down, and then dissolved in 2% distilled HNO_3 in preparation for MC-ICP-MS analysis.

Ca-isotope ratios were analysed using a Nu Instruments MC-ICP-MS at the University of Oxford, following the method of Reynard et al. (2011). Three separate batches of Ca isotopes were measured, two batches at 5ppm Ca and one at 10ppm. Samples were bracketed with NIST SRM 915a and each sample and standard measured at least five times. $\delta^{\frac{44}{42}}$Ca was reported relative to normalised NIST SRM 915a. NIST SRM 915b (purified alongside the samples) was used as a secondary standard to determine external accuracy and precision.

Across the three batches of Ca isotopes measurements, repeat average values of NIST SRM 915b were $\delta^{\frac{44}{42}}$Ca= 0.41 ± 0.15‰, $\delta^{\frac{44}{42}}$Ca = 0.40 ±0.10 ‰ and $\delta^{\frac{44}{42}}$Ca = 0.32 ±0.10‰ (2σ, n =9, 8, 5). These are all within error of each other and the reported values of NIST SRM 915b from previous studies using the same MC-ICP-MS methodology $\delta^{\frac{44}{42}}$Ca = 0.35 ± 0.11‰ (2σ, n = 40; Owen et al., 2016) and a study using an independent TIMS methodology $\delta^{\frac{44}{42}}$Ca = 0.36 ± 0.02‰ (2σ, n = 56; Heuser and

Eisenhauer, 2008).

Analytical uncertainty on Ca isotope measurements was taken as the 2σ uncertainty on either all repeat measurements of each sample, or all repeat measurements of the NIST SRM 915b secondary standard, whichever was greater.

3.2.8 Trace element analysis

Sub-samples were dissolved in 2% distilled HNO_3. The trace and major element concentrations were measured using a Perkin Elmer NexION 350D Inductively Coupled Plasma Mass Spectrometer at the Department of Earth Sciences, University of Oxford. Helium was used as a collision gas in the cell for kinetic energy discrimination. The samples were each prepared to approximately 50ppm Ca so they could be matrix matched to calibration standards. All the elements in these multi-element calibration standards were supplied from single element high-purity standards with concentrations certified against NIST Spectrometric Standard Solutions. Elemental concentrations are reported with respect to calcium, giving trace element to calcium molar ratios (X/Ca). X/Ca ratios were determined for Ba, Co, Cd, K, Li, Mg Na, Sr and U (c.f. Supplementary Data File).

This chapter reports Mg/Ca and U/Ca molar ratios as these are the elements considered by the LakeCalc modelling software. X/Ca uncertainties are reported as twice the relative standard deviation of repeat measurements of QC secondary standards generated from sample CC5. Repeat measurements of the aragonite secondary standard gave external precisions of: Mg/Ca: 2.8% and U/Ca: 4.8% (n = 3). Repeat measurements of the calcite secondary standard gave external precisions of: Mg/Ca: 4.4%; and U/Ca: 3.1% (n = 4).

3.2.9 LakeCalc

The LakeCalc single box model was designed to reconstruct the impact of changing P-E on the proportion of inflowing Ca removed by $CaCO_3$ precipitation (PICP), Mg/Ca,

U/Ca and $\delta^{\frac{44}{42}}$Ca during the rise and fall of Lake Bonneville (30 kyr BP - 13 kyr BP). A full description of LakeCalc can be found in Chapter 2.

LakeCalc reconstructs changes in P-E from an inputted lake level reconstruction of Lake Bonneville. In this chapter, LakeCalc is forced by the simplified lake level reconstruction presented in Figure 2.2.

LakeCalc also requires the Mg/Ca, U/Ca and $\delta^{\frac{44}{42}}$Ca of the riverine input to be specified. The Mg/Ca ratio of riverine input is set as the amount weighted annual mean the modern Bear, Weber and Jordan rivers which supply 90% of the modern river input to the Great Salt Lake (Jones et al., 2009): Mg/Ca = 0.82 mol mol^{-1}. Due to the lack of available data for the U/Ca and $\delta^{\frac{44}{42}}$Ca of these rivers, the average global riverine values for these parameters are used: U/Ca = 1.16×10^{-6} mol mol^{-1} (Gaillardet et al., 2003); $\delta^{\frac{44}{42}}$Ca = 0.38 ‰ (Tipper et al., 2010).

As global, rather than Bonneville specific, riverine values are used by LakeCalc, this chapter focuses on comparing relative rather than absolute changes between the LakeCalc output and measured LCC values.

3.3 Results

3.3.1 U-Th ages

A total of 12 U-Th ages were measured, five from sample CC3 and seven from sample CC5 (Table 3.2). Aragonite sub-samples had higher U concentrations (11 $\mu g\,g^{-1}$ - 21 $\mu g\,g^{-1}$) than the calcite sub-samples ($< 1.7\ \mu g\,g^{-1}$). Consequently, aragonite sub-samples have higher [^{230}Th] concentrations than the calcite sub-samples. The average 2σ uncertainty of U-Th dates calculated from aragonite sub-samples is therefore smaller ($\pm$80 Yr.) than the calcite sub-samples ($\pm$300 Yr.) (Table 3.2).

			MC-ICP-MS Measurements								Age Calculation			
Sample ID	Height (mm)	Mineralogy	$[^{238}U]$ (ppm)	$[^{232}Th]$ (ppb)	$\delta^{234}U$ (‰)	± 2σ	$\left(\frac{^{230}Th}{^{238}U}\right)$ $(\times 10^1)$	± 2σ	$\left(\frac{^{232}Th}{^{238}U}\right)$ $(\times 10^3)$	± 2σ	Uncorrected Ages (Yr BP)	± 2σ	**Corrected Ages (Yr BP)**	**± 2σ**
*CC3-1	9.1	Aragonite	13.9	61.2	962	2	4.076	0.011	1.445	0.007	24860	80	**24740**	**90**
*CC3-2	28.5	Aragonite	15.5	47.0	935	2	3.592	0.009	0.992	0.005	21950	70	**21870**	**70**
CC3-3	27.5	Aragonite	17.2	47.8	935	2	3.555	0.008	0.910	0.004	21720	60	**21640**	**70**
*CC3-4	43.1	Calcite	2.1	51.3	918	2	3.151	0.008	0.813	0.003	19230	60	**19160**	**60**
*CC3-5	48.5	Calcite	1.5	80.4	876	2	3.119	0.011	17.80	0.08	19480	80	**17970**	**370**
*CC5-1	4.9	Calcite	11.2	63.8	962	3	4.047	0.011	1.856	0.008	24660	90	**24510**	**90**
*CC5-2	33.6	Aragonite	18.9	36.7	914	2	3.350	0.009	0.635	0.004	20600	60	**20550**	**60**
CC5-3	34.0	Aragonite	18.8	56.3	911	2	3.302	0.008	0.981	0.004	20320	60	**20240**	**60**
*CC5-4	41.9	Aragonite	1.0	38.3	910	2	3.209	0.013	12.22	0.05	19700	90	**18690**	**260**
*CC5-5	45.8	Aragonite	1.7	56.7	868	2	2.964	0.010	11.09	0.05	18530	70	**17580**	**250**
*CC5-6	48.4	Aragonite	1.3	52.4	1019	3	2.891	0.012	12.82	0.07	16570	80	**15560**	**250**
CC5-8	54.9	Calcite	13.1	206.8	1047	3	3.101	0.011	5.16	0.02	16880	70	**17210**	**120**

Table 3.2: U-Th ages calculated from samples CC3 and CC5. Height is the distance above the base of the sample in mm. Years BP is years before 1950 C.E. Dates with * on their sample names indicates they were used in the generation of age models. Dates with red text were discounted due to high ^{232}Th concentrations and age reversals. Ages were corrected with an initial $^{230}Th/\ ^{232}Th$ ratio of 8 ± 2 ppm.

3.3.2 Age depth models

Age v. depth models were created for all growth periods of CC3 and CC5 using the OxCal (version 4.4) age modelling software's Poisson Process deposition model (Ramsey, 2008; Ramsey and Lee, 2013) (c.f. Section 3.4).

Only U-Th ages collected on a vertical transect immediately adjacent to the trace element and calcium isotope sampling sites were used to generate the age models due to lateral variations in growth laminar across the samples. As such, samples CC3_3 and CC5_3 were not used to generate age models (Table 3.2 and Figure 3.3). Sample CC5_8 was also not used in age model generation, due to its anomalously high detrital ^{232}Th, resulting in its corrected age not being in stratigraphic order with other U-Th ages. This could be due to a secondary source of detrital thorium with a different initial^{230}Th/^{232}Th ratio.

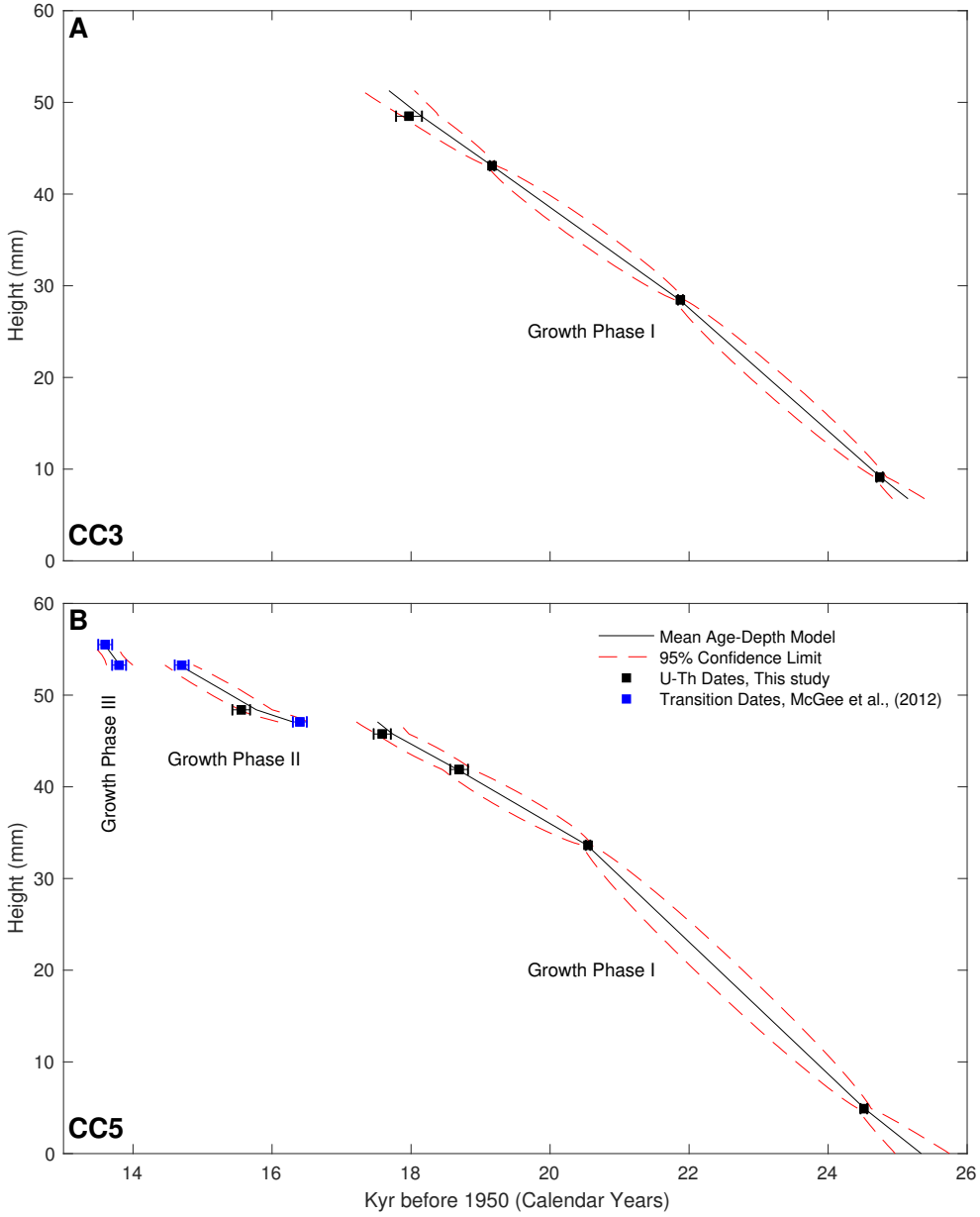


Figure 3.4: Age v. depth models for samples CC3 and CC5. A) OxCal age v. depth model for sample CC3 Growth Phase I. B) Three OxCal age v. depth models for sample CC5 for Growth Phase I, II and III. Discrete age depth constrains inputted to OxCal are shown with squares and 95% confidence intervals. Black squares are U-Th dates calculated in this study, blue squares are bounding ages for the start and end of Growth Phase II and III from McGee et al. (2012). The 95% confidence intervals of the OxCal age models are plotted with dashed red lines.

3.3.3 Ca isotopes

Two Ca isotope time series were generated, one for sample CC3 and one for CC5. Samples CC3 and CC5 both show considerable variations in $\delta^{\frac{44}{42}}$Ca. $\delta^{\frac{44}{42}}$Ca from sample CC3 varies between 0.13‰ and 0.58‰, with an average of 0.32‰ (Figure 3.5B). $\delta^{\frac{44}{42}}$Ca from sample CC5 varies between 0.12‰ and 0.69‰, with an average of 0.37‰ (Figure 3.5A).

In sample CC3, during the aragonite section of Growth Phase I, $\delta^{\frac{44}{42}}$Ca averages 0.22‰ and shows no significant trend with age (Figure 3.5B). Across the transition to calcite there is a large increase in $\delta^{\frac{44}{42}}$Ca to an average value of 0.58‰, after the transition $\delta^{\frac{44}{42}}$Ca continues to increase to its highest value (Figure 3.5B).

In sample CC5, during the aragonite section of Growth Phase I, $\delta^{\frac{44}{42}}$Ca has an average value of 0.26‰, and shows a significant trend of decreasing with decreasing age. Across the transition to calcite in Growth Phase I there is a shift to higher values, with an average $\delta^{\frac{44}{42}}$Ca of 0.43‰. $\delta^{\frac{44}{42}}$Ca briefly continues to increase, before decreasing to its lowest calcite value in Growth Phase I (Figure 3.5A). In CC5 Growth Phase II, $\delta^{\frac{44}{42}}$Ca has an average value of 0.33‰ and shows a significant decrease between 15.7 kyr (BP) and 15.1 kyr (BP). Finally, in Growth Phase III the highest values of $\delta^{\frac{44}{42}}$Ca in CC5 are recorded, with an average value of 0.60‰ (Figure 3.5A).

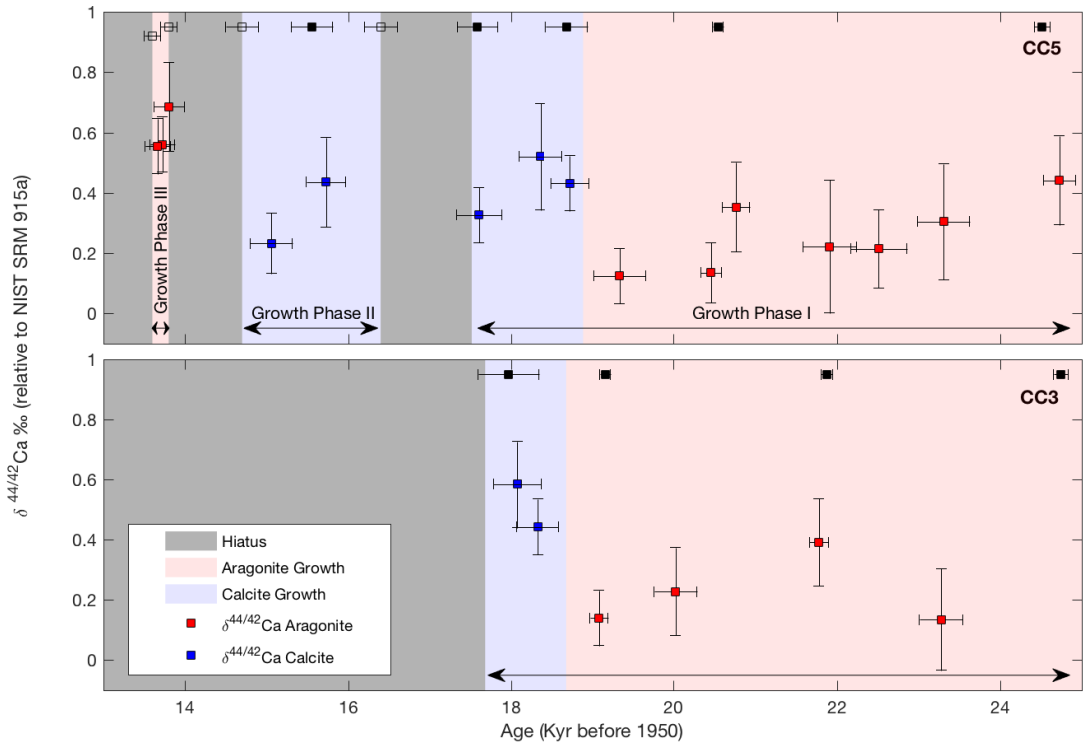


Figure 3.5: $\delta^{\frac{44}{42}}$Ca timeseries from both: A) Sample CC5 and B) Sample CC3. The mineralogy of measured sub-samples is shown with blue points referring to calcite and red points to aragonite. The mineralogy of samples CC3 and CC5 is shown with shading on the figure, with blue referring to calcite and red to aragonite. Grey shading refers to periods of no growth. The error bars refer to 2σ instrumental uncertainty.

3.3.4 Trace elements

Trace element time-series were generated for samples CC5 and CC3 for both Mg/Ca and U/Ca (Figure 3.6). CC3 and CC5 show large variability in both the Mg/Ca and U/Ca timeseries.

Mg/Ca in sample CC3 varies between 1.0 mmol mol^{-1} and 93 mmol mol^{-1} whilst U/Ca varies between 0.4 µmol mol^{-1} and 9.3 µmol mol^{-1}.

Mg/Ca in sample CC5 varies between 1.2 mmol mol^{-1} and 92 mmol mol^{-1} whilst U/Ca varies between 0.4 µmol mol^{-1} and 9.1 µmol mol^{-1}.

Coherent trends were observed in the aragonite section of Growth Phase I for both elements, with U/Ca increasing and Mg/Ca decreasing between 22 kyr (BP) - 19 kyr (BP) in both CC5 and CC3 (Figure 3.6). Step changes occur in both CC3 and CC5 for

both Mg/Ca and U/Ca over the transition between aragonite and calcite growth. The calcite section of Growth Phase I contains a rapid shift in both elements. This event starts at 18,100 ± 300 Yr. (BP) in CC5 and 18,000 ± 300 Yr. (BP) in CC3. Expressed as a rapid rise in U/Ca and a rapid fall in Mg/Ca (Figure 3.6).

In sample CC5, Growth Phase II also contains a rapid perturbation in X/Ca starting at 15,700 ± 200 years (BP). It presents as a rapid decrease in U/Ca and Mg/Ca lasting till 15,400 ± 200 years (BP), after which U/Ca and Mg/Ca increase steadily until the end of Growth Phase II (Figure 3.6).

In sample CC5, Growth Phase III, and a return to aragonite precipitation, contains the maximum Mg/Ca value measured in the aragonite portions of CC5, 18 $\mathrm{mmol\,mol^{-1}}$. U/Ca returns to levels within the range of Growth Phase I aragonite (Figure 3.6).

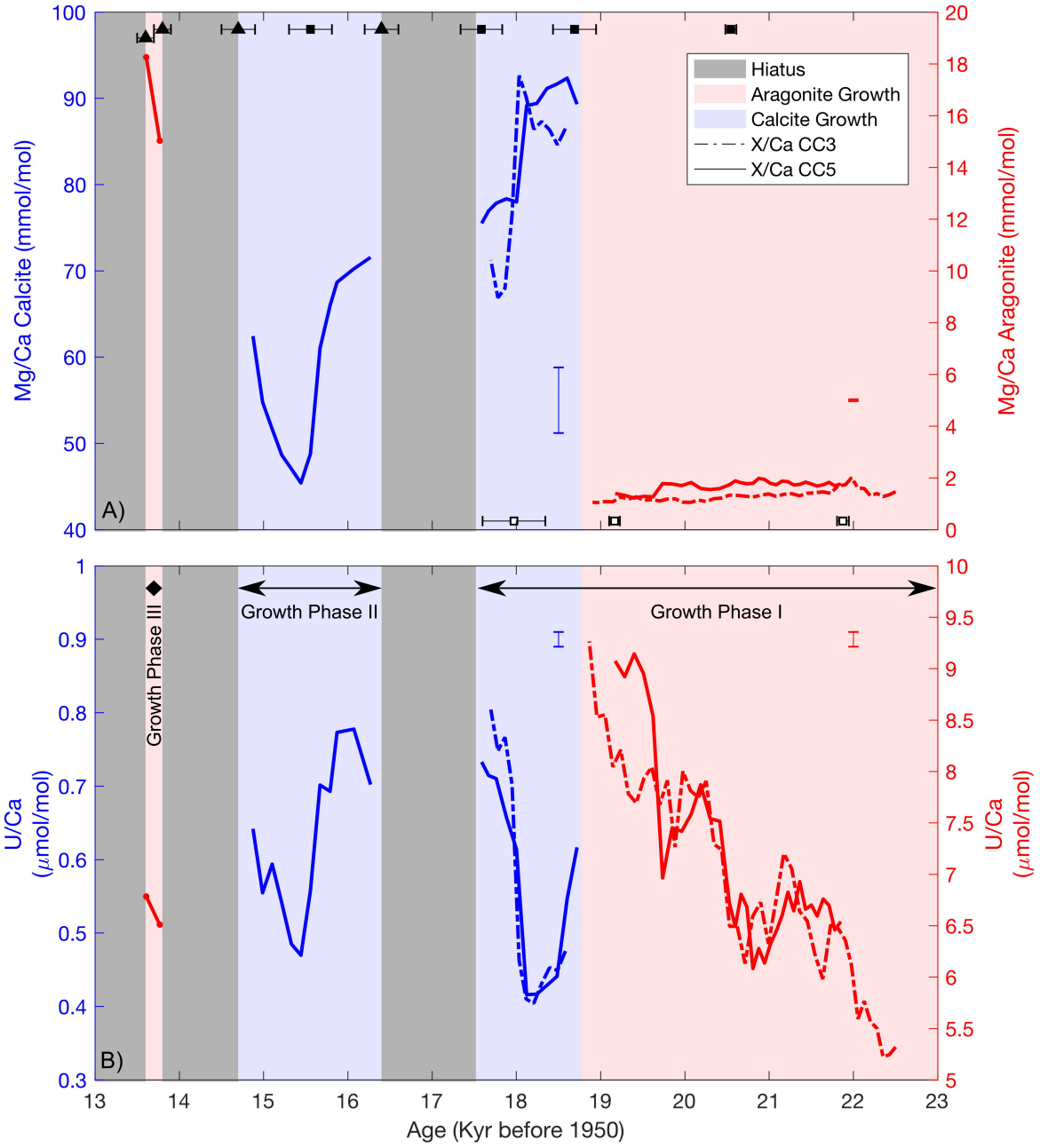


Figure 3.6: Trace element (Mg/Ca and U/Ca) timeseries for samples CC5 and CC3, showing: A) Mg/Ca; and B) U/Ca. Timeseries from CC5 are presented with a solid line and those from CC3 with a dashed line. The mineralogy of the measured sub-samples is shown in the colour of the plotted lines, with blue referring to calcite sub-samples and red to aragonite sub-samples. Coloured shading is used to show the mineralogy of samples CC3 and CC5, with blue shading referring to calcite growth, red shading to aragonite growth and grey shading hiatuses in sample CC5. Error bars are plotted to show average X/Ca 2σ uncertainties, with aragonite uncertainties plotted in red and calcite in blue. Age constrains are added as black shapes with error bars showing 2σ uncertainties. Filled black squares are U-Th dates on CC5, unfilled black squares U-Th dates on CC3 and triangles bounding ages of growth periods from McGee et al. (2012). The durations of Growth Phase I, Growth Phase II and Growth Phase III are labelled.

3.4 Discussion

3.4.1 Comparing the measured and modelled composition of LCC deposits during well constrained shifts in P-E over the Bonneville Basin (25 kyr BP - 18.8 kyr BP)

To test whether Lake Bonneville's chemistry responded to shifts in basin-wide P-E, and whether this response was recorded in LCC deposits, I compare measured shifts in Mg/Ca, U/Ca and $\delta^{\frac{44}{42}}Ca$ with the LakeCalc model output. Whilst Lake Bonneville is a closed basin, lake level provides a good approximation of basin-wide P-E (Miller et al., 2013; Oviatt, 2015). However, during periods of outflow, lake level decouples from P-E and is held constant at the height of the overflow (Miller, 2016). As LakeCalc reconstructs shifts in P-E from a simplified Lake Bonneville lake level reconstruction, LakeCalc can only accurately reconstruct shifts in P-E, and hence lake chemistry, while Lake Bonneville behaves as a closed basin. The aragonite portion of Growth Phase I (25 kyr BP - 18.8 kyr BP) precipitated exclusively in closed basin conditions during the rise of Lake Bonneville (Oviatt, 2015). It, therefore, provides a perfect natural laboratory to test whether changes in PICP are controlling the Mg/Ca, U/Ca and $\delta^{\frac{44}{42}}Ca$ composition of LCCs during well constrained shifts in basin-wide P-E. However, due to uncertainties in the composition of the modelled inputs to LakeCalc (c.f. Section 3.2.9) only the direction of the trends, as opposed to the absolute values, reconstructed by LakeCalc will be compared to measured LCC proxy values.

Between 25 kyr (BP) and 18.8 kyr (BP), LakeCalc models the rise in lake level to reduce PICP (Figure B.1B). As such, LakeCalc predicts that $\delta^{\frac{44}{42}}Ca$ and Mg/Ca will decrease throughout this period and that U/Ca will increase. These modelled behaviors are replicated in the measured LCC values (Figure 3.7). There is more variability in the measured data than in the model output, which might be explained by this application of LakeCalc not accounting for multiple short lived regressions that occur during the rising phase of Lake Bonneville (Figure 3.7A). Subtle shifts in input composition to

Lake Bonneville, or kinetic effects altering the inclusion of proxy values into LCCs may also be responsible for some of the observed variability in measured values.

In the aragonite portion of Growth Phase I, measured trends in Mg/Ca, U/Ca and $\delta^{\frac{44}{42}}Ca$ in LCCs behave as expected for well constrained shifts in basin-wide P-E, suggesting PICP is controlling the Mg/Ca, U/Ca and $\delta^{\frac{44}{42}}Ca$ composition of LCCs.

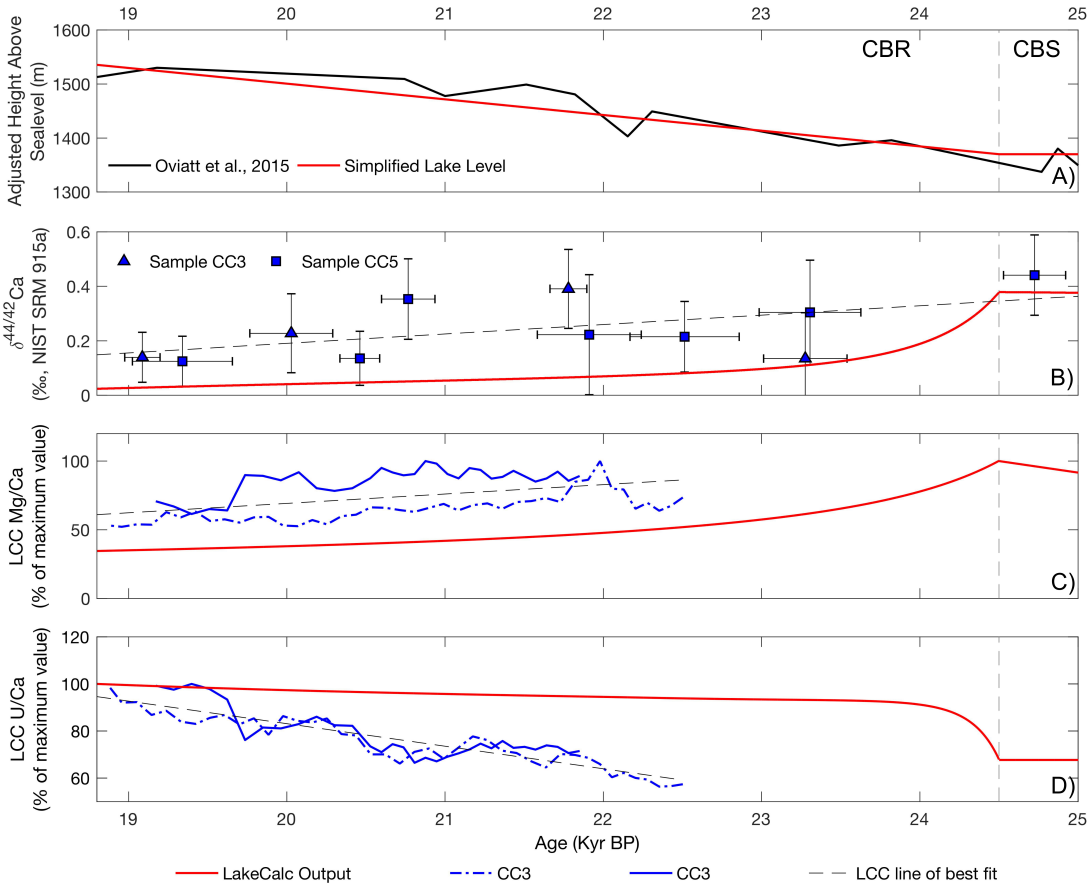


Figure 3.7: Comparison of modelled LakeCalc outputs and measured LCC proxy data during the aragonite portion of Growth Phase I. A) Comparison of the lake level reconstruction of Oviatt (2015) with the simplified lake level reconstruction used to force LakeCalc. A dashed vertical grey line separates time periods where LakeCalc models the evolution of Lake Bonneville as a rising closed basin (CBR) and a closed basin of constant volume (CBS) (Chapter 2). In sub-plots B), C) and D) a linear line of best fit is plotted through all measured LCC values in CC3 and CC5. B) LakeCalc modelled LCC $\delta^{\frac{44}{42}}Ca$ (red line) is plotted against LCC $\delta^{\frac{44}{42}}Ca$ measured in CC3 (blue triangles) and CC5 (blue squares), error bars indicate the 2σ age and $\delta^{\frac{44}{42}}Ca$ uncertainties. The equation of the line of best fit is: $f(x) = 0.0346\,(\pm 0.0392, 2\sigma)x - 0.502\,(\pm 0.848, 2\sigma)$. C) LakeCalc modelled LCC Mg/Ca (red line) plotted against Mg/Ca measured in CC3 (blue dashed line) and CC5 (blue solid line). Due to differing absolute values, modelled and measured LCC Mg/Ca is plotted as a percentage of the maximum value in the age range. The equation of the line of best fit is: $f(x) = 6.83\,(\pm 3.02, 2\sigma)x - 67.36\,(\pm 62.66, 2\sigma)$. D) LakeCalc modelled LCC U/Ca (red line) plotted against U/Ca measured in CC3 (blue dashed line) and CC5 (blue solid line). Due to differing absolute values, modelled and measured LCC U/Ca is plotted as a percentage of the maximum value in the age range. The equation of the line of best fit is: $f(x) = -9.57\,(\pm 1.15, 2\sigma)x - 274.60\,(\pm 23.95, 2\sigma)$.

3.4.2 Insights into basin structural changes using LCCs: Constraining the timing of the Bonneville Flood

The end of closed basin conditions in Lake Bonneville starts with the collapse of the basin wall and the development of an overflow at Red Rock Pass (Miller, 2016; Oviatt, 2015). This collapse event is known as the "Bonneville Flood". The exact timings of the Bonneville Flood are still debated (Miller, 2016), with the aggregated 2σ age range calculated from paleo-shoreline deposits 18.6 kyr (BP) – 17.1 kyr (BP) (Oviatt, 2015) (Figure 3.8). The main source of uncertainty on the age of this collapse event is the large age uncertainties on radiocarbon dates of paleo-shoreline deposits.

LakeCalc predicts a decrease in PICP over the Bonneville Flood. As the lake level decreases, due to the collapse of the basin wall, the lake surface area decreases significantly, decreasing evaporation from the lake. As climate conditions stay constant over this event, solution input to the lake should remain approximately constant. As such, evaporation is reduced relative to solution input, resulting in reduced precipitation of $CaCO_3$ and hence PICP. LakeCalc predicts that the Bonneville Flood would be expressed in lake water chemistry an increase in rate of U/Ca increase and an increased rate of Mg/Ca and $\delta^{\frac{44}{42}}Ca$ decrease (Figure 3.8).

U/Ca evolution at this time is complicated by the shift from aragonite to calcite precipitation in Lake Bonneville at 18.8 kyr (BP). U/Ca would normally be expected to decrease with a decreasing PICP in a calcite precipitating lake. However, LakeCalc reconstructed the previous precipitation of aragonite from Lake Bonneville left lake waters depleted with respect to U compared to riverine input, as $D(U)_{Argonite-Solution} > 1$. After the transition to calcite precipitation, as $D(U)_{Calcite-Solution} < 1$, U is enriched in lake waters with $CaCO_3$ and U/Ca starts to increase. This increase is not controlled by PICP, but by the system readjusting to the precipitation of calcite. Therefore, information U/Ca can provide about shifts in PICP during this period is limited.

Samples CC3 and CC5 both show a rapid decrease in Mg/Ca, starting at 18.1 $\pm$ 0.3 kyr (BP, 2σ) in CC5 and 18.0 $\pm$ 0.3 kyr (BP, 2σ) in CC3 (Figure 3.8C). As this

decrease occurs simultaneously in both samples, it is assumed to represent the same event. The lower resolution $\delta^{\frac{44}{42}}Ca$ timeseries also shows a decrease across this interval in CC5. However, this trend is comprised of just two data points and is consequently not very robust (Figure 3.8B). As the rapid decrease in Mg/Ca in both CC5 and CC3 occurs within the 2σ age range of the Bonneville Flood, and both measured Mg/Ca and $\delta^{\frac{44}{42}}Ca$ agree with the modelled LakeCalc behaviour for the Bonneville Flood, it is assumed the rapid shift in Mg/Ca is the expression of the Bonneville Flood in LCC deposits. The aggregate of the CC3 and CC5 ages for the onset of the rapid decrease in Mg/Ca, give the Bonneville Flood an age of 18.05 ± 0.35 kyr (BP, 2σ), a significant improvement on the paleo-shoreline derived age (Figure 3.8A).

A previous study of Lake Bonneville Cathedral Cave LCCs McGee et al. (2012) attempted to reconstruct shifts in P-E balance using $\delta^{18}O$. McGee et al. (2012) concluded that a 0.2‰ decrease $\delta^{18}O$ between 19.0 kyr (BP) and 18.8 kyr (BP) was indicative of a period of overflow from the Bonneville Shoreline prior to the Bonneville Flood. However, this interpretation in at odds with the rock record, where preserved Bonneville Shoreline deposits indicate a transgressive, rather than a stationary, shoreline suggesting lake level did not stabilise at the Bonneville Shoreline prior to the Bonneville Flood (Oviatt, 2015). A larger rapid decrease in $\delta^{18}O$ of 0.8‰ at 18.4 ±0.3 kyr (BP) (Figure3.8E) occurs within error of the rapid shift in Mg/Ca reported in this study, 18.05 ± 0.35 kyr (BP, 2σ), and could be indicative of a rapid freshening of lake waters caused by the onset of overflow during the Bonneville flood. While $\delta^{18}O$ has many controls in lake waters, the decrease in $\delta^{18}O$ provides additional evidence of a large shift in lake chemistry which occurred synchronously within error of the timing of the Bonneville Flood estimated in this study.

Two discrepancies do exist between LCC and LakeCalc modelled behaviour during the calcite portion of Growth Phase I. Firstly, LakeCalc predicts a cessation of LCC precipitation after the Bonneville Flood, while both CC3 and CC5 continue to precipitate (Figure 3.8). This discrepancy could be caused by either LakeCalc overestimating

the volume of overflow at the Provo shoreline, or the parameterisation of $CaCO_3$ precipitation failing to fully reconstruct the natural world. Secondly, at the start of calcite precipitation in Growth Phase I (18.8 kyr BP), U/Ca decreases rapidly in both CC5 and CC3, at odds with the LakeCalc predicted behavior (Figure 3.8). This discrepancy, does not necessarily mean a non PICP control on lake water U/Ca, and could be explained by mixing of calcite and aragonite growth in sub-samples collected across the aragonite to calcite transition. XRD measurements would be required to confirm this.

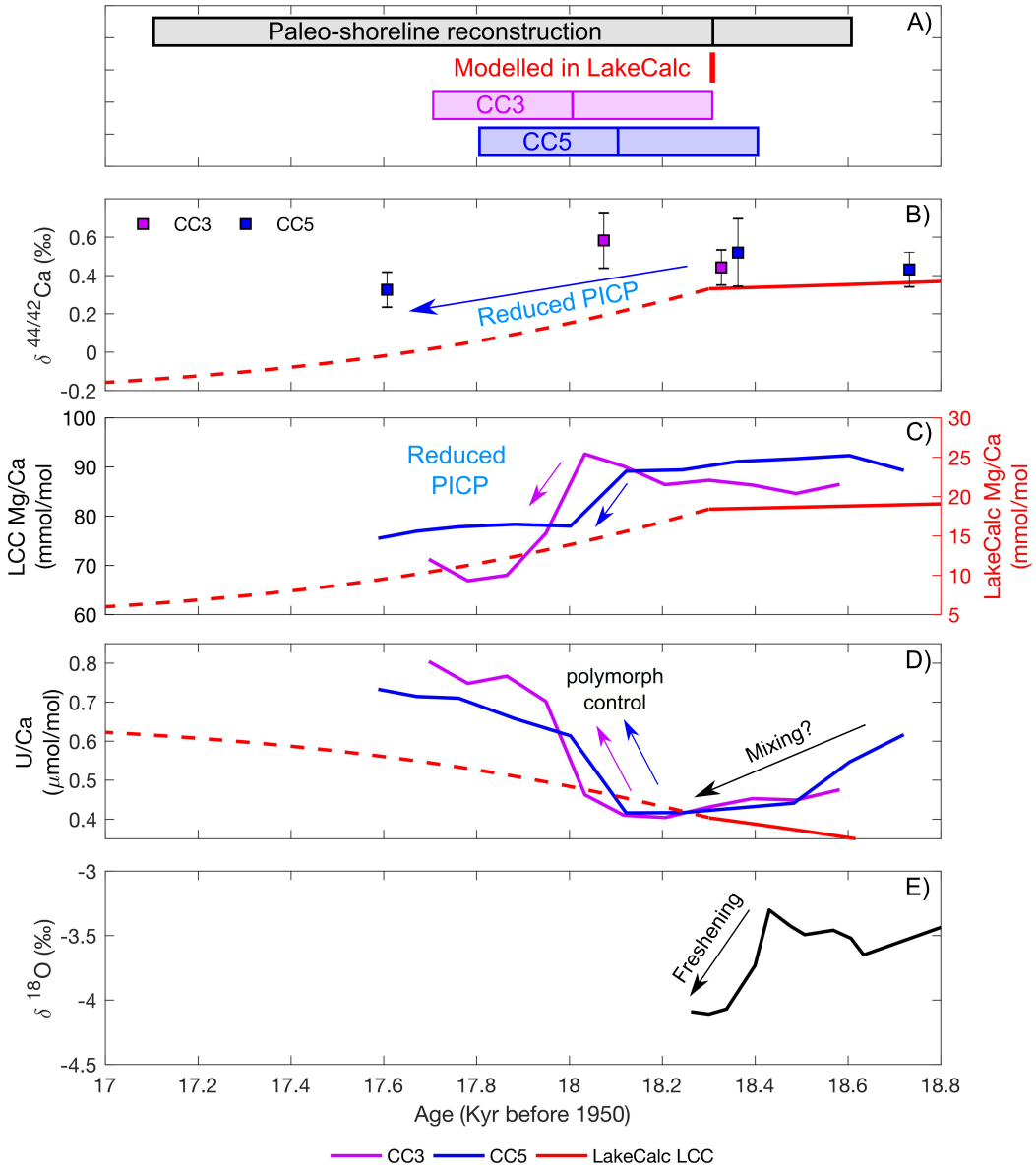


Figure 3.8: A comparison of modelled and measured LCC composition at the time of the Bonneville Flood. A) The 2σ range of estimates of the timing of the Bonneville Flood from paleo-shoreline deposits (plotted in grey) (Oviatt, 2015); the age of the Bonneville Flood in the LakeCalc model (plotted in red); the 2σ age model uncertainty on the age of the decrease in Mg/Ca in sample CC5 (plotted in purple); and the 2σ age model uncertainty on the age of the decrease in Mg/Ca in sample CC5 (plotted in blue). Dark lines indicate the mean age of the shift in Mg/Ca in CC3 and CC5; and the estimate of the age of the Bonneville Flood used in the lake level reconstruction of Oviatt (2015). B) Measured LCC $\delta^{\frac{44}{42}}Ca$ from CC3 (purple squares) and CC5 (blue squares) with error bars indicating 2σ uncertainties and LakeCalc modelled $\delta^{\frac{44}{42}}Ca$ (red line). C) Measured LCC Mg/Ca from CC3 (purple line) and CC5 (blue line) and LakeCalc modelled Mg/Ca (red line). D) Measured LCC U/Ca from CC3 (purple line) and CC5 (blue line) and LakeCalc modelled Mg/Ca (red line). During periods where LakeCalc reconstructed a hiatus in LCC precipitation, the theoretical composition of LCC deposits, if they were precipitated, is plotted with a dashed red line. E) $\delta^{18}O$ time-series generated from Cathedral Cave LCC deposits (McGee et al., 2012)

3.4.3 New insights into the period of overflow of Lake Bonneville from LCC deposits (∼18.0 kyr BP - ∼14.7 kyr BP)

During periods where Lake Bonneville behaves as an open lake (∼18.0 kyr BP - ∼14.7 kyr BP) lake height can no longer be used to assess P-E. In this open basin scenario any changes in P-E result in increased or decreased volumes of riverine outflow, as opposed to shifts in lake level. However, shifts in P-E should continue to control PICP and hence be recorded in LCCs during periods of overflow. Here I discuss the degree to which shifts in P-E can be assed using LCC growth during the overflowing period. As only sample CC5 precipitates during Growth Phase II, it is the only sample considered here.

3.4.3.1 Identifying shifts in P-E

CC5 suggests four changes in P-E during the period of overflow, which cannot be resolved from lake level. I refer to these as OI (17.5 kyr BP - 16.4 kyr BP), OII (16.4 kyr BP - 15.7 kyr BP), OIII (15.7 kyr BP - 15.4 kyr BP) and OIV (15.4 kyr BP - 14.7 kyr BP) (Figure 3.9). I consider each of these in turn. While $\delta^{\frac{44}{42}}Ca$ is measured at too low a resolution over this period to reach firm conclusions on shifts in P-E, solid agreement between higher resolution Mg/Ca and U/Ca timeseries are used to reconstruct variable P-E.

Period OI is expressed as a hiatus in the precipitation of CC5 between 17.5 ± 0.3 kyr (BP) and 16.4 ± 0.2 kyr (BP) (Figure 3.9B). LCC growth occurs while the lake is supersaturated with respect to $CaCO_3$ and Cathedral Cave is flooded by Lake Bonneville. As paleo-shoreline reconstructions suggest Cathedral Cave was below the level of Lake Bonneville for the duration of this period, the cessation of LCC precipitation suggests that Lake Bonneville freshened to the extent that $CaCO_3$ was no longer supersaturated in lake waters. The continued precipitation of CC5 for approximately 500 years after the Bonneville Flood (18.05 ± 0.35 kyr BP, 2σ) (Figure 3.8), suggests that

the onset of overflow during the Bonneville Flood was not responsible for the cessation of LCC precipitation. An increase in P-E must have occurred after the Bonneville Flood freshening lake waters sufficiently that $CaCO_3$ precipitation became unfavorable. The resumption of CC5 precipitation at 16.4 ± 0.2 kyr (BP) indicates that $CaCO_3$ was once again supersaturated in in lake waters, indicating a decrease in riverine outflow and hence a decrease in basin-wide P-E. The hiatus in LCC precipitation therefore suggests that a maximum in P-E occurred over the Bonneville Basin between 17.5 ± 0.3 kyr (BP) and 16.4 ± 0.2 kyr (BP). This agrees with other lakes in the south-west, centre and north east of the Great Basin, with highstands, and hence maxima in P-E, clustered between 17.5 kyr (BP) and 16.5 kyr (BP) (McGee et al., 2018), e.g. Lake Franklin (Figure 3.9C).

Periods OII, OIII and OIV are expressed in Growth Phase II and are identified by large rapid shifts in Mg/Ca and U/Ca. After precipitation resumes at 16.4 ± 0.2 kyr (BP) Mg/Ca and U/Ca decrease rapidly between 15.7 kyr (BP) and 15.4 kyr (BP). The lower resolution $\delta^{\frac{44}{42}}Ca$ timeseries also decreases across this period. The coherent behaviour of these three proxies suggests a reduction in PICP and hence an increase in P-E. A minimum in Mg/Ca and U/Ca occurs at 15.4 kyr (BP), after which they both increase until the end of CC5 growth at 14.7 ± 0.2 kyr (BP), indicating an increase in PICP and hence a reduction in basin-wide P-E. Period OII is identified as a period of reduced P-E balance between the start of Growth Phase II and the onset of the decrease in U/Ca and Mg/Ca (16.4 kyr BP - 15.7 kyr BP). Period OIII is identified as a period of increased P-E balance bounded by the start and end of the decrease in U/Ca and Mg/Ca (15.7 kyr BP - 15.4 kyr BP). Finally, Period OIV is identified as a period of reduced P-E between the start of the increase in U/Ca and Mg/Ca and the end of CC5 growth (15.4 kyr BP - 14.7 kyr BP) (Figure 3.9).

The cessation of Growth Phase II in CC5 could be caused by a number of factors. Lake Bonneville could have fallen below the level of Cathedral Cave (1350 masl) (McGee et al., 2012) or an increased Mg/Ca ratio in lake waters could have made the precipi-

tation of calcite thermodynamically unfavorable (Wassenburg et al., 2016). The higher solubility of aragonite coupled with a lack of nucleation sites could have led to aragonite precipitation ceasing in Cathedral Cave, even if aragonite was supersaturated in lake waters. Paleo-shoreline reconstructions suggests that Cathedral Cave should have been submerged by Lake Bonneville when CC5 precipitation ceased, however, due to the age uncertainties on both the termination of Growth Phase II and paleo-shoreline deposits, the fall of Lake Bonneville below Cathedral Cave cannot be discounted as the cause of the termination of CC5 growth.

This new Lake Bonneville P-E reconstruction is at odds with a previous reconstruction using $\delta^{18}O$ from Cathedral Cave LCC deposits (McGee et al., 2012). McGee et al. (2012) interpreted a large increase in LCC $\delta^{18}O$ of 1.6‰, starting at 15.9 ±0.2 kyr (BP) and continuing to the cessation of Growth Phase II at 14.5 ±0.2 kyr (BP), to be evidence for the onset of the continuous fall of Lake Bonneville from the Provo Shoreline to its modern day elevation, and hence a decrease in P-E (Figure 3.9C). However, the leviathan chronology (a spliced Great Basin speleothem $\delta^{18}O$ timeseries) contains an increase in $\delta^{18}O$ of 2.8‰ between 15.9 kyr (BP) and 13.6 kyr (BP) (Lachniet et al., 2014). This speleothem record suggests that the $\delta^{18}O$ of Great Basin rainfall shifted dramatically during the period of overflow from Lake Bonneville. As such, the increase in $\delta^{18}O$ of Lake Bonneville waters and hence precipitated LCCs during the period of overflow could be controlled by regional shifts in rainfall $\delta^{18}O$ instead of P-E, providing an explanation for the discrepancy between the $\delta^{18}O$ P-E reconstruction and that of this chapter.

The detailed P-E reconstruction using the multi-proxy approach developed in this Chapter for LCC deposits is a useful first attempt. It would be useful to compare this with future additional LCC records from within other sites in Lake Bonneville and other Great Basin terminal lakes.

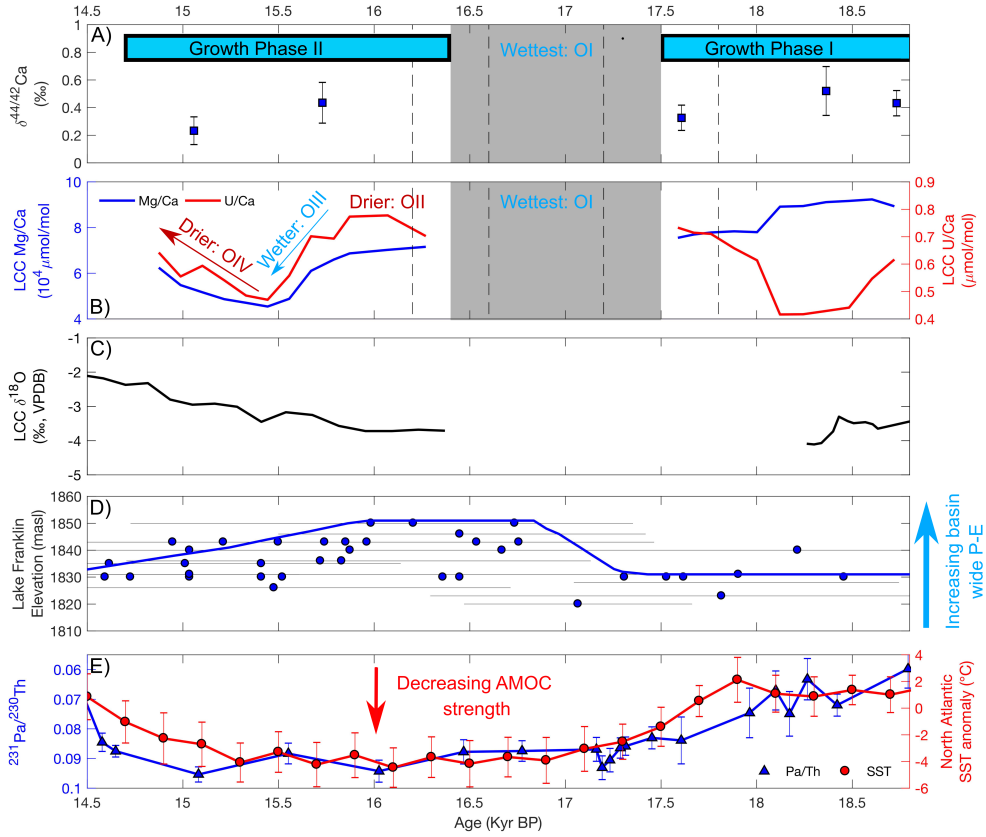


Figure 3.9: Comparison of Lake Bonneville and regional and global paleo-climate records. A) $\delta^{\frac{44}{42}}Ca$ measurements from LCC sample CC5, error bars show 2σ instrument uncertainties. Also plotted are blue rectangles showing the mean OxCal age model duration of CC5 Growth Phase I and Growth Phase II. B) Trace element X/Ca measurements from CC5, Mg/Ca is plotted in blue and U/Ca plotted in red. The four periods of differing P-E: OI (17.5 kyr BP - 16.4 kyr BP), OII (16.4 kyr BP - 15.7 kyr BP), OIII (15.7 kyr BP - 15.4 kyr BP) and OIV (15.4 kyr BP - 14.7 kyr BP) are annotated. The hiatus in CC5 precipitating is plotted with a dark grey bar in sub-plots A and B. Dashed vertical lines indicate the OxCal age model 2σ uncertainties on the start and end of this hiatus. C) $\delta^{18}O$ time-series generated from Cathedral Cave LCC deposits (McGee et al., 2012) D) Paleo-lake level reconstruction from Lake Franklin, a terminal lake in the Great Basin located 100 km west of Lake Bonneville. Blue circles indicate radiocarbon ages on paleo-shoreline deposits, and grey bars the 2σ age uncertainties (Santi et al., 2019). The continuous blue line indicates the paleo-lake level reconstruction of Santi et al. (2019) based on the plotted paleo-shoreline deposit ages. E) $^{231}Pa/^{230}Th$ excess and North Atlantic SST anomaly time-series. $^{231}Pa/^{230}Th$ excess timeseries is plotted in blue and generated from core GGC5 collected from the Bermuda Rise with error bars indicating 2σ uncertainty (McManus et al., 2004). North Atlantic near-surface summer (JAS) temperature anomaly is plotted in red with error bars indicating 2σ uncertainty and generated from a suite of 18 ocean sediment cores covering the North Atlantic (Pedro et al., 2022).

3.4.3.2 Potential mechanisms causing identified shifts in P-E

The newly identified periods of variable P-E occur during the deglaciation and Heinrich Stadial 1 (HS1) (∼18 kyr BP - ∼14.8 kyr BP), a significant period of shifting global climate. Heinrich Stadials are modelled to have a two part impact on global climate, firstly due to the freshwater hosing of the North Atlantic, and secondly due to a reduction in height of the Laurentide ice sheet altering atmospheric circulation, with the maximum reduction in height occurring at the end of the surge phase of iceberg discharge (Ziemen et al., 2019).

The freshwater hosing of the North Atlantic during HS1 led to a slow down of the Atlantic meridional overturning circulation (AMOC) and cooling of the North Atlantic (Figure 3.9E) (Heinrich, 1988). A link between North Atlantic cooling and increased P-E in the Great Basin region has previously been proposed in other records (e.g. Asmerom et al., 2010; Lachniet et al., 2014) and model outputs (e.g. McGee et al., 2018), although the underlying climate mechanism remains elusive. Increased moisture supply to the Great Basin region during HS1 is thought to be the result of a southward shift in the position of the inter tropical convergence zone (ITCZ), a result of the stalling of the AMOC (McGee et al., 2018). This could increase moisture supply in one of the following ways: i) by causing an increased southwards displacement of the winter storm track over the Great Basin region (Asmerom et al., 2010); or ii) by increased moisture supply from south westerly extra-tropical cyclones originating in the central and eastern tropical Pacific "atmospheric river events" (McGee et al., 2018; Oster et al., 2019). Both of these cases are consistent with the timing of the the maximum in P-E interpreted from CC5 during Period OI (17.5 kyr BP - 16.4 kyr BP), which occurs after the stalling of the AMOC by ∼17.5 kyr (BP) (McManus et al., 2004; Stanford et al., 2006, 2011) and the onset of North Atlantic cooling (Figure 3.9).

Once CC5 precipitation resumes at 16.4 kyr (BP), Mg/Ca and U/Ca suggests a period of oscillating P-E over the Bonneville Basin. This pattern of oscillating P-E might be explained by complex ice sheet atmosphere interactions. Reducing elevation

of the Laurentide Ice Sheet is suggested to have caused a northwestern migration of maximum moisture supply to to the Great Basin during this period, recorded in a north-western progression of closed lake highstands in the Great Basin through time (McGee et al., 2018). A northwest migration of moisture supply over the Great Basin would result in reduced moisture supply to the Bonneville Basin, which is located on the eastern edge of the Great Basin. The reverse may also be true, with a potential southeast shift of maximum moisture supply to the Great Basin as the Laurentide Ice Sheet increases in height. Periods of growth and decline of the Laurentide Ice Sheet may be responsible for the oscillating P-E reconstructed over Lake Bonneville during this period.

The complex nature of shifts in P-E over Lake Bonneville, involving multiple controls and ice sheet atmosphere feedbacks, could explain the spatially heterogeneous response to the deglaciation observed across lakes in the Great Basin region (McGee et al., 2018; Santi et al., 2019). To fully understand the mechanism linking Heinrich Stadials with southwestern United States P-E, higher resolution reconstructions of P-E with lower age uncertainties are required from multiple Great Basin lakes to reconstruct the complex spatial and temporal variations in moisture supply to this region.

3.5 Future work and outlook

The modelling (Chapter 2) and measurement (this Chapter) of the chemical composition of LCC samples from Lake Bonneville undertaken here builds a substantial platform for using combined measurements of Mg/Ca, U/Ca and $\delta^{\frac{44}{42}}Ca$ to reconstruct shifts in PICP in lake basins, which in turn responds to basin wide shifts in P-E.

This work is showing significant promise for allowing improved reconstructions of past lake behaviour, such as improved chronology of the Lake Bonneville Flood, and better constraints on shifts in P-E during periods where Lake Bonneville behaved as an overflowing basin. Refinements of many types, including additional measurements (U-Th, Mg/Ca, U/Ca and $\delta^{\frac{44}{42}}Ca$) and additional model runs, will allow for ongoing improvements in my reconstructions of lake evolution in the Bonneville Basin and hence reconstructions of past climate states.

3.6 Conclusion

The good agreement between the LakeCalc model output and measured proxy values during the rise of Lake Bonneville, a period where shifts in basin-wide P-E can be accurately reproduced, suggests that a multi-proxy approach using Mg/Ca, U/Ca and $\delta^{\frac{44}{42}}Ca$ can reconstruct shifts in P-E over the Bonneville Basin.

When applied to the overflowing portion of Lake Bonneville's history the multi-proxy approach allowed an accurate U-Th age to be ascribed to the Bonneville Flood, 18.05 $\pm$ 0.35 kyr (BP, 2σ), and suggests the maximum in P-E occurred synchronously with Heinrich Stadial 1. The maximum in P-E is followed by a brief oscillation between lower then higher P-E, before P-E falls until the end of CC5 growth, highlighting the complex nature of controls on P-E over the Great Basin region during the last deglaciation.

In order to fully understand the complex nature of temporal and spatial shifts in P-E over the southwestern United States, improved resolution P-E reconstructions with lower age uncertainties are required (McGee et al., 2018). LCCs have shown potential for providing these, and their extensive precipitation in Lake Bonneville, found in over forty localities (McGee et al., 2012), suggests similar deposits likely exist in other terminal basins. As such, a multi-proxy approach from LCCs offers the potential for generating vital high resolution P-E reconstructions from multiple lakes over the Great Basin region and beyond.

Chapter 4

Reconstructing Holocene paleo-ENSO variability using $\delta^{18}O$ from a Bornean stalagmite

Abstract

The El Niño-Southern Oscillation (ENSO) is a major source of inter-annual climate variability, impacting a large portion of the world's population. However, the frequency and magnitude of ENSO events before the existence of instrumental and historical records are still poorly constrained. This study investigates the impact of age model and $\delta^{18}O$ analytical uncertainty on speleothem based paleo-ENSO reconstructions; and to expand the number of century length ENSO variability records generated from a western tropical Pacific speleothem sample (BA03). Here I present two new centennial length sub-annual ($>$ 2 samples per year) resolution $\delta^{18}O$ time-series from stalagmite BA03 covering 3830 Yr. (BP) – 3730 Yr. (BP) and 4150 Yr. (BP) – 4010 Yr. (BP). Together with six existing high resolution BA03 $\delta^{18}O$ time-series (Chen et al., 2016) these are used to generate eight centennial length records of ENSO variability throughout the Holocene. A new methodology is developed to propagate age model and $\delta^{18}O$ uncertainties onto speleothem ENSO variability proxy values. While age model and $\delta^{18}O$ analytical uncertainty were found to introduce large uncertainties to the speleothem ENSO variability proxy, they do not preclude speleothems as paleo-ENSO archives once accounted for. ENSO variability records generated from BA03 show a reduction in ENSO variability during the mid-Holocene (5680 Yr. BP - 3780 Yr. BP) compared to the early and late Holocene. This supports the findings of existing coral, mollusc and foraminiferal paleo-ENSO records from the central and eastern tropical Pacific. The period of reduced ENSO variability inferred in the mid-Holocene coincides with a maximum in western Pacific warm pool (WPWP) convective activity (5500 Yr. BP – 3500 Yr. BP; Partin et al., 2007a), suggesting that increased WPWP convection could be related to suppressed ENSO variability in this period. Finally the termination of the mid-Holocene reduction in ENSO variability is observed to coincide with the end of the so called "4.2 Kyr Event" suggesting a link between the increase in ENSO variability and the end of this centennial scale climate perturbation.

Contents

4.1 Introduction 118

4.2 Northern Borneo intra-seasonal to inter-annual hydro-climate 121

4.3 Stalagmite $\delta^{18}O$ used as a paleo-ENSO archive 122

4.4 Methodology 127

4.4.1 Speleothem sub-sampling 127

4.4.2 U-Th disequilibrium dating 127

4.4.3 Radiocarbon dating 128

4.4.4 OxCal age v. depth model 129

4.4.5 Trace element analysis 130

4.4.6 Stable isotope analysis 131

4.4.7 Spectral analysis 132

4.4.8 Generating a speleothem-hosted ENSO variability proxy . . 132

4.5 Results 136

4.5.1 Uranium-Thorium ages 136

4.5.2 Radiocarbon ages 144

4.5.3 OxCal age model 147

4.5.4 Trace element time-series 149

4.5.5 High resolution $\delta^{18}O$ ENSO variability windows 151

4.5.6 Spectral analysis 154

4.5.7 ENSO variability proxy 155

4.6 Discussion 164

4.6.1 Stalagmite BA03 as a paleo-ENSO archive 164

4.6.2 Evolution of reconstructed ENSO variability through the Holocene 166

4.6.3 A minimum in ENSO variability coeval with the "4.2 kyr event" 170

4.6.4 Study Limitations 172

4.7 Conclusion 174

4.1 Introduction

The El Niño-Southern Oscillation (ENSO) is one of the primary drivers of global inter-annual climate variability in the tropics (Vecchi and Wittenberg, 2010). ENSO originates from coupled ocean atmosphere interactions in the tropical Pacific which are inherently unstable and oscillate between warm (El Niño) and cold (La Niña) states with a periodicity of 2-7 years (Sarachik and Cane, 2010). The effects of ENSO events are felt globally and are capable of impacting large areas of human population through costly droughts or flooding (McPhaden et al., 2006). As such, understanding how the ENSO system will evolve under increasing anthropogenic climate change is important in order to mitigate the risks of increased or altered ENSO events in the future.

While some modeling studies predict an increase in ENSO intensity under future greenhouse warming (e.g. Cai et al., 2015, 2018), the future evolution of the ENSO system remains uncertain due to the lack of inter-model agreement (Cai et al., 2018) and incomplete characterization of ENSO processes in general circulation models (GCMs) (Bellenger et al., 2014). Uncertainty arising from inter-model comparisons is exacerbated as decadal scale instrumental records are not sufficiently long to test the accuracy of a given model's performance (Cobb et al., 2013).

Paleo-ENSO archives cover a much longer duration and variety of climate forcings than the instrumental records used to develop and tune GCMs. Robust paleo-ENSO reconstructions can therefore provide an out of sample test of the ability of GCMs to accurately reconstruct the ENSO system (Schmidt, 2010; Emile-Geay et al., 2016). A large number of studies have generated proxy based reconstructions of the ENSO system from the tropical Pacific, using a wide variety of archives including corals (e.g Cobb et al., 2013; McGregor et al., 2013; Emile-Geay et al., 2016; Grothe et al., 2019), speleothems (Chen et al., 2016), molluscs (Carré et al., 2014) and foraminifera (Koutavas and Joanides, 2012). These paleo-ENSO archives attempt to reconstruct past shifts in ENSO variability, caused by increases or decreases in the size and frequency of ENSO events. Paleo-ENSO archives have suggested a broad reduction in

ENSO variability during the mid-Holocene 6000 Yr. (BP) (years before 1950 C.E.) - 3000 Yr. (BP) (Koutavas and Joanides, 2012; Carré et al., 2014; Grothe et al., 2019). However, the high level of internal ENSO variability; and short duration of many paleo-ENSO archives has made conclusively identifying long term trends in ENSO behaviour difficult (Emile-Geay et al., 2016; Grothe et al., 2019).

Multiple paleo-ENSO reconstructions have identified a minimum in Holocene ENSO variability at approx. 4.2 kyr (BP) (e.g. Cobb et al., 2013; McGregor et al., 2013; Leonard et al., 2016; Grothe et al., 2019). The timing of the minimum in ENSO variability is concurrent with the so called "4.2 kyr event": 4.26 kyr (BP) - 3.97 kyr (BP) (Carolin et al., 2019). The "4.2 kyr event" is though to be an abrupt centennial scale climate perturbation observed prominently in Middle Eastern environmental records as a centennial scale drought (e.g. Carolin et al., 2019) and suggested by some authors to be felt outside of the Middle East in localities such as: south-west Africa (Railsback et al., 2018), western Europe (Jordan et al., 2017) and southern South America (Ohlendorf et al., 2014). The lack of an obvious high latitude forcing of the "4.2 kyr event" coupled with a concurrent period of exceptionally low ENSO variability have led some authors to speculate on a link between the two (e.g. Marchant and Hooghiemstra, 2004; Li et al., 2018; Toth and Aronson, 2019). However, the high level of internal ENSO variability and short duration of many paleo-ENSO archives has made definitively identifying a temporal link between the "4.2 kyr event" and reduced ENSO variability difficult.

The potential for continuous growth and absolutely dated chronology gives speleothems excellent potential as paleo-ENSO archives. The ability to generate centennial or longer records of past ENSO dynamics allows speleothems to identify long term trends in ENSO variability and filter out shorter term internal ENSO variability. However, age model and $\delta^{18}O$ analytical uncertainties can have a large impact on speleothem paleo-ENSO reconstructions, and must be quantified and accounted for.

Here I assess the ability of speleothem $\delta^{18}O$ time-series from the western tropical Pacific to reconstruct paleo-ENSO variability. Two new and six previously measured (Chen

et al., 2016) high resolution ($>$ 2 samples year^{-1} on interpolated mean age model) $\delta^{18}O$ time-series are presented from northern Borneo stalagmite BA03. The $\delta^{18}O$ variance of the speleothem 2-7 year band filtered time-series is used as a proxy for paleo-ENSO variability. This study specifically focuses on understanding the propagation of age model and analytical $\delta^{18}O$ uncertainties onto speleothem 2-7 year band pass filtered $\delta^{18}O$ variance. The study goes on to compare BA03's paleo-ENSO time-series with other paleo-ENSO archives from the tropical Pacific to further investigate the mid-Holocene minimum in ENSO activity, particularly in relation to the "4.2 kyr event".

4.2 Northern Borneo intra-seasonal to inter-annual hydro-climate

Northern Borneo is located in the heart of the Indio-Pacific warm pool (Figure 4.1). Annual average sea surface temperatures >28℃ drive year round atmospheric deep convection, resulting in significant rainfall (>5000 mm/year) in northern Borneo (Cobb et al., 2007). As northern Borneo lies beneath the meridional migration of the inter-tropical convergence zone (ITCZ), year round seasonal rainfall variability is weak (Cobb et al., 2007; Moerman et al., 2013). Consequently rainfall amount over northern Borneo is primarily controlled by intra-seasonal and inter-annual variability associated with the Madden-Julian Oscillation and El Niño-Southern Oscillation (ENSO) respectively (Moerman et al., 2013). The eastward shift of convection during El Niño events leads to reduced rainfall in northern Borneo during boreal winter. Conversely, the strengthening of convection over the western Pacific warm pool during La Niña events, results in increased rainfall. Strong ENSO events can produce January-February (DJF) precipitation anomalies of up to ±50% over northern Borneo (Bell and Halpert, 1998; Cobb et al., 2007; Partin et al., 2007a).

Modern observations at Mulu airport (Figure 4.2) show local rainwater $\delta^{18}O$ to be negatively correlated with regional rainfall amount on daily to inter-annual timescales, with the negative correlation strengthening with increased temporal averaging (Moerman et al., 2013). Authors suggest this is caused by water vapor $\delta^{18}O$ integrating the effect of all convective activity it experiences during its transport history (Moerman et al., 2013). Consequently, the state of the ENSO system, the dominant control on inter-annual rainfall variability (Figure 4.1), should exert a strong control on northern Borneo rainfall $\delta^{18}O$. This is confirmed by a strong and significant correlation between the 2-month running mean Mulu rainfall $\delta^{18}O$ and the NIÑO4 ENSO variability index over a 12-year window ($R = 0.64$, $p<0.05$) (Ellis et al., 2020).

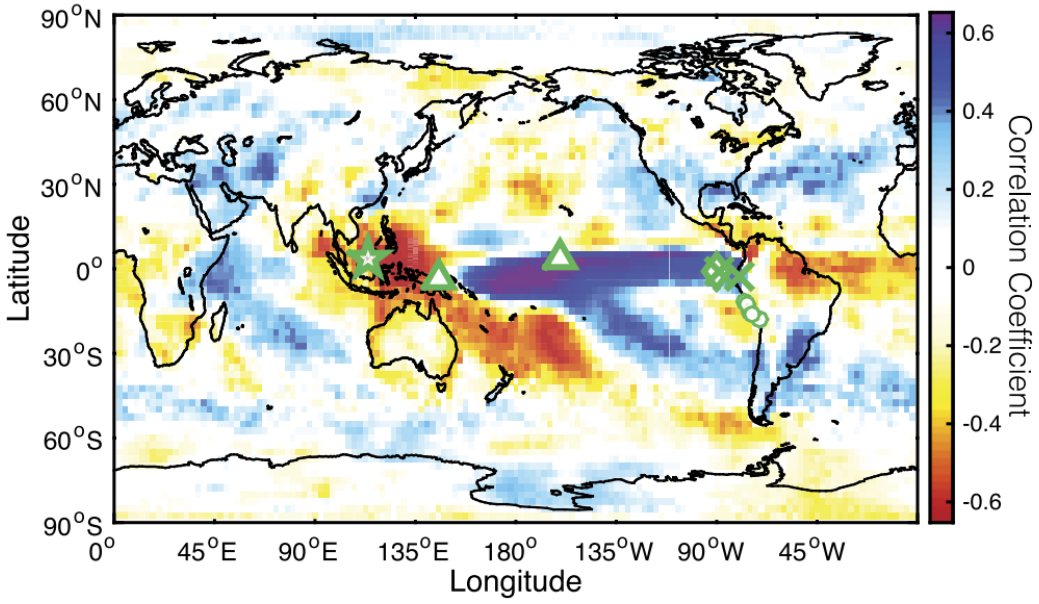


Figure 4.1: Global correlation between inter-annual (2-7 year band) rainfall and the Niño 3.4 index (1979-2014). The Niño 3.4 index is a measure of equatorial Pacific sea surface temperature anomaly and is used to define ENSO events. The green star shows the location of Bukit Assam cave. Other green symbols show the locations of other paleo-ENSO records: triangles refer to coral archives from Northern Line Islands (Cobb et al., 2013) and Papua New Guinea (Tudhope et al., 2001); crosses to lakes (Moy et al., 2002; Conroy et al., 2008); circles to mollusc shells (Carré et al., 2014); and diamonds to foraminifera (Koutavas and Joanides, 2012). Reprinted from "A high-resolution speleothem record of western equatorial Pacific rainfall: Implications for Holocene ENSO evolution" by S. Chen, 2016, Earth and Planetary Science Letters, 442, 62. Copyright 2016 by Elsevier B.V.

4.3 Stalagmite $\delta^{18}O$ used as a paleo-ENSO archive

Sample Description

Stalagmite BA03 was collected from Bukit Assam cave (4° 15' 18"N, 114° 57' 34"E), a limestone dissolution cave in Gunung Buda, Sarawak, Malaysian Borneo (Figure 4.2). Bukit Assam cave is situated within the Miocene Melinau limestone which forms a northeast oriented line of low mountains and hills, 10km long and 35km wide (Waltham and Despain, 2012). The Melinau Limestone dips to the northeast and is conformably overlain by the Setap Shale (Waltham and Despain, 2012). The surface above the cave is characterised by tropical rainforest vegetation, thin soil cover and temperatures

ranging between 23℃ - 26℃ (Partin, 2008). Bukit Assam cave comprises of 8 km of passages separated over multiple vertical levels with an overlying limestone depth of 50m - 150m (Partin, 2008; Carolin et al., 2016). Cave conditions are relatively uniform with temperature ranging from 25℃ - 26℃ and humidity >100% (Partin, 2008).

The 1.3 m long calcite stalagmite BA03 was collected in 2003 CE from beneath an active drip (Chen et al., 2016). BA03 is relatively uniform in morphology gradually thinning from a diametre of 10.5 cm at the base to 4 cm at the top (Figure 4.3). Well preserved mm-scale growth lamina are present throughout the speleothem, with precipitated calcite alternating between lighter white and thinner bands of orange to yellow calcite (Figure 4.3). The growth axis of BA03 appears to shift multiple times along its length, indicting subtle shifts in the drip location. BA03 was sectioned along its growth axis over its whole length and slabbed to a thickness of 15 mm to allow it to be fixed to an automated micro-mill for sub-sampling. Existing U-Th chronology show BA03 to have grown continuously over the entire Holocene epoch with maximum and minimum U-Th ages of 260 ±20 Yr. (BP) and 11630 ±130 Yr. (BP) (Chen et al., 2016).

BA03 as a Paleo-ENSO archive

Modern observations from nearby Gunung Api caves (Figure 4.2) show cave drip water $\delta^{18}O$ to be strongly correlated with the state of the ENSO system (Moerman et al., 2013; Ellis et al., 2020). Ellis et al. (2020) report on a 12-year long drip water sampling study, comparing the drip water $\delta^{18}O$ values from three Gunung Api caves (Figure 4.2) with local rainfall $\delta^{18}O$. While transport through the karst overburden resulted in homogenization and a reduction in amplitude of the rainfall $\delta^{18}O$ signal, with longer karst residence times leading to a greater degree of homogenization, ENSO anomalies could be resolved from all of the measured Gunung Api cave drip-waters (Ellis et al., 2020).

This study is based on the assumption that the rainwater ENSO $\delta^{18}O$ signal was maintained in both BA03 dripwater $\delta^{18}O$, and BA03 $\delta^{18}O_{calcite}$. This assumption is

supported by the almost identical geology and climate regime of Gunung Buda and Gunung Api (Waltham and Despain, 2012). This is further supported by Ellis et al. (2020) concluding that drip water karst residence times were approximately proportional to the thickness of the carbonate overburden above the cave. In the three cave sites studied by Ellis et al. (2020) the carbonate overburden was between 100m - 200m thick. As this is similar to the overburden above Bukit Assam cave (50m - 150m), the karst residence times of Bukit Assam drip waters are assumed to be comparable (3 months - 18 months). Finally, good replication of $\delta^{18}O$ time-series between BA03 and other speleothems from both Bukit Assam cave, and nearby Gunung Buda caves (Partin et al., 2007b; Chen et al., 2016) suggests BA03 $\delta^{18}O$ is recording regional rainfall $\delta^{18}O$ as opposed to cave specific karst processes.

The good agreement reported between the previously generated paleo-ENSO variability values from BA03 and other independent paleo-ENSO archives further increases the confidence that Bukit Assam drip waters, and the carbonates precipitated from them, contain a resolvable ENSO signal (Chen et al., 2016).

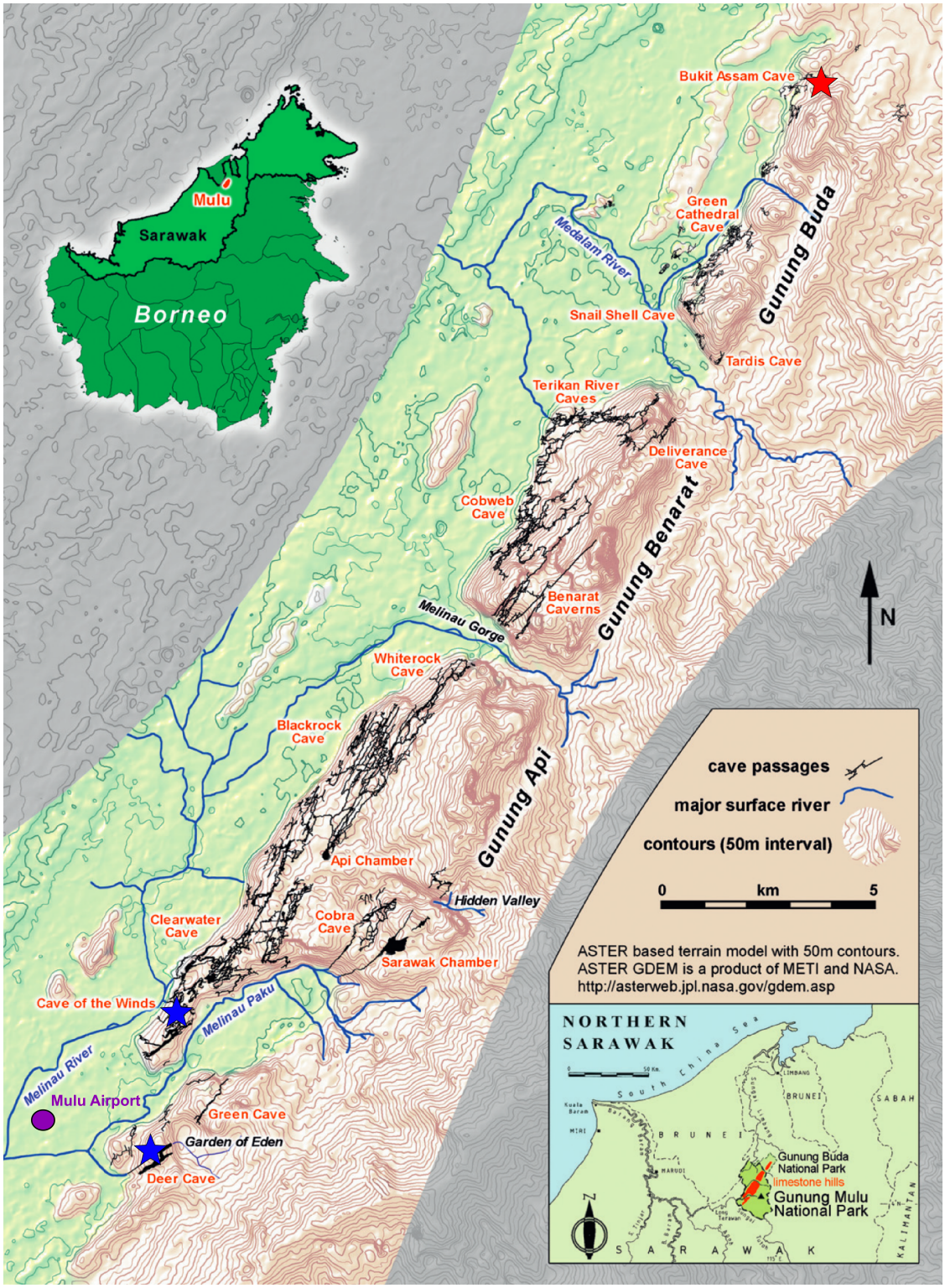


Figure 4.2: Caves of Gunung Buda and Gunung Mulu National Parks. Bukit Assam cave, the study site of this chapter, is highlighted with a red star. Caves included in the drip water survey of Ellis et al. (2020) are highlighted with blue stars. The location of Mulu airport is shown with a purple circle. Adapted from "Mulu caves, Malaysia. In Encyclopedia of Caves (2nd Edition)" by T. Waltham and J. Despain, page 553. Copyright 2012 by Elsevier Science & Technology.

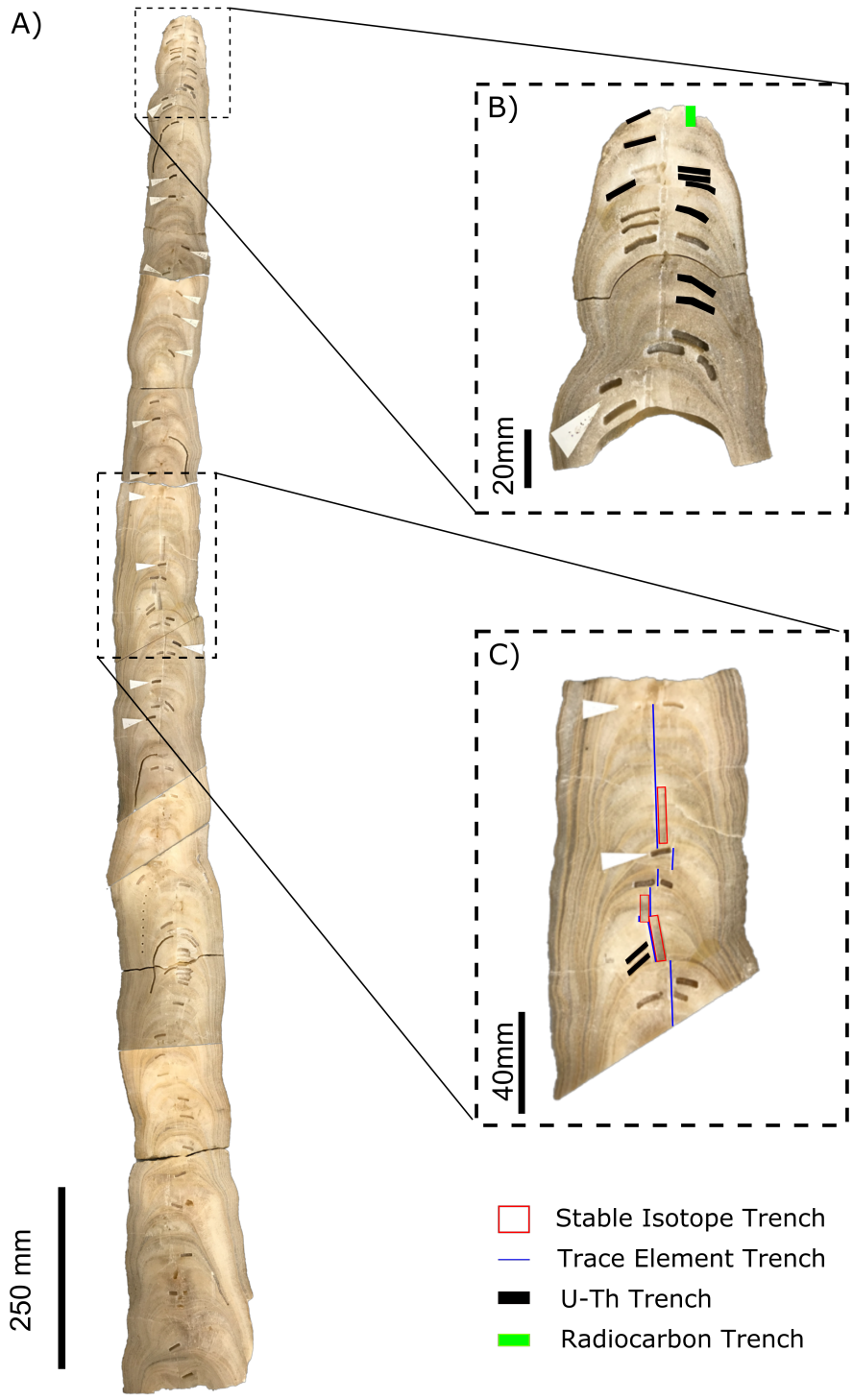


Figure 4.3: Annotated image of speleothem BA03. The entire length of speleothem growth is shown in A. B and C show enlarged sections of BA03 where this study milled sub-samples for analysis. Red rectangles represent continuously milled stable isotope trenches, blue rectangles continuously milled trace element trenches, black rectangles U-Th trenches milled in this study and the green rectangle the continuously milled radiocarbon trench.

4.4 Methodology

4.4.1 Speleothem sub-sampling

All sub-samples (U-Th, ^{14}C, stable isotope and trace element) were milled from slabbed sections of BA03 using an automated New Wave Research micro-mill and a 0.8 mm diameter tungsten carbide drill bit. The top surface of the BA03 slab was removed prior to sampling to reduce the chance of surface contaminates being included in the sub-samples. Unless specified the top surface of BA03 was removed to a depth of 100μm.

The distances along the stalagmite's growth axis that sub-samples were collected from were calculated digitally using high resolution scans of stalagmite BA03. Distances along the growth axis of sub-samples collected by the study of Chen et al. (2016) were recalculated to ensure consistency with the sub-samples milled in this chapter.

4.4.2 U-Th disequilibrium dating

Eleven sub-samples with masses between 175mg - 235mg were collected for U-Th analysis. Sub-samples were milled from trenches adjacent to the speleothem growth axis, with milling following visible stalagmite laminae to minimise the age range of collected calcite. Nine sub-samples were milled in the top 65 mm of speleothem growth, with the remaining two milled at depths of 622 mm and 627 mm respectively (Figure 4.3). Uranium and thorium were chemically separated following procedures adapted from Edwards et al. (1987a). Uranium and thorium isotope ratios were measured on a Nu Plasma Multi-collector Inductively Coupled Plasma Mass Spectrometer (MC-ICP-MS) at the Department of Earth Sciences, University of Oxford, following the procedures described in Vaks et al. (2013). An initial $^{230}Th/^{232}Th$ atomic ratio of 69 $\pm$5 ppm was used to correct for detrital ^{230}Th contamination. This value was used in BA03's original chronology and calculated from four isochrons drilled at depths of 114 mm, 456 mm, 765 mm and 926 mm (Chen et al., 2016). However, a speleothem's detrital $^{230}Th/^{232}Th$ ratio can vary over time due to the incorporation varying amounts of distinct detrital

material (Richards and Dorale, 2003). In the youngest section of BA03, the top 114 mm of growth (outside the range of depths covered by the isochrons published in Chen et al., 2016), a variety of initial $^{230}Th/^{232}Th$ ratio ratios were tested to find a suitable range of values which allowed U-Th ages to be in stratigraphic order within instrument uncertainty. The reported U-Th ages and uncertainties were calculated using an in-house Matlab script which solved the U-Th disequilibrium age equation using 10,000 monte-carlo simulations and accounting for uncertainties in the measured isotope ratios and initial $^{230}Th/^{232}Th$ ratio.

4.4.3 Radiocarbon dating

14 radiocarbon sub-samples, in the mass range 10.2 mg - 12.8 mg, were collected from BA03. The top 12 radiocarbon sub-samples were milled from a continuous trench in the top 6 mm of speleothem growth. The other two sub-samples were collected from older calcite milled individually adjacent to low uncertainty U-Th dates (Chen_6 and Chen_15, Table 4.1). Prior to milling, 200μm of the sample surface was removed to ensure calcite which had interacted with the modern atmosphere was not collected. After milling, sub-samples were immediately transferred to 6ml air tight Exetainers®, weighed and the Exetainers® flushed for 1 minute with BOC CP grade Helium (> 99.999% purity) at a flow rate between 80 cc $min^{-1}$and 100 cc min^{-1}. This ensured minimal interaction of the milled sub-samples with the modern atmosphere. The radiocarbon sub-samples were sent to the NEIF Radiocarbon (Environment) laboratory where they were transformed to graphite. The samples were etched to remove 20% of the dry weight of material by controlled hydrolysis with dilute HCl. The evolved CO_2 from the etching process was purged from the hydrolysis vessel with N_2 gas and the etched sample then hydrolysed to CO_2 using 2M HCl. The sample CO_2 was converted to graphite by Fe/Zn reduction. Samples were then analysed for ^{14}C content using an accelerator mass spectrometer (AMS) at Keck Carbon Cycle AMS Facility, University of California, Irvine, USA. $^{13}C/^{12}C$ ratios were measured by AMS during ^{14}C deter-

mination and used to correct for isotopic fractionation according to the conventions of Stuiver and Polach (1977) by normalising ^{14}C data to $\delta^{13}C$ = -25 ‰ (V-PDB). The data were corrected for modern carbon contamination using data from process background and standard materials following the methods of Santos et al. (2007). All radiocarbon data can be found in Table C.1.

4.4.4 OxCal age v. depth model

An age v. depth model was created for BA03 using the OxCal (version 4.4) age modelling software's Poisson Process deposition model (Ramsey, 2008; Ramsey and Lee, 2013).

OxCal is a bayesian deposition model which uses Markov Chain Monte Carlo (MCMC) sampling to generate an ensemble of possible age model solutions from which a mean age model and confidence intervals are calculated (Ramsey, 2008). When using the Poisson Process deposition model, users must specify the model's interpolation rate and poisson parameter, k. k must be specified as both the base value of k, k_0 and a range of values over which k is allowed to vary during the model run, the default setting of ± 2 orders of magnitude, uniform distribution, (U(-2,2)) is used in this chapter.

k, represents the number of individual deposition events modelled to occur per unit depth (mm^{-1}). As k increases the modelled size of individual deposition events decreases, decreasing both the flexibility of the age model (the model's ability for growth rate to change) and the amplitude of the age model's uncertainties. Selecting a suitable k value is therefore crucial in the generation of an accurate age model. Too small k values generate age models with unrealistically large age uncertainties (Trachsel and Telford, 2017). Too large k values generate age models with unrealistically small age uncertainties (Trachsel and Telford, 2017) which are too rigid to fit all of the inputted discrete age depth data (Hua et al., 2012).

To determine a suitable value for k_0, I followed the method of Scholz et al. (2012) selecting the highest value of k_0 which did not significantly reduce the agreement be-

tween the age model and inputted discrete age depth data. This method ensures an age model is generated which is sufficiently flexible to fit all of the inputted discrete age depth data, but restricts growth rate variability to the minimum required to accurately fit the age depth data.

OxCal measures the agreement between a generated age model and the inputted discrete age depth data by generating separate agreement indices for the whole age depth dataset (A_{model}) and each individual age (A). The threshold for an acceptable agreement index is 60 (Ramsey, 2008). k_0 values between 0.1 mm^{-1} and 100 mm^{-1}were tested in order to determine the largest k_0 which gave both an overall $A_{model} > 60$ and $A > 60$ for each individual inputted age. This k_0 was then used to generate the finalised BA03 age depth model.

4.4.5 Trace element analysis

Medium resolution micro-mill sampling was performed to collect BA03 sub-samples for trace element analysis. Sub-samples were milled at 0.2 mm intervals along a continuous trench 0.4 mm deep and 0.8 mm wide from 517.6 mm - 690.7 mm along the stalagmite's growth axis (Figure 4.3). The sub-samples were collected and stored in acid leached polypropylene centrifuge tubes. The sub-samples were then dissolved in distilled 2% HNO_3, concentration matched to approx. 20ppm Ca and analysed on a PerkinElmer NexION 350D ICP-MS (Inductively Coupled Plasma Mass Spectrometer) at the Department of Earth Sciences, University of Oxford. Helium was used as a collision gas in the cell for kinetic energy discrimination (KED). Multi-element calibration standards were run alongside the sub-samples. All the elements in these multi-element calibration standards were supplied from single element high-purity standards whose concentrations were certified against NIST Spectrometric Standard Solutions. A stock of each standard was diluted using the ESI prepFAST dilution system between 2 and 150 times to create calibration standards over a wide concentration range to cover the varying elemental concentrations in the samples. Bracketing standards were run every

tenth sample to account for machine drift. The concentration of trace elements Mg, Sr and Ba are reported as molar ratios relative to the major element Ca. The analytical uncertainties of each measured elemental concentration are reported as twice the relative standard deviation of a QC standard (Mg/Ca = ±3%, Sr/Ca = ±3% mol $mol^{-1}$and Ba/Ca = ±5%; n = 5).

4.4.6 Stable isotope analysis

BA03 was milled at high resolution between 557.1 mm - 576.1 mm and 603.4 mm - 623.1 mm from the top of the stalagmite to extract powders for stable isotope measurements. Sub-samples for stable isotope analysis were milled from continuous trenches along the growth axis of BA03 which were 3 mm wide and 1.5 mm deep (Figure 4.3). Two separate milling resolutions were used for the two milling locations, with a resolution of 60 μm per sample used for the tench centred at 567 mm from the top of the stalagmite and 50μm per sample for the trench centred at 613 mm.

Samples, in the mass range 30 μg to 80 μg, were analysed for oxygen and carbon stable isotopic compositions at the Department of Earth Sciences, University of Oxford, using a Thermo Delta V Advantage Isotope Ratio Mass Spectrometer (IRMS). The relative $^{13}C/^{12}C$ values are reported in the conventional $\delta^{13}C$ (‰) notation, relative to the Vienna Pee Dee Belemnite (V-PDB), by assigning a value of +1.95‰ exactly to reference material NBS-19. The relative $^{18}O/^{16}O$ values are reported in the conventional $\delta^{18}O$ (‰) notation, relative to V-PDB, on a normalised scale such that the $\delta^{18}O$ of NBS-19 is -2.2‰.

Two different methods were used to convert the carbonate sub-samples to CO_2 for IRMS analysis:

Sub-samples from the record centred at 613 mm depth were processed using a Thermo Finnigan Kiel IV device which reacted the carbonates with 100% H_3PO_4 at 71℃ and further purified the product-CO_2 prior to IRMS isotopic analysis. Reproducibility of in-house marble standard NOCZ during these analytical runs was 0.03‰

for $\delta^{13}C$ and 0.05‰ for $\delta^{18}O$ (1s, n=34), with average $\delta^{13}C$ = 2.21 ±0.03 (1s, n=34) and $\delta^{18}O$ = -1.85 ±0.05‰ (1s, n=34) within the uncertainty of the long-term average of NOCZ ($\delta^{13}C$ = 2.17 ±0.06; $\delta^{18}O$ = -1.90 ±0.09‰; 1s; n=120).

Sub-samples from the record centred at 567 mm depth were processed with a Gas Bench II peripheral. Within the Gas Bench II sample block, the powdered samples, in 6 mL He-flushed Exetainers®, were reacted with 100% phosphoric acid at 52 ℃. Reproducibility of in-house marble standard NOCZ during these analytical runs was ±0.04‰ for $\delta^{13}C$ and ±0.06‰ for $\delta^{18}O$ (1s, n=21), with average $\delta^{13}C$ = 2.16 (1s, n=21) and $\delta^{18}O$ = -1.96 (1s, n=34) within the uncertainty of the long-term average of NOCZ ($\delta^{13}C$ = 2.17 ±0.06; $\delta^{18}O$ = -1.90 ±0.09‰; 1s; n=120).

4.4.7 Spectral analysis

All eight high resolution BA03 $\delta^{18}O$ depth-series (two from this study and six from Chen et al., 2016) were combined with the mean OxCal age model and multi-taper spectral analysis performed on the resulting $\delta^{18}O$ time-series. The power spectra of each time-series are compared to the mean and 95% confidence limits of 100 fitted red noise power spectra. 95% confidence limits were calculated by multiplying the mean red noise power spectrum with the chi-squared values at the 95% confidence level with two degrees of freedom. The spectral analysis, red noise background and confidence intervals were computed using Matlab scripts provided by Peter Huybers[1].

4.4.8 Generating a speleothem-hosted ENSO variability proxy

To generate a speleothem hosted proxy for ENSO variability I followed the methodology of Chen et al. (2016), which previously used BA03 as a paleo-ENSO archive. High resolution $\delta^{18}O$ depth series were combined with BA03's mean OxCal age-depth model to generate high resolution (> 2 samples per year) $\delta^{18}O$ time-series. The time-series

[1]The Matlab scripts for the multi-taper spectral analysis, red noise and confidence intervals were downloaded on 20/10/2020 from: https://github.com/CommonClimate/common-climate/blob/master/wavelet_filter.m ; and https://www.people.fas.harvard.edu/~phuybers/Mfiles/Toolbox/.

were then interpolated using the Matlab shape preserving piecewise cubic interpolation ("pchip") to a resolution of 2 samples per year and processed using a 2-7 year band wavelet filter to remove variability with a periodicity outside the range associated with ENSO events (2 - 7 years) (Chen et al., 2016). Band pass filtering was carried out using a Matlab script developed from Torrence C. and Compo G. (1998)[2]. $\delta^{18}O$ time-series had to be interpolated to a uniform temporal resolution as the band wavelet filter requires a uniform sampling rate. The standard deviations of the band-pass filtered time-series were then calculated as a measure of the remaining variability left in the time-series, which is assumed to be dominated by the ENSO signal. This was done for both the whole time-series and sliding 30-year windows with a 5-year time step within each time-series, in order to investigate how the standard deviations varied within the measured interval. We define here "ENSO variability" as the standard deviation of the 2-7 year bandpass filtered $\delta^{18}O$ time-series. These are subsequently referred to as mean OxCal ENSO variability values.

4.4.8.1 Propagating age model uncertainty onto the ENSO variability proxy

The ENSO variability proxies are frequency dependent with the amount of variability passing through the 2-7 year band pass filter dependent on the age depth model used to convert $\delta^{18}O$ depth-series to time-series. However, speleothem age depth models are not unique with an infinite array of possible solutions capable of fitting the measured U-Th ages. To generate a mean age model with 95% confidence intervals, OxCal generates an ensemble of possible age models capable of fitting the inputted U-Th age depth data. To test the effect of different age models on the ENSO variability proxy, 1000 of the underlying OxCal ensemble age models were randomly selected and each combined with the $\delta^{18}O$ depth series to generate 1000 individual $\delta^{18}O$ time-series. These time-series were then processed using the method described in Section 4.4.8 generating

[2]The Matlab script for the wavelet filter was downloaded on 18/07/2019 from: https://github.com/CommonClimate/common-climate/blob/master/wavelet_filter.m.

1000 individual values of ENSO variability for each $\delta^{18}O$ depth-series. The mean and standard deviation of this ensemble of 1000 ENSO variability values are then used to calculate an overall mean ENSO variability value with confidence intervals. These are subsequently referred to as ensemble mean ENSO variability values.

4.4.8.2 Investigating the impact of differing analytical $\delta^{18}O$ uncertainties

A $\delta^{18}O$ record contains variability supplied by both changes in speleothem calcite $\delta^{18}O$ and the analytical uncertainty of the $\delta^{18}O$ measurements. A proportion of $\delta^{18}O$ variability supplied by analytical uncertainty may fit through the 2-7 year band pass filter and be included in the ENSO variability proxy. As such, it is important to understand the proportion of 2-7 year band pass variability supplied by analytical uncertainty. To test this, artificial $\delta^{18}O$ records containing just analytical $\delta^{18}O$ variability were generated for each high resolution $\delta^{18}O$ depth record by replacing each of the measured $\delta^{18}O$ values with a randomly generated value from a normal distribution with: $\mu = 0‰$; and $\sigma = 1\sigma$ analytical uncertainty of the $\delta^{18}O$ measurements. This was done 1000 times for each milled $\delta^{18}O$ record, generating 1000 unique $\delta^{18}O$ analytical uncertainty records. These were each combined with the mean OxCal age depth model and processed using the method described in Section 4.4.8, generating 1000 individual values of the ENSO variability proxy. The mean and standard deviation of these 1000 values were then used to calculate a mean and confidence intervals for the contribution of analytical uncertainty to the ENSO variability proxy.

To correct for the difference in $\delta^{18}O$ uncertainties between the two $\delta^{18}O$ records generated in this chapter, the analytical uncertainty of the $\delta^{18}O$ record centred at 613 mm ($\pm 0.05‰$) was artificially increased to equal that of the record centred at 567 mm ($\pm 0.06‰$). This correction was only attempted between the records generated in this study as Chen et al. (2016) did not report $\delta^{18}O$ uncertainties per record but as an average over all $\delta^{18}O$ measurements. To artificially increase $\delta^{18}O$ uncertainty a random normally distributed variable with: $\mu = 0‰$; and $\sigma = x$; was added to each value of

the $\delta^{18}O$ record centred at 613 mm, where x equals:

$$x = \sqrt{\sigma^2_{567mm} - \sigma^2_{613mm}} \tag{4.1}$$

where σ_{567mm} and σ_{613mm} are the $\pm 1\sigma$ $\delta^{18}O$ analytical uncertainties of the $\delta^{18}O$ records centred at 567 mm and 613 mm respectively; and Equation 4.1 is derived from the equation for propagating errors through addition: $\sigma_{a+b} = \sqrt{\sigma_a^2 + \sigma_b^2}$. In this study x = 0.03‰.

This was done a 100 times, generating a 100 unique $\delta^{18}O$ depth series. These depth series were then each combined with the 1000 ensemble OxCal age models generating 100,000 unique $\delta^{18}O$ time-series. The time-series were then processed using the method described in Section 4.4.8 generating 100,000 individual values of ENSO variability. The mean and standard deviation of these 100,000 ENSO variability values were then used to calculate the ensemble mean ENSO variability value and confidence intervals.

4.5 Results

4.5.1 Uranium-Thorium ages

This chapter generated eleven new U-Th ages on stalagmite BA03 to supplement the existing U-Th chronology of Chen et al. (2016). The new U-Th ages were targeted at both resolving an age reversal between the youngest two BA03 U-Th ages (Chen et al., 2016) and better constraining the age model around 4000 Yr. (BP).

An initial thorium ratio of 69 ±5 ppm (Chen et al., 2016) results in age inversions in the top 90 mm of speleothem growth (Figure 4.4A). In speleothems the law of superposition requires sample age to increase with increasing distance along the speleothems growth axis. Five U-Th dates within a 4 mm depth window in the top 90 mm of speleothem growth (Chen_1, CT-3, CT-7, CT-8 and CT-9) were used to test for suitable initial thorium values which allowed sample age to increase with sample depth. No singular initial thorium ratio was found which could remove all age reversals. However, when considering only samples with an initial ^{232}Th < 5 pmol g^{-1} a ^{230}Th/^{232}Th atomic ratio between 2ppm to 34ppm resulted in sample age increasing with depth within analytical uncertainty (Figure 4.4B). This implies that samples with a greater ^{232}Th concentration may have multiple sources of initial thorium with different initial ^{230}Th/^{232}Th ratios. Therefore, an initial Th ratio of 18 ± 16 ppm was used to correct U-Th ages drilled in the top 90 mm of speleothem growth (including dates measured by Chen et al., 2016), 69 ±5 ppm in ages further than 90 mm from the top of the stalagmite and all ages with an initial ^{232}Th > 5 pmol g^{-1} discounted.

The raw MC-ICP-MS data, estimated initial ^{230}Th/^{232}Th ratio, and estimated U-Th ages for each sample processed in this chapter are listed in Table 4.1.

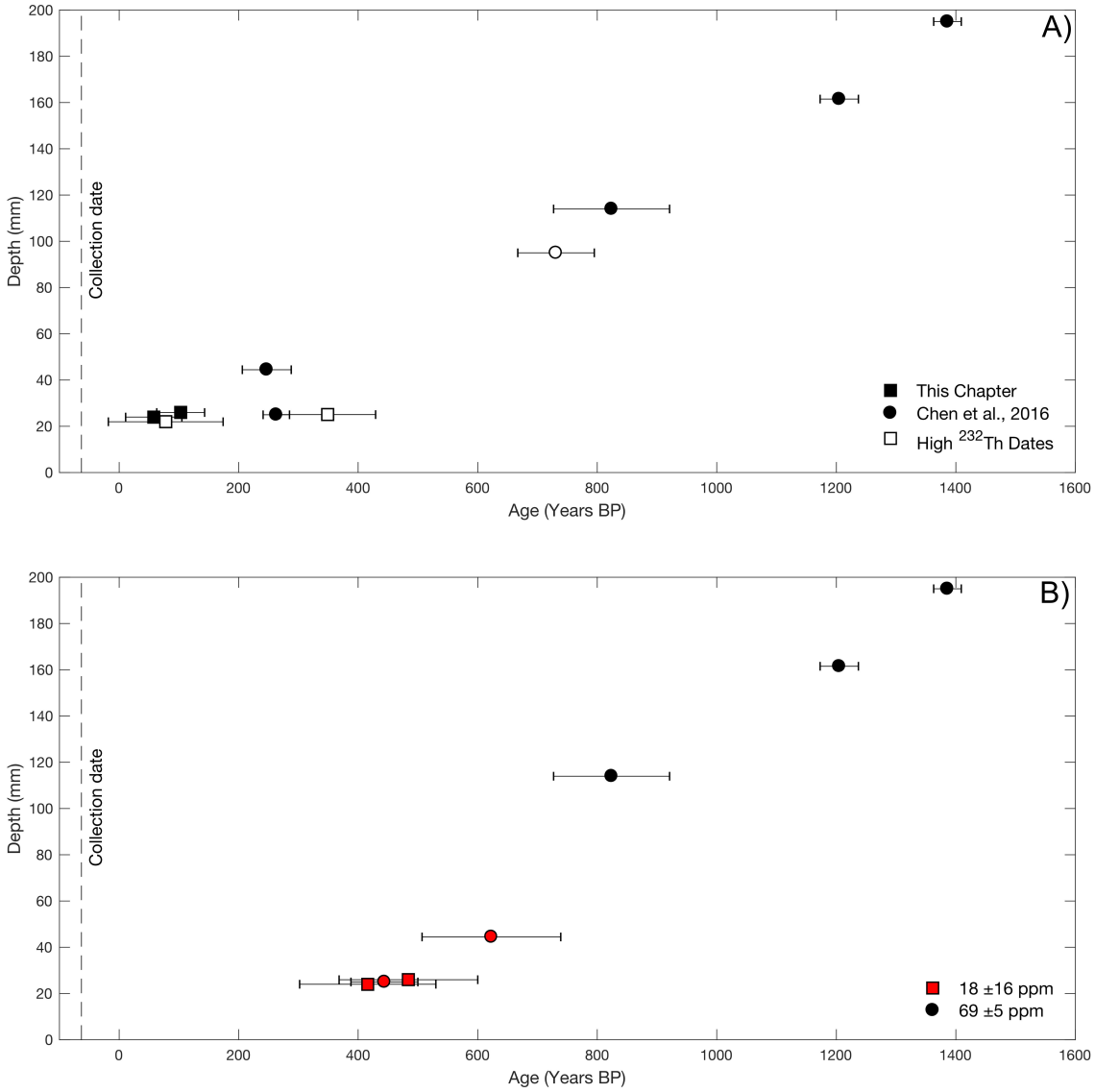


Figure 4.4: Depth vs age plots for: A) U-Th ages in the top 200 mm of BA03 growth corrected using the initial Th ratio of Chen et al. (2016), 69 ±5 ppm. B) U-Th ages in the top 200 mm of BA03 growth with ages in the top 90 mm corrected using an initial Th ratio of 18 ±16 ppm and all other ages with an initial Th ratio of 69 ±5 ppm. Dirty ($>$ 5 pmol g^{-1} ^{232}Th) U-Th samples are discounted. In all figures colour denotes the initial Th ratio used to correct the U-Th age: Black = 69 ± 5 ppm; and Red = 18 ± 16 ppm. Unfilled points indicate "dirty" ($>$ 5 pmol g^{-1} ^{232}Th) U-Th ages.

		MC-ICP-MS Measurements						Age Calculation				
Sample ID	Depth (mm)	$[^{238}U]$ (ppb)	$[^{232}Th]$ (pmol g^{-1})	$\delta^{234}U$ (‰)	± 2σ	$\left(\frac{^{230}Th}{^{238}U}\right)$ ($\times 10^{-3}$)	± 2σ	Uncorrected Ages (Yr. BP)	Initial $\frac{^{230}Th}{^{232}Th}$ (ppm)	± 2σ	Corrected Ages (Yr BP)	± 2σ
CT_1	0.0	1928	124	-616.3	1.8	30.54	0.08	9175	18	16	**4280**	**4186**
CT_2	10.9	1910	33	-630.4	1.9	9.65	0.07	2836	18	16	**1533**	**1107**
CT_8	22.0	1943	8	-632.2	1.8	4.54	0.13	1288	18	16	**973**	**273**
CT_7	24.0	1976	3	-632.1	1.8	2.06	0.10	543	18	16	**416**	**114**
Chen_1	25.0	1764	2	-633.0	0.1	1.91	0.02	510	18	16	**444**	**56**
CT_9	25.1	1751	6	-632.2	1.9	4.79	0.11	1364	18	16	**1099**	**229**
CT_3	26.0	1944	3	-633.2	1.9	2.31	0.05	620	18	16	**484**	**116**
CT_4	34.3	1878	26	-629.6	2.1	8.19	0.08	2383	18	16	**1350**	**888**
Chen_2	44.5	1721	3	-633.3	1.0	2.74	0.03	759	18	16	**622**	**116**

		MC-ICP-MS Measurements						Age Calculation				
Sample ID	Depth (mm)	$[^{238}U]$ (ppb)	$[^{232}Th]$ (pmol g^{-1})	$\delta^{234}U$ (‰)	± 2σ	$\left(\frac{^{230}Th}{^{238}U}\right)$ ($\times 10^{-3}$)	± 2σ	Uncorrected Ages (Yr. BP)	Initial $\frac{^{230}Th}{^{232}Th}$ (ppm)	± 2σ	Corrected Ages (Yr BP)	± 2σ
CT_5	56.8	1637	52	-627.8	1.9	23.12	0.12	7047	18	16	**4611**	**2089**
CT_6	63.4	1800	163	-628.3	1.9	23.56	0.12	7202	18	10	**69**	**6067**
Chen_3	95.0	1726	5	-631.0	0.2	5.43	0.02	1563	69	5	**731**	**64**
Chen_4	114.0	1779	4	-631.7	0.2	5.09	0.14	1463	69	5	**824**	**97**
Chen_5	161.5	1847	3	-630.1	0.2	5.56	0.02	1598	69	5	**1205**	**32**
Chen_6	195.0	2113	1	-631.1	0.2	5.47	0.03	1575	69	5	**1386**	**23**
Chen_7	247.8	1941	6	-631.2	0.2	8.42	0.04	2474	69	5	**1596**	**69**
Chen_8	277.1	1838	8	-630.4	0.2	10.43	0.03	3085	69	5	**1813**	**97**
Chen_9	296.6	1619	1	-630.3	0.2	7.00	0.03	2035	69	5	**1932**	**18**

		MC-ICP-MS Measurements						Age Calculation				
Sample ID	Depth (mm)	$[^{238}U]$ (ppb)	$[^{232}Th]$ (pmol g^{-1})	$\delta^{234}U$ (‰)	± 2σ	$\left(\frac{^{230}Th}{^{238}U}\right)$ ($\times 10^{-3}$)	± 2σ	Uncorrected Ages (Yr. BP)	Initial $\frac{^{230}Th}{^{232}Th}$ (ppm)	± 2σ	Corrected Ages (Yr BP)	± 2σ
Chen_10	321.4	1507	1	-625.0	0.2	7.98	0.03	2299	69	5	**2169**	**20**
Chen_11	361.2	1931	2	-630.2	0.2	9.55	0.03	2813	69	5	**2472**	**32**
Chen_12	418.2	1928	5	-627.0	0.2	11.87	0.03	3497	69	5	**2747**	**59**
Chen_13	456.7	1773	1	-630.3	0.2	11.24	0.15	3335	69	5	**3116**	**93**
Chen_14	495.7	1782	1	-628.0	0.2	11.76	0.03	3473	69	5	**3402**	**22**
Chen_15	518.5	1856	1	-626.5	0.2	12.45	0.04	3670	69	5	**3516**	**25**
Chen_16	583.9	1663	3	-626.4	0.2	14.49	0.04	4299	69	5	**3870**	**41**
CT_10	621.9	1621	60	-624.0	1.8	29.97	0.18	9199	69	5	**-1953**	**418**
CT_11	626.9	1653	10	-626.3	2.0	16.76	0.14	4994	69	5	**3207**	**68**

		MC-ICP-MS Measurements						Age Calculation					
Sample ID	Depth (mm)	$[^{238}U]$ (ppb)	$[^{232}Th]$ (pmol g^{-1})	$\delta^{234}U$ (‰)	± 2σ	$\left(\frac{^{230}Th}{^{238}U}\right)$ ($\times 10^{-3}$)	± 2σ	Uncorrected Ages (Yr. BP)	Initial $\frac{^{230}Th}{^{232}Th}$ (ppm)	± 2σ	Corrected Ages (Yr BP)	± 2σ
Chen_17	643.4	1549	3	-625.9	0.1	16.30	0.02	4856	69	5	**4276**	**44**
Chen_18	699.2	1609	2	-625.1	0.2	17.59	0.05	5247	69	5	**4910**	**40**
Chen_19	764.8	1726	5	-625.0	0.2	19.53	0.14	5856	69	5	**5032**	**110**
Chen_20	775.0	1721	2	-624.3	0.1	19.22	0.02	5747	69	5	**5392**	**29**
Chen_21	804.2	1706	3	-624.8	0.1	19.80	0.02	5939	69	5	**5444**	**38**
Chen_22	866.4	1995	3	-624.0	0.2	20.87	0.03	6264	69	5	**5913**	**36**
Chen_23	883.8	1255	3	-618.4	0.1	22.67	0.05	6726	69	5	**6078**	**59**
Chen_24	918.1	1368	1	-621.5	0.2	22.09	0.04	6603	69	5	**6353**	**35**
Chen_25	942.3	1516	1	-622.2	0.2	22.70	0.05	6810	69	5	**6601**	**34**

		MC-ICP-MS Measurements						Age Calculation				
Sample ID	Depth (mm)	[^{238}U] (ppb)	[^{232}Th] (pmol g^{-1})	δ^{234}U (‰)	± 2σ	$\left(\frac{^{230}Th}{^{238}U}\right)$ ($\times 10^{-3}$)	± 2σ	Uncorrected Ages (Yr. BP)	Initial $\frac{^{230}Th}{^{232}Th}$ (ppm)	± 2σ	Corrected Ages (Yr BP)	± 2σ
Chen_26	966.8	1518	3	-619.3	0.2	24.35	0.05	7275	69	5	**6785**	**48**
Chen_27	990.1	1806	6	-618.6	0.2	25.72	0.04	7695	69	5	**6869**	**69**
Chen_28	1018.0	1150	7	-614.6	0.2	29.90	0.06	8935	69	5	**7217**	**132**
Chen_29	1037.8	1306	6	-613.7	1.3	29.99	0.07	8940	69	5	**7750**	**116**
Chen_30	1056.0	1745	3	-619.0	0.2	28.55	0.04	8611	69	5	**8132**	**48**
Chen_31	1079.8	2183	6	-618.4	0.2	30.05	0.04	9083	69	5	**8385**	**61**
Chen_32	1096.1	2210	1	-618.3	0.8	28.62	0.05	8617	69	5	**8501**	**52**
Chen_33	1123.2	1941	3	-617.9	0.4	32.63	0.05	9909	69	5	**9558**	**50**
Chen_34	1171.4	1380	1	-613.8	1.3	33.45	0.08	10057	69	5	**9806**	**90**

		MC-ICP-MS Measurements						Age Calculation				
Sample ID	Depth (mm)	$[^{238}U]$ (ppb)	$[^{232}Th]$ (pmol g^{-1})	$\delta^{234}U$ (‰)	± 2σ	$\left(\frac{^{230}Th}{^{238}U}\right)$ ($\times 10^{-3}$)	± 2σ	Uncorrected Ages (Yr BP)	Initial $\frac{^{230}Th}{^{232}Th}$ (ppm)	± 2σ	Corrected Ages (Yr BP)	± 2σ
Chen_35	1217.7	1332	3	-612.8	1.3	38.71	0.09	11753	69	5	**11128**	**112**
Chen_36	1247.6	1187	2	-614.5	1.5	39.37	0.10	12031	69	5	**11627**	**128**

Table 4.1: Data for of all U-Th ages measured on BA03. Ages calculated by this study have sample IDs: CT_#; and those of Chen et al. (2016): Chen_#. Ages in red have ^{232}Th concentrations > 5 pmol g^{-1} and are discounted from the BA03 age model. Samples Chen_1 and Chen_2 were reprocessed in this study using the new initial Th ratio of 18 ±16 ppm. Depth refers to the average vertical distance along the growth axis the samples were collected from. Depths for all U-Th ages calculated by Chen et al. (2016) are stated as the values recalculated in this study.

4.5.2 Radiocarbon ages

To improve the poorly constrained U-Th chronology in the top 100 mm of BA03 growth 14 radiocarbon dates were measured to identify the 1950's radiocarbon bombspike and use this as a precise temporal tie-point.

To test for the presence of the 1950's radiocarbon bombspike each of the radiocarbon sub-samples was given an estimated U-Th age. A linear interpolation between the top of the stalagmite (estimated to have an age of -53 Yr (BP); Chen et al., 2016) and the shallowest U-Th date (CT-7, Table 4.1) generated ages for the top 12 radiocarbon sub-samples. The two deeper sub-samples were given ages equal to the U-Th pits they were milled adjacent too (Chen_6 and Chen_15, Table 4.1).

The ^{14}C activities of sub-samples in the top 6 mm of BA03 are highly variable (Figure 4.5A and B). The observed variability is too large to be caused by non-anthropogenic shifts in atmospheric ^{14}C activity and does not fit the stereotypical shape associated with the radiocarbon bombspike (Figure 4.5A). As such, the variability in^{14}C activity is likely caused by the incorporation of variable amounts of ^{14}C depleted ancient carbon, from either the soil or bedrock, into BA03. This reservoir effect is commonly referred to as the dead carbon fraction (DCF) and expressed as:

$$DCF = \left(1 - a^{14}C_{Stal.init}/a^{14}C_{Atm.init}\right) \times 100\% \tag{4.2}$$

where $a^{14}C_{Stal.init}$ and $a^{14}C_{Atm.init}$ represent the stalagmite and atmospheric ^{14}C at the time of speleothem deposition, equation adapted from Lechleitner et al. (2016).

The DCF of BA03 is calculated[3] for sub-samples estimated to be older than 0 Yr. (BP) (Figure 4.5C). The calculated DCF values are amongst the highest reported in the literature for a speleothem sample, suggesting a large contribution of carbon from ancient organic matter or bedrock dissolution by a process other than carbonic acid (Bajo et al., 2017). While the estimated DCF is relatively constant over millennial

[3]The R Script for the DCF calculator can be obtained from: https://github.com/flechleitner/DCF_calculator

timescales, small shifts in the DCF between 76% - 86% can account for the observed variability in ^{14}C activity at the top of BA03 (Figure 4.5C).

Whilst it is possible that the radiocarbon bombspike is present and merely masked by shifts in the DCF of BA03 (Figure 4.5C) it is equally likely that the bombspike is not present due to speleothem growth ceasing prior to the radiocarbon bombspike or the signal being dampened during its transmission from the atmosphere to BA03. As such, the radiocarbon bombspike cannot be identified in speleothem BA03 and used as a precise temporal tie-point.

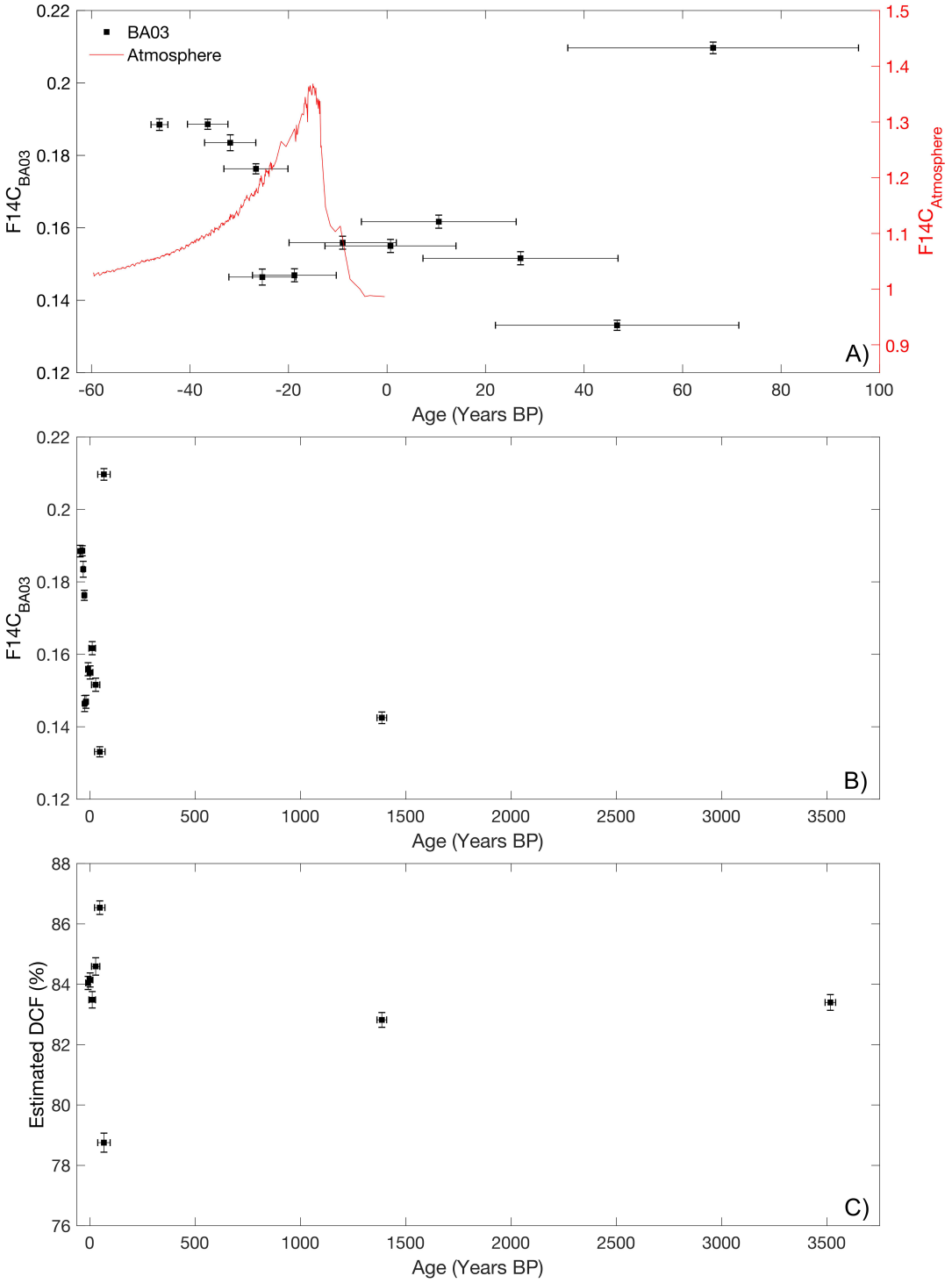


Figure 4.5: Radiocarbon measurements from BA03 showing: A) The fraction of modern ^{14}C activity (F^{14}C) of BA03 for sub-samples milled in the top 6mm. These are compared with the reconstructed shape of the atmospheric radiocarbon bombspike from Northern Hemisphere zone 3 above Borneo (red line) (Hua et al., 2013). B) The fraction of modern^{14}C activity (F^{14}C) of all radiocarbon sub-samples from BA03. C) The estimated DCF of radiocarbon sub-samples from BA03. Error bars show the 95% confidence intervals of data points. Plotted ages were calculated from a linear interpolation between the top of the stalagmite (estimated to have an age of -53 Yr (BP); Chen et al., 2016) and the shallowest U-Th date (CT-7, Table 4.1) for the top 12 radiocarbon sub-samples. The two deeper sub-samples were given ages equal to the U-Th pits they were milled adjacent too (Chen_6 and Chen_15, Table 4.1).

4.5.3 OxCal age model

An age v. depth model was generated for BA03 using all of the U-Th ages measured on BA03 with a ^{232}Th concentration < 5 pmol g^{-1} (Table 4.1) and the OxCal (version 4.4) age modelling software's Poisson Process deposition model (Ramsey, 2008; Ramsey and Lee, 2013). After trialling k_0 values between 0.1 mm^{-1} to 100 mm^{-1}, a value of 30 mm^{-1} was found to be optimum (Figure 4.6).

A finalised age model was generated using OxCal with inputs of k_0= 30 mm^{-1}, $\log_{10}(k/k_0)$ = U(−2,2), and an interpolation rate of 0.2 mm^{-1}. The age model was generated between the top of the stalagmite and the oldest U-Th age (Chen_36, Table 4.1) requiring the age model to be extrapolated for the top 24 mm of speleothem growth between the youngest U-Th age (CT_7, Table 4.1) and the top of the stalagmite (Figure 4.7).

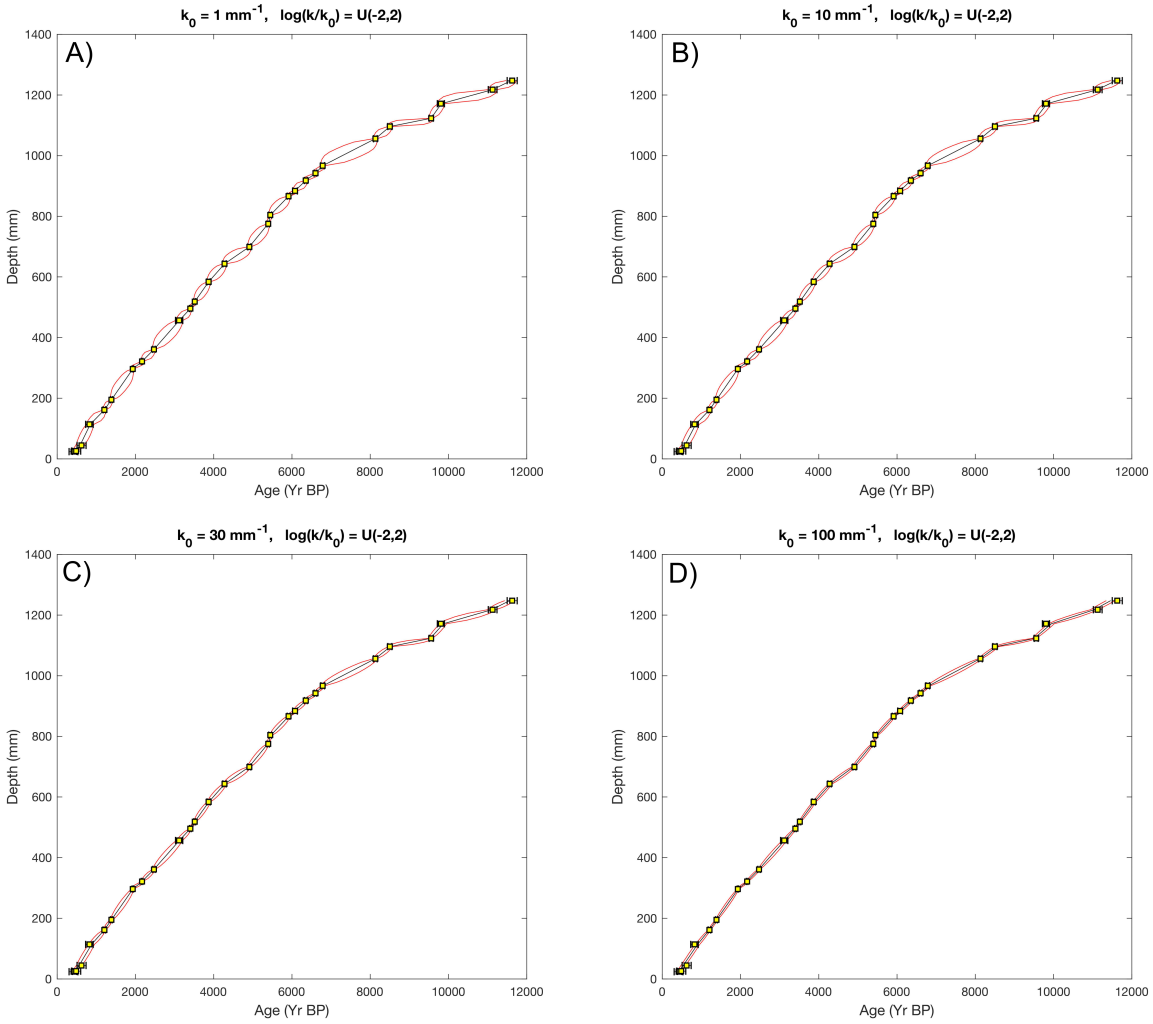


Figure 4.6: Age v. depth plots showing the outputted OxCal age models generated using different values of k_0 and measured U-Th ages. The mean age model is plotted in black and its 95% confidence intervals in red. U-Th ages are plotted in yellow, with the error bars denoting the 95% confidence intervals. A) k_0= 1mm^{-1}, this age model gave an average k = 0.06mm^{-1}; and A$_{\text{model}}$= 106. B) k_0= 10mm^{-1}, this age model gave an average k = 0.11mm^{-1}; and A$_{\text{model}}$= 104. C) k_0= 30mm^{-1}, this age model gave an average k = 0.31mm^{-1}; and A$_{\text{model}}$= 76.8. D) k_0= 100mm^{-1}, this age model gave an average k = 1.01mm^{-1}; and A$_{\text{model}}$= 13.5.

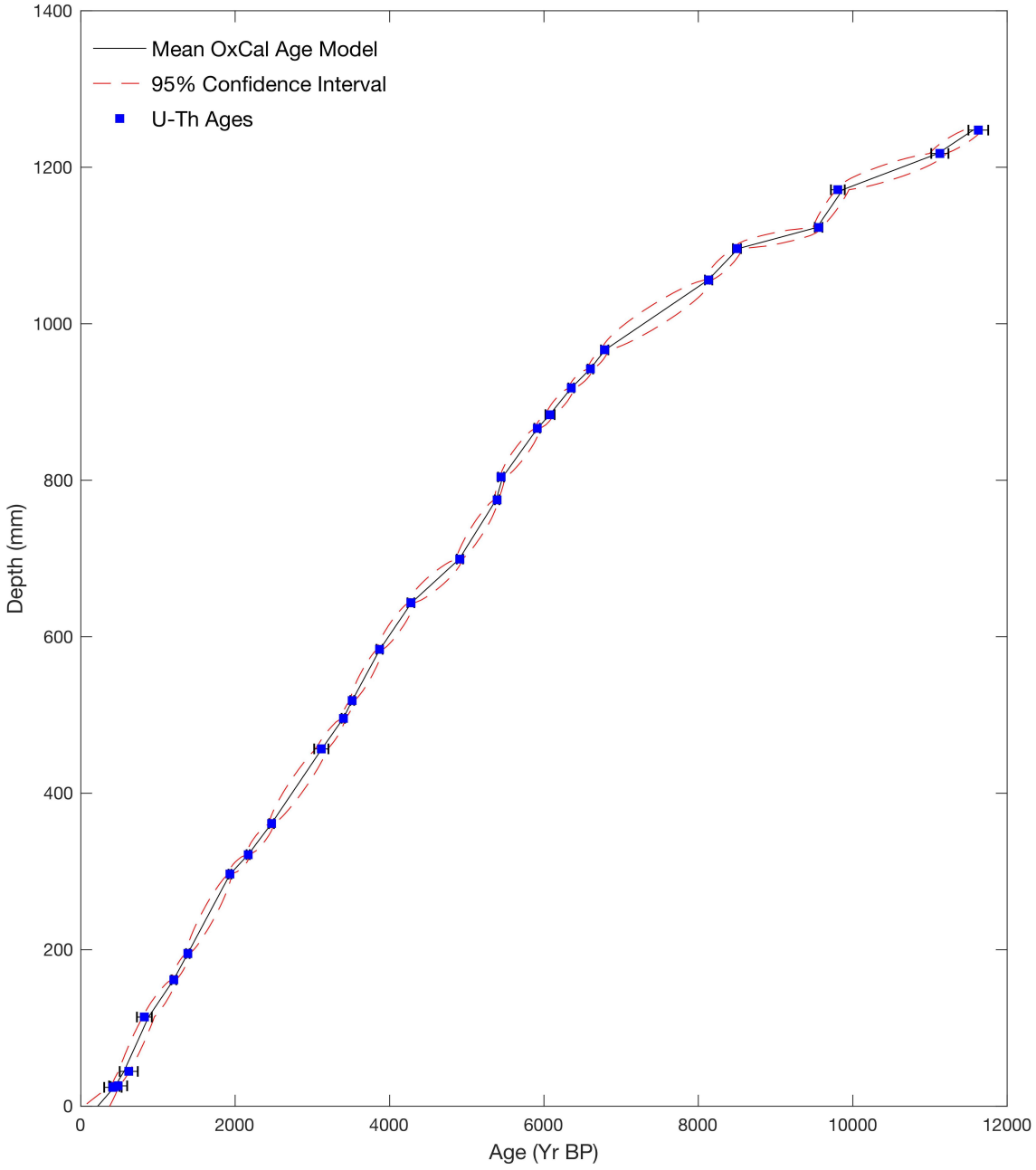


Figure 4.7: OxCal age v. depth model for BA03. U-Th ages used to constrain the OxCal age model are also plotted. The mean age model is plotted as a solid black line and red dashed lines used to denote the 95% confidence intervals. U-Th ages are plotted as blue squares with the error bars representing the 95% confidence intervals.

4.5.4 Trace element time-series

Decadal scale trace element time-series were generated from BA03 for barium (Ba), magnesium (Mg) and strontium (Sr). The trace element time-series cover 1300 years

of speleothem growth between 3510 Yr. (BP) and 4800 Yr. (BP), with an average temporal resolution of 15 years per sample (Figure 4.8).

The Ba/Ca time-series has an average concentration of 34.3 μmol mol^{-1}, with a maximum of 46.3 μmol mol^{-1} and a minimum of 26.5 μmol mol^{-1} (Figure 4.8A). The Mg/Ca time-series has an average concentration of 34.3 mmol mol^{-1}, with a maximum of 43.7 mmol mol^{-1} and a minimum of 30.2 mmol mol^{-1} (Figure 4.8B). The Sr/Ca time-series has an average concentration 11.2 mmol mol^{-1}, with a maximum of 13.7 mmol mol^{-1} and a minimum of 9.2 mmol mol^{-1}. All three elements show a significant negative correlation between age and concentration (Figure 4.8). Positive relationships exist between Ba/Ca and Mg/Ca: $R^2 = 0.34$; Ba/Ca and Sr/Ca: $R^2 = 0.73$; and Sr/Ca and Mg/Ca: $R^2 = 0.55$ (Supplementary Figure C.1).

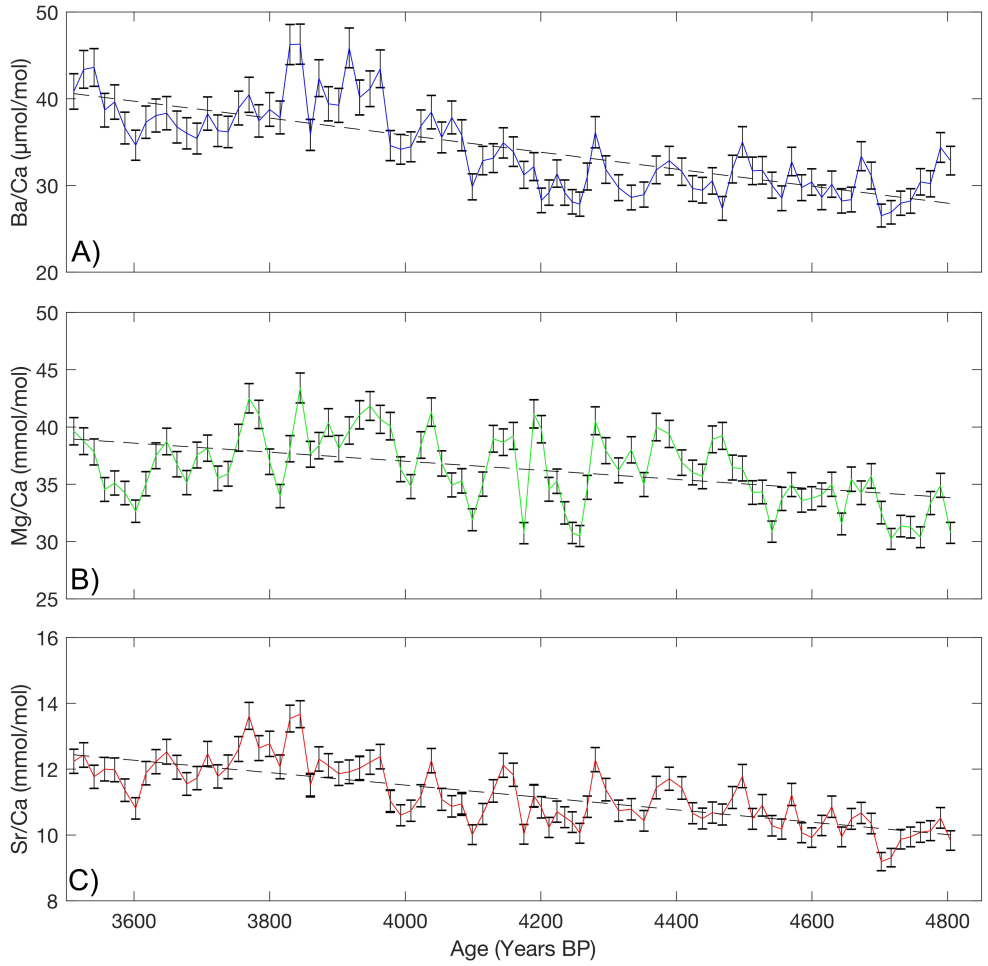


Figure 4.8: BA03 trace element time-series. Trace element concentrations are plotted with coloured lines (Blue = Ba/Ca; Green = Mg/Ca; Red = Sr/Ca) and error bars representing 95% confidence intervals. A first order polynomial line of best fit is plotted for each time-series with a black dashed line. A) Ba/Ca: line of best fit: $y = -9.804(\pm 1.82, 2\sigma) \times 10^{-3}x + 75.02(\pm 7.6, 2\sigma)$. B) Mg/Ca: line of best fit: $y = -3.957(\pm 1.61, 2\sigma) \times 10^{-3}x + 52.8(\pm 6.7, 2\sigma)$. C) Sr/Ca: line of best fit: $y = -1.83(\pm 0.37, 2\sigma) \times 10^{-3}x + 19.05(\pm 1.54, 2\sigma)$.

4.5.5 High resolution $\delta^{18}O$ ENSO variability windows

Two new high resolution (> 2 samples per year) stable isotope time-series were generated from speleothem BA03, one centered at 3780 Yr. (BP) (Figure 4.9) and the other at 4080 Yr. (BP) (Figure 4.10).

4.5.5.1 3780 Yr. (BP) Window

The stable isotope record centred at 3870 Yr. (BP) comprises of 318 samples at an average temporal resolution of 0.33 years per sample. $\delta^{18}O$ has a range of 0.86‰ with a mean of -9.76‰, a maximum of -9.29‰ and a minimum of -10.15‰ (Figure 4.9A). $\delta^{13}C$ has a range of 0.86‰ between -0.74‰ and -1.60‰, with a mean of -1.06‰ (Figure 4.9B). The stable isotope time-series shows pronounced sub-decadal scale variability with $\delta^{18}O$ varying by up to 0.4‰ and $\delta^{13}C$ by up to 0.7‰ within 10-year intervals (Figure 4.9).

4.5.5.2 4080 Yr. (BP) Window

The stable isotope record centred at 4080 Yr. (BP) comprises of 397 samples at an average temporal resolution of 0.34 years per sample. $\delta^{18}O$ has a range of 0.75‰ with a mean of -9.80‰, a maximum of -9.42‰ and a minimum of -10.17‰ (Figure 4.10A). $\delta^{13}C$ has a range of 1.04‰ between -0.48‰ and -1.52‰, with a mean of -0.97‰ (Figure 4.10B). The stable isotope time-series shows pronounced sub-decadal scale variability with $\delta^{18}O$ varying by up to 0.6‰ and $\delta^{13}C$ by up to 1‰ within 10-year intervals (Figure 4.10). The 4080 Yr. (BP) $\delta^{18}O$ time-series has the lowest average $\delta^{18}O$ of all the high resolution windows generated from BA03 (-9.80‰), although comparable with the average values of the 3310 Yr. (BP) (-9.74‰) and 3780 Yr. (BP) (-9.75‰) windows.

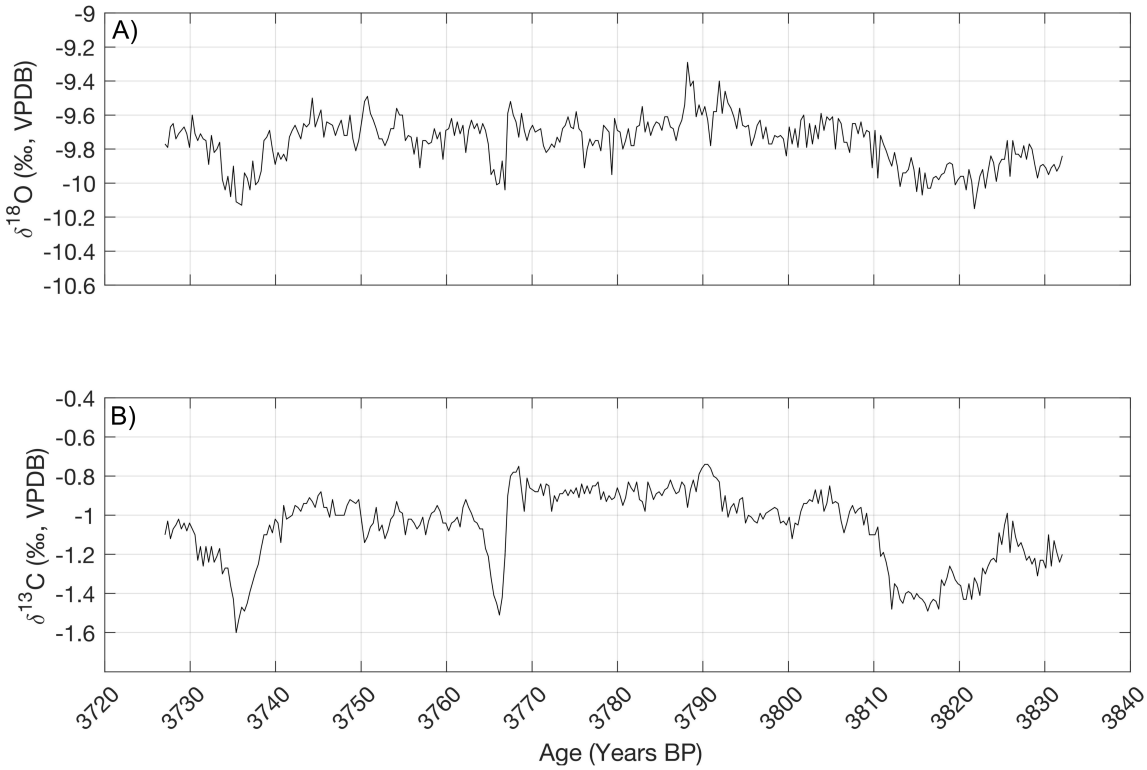


Figure 4.9: The BA03 high resolution stable isotope time-series centered on 3780 Yr. (BP). A) δ^{18}O time-series, 1σ uncertainty = 0.06‰. B) δ^{13}C time-series, 1σ uncertainty = 0.04‰.



Figure 4.10: The BA03 high resolution stable isotope time-series centered on 4080 Yr. (BP). A) δ^{18}O time-series, 1σ uncertainty = 0.05‰. B) δ^{13}C time-series, 1σ uncertainty = 0.03‰.

4.5.6 Spectral analysis

The multi-taper spectral analysis of all eight high resolution BA03 δ^{18}O time-series show at least one peak above the 95% confidence limit of the red noise background within the 2-7 year periodicity band (Figure 4.11). While all other records are close to or above the 95% red noise confidence limit for the majority of the 2-7 year periodicity band, the power spectrum of the 4080 Yr. (BP) time-series plots close to the mean red noise background for the majority of ENSO periodicities (Figure 4.11).

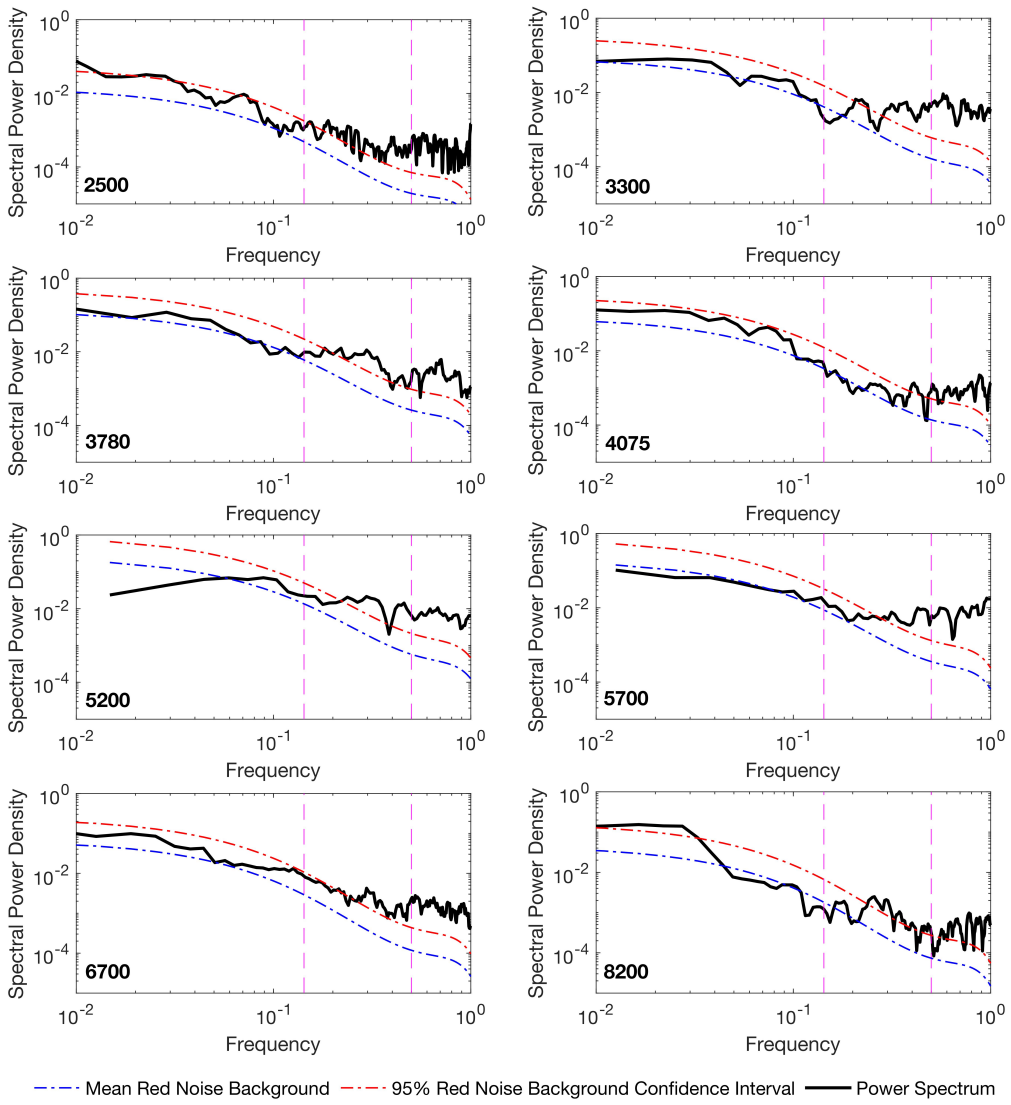


Figure 4.11: Power spectra of the eight high resolution BA03 $\delta^{18}O$ time-series plotted against fitted red noise backgrounds. The blue and red dashed lines represent the mean and 95% confidence limit of the power spectra of 100 generated red noise time-series. Vertical dashed magenta lines mark the 2-7 year band of ENSO periodicities.

4.5.7 ENSO variability proxy

4.5.7.1 Mean OxCal age model ENSO variability

ENSO variability values were calculated for both the two new $\delta^{18}O$ depth records generated in this study and recalculated for the original six $\delta^{18}O$ depth records from Chen et al. (2016) (Table 4.2), using the mean OxCal age model.

Interpolating the $\delta^{18}O$ time-series to a temporal resolution of 0.5 years per sample was observed to reduce the variability present in all time-series. However, the effect was minimal with a maximum reduction in standard deviation of 6% observed for the time-series centered at 5220 Yr. (BP) (Figure 4.12; Table 4.2).

The 2-7 year band pass filtered $\delta^{18}O$ time-series show a minimum in variability in the mid-Holocene compared to the early and late Holocene. Variations of $\pm$ 0.1‰ are common in the early (2560 Yr. BP, 3310 Yr. BP and 3780 Yr. BP), and late (6670 Yr. BP and 8215 Yr. BP) Holocene time-series but are much less common in the mid-Holocene time-series (4080 Yr. BP, 5220 Yr. BP and 5680 Yr. BP) (Figure 4.13). The 4080 Yr. (BP) time-series contains the least variation with values rarely exceeding $\pm$0.05‰ (Figure 4.13D).

The standard deviations of the entire bandpass filtered time-series (the ENSO variability proxy) have a range of 0.030‰ over the holocene, between a maximum of 0.059‰ in the 3780 Yr. (BP) window and a minimum of 0.029‰ in the 4080 Yr. (BP) window (Figure 4.14; Table 4.2). Excluding the maximum and minimum values, the rest of the band-pass filtered time-series have relatively constant standard deviations between 0.041‰ - 0.049‰.

The standard deviations of 30-year sliding windows of the band pass filtered time-series show the majority of individual time-series contain large decadal scale variability, with the range of standard deviations present within the 3780 Yr. (BP) window greater than the inter-time-series variability over the Holocene (Figure 4.14). The range of decadal scale variability is reduced in the mid-Holocene windows (4080 Yr. BP, 5220 Yr. BP and 5680 Yr. BP) compared to the early and late Holocene windows (Figure 4.14 and Figure 4.14).

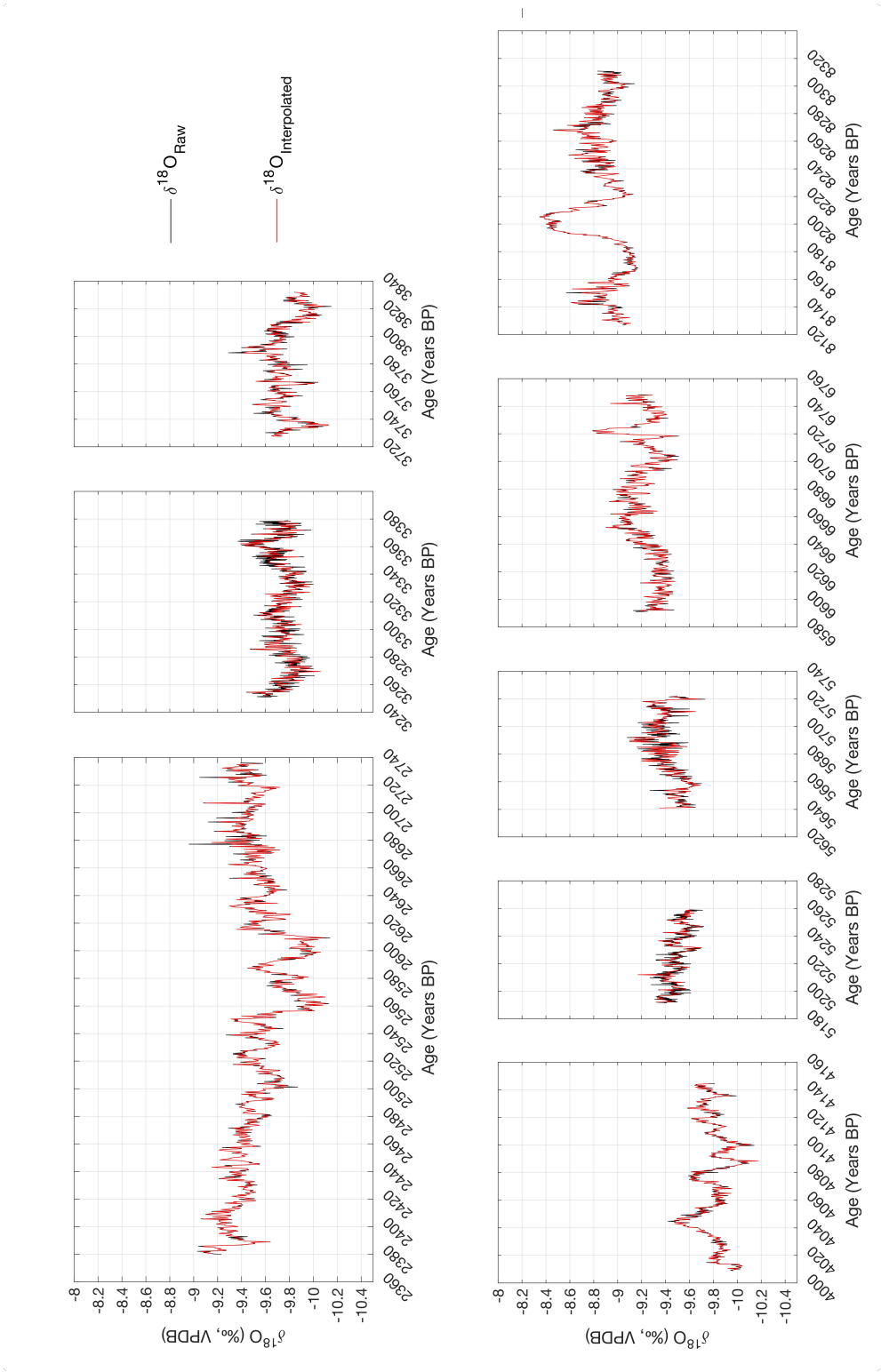


Figure 4.12: High resolution BA03 $\delta^{18}O$ time-series. The time-series are generated by combining the mean output of the OxCal age model and $\delta^{18}O$ depth records. The raw $\delta^{18}O$ time-series are plotted with black lines and the 0.5 year per sample interpolated time-series plotted with red lines.

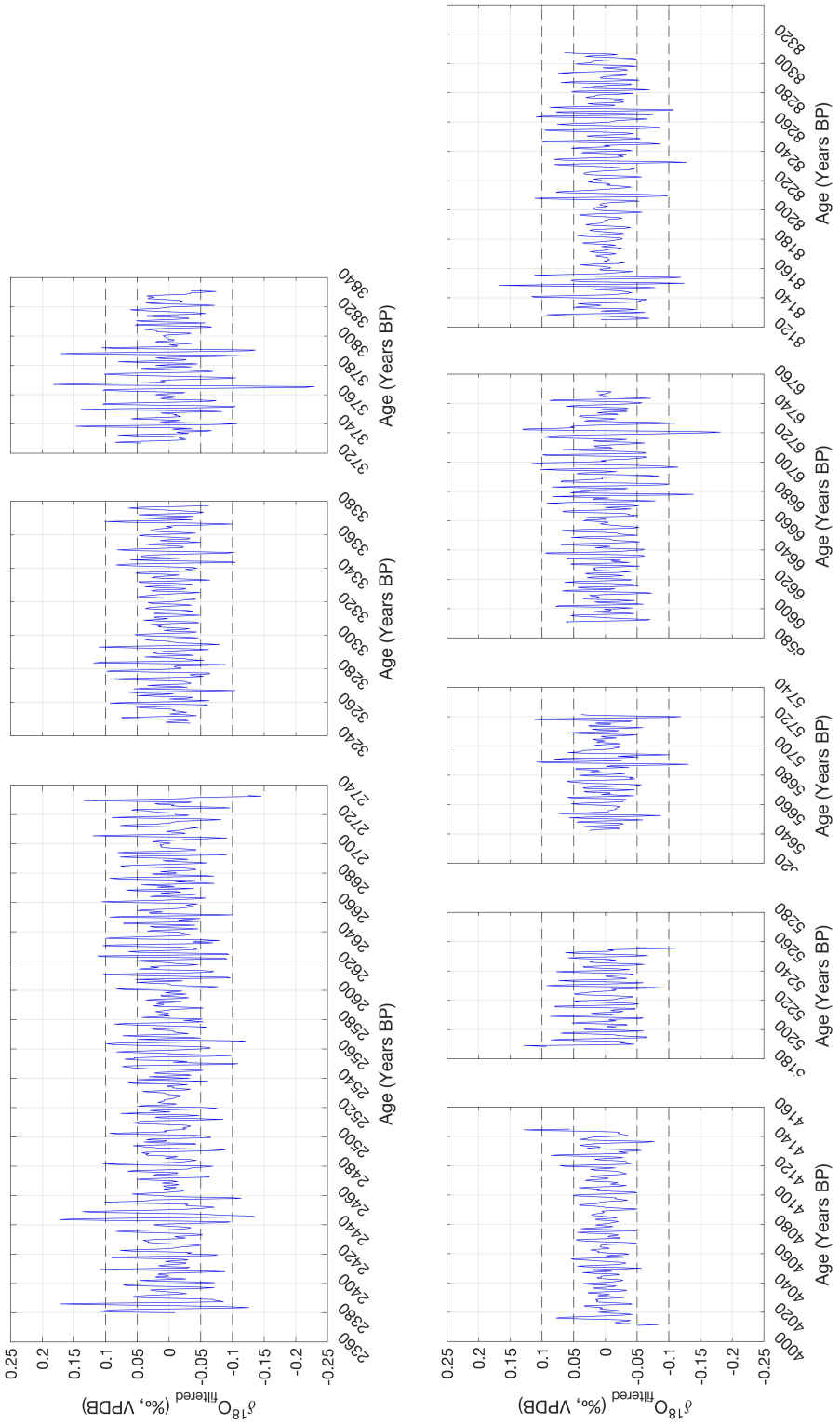


Figure 4.13: Bandpass (2-7 year) filtered $\delta^{18}O$ time-series of the eight interpolated high resolution BA03 $\delta^{18}O$ time-series. The bandpass filtered time-series are plotted in blue. Black dashed lines indicate the $\pm 0.05‰$ and $\pm$ 0.1‰ range.

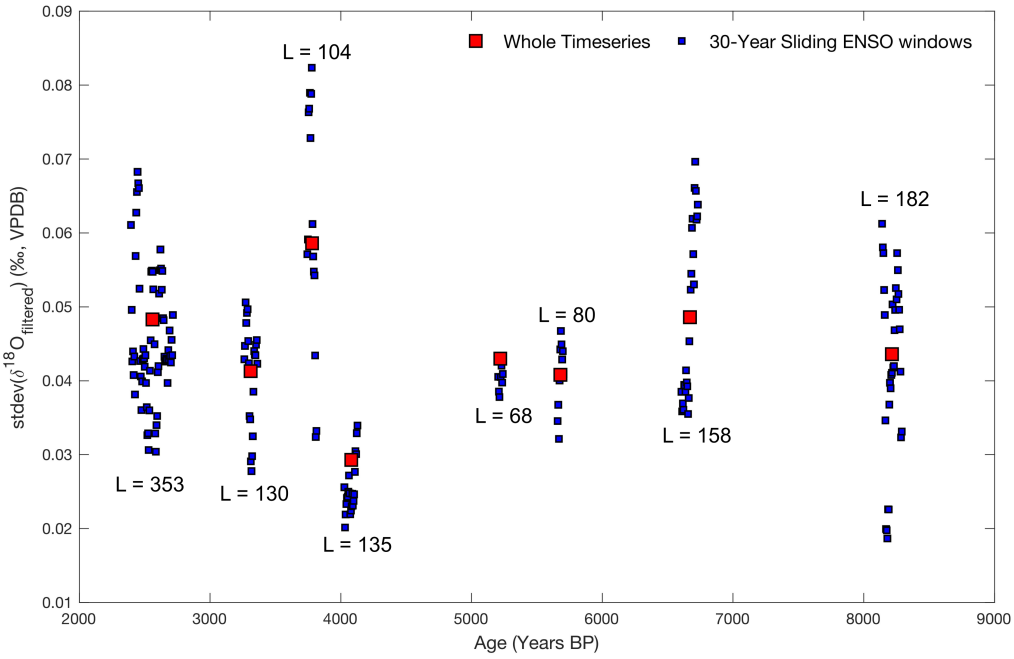


Figure 4.14: Mean and 30-year sliding window mean OxCal ENSO variability values for all eight of the high resolution BA03 $\delta^{18}O$ time-series. Red squares indicate the standard deviation of the whole band pass filtered $\delta^{18}O$ time-series. Blue squares are the standard deviations of 30-year sliding windows (5-year step) of the band pass filtered $\delta^{18}O$ time-series. The graph is annotated with the length in years (L) of each high resolution BA03 $\delta^{18}O$ record.

4.5.7.2 Propagating age model uncertainty onto the ENSO variability proxy

Age model uncertainty was propagated onto the ENSO variability proxy for all eight of the high resolution BA03 $\delta^{18}O$ time-series. The distributions of the 1000 ENSO variability proxy values generated from the 1000 OxCal ensemble age models are approximately normal for all of the time-series, despite the presence of a slight negative skew (Figure 4.15). The mean and standard deviation of the distribution of ensemble ENSO variability values can therefore be used as an approximation for the distribution of possible ENSO variability values for each time-series.

The ensemble means of the ENSO variability proxy have a range of 0.017‰ over the Holocene between a maximum of 0.053‰ at the 3780 Yr. (BP) window and a minimum of 0.036‰ at the 4080 Yr. (BP) window (Figure 4.16; Table 4.2). A reduction in the

Centre of time-series (Yr. BP)	N	Spatial Resolution (µm/sample)	Average Temporal Resolution (years/sample)	Length (Yr.)	Mean $\delta^{18}O$ (‰)	Analytical Uncertainty (‰)	stdev $\delta^{18}O_{Raw}$ (‰)	stdev $\delta^{18}O_{Interpolated}$ (‰)	Mean OxCal age model stdev $\delta^{18}O_{Band-Pass}$ (‰)	Ensemble mean stdev $\delta^{18}O_{Band-Pass}$ (‰)	$\pm 2\sigma$ (‰)
2560	847	60	0.42	353	-9.53	0.07	0.20	0.19	0.048	0.052	0.008
3310	600	60	0.22	130	-9.74	0.07	0.18	0.11	0.041	0.048	0.011
3780	318	60	0.33	104	-9.76	0.06	0.14	0.14	0.059	0.053	0.012
4080	397	50	0.34	135	-9.80	0.05	0.12	0.12	0.029	0.036	0.013
5220	357	60	0.19	68	-9.50	0.07	0.09	0.09	0.043	0.041	0.012
5680	319	60	0.25	80	-9.42	0.07	0.13	0.12	0.041	0.051	0.013
6670	394	60	0.40	158	-9.24	0.07	0.14	0.14	0.049	0.050	0.009
8215	515	60	0.35	182	-8.87	0.07	0.18	0.18	0.044	0.045	0.015

Table 4.2: ENSO variability values of the high resolution BA03 $\delta^{18}O$ time-series. N represents the number of $\delta^{18}O$ samples in each time-series. Mean age model stdev $\delta^{18}O_{\text{Band-Pass}}$ (‰) represents the standard deviation of the band pass filtered $\delta^{18}O$ time-series generated from the mean OxCal age model. Ensemble mean stdev $\delta^{18}O_{\text{Band-Pass}}$ (‰) represents the mean standard deviation of band pass filtered $\delta^{18}O$ time-series generated from 1000 ensemble OxCal age models.

ensemble mean ENSO variability is observed in the mid-Holocene with ENSO variability decreasing from the 5680 Yr. (BP) window until the 4080 Yr. (BP) window, before rapidly increasing to its maximum value at the 3780 Yr (BP) window. The ensemble mean ENSO variability for the 4080 Yr. (BP) window is significantly reduced (outside the 95% confidence limits) compared to the bounding windows of the mid-Holocene reduction in ENSO variability, the 3780 Yr. (BP) and 5680 Yr. (BP) windows (Figure 4.16).

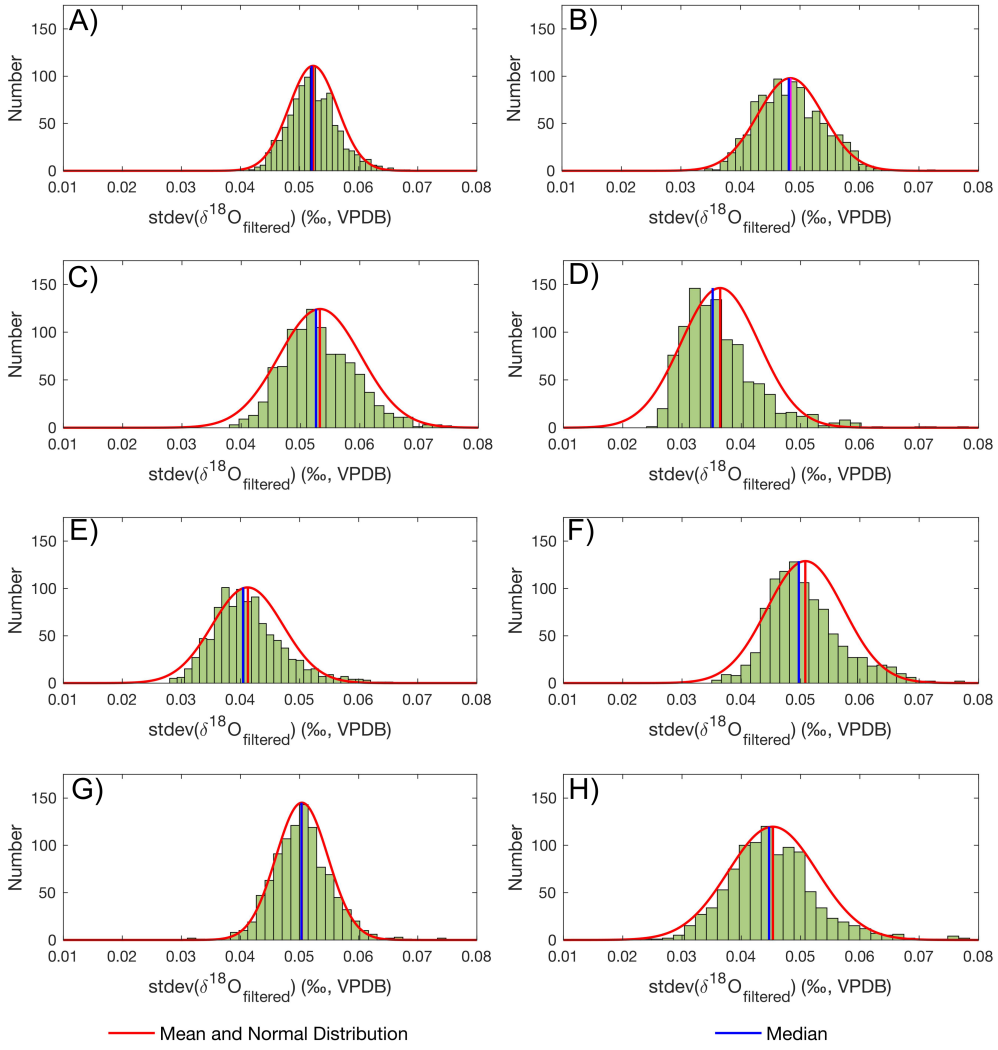


Figure 4.15: The distribution of ENSO variably values generated from the 1000 ensemble age models for all eight high resolution BA03 $\delta^{18}O$ time-series plotted as green histograms. The median values of each distribution are plotted as blue vertical lines. A normal distribution generated from the mean and standard deviation of each distribution is plotted in red, with a vertical red line indicating the mean.

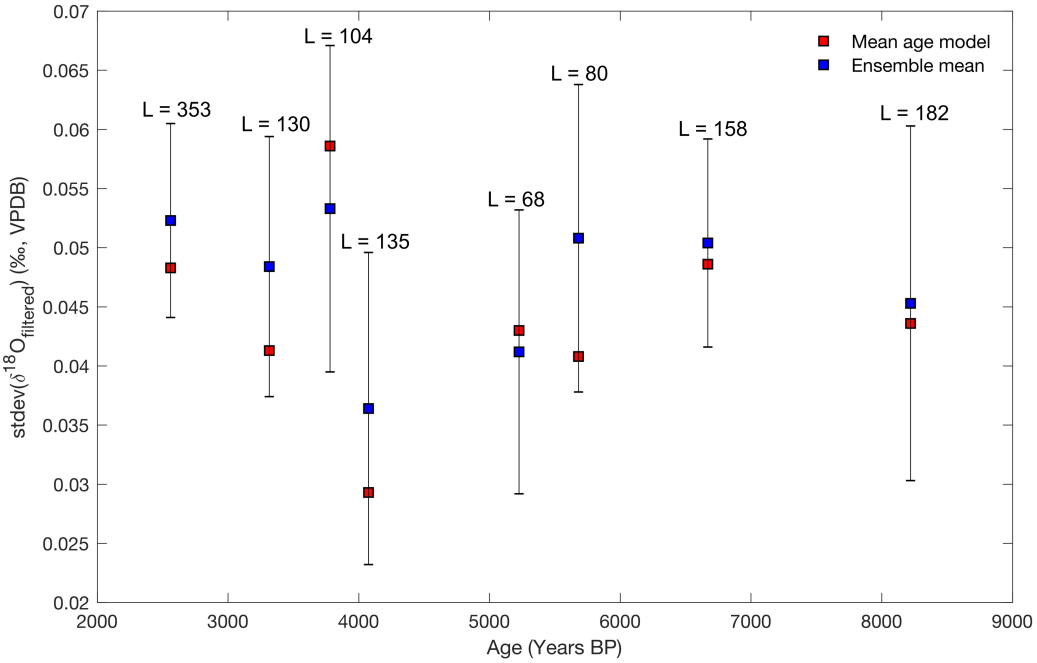


Figure 4.16: A comparison of mean OxCal ENSO variability values and ensemble mean ENSO variability values. Mean OxCal ENSO variability values are plotted in red. Ensemble mean ENSO variability values are plotted in blue. The vertical error bars indicate the 2σ confidence intervals on ensemble mean ENSO variability values.

4.5.7.3 $\delta^{18}O$ analytical uncertainty propagation

Artificial $\delta^{18}O$ time-series containing exclusively analytical instrument uncertainty were generated for all eight BA03 $\delta^{18}O$ time-series. Approximately half of the inputted $\delta^{18}O$ analytical uncertainty was observed to pass through the 2-7 year band-pass filter (Figure 4.17).

To correct for differences in $\delta^{18}O$ analytical uncertainty between records generated in this study, the $\delta^{18}O$ uncertainty of the 4080 Yr. (BP) timeseries was artificially increased to match that of the 3780 Yr. (BP) timeseries, ±0.06‰. This resulted in the ensemble mean ENSO variability value for the 4080 Yr. (BP) window increasing from 0.036 ± 0.013‰ to 0.040 ± 0.012‰. While correcting for the differing analytical uncertainties reduced the difference in ENSO variability between the 3780 Yr. (BP) and 4050 Yr. (BP) windows, ENSO variability in the 4050 Yr. (BP) (0.040 ± 0.012‰) window remained significantly lower than in the 3780 Yr. (BP) window (0.053 ± 0.012‰).

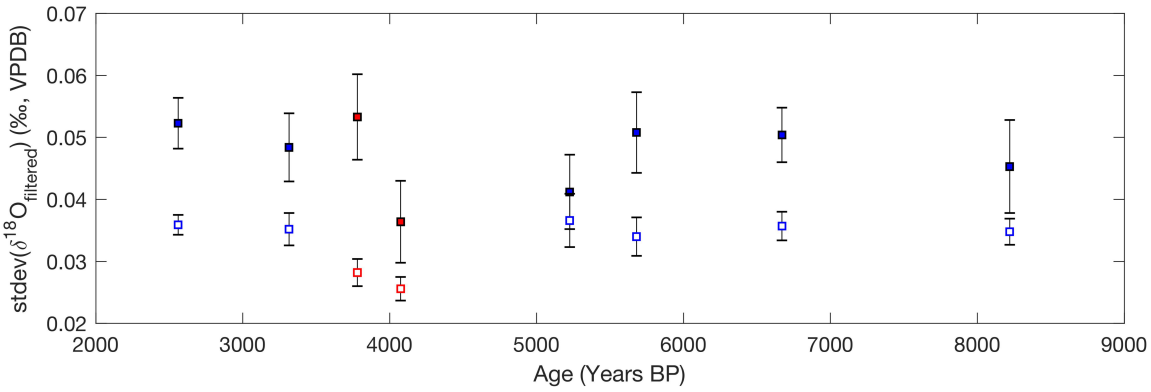


Figure 4.17: Comparison of ensemble mean ENSO variability values and propagated analytical instrument uncertainty. Ensemble mean ENSO variability values (solid squares) are plotted against the mean standard deviation of the 2-7 year band pass filtered analytical uncertainty time-series (unfilled squares). Error bars indicate the 1σ confidence interval of the 2-7 year band pass filtered time-series standard deviations.

4.6 Discussion

4.6.1 Stalagmite BA03 as a paleo-ENSO archive

Using the 2-7 year variance of BA03 $\delta^{18}O$ as a paleo-ENSO proxy is complicated by three factors: karst distortion of the rainfall $\delta^{18}O$ ENSO signal; age-model uncertainty; and $\delta^{18}O$ analytical uncertainty.

Cave monitoring in Mulu national park shows drip water karst residence time to be inversely proportional to the amplitude of inter-annual $\delta^{18}O$ variability (Moerman et al., 2014). Shifts in karst residence time would therefore alter the amplitude of the 2-7 year variance of cave drip waters, and hence BA03 calcite. A bootstrap test showed no significant reduction ($p<0.05$) in the 2-7 year band variance of the Niño3.4 index with varying amounts of smoothing simulating karst residence times of up to 18 months (Chen et al., 2016). As this covers the range of all measured Mulu cave karst residence times (Ellis et al., 2020), it is assumed that the karst residence time of BA03 drip waters did not exceed 18 months over the Holocene. Hence shifting karst residence times are assumed to have an insignificant impact on BA03 $\delta^{18}O$ 2-7 year variance. This is supported by the presence of significant peaks in the 2-7 year periodicity of the power spectra of all $\delta^{18}O$ time-series (Figure 4.11) showing ENSO band variability is

present in all time-series.

The large range of ENSO variability values calculated from the 1000 underlying ensemble age models (Figure 4.16) shows the ENSO variability proxy to be strongly age model dependent. To allow for the impact of age model uncertainty, the ensemble mean ENSO variability values and 2-sigma uncertainties will be considered the most reliable estimate of ENSO variability. Whilst age model uncertainty results in the propagation of large uncertainties onto the ENSO variability values, significant variations in ENSO variability are still observed throughout the Holocene (Figure 4.16). Therefore, BA03's age model uncertainties do not preclude BA03 from reconstructing shifts in Holocene ENSO variability.

While a portion of analytical instrument $\delta^{18}O$ uncertainty passes through the 2-7 year band pass filter, biasing time-series with greater $\delta^{18}O$ uncertainties towards greater 2-7 year variances (Figure 4.17), the impact of this on the ENSO variability values measured in this study appears small. The analytical uncertainty of the 4080 Yr. (BP) window was increased from ±0.05 ‰ to equal that of the 3780 Yr. (BP) window, ±0.06 ‰. This analytical uncertainty correction only resulted in a small increase in the ensemble mean ENSO variably value of 0.004 ‰. While this reduced the measured difference in ensemble mean ENSO variably values between the two windows, there is still a significant increase between the 4080 Yr. (BP) window and the 3780 Yr. (BP) window, so would not impact the interpretation of the ENSO variability timeseries. However, the impact of analytical uncertainties on all ENSO variability values cannot be accounted for as Chen et al. (2016) only reported one analytical uncertainty for all $\delta^{18}O$ measurements, as opposed to individual uncertainties per $\delta^{18}O$ timeseries. When combining all $\delta^{18}O$ measurements from this chapter the reproducibility of in-house marble standard NOCZ is ±0.07‰ (1σ, n = 55), equal to the $\delta^{18}O$ uncertainty value reported across all $\delta^{18}O$ measurements in Chen et al. (2016). As the two $\delta^{18}O$ uncertainties are approximately equal between studies when calculated over all $\delta^{18}O$ measurements, and the impact of the $\delta^{18}O$ uncertainty small when corrected for between

the 3780 Yr. (BP) window and 4080 Yr. (BP) window, when comparing all ENSO variability windows the contributions of $\delta^{18}O$ uncertainty to the ENSO variability values is assumed equal and no correction is attempted.

One further complication using BA03 as a paleo-ENSO archive could be rapidly shifting speleothem growth rates, allowing seasonal $\delta^{18}O$ signals to pass through the 2-7 year bandpass filter, and hence supply a large amount of the reported ENSO variability. For this to occur, both large short lived fluctuations in growth rate must occur, allowing seasonal signals to be interpreted as inter-annual, along side a large seasonal signal in rainwater $\delta^{18}O$. However, while it is difficult rule rule out rapid fluctuations in growth rate between U-Th ages, rainwater monitoring studies from Borneo have shown that seasonal variability is absent in both rainfall amount and $\delta^{18}O$ (Ellis et al., 2020; Moerman et al., 2013). As such, the inclusion of seasonal variability is uniquely to bias the estimated ENSO variability using this method.

Provided karst processes and shifts in $\delta^{18}O$ uncertainty are negligible over all measured BA03 $\delta^{18}O$ time-series, BA03 has the potential to provide high fidelity centennial scale reconstructions of ENSO variability over the Holocene.

4.6.2 Evolution of reconstructed ENSO variability through the Holocene

The ensemble mean ENSO variability time-series generated from both the reanalysed and new $\delta^{18}O$ time-series from BA03 show significant shifts in ENSO variability over the Holocene (Figure 4.18). The most pronounced feature of the time-series is a reduction in ENSO variability in the mid-Holocene bounded by the ENSO windows centred at 3780 Yr. (BP) and 5680 Yr. (BP), with the greatest reduction observed in the 4080 Yr. (BP) window (Figure 4.18). The mid-Holocene reduction in ENSO variability is superimposed on large decadal scale changes in ENSO variability (Figure 4.14), consistent with coral paleo-ENSO records (e.g. Cobb et al., 2013; McGregor et al., 2013; Grothe et al., 2019), and model ENSO simulations (e.g. Wittenberg, 2009; Liu et al.,

2014; Emile-Geay et al., 2016).

This study adds to a growing number of Pacific paleo-ENSO reconstructions which suggest that the mid-Holocene contains a period of anomalously low ENSO activity compared with the early and late Holocene (Figure 4.18) (e.g. Koutavas and Joanides, 2012; Carré et al., 2014; Emile-Geay et al., 2016; Thompson et al., 2017; Grothe et al., 2019). Whilst the exact timings of the minimum in ENSO variability are still debated, being recorded between 5.68 kyr (BP) – 3.78 kyr (BP) in this study; 5 kyr (BP) – 3 kyr (BP) in corals archives (Grothe et al., 2019); 6 kyr (BP) – 4 kyr BP in foraminifera (Koutavas and Joanides, 2012); and 5 kyr (BP) – 4 kyr BP in molluscs (Carré et al., 2014); there is strong evidence for a change in ENSO behaviour during the mid-Holocene. The difference in timings of the mid-Holocene ENSO minimum could be explained by either a spatially heterogenous response of the ENSO system during the mid-Holocene minimum (Emile-Geay et al., 2016), non-linear responses of archives to shifts in ENSO dynamics (Emile-Geay and Tingley, 2016) or the large uncertainties in reconstructing the highly variable ENSO system (Grothe et al., 2019).

While a spatial heterogenous shift in ENSO activity in the mid-Holocene cannot be ruled out, paleo-ENSO archives have now been identified showing a mid-Holocene reduction in ENSO activity in the eastern (Koutavas and Joanides, 2012; Carré et al., 2014), central (Emile-Geay et al., 2016; Grothe et al., 2019) and western tropical Pacific (this study), suggesting the mid-Holocene minimum is a basin wide phenomena.

The ENSO system is observed to contain a a high level of short term variability in both this study, other paleo-ENSO archives (Cobb et al., 2013; Emile-Geay et al., 2016; Grothe et al., 2019) and model reconstructions (Emile-Geay et al., 2016) (Figure 4.14). As such, there are inherent uncertainties in attempting to reconstruct the ENSO system using temporally short time-series as these might introduces biases from under sampling a highly variable system (Emile-Geay et al., 2016). Longer ENSO variability records therefore allow for a better understanding of long term trends in ENSO variability (Chen et al., 2016; Emile-Geay et al., 2016). The majority of paleo-ENSO records are less than

50 years in length, with few exceeding 100 years (Emile-Geay et al., 2016). This could account for disparities in the recorded length of the mid-Holocene ENSO minimum in different archives. The centennial length ENSO reconstructions produced from BA03 thus allow for a higher degree of confidence than most previous paleo-ENSO archives that centennial scale trends in ENSO behaviour, rather than decadal scale variability, are being reconstructed.

Various mechanisms have been suggested as a potential cause of the mid-Holocene reduction in ENSO variability, ranging from reduced dust production during the greening of the Sahara (Pausata et al., 2017) to orbital forcing (e.g. Chen et al., 2016; Grothe et al., 2019). $\delta^{18}O$ time-series from Borneo stalagmites suggest 5.5 kyr (BP) – 3.5 kyr (BP) to be a period of exceptionally high convective activity in the WPWP compared with the rest of the Holocene (Partin et al., 2007a; Chen et al., 2016), coincident with a maximum in equatorial September - October - November (SON) insolation between 5.5 kyr (BP) – 3.5 kyr (BP) (Berger and Loutre, 1991) (Figure 4.18). In the modern day ENSO's strongest growth phase falls in boreal Autumn (Chen et al., 2016; Grothe et al., 2019). Chen et al. (2016) proposed that a persistent increase in WPWP convective activity, associated with increased SON equatorial insolation, would result in enhanced Walker circulation, easterly winds and upwelling in the eastern tropical Pacific. A shift in the mean state of the tropical Pacific to more La Niña like conditions would suppress the development of El Niño events, accounting for the observed reduction in ENSO variability.

At approximately 4000 Yr. (BP) shifts in climate are reported from multiple tropical archives, from South America to Africa (Marchant and Hooghiemstra, 2004). A review of these archives identified a trend of increased rainfall in South America and reduced rainfall in Africa across the 4000 Yr. (BP) transition (Marchant and Hooghiemstra, 2004). This is consistent with a shift from a more La Niña like mean state, to a modern tropical mean state with ENSO activity (Marchant and Hooghiemstra, 2004). Furthermore, in stalagmite BA03 all measured trace elements (Mg/Ca, Sr/Ca and

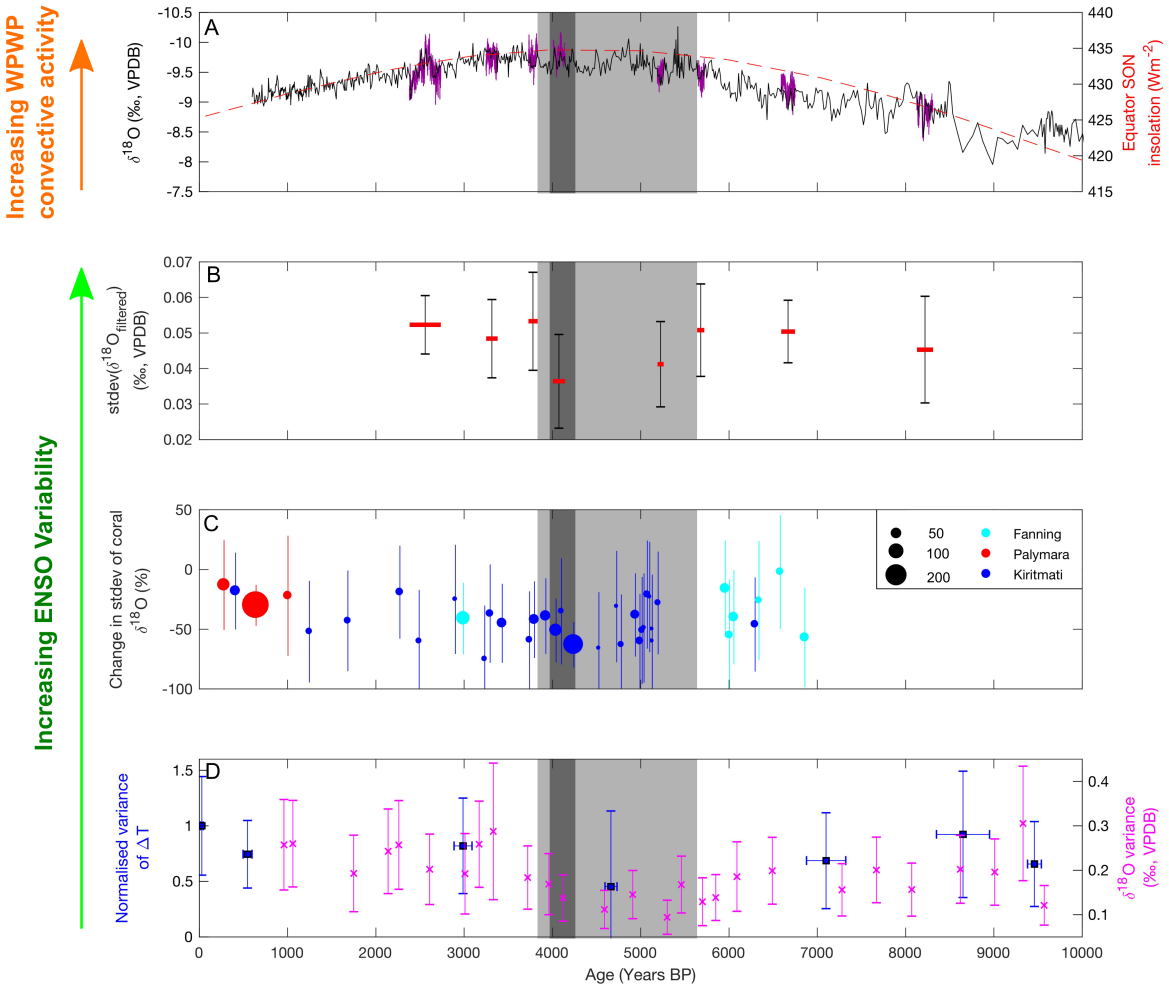


Figure 4.18: Comparison of tropical Pacific paleo-ENSO archives and western warm pool convective activity over the Holocene. A) BA03 $\delta^{18}O$ time-series plotted against SON equatorial insolation. The decadal resolution BA03 $\delta^{18}O$ time-series (Chen et al., 2016) (black line) is overlain with sub-annual resolution $\delta^{18}O$ time-series (purple) generated in this study and Chen et al. (2016). Also plotted is SON equatorial insolation (red dashed line) (Berger and Loutre, 1991). B) Western tropical Pacific paleo-ENSO reconstruction from speleothem BA03; this study. Thick red lines show the ensemble mean ENSO variability values and time-series duration. Error bars indicate the 2σ confidence intervals. C) Central tropical Pacific coral paleo-ENSO reconstructions (Grothe et al., 2019). Values are plotted as the percentage change from modern (1997 - 2007 CE) values. Marker size indicates the duration of the coral $\delta^{18}O$ time-series (years), and color indicates the island fossil corals were collected from: Fanning (cyan); Kiritimati (blue); or Palmyra (red). Uncertainty bars are plotted based on coral length (Grothe et al., 2019). D) Eastern tropical Pacific paleo-ENSO reconstructions from molluscs (blue squares) (Koutavas and Joanides, 2012) and foraminifera (purple crosses) (Carré et al., 2014). Mollusc data is plotted as a proportion of modern variance, with horizontal error bars indicating the time period covered by the record. Foraminifera data is plotted as total foraminifera $\delta^{18}O$ variance. Vertical error bars indicate 2σ confidence intervals. Light grey shading indicates the maximum length of the ENSO minimum observed in BA03, with dark grey shading showing the duration of the proposed "4.2 kyr event" (Carolin et al., 2019).

Ba/Ca) (Figure 4.8) are observed to increase between 4.8 kyr (BP) - 3.6 kyr (BP). Trace element concentrations in another speleothem from Bukit Assam cave were found to be controlled by prior calcite precipitation (PCP) on centennial time scales (Partin et al., 2013). The positive correlations between Ba, Mg and Sr in BA03 (Appendix Figure C.1) suggests PCP could also be the control of trace element concentrations in BA03. The trend of increasing trace element concentrations would therefore suggest increased PCP and reduced rainfall above Bukit Assam Cave (Fairchild and Treble, 2009). Reducing rainfall in northern Borneo is consistent with a shift away from a more La Niña like mean state in the tropical Pacific.

While an increase in SON equatorial insolation could result in the suppression of El Niño events, the response between SON equatorial insolation and ENSO variability cannot be linear. ENSO variability remains constant in the early Holocene despite increasing SON equatorial insolation (Figure 4.18). Therefore, if SON equatorial insolation and increased WPWP convective activity are capable of producing the observed mid-Holocene reduction in ENSO variability, non-linear responses must trigger a critical threshold at which El Niño events are sufficiently suppressed to significantly reduce ENSO variability.

4.6.3 A minimum in ENSO variability coeval with the "4.2 kyr event"

The lack of a clear high latitude forcing for the proposed "4.2 kyr event", unlike other Holocene centennial scale climate perturbations e.g. the 8.2 kyr event, has led authors to suggest a tropical forcing (e.g. Toth and Aronson, 2019; Renssen, 2022). As the greatest source of tropical inter-annual variability, the ENSO system has been suggested as a potential causal mechanism. There is now growing evidence for a temporal link between the "4.2 kyr event" and the mid-Holocene minimum in ENSO variability. Minimum values of ENSO variability, in multiple paleo-ENSO archives (McGregor et al., 2013; Carré et al., 2014; Emile-Geay et al., 2016; Leonard et al., 2016; Grothe et al., 2019) including

BA03, coincide with the "4.2 kyr event": 4260 Yr. (BP) – 3970 Yr. (BP) (Carolin et al., 2019). Furthermore, the significant increase in ENSO variability recorded in BA03, occurring between the 4080 Yr. (BP) and 3780 Yr. (BP) windows, coincides with the termination of the "4.2 kyr event" at 3970 Yr. (BP) (Carolin et al., 2019) (Figure 4.18). This increase in ENSO variability is robustly recorded in BA03 between two ENSO windows generated solely in this study and remains significant when corrected for the differing $\delta^{18}O$ uncertainties of the two $\delta^{18}O$ timeseries.

A further link connecting the "4.2 kyr event" and the ENSO system is provided by the spatial correlation between the global signature of ENSO events and the "4.2 kyr event" (Toth and Aronson, 2019; Renssen, 2022). The "4.2 kyr event" has been identified to be coeval with dry events in Northern and equatorial Africa (e.g. Ruan et al., 2015), the Middle East (e.g. Carolin et al., 2019), central North America (e.g. Booth et al., 2005) and most of South and East Asia (e.g. Berkelhammer et al., 2012); with wet conditions throughout South America (e.g. Marchant and Hooghiemstra, 2004, and references therein), Western North America (e.g. Menounos et al., 2008)and south west Africa (Railsback et al., 2018). A full review of locations with precipitation anomalies coeval with the "4.2 kyr event" is available in Renssen (2022). While the expression of El Niño and La Niña events can vary significantly between events these locations are consistent with precipitation anomalies observed during ENSO events (Davey et al., 2014).

The simultaneous termination of the mid-Holocene minimum in ENSO variability and the "4.2 kyr event" recorded in BA03 and the similarity between the global impacts of ENSO and the "4.2 kyr event" suggest a potential connection between the two. This could be either that the "4.2 kyr event" and a further reduction in ENSO variability on top of the mid-Holocene low were caused by the same mechanism; or the unique climatic setting in the mid-Holocene caused by the extreme reduction in ENSO variability could provide the conditions required for an otherwise unforced centennial climate perturbation to occur. Proving and explaining a link between the "4.2 kyr event" and reduced

ENSO variability is beyond the scope of this study.

4.6.4 Study Limitations

While this study finds stalagmite BA03 to be a robust archive for reconstructing paleo-ENSO variability, improvements can be made in future studies aimed at reconstructing ENSO variability from speleothems.

Firstly, if present, large changes in karst dynamics over Bukit Assam cave during the past 10,000 years would result in shifts in the 2-7 year variability of BA03 $\delta^{18}O$ driven by varying amounts of karst smoothing of the rainfall $\delta^{18}O$ signal, as opposed to shifts in rainfall 2-7 year variability. While modern karst dynamics should not significantly impact the recording of ENSO variability in speleothems, in order to fully discount cave specific controls on reconstructed ENSO variability future studies should aim to generate paleo-ENSO records from multiple Northern Borneo caves. This way, site specific impacts on reconstructed paleo-ENSO variability values can be identified if present.

Secondly, analytical $\delta^{18}O$ uncertainties should be reported for individual speleothem $\delta^{18}O$ time-series used to reconstruct paleo-ENSO variability. This would allow periods of greater instrument uncertainty to be identified and corrected for in order to remove any instrumental introduced bias in 2-7 year $\delta^{18}O$ variance.

Thirdly, the greatest degree of uncertainty in the BA03 ENSO variability record comes from age model uncertainty. High detrital thorium concentrations and shifting initial thorium ratios in stalagmite BA03 result in large age model uncertainties. Identifying relatively low thorium speleothems, or speleothems with annual laminar, would decrease age model uncertainty resulting in smaller uncertainties for future speleothem paleo-ENSO archives.

Finally, the majority of paleo-ENSO archives report past ENSO variability as a proportion of modern ENSO variability (e.g. McGregor et al., 2013; Cobb et al., 2013; Carré et al., 2014; Emile-Geay et al., 2016; Grothe et al., 2019). This could not be

achieved for speleothem BA03, as although it was collected from underneath an active drip (Chen et al., 2016), the Oxcal age model estimates stalagmite growth to have ceased at 220 Yr. (BP) (Figure 4.7). Future paleo-ENSO reconstructions should use speleothems which contain modern growth, allowing paleo-ENSO variability to be reported as a proportion of modern variability and hence increasing comparability with other paleo-ENSO proxies.

4.7 Conclusion

While this study shows that northern Borneo speleothems have the capacity to provide excellent archives of paleo-ENSO variability, care must be taken to thoroughly account for age model and $\delta^{18}O$ uncertainties which can supply uncertainties and bias to the generated paleo-ENSO variability proxy. In addition, this study recommends the generation of replicate speleothem records to ensure the changes in 2-7 year $\delta^{18}O$ variability recorded in speleothem BA03 are recording changes in the rainfall $\delta^{18}O$ as opposed to karst processes.

Suggested (based on the mean OxCal age model) sub-annual ($>$ 2 samples per year) resolution $\delta^{18}O$ time-series from stalagmite BA03 agree with other coral, mollusc and foraminifera paleo-ENSO archives from the tropical Pacific, observing the ENSO system to be active in the early and late Holocene, with suppressed ENSO variability in the mid-Holocene. The reduced ENSO variability in the mid-Holocene coincides with a maximum in convective activity over northern Borneo, suggesting that increased WPWP convection, paced by SON equatorial insolation, could suppress ENSO variability.

The new sub-annual ($>$ 2 samples per year) resolution $\delta^{18}O$ time-series generated from BA03 by this study constrains the termination of the mid-Holocene ENSO minimum to be abrupt and to coincide with the end of the "4.2 kyr event". This suggests a possible link between the resumption of ENSO variability and the termination of the "4.2 kyr event". The future generation of additional speleothem hosted paleo-ENSO records covering the whole "4.2 kyr event" will assist in supporting or rejecting this link.

Chapter 5

Concluding remarks and future outlook

In this thesis I have developed new, and expanded existing, methods of reconstructing paleoclimate from geochemical proxies hosted in secondary carbonate precipitates. This has been done by: i) Developing a new multi-proxy approach for using lacustrine cave carbonates to reconstruct past shifts in P-E and; ii) Investigating the suitability of speleothems as paleo-ENSO archives. Both of these research themes answer critical paleoclimate questions, and lay the foundation for future projects.

The modelling (Chapter 2) and measurement (Chapter 3) of the chemical composition of LCC samples from Lake Bonneville undertaken in this thesis builds a substantial platform for using combined measurements of Mg/Ca, U/Ca and $\delta^{\frac{44}{42}}Ca$ to reconstruct basin wide shifts in P-E. Lacustrine cave carbonates deposits have, so far, only been reported in the Bonneville Basin. However, their abundant precipitation in the Bonneville Basin, found in over forty locations (McGee et al., 2012), suggests that similar deposits should be extensive in other terminal lake basins. The global distribution of endoheric basins, in which terminal lakes reside, suggests this framework could be applied to help provide high resolution, continuous, reconstructions of regional hydrology throughout the globe. This would be particularly useful in other Great Basin terminal lakes, where LakeCalc and LCC measurements could be combined with existing paleo-shoreline re-

constructions, to add high precision U-Th chronology and continuous records to existing P-E reconstructions. This would help constrain the complex nature of temporal and spatial shifts in P-E over the southwestern United States, and identify the mechanism linking moisture availability in the southwestern United States with Heinrich Stadials. As such, the identification of new terminal lake basins which host LCC deposits would provide useful new sites for reconstructing past shifts in P-E balance.

Chapter 4 demonstrated the suitability of speleothem BA03 to provide robust reconstructions of paleo-ENSO variability throughout the Holocene. Speleothems have useful benefits over other paleo-ENSO records due to their long continuous periods of growth and protection from post depositional alteration in the cave environment. However, they are not without limitations. Karst processes, analytical oxygen isotope uncertainties and age model uncertainties, all introduce uncertainties to generated paleo-ENSO reconstructions. This work, therefore, recommends the careful selection of speleothems for future paleo-ENSO reconstructions, focusing on identifying relatively low thorium speleothems, or speleothems with annual laminar, which would reduce age model uncertainty. A second recommendation would be the generation of replicate paleo-ENSO reconstructions from speleothems hosted in different caves in order to identify and remove site specific processes from paleo-ENSO reconstructions. Despite these limitations, speleothem BA03 was shown in this thesis to provide a robust paleo-ENSO reconstruction, showing a marked increase in ENSO variability over the termination of the "4.2 kyr event" from a single paleo-ENSO archive. This suggest a potential link between the the ENSO system and the currently unknown cause of the "4.2 kyr event". The future generation of additional speleothem hosted paleo-ENSO records covering the whole "4.2 kyr event" would assist in supporting or rejecting this link.

I hope the methods developed in this thesis will be of interest to a wide range of geochemists and prove useful in future reconstructions of regional P-E and the ENSO system. Thank you for reading.

Bibliography

Armitage, S. J., Bristow, C. S., and Drake, N. A. (2015). West African monsoon dynamics inferred from abrupt fluctuations of Lake Mega-Chad. *Proceedings of the National Academy of Sciences of the United States of America*, 112(28):8543–8548.

Asmerom, Y., Polyak, V. J., and Burns, S. J. (2010). Variable winter moisture in the southwestern United States linked to rapid glacial climate shifts. *Nature Geoscience*, 3(2):114–117.

Ayalon, A., Bar-Matthews, M., and Sass, E. (1998). Rainfall-recharge relationships within a karstic terrain in the Eastern Mediterranean semi-arid region, Israel: δ18O and δD characteristics. *Journal of Hydrology*, 207(1-2):18–31.

Bajo, P., Borsato, A., Drysdale, R., Hua, Q., Frisia, S., Zanchetta, G., Hellstrom, J., and Woodhead, J. (2017). Stalagmite carbon isotopes and dead carbon proportion (DCP) in a near-closed-system situation: An interplay between sulphuric and carbonic acid dissolution. *Geochimica et Cosmochimica Acta*, 210:208–227.

Baldini, L. M., Baldini, J. U., McDermott, F., Arias, P., Cueto, M., Fairchild, I. J., Hoffmann, D. L., Mattey, D. P., Müller, W., Nita, D. C., Ontañón, R., Garciá-Moncó, C., and Richards, D. A. (2019). North Iberian temperature and rainfall seasonality over the Younger Dryas and Holocene. *Quaternary Science Reviews*, 226.

Bamston, A. G., Chelliah, M., and Goldenberg, S. B. (1997). Documentation of a highly enso-related sst region in the equatorial pacific: Research note. *Atmosphere - Ocean*, 35(3):367–383.

Bell, G. D. and Halpert, M. S. (1998). Climate Assessment for 1997. *Bulletin of the American Meteorological Society*, 79(5s):S1–S50.

Bellenger, H., Guilyardi, E., Leloup, J., Lengaigne, M., and Vialard, J. (2014). ENSO representation in climate models: From CMIP3 to CMIP5. *Climate Dynamics*, 42(7-8):1999–2018.

Benson, L. V., Lund, S. P., Smoot, J. P., Rhode, D. E., Spencer, R. J., Verosub, K. L., Louderback, L. A., Johnson, C. A., Rye, R. O., and Negrini, R. M. (2011). The rise and fall of Lake Bonneville between 45 and 10.5 ka. *Quaternary International*, 235(1-2):57–69.

Berger, A. and Loutre, M. F. (1991). Insolation values for the climate of the last 10 million years. *Quaternary Science Reviews*, 10(4):297–317.

Berkelhammer, M., Sinha, A., Stott, L., Cheng, H., Pausata, F. S. R., and Yoshimura, K. (2012). An Abrupt Shift in the Indian Monsoon 4000 Years Ago. *Climate of the Past Discussions*.

Berner, R. A. (1975). The role of magnesium in the crystal growth of calcite and aragonite from sea water. *Geochimica et Cosmochimica Acta*, 39(4):489–504.

Bjerknes, J. (1969). Monthly Weather Reyiew Atmospheric Teleconnections From the Equatorial Pacific. *Monthly Weather Review*, 97(3):163–172.

Blättler, C. L., Jenkyns, H. C., Reynard, L. M., and Henderson, G. M. (2011). Significant increases in global weathering during Oceanic Anoxic Events 1a and 2 indicated by calcium isotopes. *Earth and Planetary Science Letters*, 309(1-2):77–88.

Booth, R. K., Jackson, S. T., Forman, S. L., Kutzbach, J. E., Bettis, E. A., Kreig, J., and Wright, D. K. (2005). A severe centennial-scale drought in mid-continental North America 4200 years ago and apparent global linkages. *Holocene*, 15(3):321–328.

Borsato, A., Frisia, S., Fairchild, I. J., Somogyi, A., and Susini, J. (2007). Trace element distribution in annual stalagmite laminae mapped by micrometer-resolution X-ray fluorescence: Implications for incorporation of environmentally significant species. *Geochimica et Cosmochimica Acta*, 71(6):1494–1512.

Bowen, G. J. (2008). Spatial analysis of the intra-annual variation of precipitation isotope ratios and its climatological corollaries. *Journal of Geophysical Research At-*

mospheres, 113(5):1–10.

Broecker, W. and Putnam, A. E. (2012). How did the hydrologic cycle respond to the two-phase mystery interval? *Quaternary Science Reviews*, 57:17–25.

Broecker, W. S., McGee, D., Adams, K. D., Cheng, H., Edwards, R. L., Oviatt, C. G., and Quade, J. (2009). A Great Basin-wide dry episode during the first half of the Mystery Interval? *Quaternary Science Reviews*, 28(25-26):2557–2563.

Cai, W., Santoso, A., Wang, G., Yeh, S. W., An, S. I., Cobb, K. M., Collins, M., Guilyardi, E., Jin, F. F., Kug, J. S., Lengaigne, M., Mcphaden, M. J., Takahashi, K., Timmermann, A., Vecchi, G., Watanabe, M., and Wu, L. (2015). ENSO and greenhouse warming. *Nature Climate Change*, 5(9):849–859.

Cai, W., Wang, G., Dewitte, B., Wu, L., Santoso, A., Takahashi, K., Yang, Y., Carréric, A., and McPhaden, M. J. (2018). Increased variability of eastern Pacific El Niño under greenhouse warming. *Nature*, 564(7735):201–206.

Cane, M. A. (2005). The evolution of El Niño, past and future. *Earth and Planetary Science Letters*, 230(3-4):227–240.

Carolin, S. A., Cobb, K. M., Lynch-Stieglitz, J., Moerman, J. W., Partin, J. W., Lejau, S., Malang, J., Clark, B., Tuen, A. A., and Adkins, J. F. (2016). Northern Borneo stalagmite records reveal West Pacific hydroclimate across MIS 5 and 6. *Earth and Planetary Science Letters*, 439:182–193.

Carolin, S. A., Walker, R. T., Day, C. C., Ersek, V., Alastair Sloan, R., Dee, M. W., Talebian, M., and Henderson, G. M. (2019). Precise timing of abrupt increase in dust activity in the Middle East coincident with 4.2 ka social change. *Proceedings of the National Academy of Sciences of the United States of America*, 116(1):67–72.

Carré, M., Sachs, J. P., Purca, S., Schauer, A. J., Braconnot, P., Angeles Falcón, R., Julien, M., and Lavallée, D. (2014). Holocene history of ENSO variance and asymmetry in the eastern tropical Pacific. *Science*, 345(6200):1045–1047.

Cayan, D. R., Redmond, K. T., and Riddle, L. G. (1999). ENSO and hydrologic extremes in the western United States. *Journal of Climate*, 12(9):2881–2893.

Chen, C. Y., McGee, D., Woods, A., Pérez, L., Hatfield, R. G., Edwards, R. L., Cheng, H., Valero-Garcés, B. L., Lehmann, S. B., Stoner, J. S., Schwalb, A., Tal, I., Seltzer, G. O., Tapia, P. M., Abbott, M. B., and Rodbell, D. T. (2020). U-Th dating of lake sediments: Lessons from the 700 ka sediment record of Lake Junín, Peru. *Quaternary Science Reviews*, 244.

Chen, D. and Chen, H. W. (2013). Using the Köppen classification to quantify climate variation and change: An example for 1901-2010. *Environmental Development*, 6(1):69–79.

Chen, S., Hoffmann, S. S., Lund, D. C., Cobb, K. M., Emile-Geay, J., and Adkins, J. F. (2016). A high-resolution speleothem record of western equatorial Pacific rainfall: Implications for Holocene ENSO evolution. *Earth and Planetary Science Letters*, 442:61–71.

Cobb, K., Westphal, N., Sayani, H., Watson, J., Di Lorenzo, E., Cheng, H., Edwards, R., and Charles, C. (2013). Highly Variable El Niño Southern Oscillation Throughout the Holocene. *Science*, 339(January):67–70.

Cobb, K. M., Adkins, J. F., Partin, J. W., and Clark, B. (2007). Regional-scale climate influences on temporal variations of rainwater and cave dripwater oxygen isotopes in northern Borneo. *Earth and Planetary Science Letters*, 263(3-4):207–220.

Conroy, J. L., Overpeck, J. T., Cole, J. E., Shanahan, T. M., and Steinitz-Kannan, M. (2008). Holocene changes in eastern tropical Pacific climate inferred from a Galápagos lake sediment record. *Quaternary Science Reviews*, 27(11-12):1166–1180.

Currey, D. R. (1983). Lake Bonneville; selected features of relevance to neotectonic analysis. Technical report.

Currey, D. R. (1990). Quaternary palaeolakes in the evolution of semidesert basins, with special emphasis on Lake Bonneville and the Great Basin, U.S.A. *Palaeogeography, Palaeoclimatology, Palaeoecology*, 76(3-4):189–214.

Dansgaard, W. (1964). Stable isotopes in precipitation. *Tellus*, 16(4):436–468.

D'Arrigo, R. D., Cook, E. R., Jacoby, G. C., and Briffa, K. R. (1993). Nao and sea

surface temperature signatures in tree-ring records from the North Atlantic sector. *Quaternary Science Reviews*, 12(6):431–440.

Davey, M. K., Brookshaw, A., and Ineson, S. (2014). The probability of the impact of ENSO on precipitation and near-surface temperature. *Climate Risk Management*, 1:5–24.

Day, C. C. and Henderson, G. M. (2011). Oxygen isotopes in calcite grown under cave-analogue conditions. *Geochimica et Cosmochimica Acta*, 75(14):3956–3972.

Day, C. C. and Henderson, G. M. (2013). Controls on trace-element partitioning in cave-analogue calcite. *Geochimica et Cosmochimica Acta*, 120:612–627.

Deininger, M., Fohlmeister, J., Scholz, D., and Mangini, A. (2012). Isotope disequilibrium effects: The influence of evaporation and ventilation effects on the carbon and oxygen isotope composition of speleothems - A model approach. *Geochimica et Cosmochimica Acta*, 96:57–79.

Denton, G. H., Broecker, W. S., and Alley, R. B. (2006). The mystery interval 17.5 to 14.5 kyrs ago. *PAGES news*, 14(2):14–16.

DePaolo, D. J. (2011). Surface kinetic model for isotopic and trace element fractionation during precipitation of calcite from aqueous solutions. *Geochimica et Cosmochimica Acta*, 75(4):1039–1056.

Dettinger, M. (2011). Climate change, atmospheric rivers, and floods in California - a multimodel analysis of storm frequency and magnitude changes. *Journal of the American Water Resources Association*, 47(3):514–523.

Dreybrodt, W. (2012). Comment on "Oxygen isotopes in calcite grown under cave-analogue conditions" by C. C. Day and G. M. Henderson. *Geochimica et Cosmochimica Acta*, 85:383–387.

Edwards, R., Chen, J., and Wasserburg, G. (1987a). U-238-U-234-Th-230-Th-232 systematics and the precise measurement of time over the past 500,000 years. *Earth and Planetary Science Letters*, 81:81–3.

Edwards, R. L., Chen, J. H., Ku, T. L., and Wasserburg, G. J. (1987b). Precise timing

of the last interglacial period from mass spectrometric determination of thorium-230 in corals. *Science*, 236(4808):1547–1553.

Ellis, S. A., Cobb, K. M., Moerman, J. W., Partin, J. W., Bennett, A. L., Malang, J., Gerstner, H., and Tuen, A. A. (2020). Extended Cave Drip Water Time Series Captures the 2015 2016 El Niño in Northern Borneo. *Geophysical Research Letters*, 47(5):no.

Emile-Geay, J., Cobb, K. M., Carre, M., Braconnot, P., Leloup, J., Zhou, Y., Harrison, S. P., Corrège, T., McGregor, H. V., Collins, M., Driscoll, R., Elliot, M., Schneider, B., and Tudhope, A. (2016). Links between tropical Pacific seasonal, interannual and orbital variability during the Holocene. *Nature Geoscience*, 9(2):168–173.

Emile-Geay, J. and Tingley, M. (2016). Inferring climate variability from nonlinear proxies: Application to palaeo-ENSO studies. *Climate of the Past*, 12(1):31–50.

Fairchild, I. and Baker, A. (2012). *Speleothem science: from process to past environments (Vol. 3).*

Fairchild, I. J., Borsato, A., Tooth, A. F., Frisia, S., Hawkesworth, C. J., Huang, Y., McDermott, F., and Spiro, B. (2000). Controls on trace element (Sr-Mg) compositions of carbonate cave waters: Implications for speleothem climatic records. *Chemical Geology*, 166(3-4):255–269.

Fairchild, I. J. and Treble, P. C. (2009). Trace elements in speleothems as recorders of environmental change. *Quaternary Science Reviews*, 28(5-6):449–468.

Fantle, M. S. (2010). Evaluating the Ca isotope proxy. *American Journal of Science*, 310(3):194–230.

Fantle, M. S. and DePaolo, D. J. (2007). Ca isotopes in carbonate sediment and pore fluid from ODP Site 807A: The Ca2+(aq)-calcite equilibrium fractionation factor and calcite recrystallization rates in Pleistocene sediments. *Geochimica et Cosmochimica Acta*, 71(10):2524–2546.

Fantle, M. S. and Tipper, E. T. (2014). Calcium isotopes in the global biogeochemical Ca cycle: Implications for development of a Ca isotope proxy. *Earth-Science Reviews*,

129:148–177.

FETH, J. H. (1959). RE-EVALUATION OF THE SALT CHRONOLOGY OF SEVERAL GREAT BASIN LAKES: A DISCUSSION. *GSA Bulletin*, 70(5):637–640.

Frischknecht, M., Münnich, M., and Gruber, N. (2015). Remote versus local influence of ENSO on the California Current System. *Journal of Geophysical Research: Oceans*, pages 775–791.

Gabitov, R. I., Sadekov, A., and Leinweber, A. (2014). Crystal growth rate effect on Mg/Ca and Sr/Ca partitioning between calcite and fluid: An in situ approach. *Chemical Geology*, 367:70–82.

Gaillardet, J., Viers, J., and Dupre, B. (2003). Trace Elements in River Waters. *Treatise on Geochemistry*, 5:225–272.

Gascoyne, M. (1983). Trace-element partition coefficients in the calcite-water system and their paleoclimatic significance in cave studies. *Journal of Hydrology*, 61(1-3):213–222.

Gilbert, G. (1890). Lake Bonneville. Technical report, Washington, D.C.

Godsey, H. S., Oviatt, C. G., Miller, D. M., and Chan, M. A. (2011). Stratigraphy and chronology of offshore to nearshore deposits associated with the Provo shoreline, Pleistocene Lake Bonneville, Utah. *Palaeogeography, Palaeoclimatology, Palaeoecology*, 310(3-4):442–450.

Gordon, A. L. and Fine, R. A. (1996). Pathways of water between the Pacific and Indian oceans in the Indonesian seas. *Nature*, 379(6561):146–149.

Grothe, P. R., Cobb, K. M., Liguori, G., Di Lorenzo, E., Capotondi, A., Lu, Y., Cheng, H., Edwards, R. L., Southon, J. R., Santos, G. M., Deocampo, D. M., Lynch-Stieglitz, J., Chen, T., Sayani, H. R., Thompson, D. M., Conroy, J. L., Moore, A. L., Townsend, K., Hagos, M., O'Connor, G., and Toth, L. T. (2019). Enhanced El Niño Southern Oscillation Variability in Recent Decades. *Geophysical Research Letters*, 47(7):1–8.

Gussone, N., Böhm, F., Eisenhauer, A., Dietzel, M., Heuser, A., Teichert, B. M., Reitner, J., Wörheide, G., and Dullo, W. C. (2005). Calcium isotope fractionation in

calcite and aragonite. *Geochimica et Cosmochimica Acta*, 69(18):4485–4494.

Gussone, N., Eisenhauer, A., Heuser, A., Dietzel, M., Bock, B., Böhm, F., Spero, H. J., Lea, D. W., Bijma, J., and Nägler, T. F. (2003). Model for kinetic effects on calcium isotope fractionation (δ44Ca) in inorganic aragonite and cultured planktonic foraminifera. *Geochimica et Cosmochimica Acta*, 67(7):1375–1382.

Hart, W. S., Quade, J., Madsen, D. B., Kaufman, D. S., and Oviatt, C. G. (2004). The 87Sr/86Sr ratios of lacustrine carbonates and lake-level history of the Bonneville paleolake system. *Bulletin of the Geological Society of America*, 116(9-10):1107–1119.

Heinrich, H. (1988). Origin and consequences of cyclic ice rafting in the Northeast Atlantic Ocean during the past 130,000 years. *Quaternary Research*, 29(2):142–152.

Heuser, A. and Eisenhauer, A. (2008). The calcium isotope composition (δ44/40Ca) of NIST SRM 915b and NIST SRM 1486. *Geostandards and Geoanalytical Research*, 32(3):311–315.

Hostetler, S. and Benson, L. V. (1990). Paleoclimatic implications of the high stand of Lake Lahontan derived from models of evaporation and lake level. *Climate Dynamics*, 4(3):207–217.

Hua, Q., Barbetti, M., and Rakowski, A. Z. (2013). Atmospheric Radiocarbon for the Period 1950 2010. *Radiocarbon*, 55(4):2059–2072.

Hua, Q., McDonald, J., Redwood, D., Drysdale, R., Lee, S., Fallon, S., and Hellstrom, J. (2012). Robust chronological reconstruction for young speleothems using radiocarbon. *Quaternary Geochronology*, 14:67–80.

Huang, Y. and Fairchild, I. J. (2001). Partitioning of Sr2+ and Mg2+ into calcite under karst-analogue experimental conditions. *Geochimica et Cosmochimica Acta*, 65(1):47–62.

Jacobson, A. D. and Holmden, C. (2008). δ44Ca evolution in a carbonate aquifer and its bearing on the equilibrium isotope fractionation factor for calcite. *Earth and Planetary Science Letters*, 270(3-4):349–353.

Jamieson, R. A., Baldini, J. U., Brett, M. J., Taylor, J., Ridley, H. E., Ottley, C. J.,

Prufer, K. M., Wassenburg, J. A., Scholz, D., and Breitenbach, S. F. (2016). Intra- and inter-annual uranium concentration variability in a Belizean stalagmite controlled by prior aragonite precipitation: A new tool for reconstructing hydro-climate using aragonitic speleothems. *Geochimica et Cosmochimica Acta*, 190:332–346.

Jones, B. F., Naftz, D. L., Spencer, R. J., and Oviatt, C. G. (2009). Geochemical evolution of Great Salt Lake, Utah, USA. *Aquatic Geochemistry*, 15(1-2):95–121.

Jordan, S. F., Murphy, B. T., O'Reilly, S. S., Doyle, K. P., Williams, M. D., Grey, A., Lee, S., McCaul, M. V., and Kelleher, B. P. (2017). Mid-Holocene climate change and landscape formation in Ireland: Evidence from a geochemical investigation of a coastal peat bog. *Organic Geochemistry*, 109:67–76.

Kaplan, A., Cane, M. A., Kushnir, Y., Clement, A. C., Blumenthal, M. B., and Rajagopalan, B. (1998). Analyses of global sea surface temperature 1856-1991. *Journal of Geophysical Research: Oceans*, 103(C9):18567–18589.

Kim, S.-T. and O'Neil, J. R. (1997). Equilibrium and nonequilibrium oxygen isotope effects in synthetic carbonates. *Geochimica et Cosmochimica Acta*, 61(16):3461–3475.

Kim, S. T., O'Neil, J. R., Hillaire-Marcel, C., and Mucci, A. (2007). Oxygen isotope fractionation between synthetic aragonite and water: Influence of temperature and Mg2+concentration. *Geochimica et Cosmochimica Acta*, 71(19):4704–4715.

Koutavas, A. and Joanides, S. (2012). El Niño-Southern Oscillation extrema in the Holocene and Last Glacial Maximum. *Paleoceanography*, 27(4):1–15.

Kowalczk, A. J. and Froelich, P. N. (2010). Cave air ventilation and CO2 outgassing by radon-222 modeling: How fast do caves breathe? *Earth and Planetary Science Letters*, 289(1-2):209–219.

Lachniet, M. S., Denniston, R. F., Asmerom, Y., and Polyak, V. J. (2014). Orbital control of western North America atmospheric circulation and climate over two glacial cycles. *Nature Communications*, 5(May).

Laxen, D. P. and Harrison, R. M. (1981). Cleaning Methods for Polythene Containers Prior to the Determination of Trace Metals in Freshwater Samples. *Analytical*

Chemistry, 53(2):345–350.

Lechleitner, F. A., Day, C. C., Kost, O., Wilhelm, M., Haghipour, N., Henderson, G. M., and Stoll, H. M. (2021). Stalagmite carbon isotopes suggest deglacial increase in soil respiration in western Europe driven by temperature change. *Climate of the Past*, 17(5):1903–1918.

Lechleitner, F. A., Fohlmeister, J., McIntyre, C., Baldini, L. M., Jamieson, R. A., Hercman, H., Gasiorowski, M., Pawlak, J., Stefaniak, K., Socha, P., Eglinton, T. I., and Baldini, J. U. (2016). A novel approach for construction of radiocarbon-based chronologies for speleothems. *Quaternary Geochronology*, 35:54–66.

LeGrande, A. N. and Schmidt, G. A. (2006). Global gridded data set of the oxygen isotopic composition in seawater. *Geophysical Research Letters*, 33(12):1–5.

Leonard, N. D., Welsh, K. J., Lough, J. M., Feng, Y., Pandolfi, J. M., Clark, T. R., and Zhao, J. (2016). Evidence of reduced mid-Holocene ENSO variance on the Great Barrier Reef, Australia. *Paleoceanography*, 31(9):1248–1260.

Li, C.-H., Li, Y.-X., Zheng, Y.-F., Yu, S.-Y., Tang, L.-Y., Li, B.-B., and Cui, Q.-Y. (2018). A high-resolution pollen record from East China reveals large climate variability near the Northgrippian-Meghalayan boundary (around 4200 years ago) exerted societal influence. *Palaeogeography, Palaeoclimatology, Palaeoecology*, 512:156–165.

Liu, Z., Lu, Z., Wen, X., Otto-Bliesner, B. L., Timmermann, A., and Cobb, K. M. (2014). Evolution and forcing mechanisms of El Niño over the past 21,000 years. *Nature*, 515(7528):550–553.

Lora, J. M., Mitchell, J. L., Risi, C., and Tripati, A. E. (2017). North Pacific atmospheric rivers and their influence on western North America at the Last Glacial Maximum. *Geophysical Research Letters*, 44(2):1051–1059.

Lu, J., Zhang, H., Li, H., Sha, L., Zhao, J., Li, Y., Wang, J., Dong, X., Edwards, R. L., Qian, Z., and Cheng, H. (2021). A 120-year seasonally resolved speleothem record of precipitation seasonality from southeastern China. *Quaternary Science Reviews*, 264:107023.

Marchant, R. and Hooghiemstra, H. (2004). Rapid environmental change in African and South American tropics around 4000 years before present: A review. *Earth-Science Reviews*, 66(3-4):217–260.

McDermott, F., Atkinson, T. C., Fairchild, I. J., Baldini, L. M., and Mattey, D. P. (2011). A first evaluation of the spatial gradients in δ18O recorded by European Holocene speleothems. *Global and Planetary Change*, 79(3-4):275–287.

McGee, D., Moreno-Chamarro, E., Marshall, J., and Galbraith, E. D. (2018). Western U.S. lake expansions during Heinrich stadials linked to Pacific Hadley circulation. *Science Advances*, 4(11):1–11.

McGee, D., Quade, J., Edwards, R. L., Broecker, W. S., Cheng, H., Reiners, P. W., and Evenson, N. (2012). Lacustrine cave carbonates: Novel archives of paleohydrologic change in the Bonneville Basin (Utah, USA). *Earth and Planetary Science Letters*, 351-352:182–194.

McGregor, H. V., Fischer, M. J., Gagan, M. K., Fink, D., Phipps, S. J., Wong, H., and Woodroffe, C. D. (2013). A weak El Niño/Southern Oscillation with delayed seasonal growth around 4,300 years ago. *Nature Geoscience*, 6(11):949–953.

McManus, J., Francois, R., Gherardi, J.-M., Keigwin, L., and Brown-Leger, S. (2004). Collapse and rapid resumption of Atlantic meridional circualtion linked to deglacial climate changes. *Nature*, 428(April):834–837.

McPhaden, M. J., Zebiak, S. E., and Glantz, M. H. (2006). ENSO as an integrating concept in earth science. *Science*, 314(5806):1740–1745.

Menounos, B., Clague, J. J., Osborn, G., Luckman, B. H., Lakeman, T. R., and Minkus, R. (2008). Western Canadian glaciers advance in concert with climate change circa 4.2 ka. *Geophysical Research Letters*, 35(7):2–7.

Miller, D. M. (2016). The Provo Shoreline of Lake Bonneville. In *Lake Bonneville: A Scientific Update, Volume 20*, chapter 7, pages 127–144.

Miller, D. M., Oviatt, C. G., and Mcgeehin, J. P. (2013). Stratigraphy and chronology of Provo shoreline deposits and lake-level implications, Late Pleistocene Lake Bonneville,

eastern Great Basin, USA. *Boreas*, 42(2):342–361.

Moerman, J. W., Cobb, K. M., Adkins, J. F., Sodemann, H., Clark, B., and Tuen, A. A. (2013). Diurnal to interannual rainfall δ18O variations in northern Borneo driven by regional hydrology. *Earth and Planetary Science Letters*, 369-370:108–119.

Moerman, J. W., Cobb, K. M., Partin, J. W., Meckler, A. N., Carolin, S. A., Adkins, J. F., Lejau, S., Malang, J., Clark, B., and Tuen, A. A. (2014). Transformation of ENSO-related rainwater to dripwater δ18O variability by vadose water mixing. *Geophysical Research Letters*, 41(22):7907–7915.

Morse, J. W. and Bender, M. L. (1990). Partition coefficients in calcite: Examination of factors influencing the validity of experimental results and their application to natural systems. *Chemical Geology*, 82(C):265–277.

Moy, C., Seltzer, G., Rodbell, D., and Anderson, D. (2002). Variability of El Nino/Southern Oscillation activity at millennial timescales during the Holocene epoch. *Nature*, 420(November):162–165.

Munroe, J. S. and Laabs, B. J. (2013). Temporal correspondence between pluvial lake highstands in the southwestern US and Heinrich Event 1. *Journal of Quaternary Science*, 28(1):49–58.

Nielsen, L. C. and DePaolo, D. J. (2013). Ca isotope fractionation in a high-alkalinity lake system: Mono Lake, California. *Geochimica et Cosmochimica Acta*, 118:276–294.

Ohlendorf, C., Fey, M., Massaferro, J., Haberzettl, T., Laprida, C., Lücke, A., Maidana, N., Mayr, C., Oehlerich, M., Ramón Mercau, J., Wille, M., Corbella, H., St-Onge, G., Schäbitz, F., and Zolitschka, B. (2014). Late Holocene hydrology inferred from lacustrine sediments of Laguna ChaÂŽltel (southeastern Argentina). *Palaeogeography, Palaeoclimatology, Palaeoecology*, 411:229–248.

Oster, J., Warken, S., Sekhon, N., Arienzo, M., and Lachniet, M. (2019). Speleothem Paleoclimatology for the Caribbean, Central America, and North America. *Quaternary*, 2(1):5.

Oster, J. L., Ibarra, D. E., Winnick, M. J., and Maher, K. (2015a). Steering of westerly

storms over western North America at the Last Glacial Maximum. *Nature Geoscience*, 8(3):201–205.

Oster, J. L., Montañez, I. P., Santare, L. R., Sharp, W. D., Wong, C., and Cooper, K. M. (2015b). Stalagmite records of hydroclimate in central California during termination 1. *Quaternary Science Reviews*, 127:199–214.

Oviatt, C. G. (1997). Lake Bonneville fluctuations and global climate change. *Geology*, 25(2):155–158.

Oviatt, C. G. (2015). Chronology of Lake Bonneville, 30,000 to 10,000 yr B.P. *Quaternary Science Reviews*, 110:166–171.

Oviatt, C. G., Currey, D. R., and Sack, D. (1992). Radiocarbon chronology of Lake Bonneville, Eastern Great Basin, USA. *Palaeogeography, Palaeoclimatology, Palaeoecology*, 99(3-4):225–241.

Oviatt, C. G., Habiger, G. D., and Hay, J. E. (1994). Variation in the composition of Lake Bonneville marl: a potential key to lake-level fluctuations and paleoclimate. *Journal of Paleolimnology*, 11(1):19–30.

Owen, R. A. (2017). *Development and Application of speleothem-based proxies for Past Climate Change*. PhD thesis.

Owen, R. A., Day, C. C., Hu, C. Y., Liu, Y. H., Pointing, M. D., Blättler, C. L., and Henderson, G. M. (2016). Calcium isotopes in caves as a proxy for aridity: Modern calibration and application to the 8.2 kyr event. *Earth and Planetary Science Letters*, 443:129–138.

Parkhurst, D. L. and Appelo, C. A. J. (1999). User's guide to PHREEQC (Version 2): A computer program for speciation, batch-reaction, one-dimensional transport, and inverse geochemical calculations. Technical report.

Parkhurst, D. L. and Appelo, C. A. J. (2013). Description of input and examples for PHREEQC version 3: a computer program for speciation, batch-reaction, one-dimensional transport, and inverse geochemical calculations. Technical report, Reston, VA.

Partin, J. W. (2008). *Stalagmite reconstructions of western tropical pacific climate from the last glacial maximum to present*. PhD thesis.

Partin, J. W., Cobb, K. M., Adkins, J. F., Clark, B., and Fernandez, D. P. (2007a). Millennial-scale trends in west Pacific warm pool hydrology since the Last Glacial Maximum. *Nature*, 449(7161):452–455.

Partin, J. W., Cobb, K. M., Adkins, J. F., Clark, B., and Fernandez, D. P. (2007b). Millennial-scale trends in west Pacific warm pool hydrology since the Last Glacial Maximum. *Nature*, 449(7161):452–455.

Partin, J. W., Cobb, K. M., Adkins, J. F., Tuen, A. A., and Clark, B. (2013). Trace metal and carbon isotopic variations in cave dripwater and stalagmite geochemistry from northern Borneo. *Geochemistry, Geophysics, Geosystems*, 14(9):3567–3585.

Patrickson, S. J., Sack, D., Brunelle, A. R., and Moser, K. A. (2010). Late Pleistocene to early Holocene lake level and paleoclimate insights from Stansbury Island, Bonneville basin, Utah. *Quaternary Research*, 73(2):237–246.

Pausata, F. S., Zhang, Q., Muschitiello, F., Lu, Z., Chafik, L., Niedermeyer, E. M., Stager, J. C., Cobb, K. M., and Liu, Z. (2017). Greening of the Sahara suppressed ENSO activity during the mid-Holocene. *Nature Communications*, 8(May).

Pedro, J., Andersson, C., Vettoretti, G., Voelker, A., Waelbroeck, C., Dokken, T., Jensen, M., Rasmussen, S., Sessford, E., Jochum, M., and Nisancioglu, K. (2022). Dansgaard-Oeschger and Heinrich event temperature anomalies in the North Atlantic set by sea ice, frontal position and thermocline structure. *Quaternary Science Reviews*, 289:107599.

Petit, J. R., Jouzel, J., Raynaud, D., Barkov, N. I., Barnola, J.-M., Basile, I., Bender, M., Chappellaz, J., Davisk, M., Delaygue, G., Delmotte, M., Kotlyakov, V. M., Legrand, M., Lipenkov, V. Y., Lorius, C., Pépin, L., Ritz, C., Saltzmank, E., and Stievenard, M. (1999). Climate and atmospheric history of the past 420,000 years from the Vostok ice core, Antarctica The recent completion of drilling at Vostok station in East. *Nature*, 399:429–436.

Railsback, L. B., Liang, F., Brook, G. A., Voarintsoa, N. R. G., Sletten, H. R., Marais, E., Hardt, B., Cheng, H., and Edwards, R. L. (2018). The timing, two-pulsed nature, and variable climatic expression of the 4.2 ka event: A review and new high-resolution stalagmite data from Namibia. *Quaternary Science Reviews*, 186:78–90.

Ralph, F. M. and Dettinger, M. D. (2011). Storms, floods, and the science of atmospheric rivers. *Eos*, 92(32):265–266.

Ramsey, C. B. (2008). Deposition models for chronological records. *Quaternary Science Reviews*, 27(1-2):42–60.

Ramsey, C. B. (2009). Bayesian analysis of radiocarbon dates. *Radiocarbon*, 51(1):337–360.

Ramsey, C. B. and Lee, S. (2013). Recent and Planned Developments of the Program OxCal. *Radiocarbon*, 55(2):720–730.

Rasmussen, S. O., Andersen, K. K., Svensson, A. M., Steffensen, J. P., Vinther, B. M., Clausen, H. B., Siggaard-Andersen, M. L., Johnsen, S. J., Larsen, L. B., Dahl-Jensen, D., Bigler, M., Röthlisberger, R., Fischer, H., Goto-Azuma, K., Hansson, M. E., and Ruth, U. (2006). A new Greenland ice core chronology for the last glacial termination. *Journal of Geophysical Research Atmospheres*, 111(6):1–16.

Redmond, K. T. and Koch, R. W. (1991). Surface Climate and Stream flow Variability in the Western United States and their Relationship to Large-Scale Circulation Indicies. *Water Resources Research*, 27(9):2381–2399.

Renforth, P. and Henderson, G. (2017). Assessing ocean alkalinity for carbon sequestration. *Reviews of Geophysics*, 55(3):636–674.

Renssen, H. (2022). Climate model experiments on the 4.2 ka event: The impact of tropical sea-surface temperature anomalies and desertification. *Holocene*, 32(5):378–389.

Reynard, L. M., Day, C. C., and Henderson, G. M. (2011). Large fractionation of calcium isotopes during cave-analogue calcium carbonate growth. *Geochimica et Cosmochimica Acta*, 75(13):3726–3740.

Richards, D. A. and Dorale, J. A. (2003). Uranium-series Chronology and Environmental Applications of Speleothems. *Reviews in Mineralogy and Geochemistry*, 52(1):407–460.

Riechelmann, S., Schröder-Ritzrau, A., Wassenburg, J. A., Schreuer, J., Richter, D. K., Riechelmann, D. F. C., Terente, M., Constantin, S., Mangini, A., and Immenhauser, A. (2014). Physicochemical characteristics of drip waters: Influence on mineralogy and crystal morphology of recent cave carbonate precipitates. *Geochimica et Cosmochimica Acta*, 145:13–29.

Roland, T. P., Caseldine, C. J., Charman, D. J., Turney, C. S., and Amesbury, M. J. (2014). Was there a '4.2ka event' in Great Britain and Ireland? Evidence from the peatland record. *Quaternary Science Reviews*, 83:11–27.

Rosenberry, D. O., Lewandowski, J., Meinikmann, K., and Nützmann, G. (2015). Groundwater - the disregarded component in lake water and nutrient budgets. Part 1: Effects of groundwater on hydrology. *Hydrological Processes*, 29(13):2895–2921.

Ruan, J., Kherbouche, F., Genty, D., Blamart, D., Cheng, H., Dewilde, F., Hachi, S., Edwards, L. R., Régnier, E., and Michelot, J. L. (2015). Evidence of a prolonged drought ca. 4200 yr BP correlated with prehistoric settlement abandonment from the Gueldaman GLD1 Cave, N-Algeria. *Climate of the Past Discussions*, 11(4):2729–2762.

Santi, L., Arnold, A., Ibarra, D. E., Whicker, C., Mering, J., and Oviatt, C. G. (2019). Lake level fluctuations in the Northern Great Basin for the last 25 , 000 years. (April).

Santos, G. M., Southon, J. R., Griffin, S., Beaupre, S. R., and Druffel, E. R. (2007). Ultra small-mass AMS 14C sample preparation and analyses at KCCAMS/UCI Facility. *Nuclear Instruments and Methods in Physics Research, Section B: Beam Interactions with Materials and Atoms*, 259(1):293–302.

Sarachik, E. S. and Cane, M. A. (2010). *The El Nino-Southern oscillation phenomenon [electronic resource]*. Ebook central. Cambridge University Press, Cambridge.

Scheff, J. and Frierson, D. M. (2012). Robust future precipitation declines in CMIP5

largely reflect the poleward expansion of model subtropical dry zones. *Geophysical Research Letters*, 39(17):1–6.

Schmidt, G. A. (2010). Enhancing the relevance of palaeoclimate model/ data comparisons for assessments of future climate change. *Journal of Quaternary Science*, 25(1):79–87.

Scholz, D., Hoffmann, D. L., Hellstrom, J., and Bronk Ramsey, C. (2012). A comparison of different methods for speleothem age modelling. *Quaternary Geochronology*, 14:94–104.

Seager, R. and Vecchi, G. A. (2010). Greenhouse warming and the 21st century hydroclimate of southwestern North America. *Proceedings of the National Academy of Sciences*, 107(50):21277–21282.

Spencer, R. J., Baedecker, M. J., Eugster, H. P., Forester, R. M., Goldhaber, M. B., Jones, B. F., Kelts, K., Mckenzie, J., Madsen, D. B., Rettig, S. L., Rubin, M., and Bowser, C. J. (1984). Great Salt Lake, and precursors, Utah: The last 30,000 years. *Contributions to Mineralogy and Petrology*, 86(4):321–334.

Spencer, R. J., Eugster, H. P., and Jones, B. F. (1985). Geochemistry of great Salt Lake, Utah II: Pleistocene-Holocene evolution. *Geochimica et Cosmochimica Acta*, 49(3):739–747.

Stan, C., Straus, D. M., Frederiksen, J. S., Lin, H., Maloney, E. D., and Schumacher, C. (2017). Review of Tropical-Extratropical Teleconnections on Intraseasonal Time Scales. *Reviews of Geophysics*, 55(4):902–937.

Stanford, J. D., Rohling, E. J., Bacon, S., Roberts, A. P., Grousset, F. E., and Bolshaw, M. (2011). A new concept for the paleoceanographic evolution of Heinrich event 1 in the North Atlantic. *Quaternary Science Reviews*, 30(9-10):1047–1066.

Stanford, J. D., Rohling, E. J., Hunter, S. E., Roberts, A. P., Rasmussen, S. O., Bard, E., Mcmanus, J., and Fairbanks, R. G. (2006). Timing of meltwater pulse 1a and climate responses to meltwater injections. *Paleoceanography*, 21:1–9.

Steuber, T. and Buhl, D. (2006). Calcium-isotope fractionation in selected modern and

ancient marine carbonates. *Geochimica et Cosmochimica Acta*, 70(22):5507–5521.

Stuiver, M. and Polach, H. A. (1977). Discussion Reporting of 14C Data. *Radiocarbon*, 19(3):355–363.

Talbot, M. R. (1990). A review of the palaeohydrological interpretation of carbon and oxygen isotopic ratios in primary lacustrine carbonates. *Chemical Geology: Isotope Geoscience Section*, 80(4):261–279.

Tang, J., Dietzel, M., Böhm, F., Köhler, S. J., and Eisenhauer, A. (2008). Sr2+/Ca2+ and 44Ca/40Ca fractionation during inorganic calcite formation: II. Ca isotopes. *Geochimica et Cosmochimica Acta*, 72(15):3733–3745.

Thompson, D. M., Conroy, J. L., Collins, A., Hlohowskyj, S. R., Overpeck, J. T., Riedinger-Whitmore, M., Cole, J. E., Bush, M. B., Whitney, H., Corley, T. L., and Kannan, M. S. (2017). Tropical Pacific climate variability over the last 6000Â years as recorded in Bainbridge Crater Lake, Galápagos. *Paleoceanography*, 32(8):903–922.

Tipper, E. T., Gaillardet, J., Galy, A., Louvat, P., Bickle, M. J., and Capmas, F. (2010). Calcium isotope ratios in the world's largest rivers: A constraint on the maximum imbalance of oceanic calcium fluxes. *Global Biogeochemical Cycles*, 24(3).

Torrence C. and Compo G. (1998). A practical guide to wavelet analysis. *Bulletin of the American Meteorological Society*, 79 (1):61—-78.

Toth, L. T. and Aronson, R. B. (2019). The 4.2 ka event, ENSO, and coral reef development. *Climate of the Past*, 15(1):105–119.

Trachsel, M. and Telford, R. J. (2017). All age depth models are wrong, but are getting better. *Holocene*, 27(6):860–869.

Treble, P. C., Baker, A., Abram, N. J., Hellstrom, J. C., Crawford, J., Gagan, M. K., Borsato, A., Griffiths, A. D., Bajo, P., Markowska, M., Priestley, S. C., Hankin, S., and Paterson, D. (2022). Ubiquitous karst hydrological control on speleothem oxygen isotope variability in a global study. *Communications Earth & Environment*, 3(1).

Trenberth, K. E. (1997). The Definition of El Niño. *Bulletin of the American Meteorological Society*, 78(12):2771–2777.

Trouet, V. and Van Oldenborgh, G. J. (2013). KNMI climate explorer: A web-based research tool for high-resolution paleoclimatology. *Tree-Ring Research*, 69(1):3–13.

Tudhope, A., Chilcott, C., McCulloch, M., Cook, E., Chappell, J., Ellam, R., Lea, D., Lough, J., and Graham, S. (2001). Variability in the El Niño-Southern Oscillation through a glacial-interglacial cycle. *Science*, 291(5508):1511–1517.

Vaks, A., Gutareva, O. S., Breitenbach, S. F., Avirmed, E., Mason, A. J., Thomas, A. L., Osinzev, A. V., Kononov, A. M., and Henderson, G. M. (2013). Speleothems reveal 500,000-year history of Siberian permafrost. *Science*, 340(6129):183–186.

Vecchi, G. A. and Wittenberg, A. T. (2010). El Niño and our future climate: Where do we stand? *Wiley Interdisciplinary Reviews: Climate Change*, 1(2):260–270.

Vennin, E., Bouton, A., Bourillot, R., Pace, A., Roche, A., Brayard, A., Thomazo, C., Virgone, A., Gaucher, E. C., Desaubliaux, G., and Visscher, P. T. (2019). The lacustrine microbial carbonate factory of the successive Lake Bonneville and Great Salt Lake, Utah, USA. *Sedimentology*, 66(1):165–204.

Vergara, O., Dewitte, B., Ramos, M., and Pizarro, O. (2017). Vertical energy flux at ENSO time scales in the subthermocline of the Southeastern Pacific. *Journal of Geophysical Research: Oceans*, 122(5423):1–22.

Verheyden, S., Keppens, E., Fairchild, I. J., McDermott, F., and Weis, D. (2000). Mg, Sr and Sr isotope geochemistry of a Belgian Holocene speleothem: Implications for paleoclimate reconstructions. *Chemical Geology*, 169(1-2):131–144.

Waltham, T. and Despain, J. (2012). Mulu caves, Malaysia. In *Encyclopedia of Caves (2nd Edition)*, pages 531–538.

Wang, J., Song, C., Reager, J. T., Yao, F., Famiglietti, J. S., Sheng, Y., MacDonald, G. M., Brun, F., Schmied, H. M., Marston, R. A., and Wada, Y. (2018). Recent global decline in endorheic basin water storages. *Nature Geoscience*, 11(12):926–932.

Wassenburg, J. A., Scholz, D., Jochum, K. P., Cheng, H., Oster, J., Immenhauser, A., Richter, D. K., Häger, T., Jamieson, R. A., Baldini, J. U., Hoffmann, D., and Breitenbach, S. F. (2016). Determination of aragonite trace element distribution co-

efficients from speleothem calcite aragonite transitions. *Geochimica et Cosmochimica Acta*, 190:347–367.

Weber, M., Scholz, D., Schröder-Ritzrau, A., Deininger, M., Spötl, C., Lugli, F., Mertz-Kraus, R., Jochum, K. P., Fohlmeister, J., Stumpf, C. F., and Riechelmann, D. F. (2018). Evidence of warm and humid interstadials in central Europe during early MIS 3 revealed by a multi-proxy speleothem record. *Quaternary Science Reviews*, 200:276–286.

Wittenberg, A. T. (2009). Are historical records sufficient to constrain ENSO simulations? *Geophysical Research Letters*, 36(12):1–5.

Woolway, R. I. and Merchant, C. J. (2019). Worldwide alteration of lake mixing regimes in response to climate change. *Nature Geoscience*, 12(4):271–276.

Yeh, S. W., Cai, W., Min, S. K., McPhaden, M. J., Dommenget, D., Dewitte, B., Collins, M., Ashok, K., An, S. I., Yim, B. Y., and Kug, J. S. (2018). ENSO Atmospheric Teleconnections and Their Response to Greenhouse Gas Forcing. *Reviews of Geophysics*, 56(1):185–206.

Zhu, Y. and Newell, R. E. (1998). A proposed algorithm for moisture fluxes from atmospheric rivers. *Monthly Weather Review*, 126(3):725–735.

Ziemen, F. A., Kapsch, M. L., Klockmann, M., and Mikolajewicz, U. (2019). Heinrich events show two-stage climate response in transient glacial simulations. *Climate of the Past*, 15(1):153–168.

Appendix A

Chapter 2 Appendix

A.1 LakeCalc Matlab script

```
%% LakeCalc

%% Model INPUTS

%Lake Starting Characteristics
Lake_Volume_Start      =  (0.3*10^15); %Lake Volume at start of
    run liters
Lake_Ca_Conc_Start     =  [1.348 * 10^-3]; % Lake Ca conc at
    start
Lake_44_42_Ca_Start    =  0.38; % Calcium isotope ratio (per
    mille)
Lake_MgCa_Ratio_Start  =  0.50; % Mass Ratio of Mg/Ca  (gg-1)
Lake_UCa_Ratio_Start   =  [6.90*10^-6] ; % Mass Ratio of U/Ca
    (gg-1)
dH2O                   =  [2.2222E+11]; % change in lake volume
    per timestep

% Inflows

%River
River_Ca_Input         =  [1.348 * 10^-3]; % Conc of Calcium (
    moles/litre)
River_44_42_Ca         =  [0.38];          % River calcium
    isotope ratio (per mille)
River_MgCa_Ratio       =  [0.50];          % Mass ratio of Mg/Ca
    (gg-1)
River_UCa_Ratio        =  [6.90*10^-6];    % Mass ratio of U/Ca
```

```
    (gg-1)

Riverine_Input      =   [0, River_Ca_Input   , River_44_42_Ca ,
    ...
    River_MgCa_Ratio,  River_MgCa_Ratio* (River_Ca_Input
        *40.078)/24.305  ...
    , River_UCa_Ratio, River_UCa_Ratio* (River_Ca_Input
        *40.078)/238.0 ];


%Hyrdothermal
Hydro_Ca_Input      =   [0];            % Input of Calcium (
    moles/litre)
Hydro_44_42_Ca      =   [0];            % Calcium isotope
    ratio (per mille)
Hydro_MgCa_Ratio    =   [0];            % Mass Ratio of Mg/Ca
    (gg-1)
Hydro_UCa_Ratio     =   [0];            % Mass Ratio of U/Ca (
    gg-1)

Hydrothermal_Input  =   [0, Hydro_Ca_Input   , Hydro_44_42_Ca ,
    ...
    Hydro_MgCa_Ratio,  Hydro_MgCa_Ratio* (Hydro_Ca_Input
        *40.078)/24.305  ,...
    Hydro_UCa_Ratio, Hydro_UCa_Ratio* (Hydro_Ca_Input*40.078)
        /238.0 ];


```

```
37 %Rain
38 Rain_Ca_Input        =    [0];              % Conc of Calcium (
       moles/litre)
39 Rain_44_42_Ca        =    [0];              % Calcium isotope
       ratio in rain (per mille)
40 Rain_MgCa_Ratio      =    [0];              % Mass Ratio of Mg/Ca
       in rain  gg-1
41 Rain_UCa_Ratio       =    [0];              % Mass Ratio of Mg/Ca
       in rain  gg-1
42
43 Rain_Input           =    [0, Rain_Ca_Input   , Rain_44_42_Ca ,
       ...
44      Rain_MgCa_Ratio,  Rain_MgCa_Ratio* (Rain_Ca_Input*40.078)
           /24.305 , ...
45      Rain_UCa_Ratio, Rain_UCa_Ratio* (Rain_Ca_Input*40.078)
           /238.0 ];
46
47 % Outflows
48
49 %Evaporation
50 Evap_Ca_Output        =    [0];              % Conc of Calcium (
       moles/litre)
51 Evap_44_42_Ca        =    [0];              % Calcium isotope
       ratio in rain (per mille)
52 Evap_MgCa_Ratio      =    [0];              % Mass Ratio of Mg/Ca
       (gg-1)
53 Evap_UCa_Ratio       =    [0];              % Mass Ratio of U/Ca (
       gg-1)
```

```
54
55 Evaporation          =    [0, Evap_Ca_Output   , Evap_44_42_Ca  ,
       ...
56      Evap_MgCa_Ratio,  Evap_MgCa_Ratio* (Evap_Ca_Output*40.078)
           /24.305, ...
57      Evap_UCa_Ratio, Evap_UCa_Ratio* (Evap_Ca_Output*40.078)
           /238.0 ];
58
59
60
61 %Model Values
62
63 Steps                    =            726;
64 % Number of years model is run for
65
66 Alpha                    =            [0.99937, 0.99914];
67 % Fractionation factor between carbonate and solution for
       44/42 Ca
68 %[Calcite, Aragonite]
69 Partition_Coefficent_Mg =             [0.0073, 9.7*10^-5];
70 % D(Mg)carbonate-solution  [calcite,aragonite]
71 Partition_Coefficent_U  =             [ 0.09622,  3.74];
72 % D(U)carbonate-solution  [calcite,aragonite]
73
74 Polymorph                =            2;
75 % Polymoprph of CaCO3 precipitated
76 %(calcite = 1, Aragonite = 2)
77 Switch                   =            4303;
```

```
78 % Timestep when lake changes from aragonite to calcite
       precipitation
79
80 Max_Lake_Volume          =          [6.5 * 10^15, 3.0*10^15];
81 % Max lake volume before and after basin collapse,
82 %volume above this will outflow as riverine output
83
84 bc                        =           1000;
85 % Timing of basin collapse
86
87 Lake_Carb_Precip          =          [1.25*10^-3, 1.53*10^-3];
88 % Saturation limit of Ca (moles/litre) for calcite and
       aragonite
89
90 % Volume to Surface area
91 % Specifies the basin dimensions, allowing volume and surface
       area to be
92 % related
93
94 Vo  =   [0.3, 1.1, 3.0, 6.5]*10^15;
95 % Volume for the modern gsl, stansbury, provo, bonneville
       shorelines
96 Sa  =   [4.2, 24.5, 33.1, 41.2]*10^9;
97 % Surface Area for the modern gsl, stansbury, provo,
       bonneville shorelines
98
99 %SA to Rain Input / Total water influx; this sections does not
       include the
```

```
100 %prove shore
101
102 Sa2      =    [4.2, 24.5, 41.2]*10^9;
103 % Surface area modern gsl, stansbury and bonneville
104 Per      =    [33 80 90.9];
105 % Percentage rain input in modern gsl, stansbury and
        bonneville
106 I        =    [0.2, 1.3, 2.2]*10^13;
107 % Total water input in post regression lake, stansbury and
        bonneville
108
109 %% HOLDING VECTORS
110
111 Lake                    =    zeros(Steps, 5);
112 % [Volume (litres), Conc (Ca moles per litre), ...
113 %  Ca sotopic ratio (per mille), Mg (moles/litre), U (moles/
        litre)]
114 Carbonate               =    zeros(Steps, 4);
115 % [Ca moles, Ca isotopes (per mille), Mg/ca (gg-1), U/ca (gg
        -1)]
116 River_Outflow          =    zeros(Steps, 5);
117 % [H2O, Ca, Ca isotopes (per mille), Mg conc (moles/litre), U
        conc conc (moles/litre)]
118 f                      =    zeros(1, Steps);
119 dt                     =    1;                  % Years per
        time step
120
121 ma                     =          1;
```

```
122 % Equals max volume of lake 1 = before basin collapse,
123 %2 = after basin collapse
124
125
126 Lake_Mg_Conc_Start        = ((Lake_Ca_Conc_Start(1)*40.078)*...
127     Lake_MgCa_Ratio_Start)/24.305; % Lake Mg Conc Start (moles
        /litre)
128 Lake_U_Conc_Start         = ((Lake_Ca_Conc_Start(1)*40.078)*...
129     Lake_UCa_Ratio_Start)/238.0;    % Lake Mg Conc Start (moles
        /litre)
130 %% MATHS
131
132 %Lake Starting conditions
133 Lake(1,1)    =    Lake_Volume_Start;
134 Lake(1,2)    =    Lake_Ca_Conc_Start(1);
135 Lake(1,3)    =    Lake_44_42_Ca_Start;
136 Lake(1,4)    =    Lake_Mg_Conc_Start(1);
137 Lake(1,5)    =    Lake_U_Conc_Start(1);
138
139 Lake_Starting_Surface_Area  = interp1(Vo,Sa,Lake_Volume_Start)
    ;
140 % Calculates the starting SA of the lake from its volume,
141
142 Total_H_Influx                = interp1(Sa2, I,
    Lake_Starting_Surface_Area);
143 % Calculates the starting inflow volume from SA
144 per_ri_in                     = 1-(interp1(Sa2, Per,
    Lake_Starting_Surface_Area))/100;
```

```
145 % Calculates the estimated starting proportion of riverine
      inflow riverine input
146 Riverine_Input(1)            = per_ri_in * Total_H_Influx;
147 % Calculates the estimated starting riverine influx
148 Rain_Input(1)                = (1-per_ri_in) * Total_H_Influx;
149 % Calculates the estimated starting riverine influx
150
151
152
153 %RiverOutflow Starting
154 River_Outflow(1,1)  =   Lake(1,1) - Max_Lake_Volume(ma);
155 % River outflow = volume of lake - volume of basin
156 River_Outflow(1,2)  =   Lake(1,2);
157 % River outflow = lake composition
158 River_Outflow(1,3)  =   Lake(1,3);
159 River_Outflow(1,4)  =   Lake(1,4);
160 River_Outflow(1,5)  =    Lake(1,5);
161
162 if River_Outflow(1,1) < 0
163     % If modelled lake volume is less than basin volume no
        outflow
164     River_Outflow(1,1) = 0;
165 end
166
167
168
169 %Ca FLuxes
170 F_Ca_River_In       =   Riverine_Input(1) * Riverine_Input(2);
```

```
171 % Volume of water input times Ca concentration of input
172 F_Ca_Hydrothermal    =    Hydrothermal_Input (1) *
        Hydrothermal_Input (2);
173 F_Ca_Rain           =    Rain_Input(1) * Rain_Input(2);
174 F_Ca_Evaporation     =    Evaporation(1)*Evaporation(2);
175
176 %Mg Fluxes
177 F_Mg_River_In       =    Riverine_Input(1)*Riverine_Input(5);
178 F_Mg_Rain_In        =    Rain_Input(1) * Rain_Input(5);
179 F_Mg_Hydrothermal   =    Rain_Input(1) * Rain_Input(5);
180 F_Mg_Evaporation    =    Evaporation(1)*Evaporation(5);
181
182 % U Fluxes
183 F_U_River_In        =    Riverine_Input(1)*Riverine_Input(7);
184 F_U_Rain_In         =    Rain_Input(1) * Rain_Input(7);
185 F_U_Hydrothermal    =    Rain_Input(1) * Rain_Input(7);
186 F_U_Evaporation     =    Evaporation(1)*Evaporation(7);
187 Total_U_Precipitated_C = [];
188 F_U_River_In_c = [];
189 Total_U_Lake_c = [];
190
191 River_Input_C = [];
192 Rain_Input_C = [];
193 Evaporation_C = [];
194 for      i    =    linspace(1, Steps, Steps)
195
196         if Switch    ==  i %Switch from arg to calc
197             if Polymorph ==  1
```

```
198                         Polymorph = 2;
199                 elseif Polymorph ==  2
200                         Polymorph = 1;
201                 end
202             end
203
204             if bc == i %basin collapse
205                 ma = 2;     %Switch to smaller confining basin
206             end
207
208 Lake_Surface_Area    =    interp1(Vo, Sa, Lake(i,1));
209 % Lake surface area at time i, estimated from lake volume
210
211 Total_H_Influx       =    interp1(Sa2, I, Lake_Surface_Area);
212 % Riverine input estimated from lake surface area
213 per_ri_in            =    1-(interp1(Sa2, Per, Lake_Surface_Area
        ))/100;
214 % Percentage riverine input estimated
215 Riverine_Input(1)    =    per_ri_in * Total_H_Influx;
216 % Volume of riverine input estimated from lake surface area
217 Rain_Input(1)        =    (1-per_ri_in) * Total_H_Influx;
218 % Volume of rain input estimated from lake surface area
219
220
221
222
223
224
```

```
225 Evaporation(1)        =    Total_H_Influx - dH2O;
226 % Volume of evaporation, specified from input volume
227 %and change in lake volume per year
228
229 River_Input_C = [River_Input_C, Riverine_Input(1)];
230 Rain_Input_C = [Rain_Input_C, Rain_Input(1)];
231 Evaporation_C = [Evaporation_C, Evaporation(1)];
232
233 %Ca FLuxes
234 F_Ca_River_In         =    Riverine_Input(1) * Riverine_Input(2);
235 % Moles per year (volume of infow per year * concentration
      moles per litre)
236 F_Ca_Hydrothermal     =    Hydrothermal_Input (1) *
      Hydrothermal_Input (2);
237 F_Ca_Rain             =    Rain_Input(1) * Rain_Input(2);
238 F_Ca_Evaporation      =    Evaporation(1)*Evaporation(2);
239
240 %Mg Fluxes
241 F_Mg_River_In         =    Riverine_Input(1)*Riverine_Input(5);
242 % Moles per year (volume of infow per year * concentration
      moles per litre)
243 F_Mg_Hydrothermal     =    Hydrothermal_Input (1) *
      Hydrothermal_Input (5);
244 F_Mg_Rain_In          =    Rain_Input(1) * Rain_Input(5);
245 F_Mg_Evaporation      =    Evaporation(1)*Evaporation(5);
246
247 % U Fluxes
248 F_U_River_In          =    Riverine_Input(1)*Riverine_Input(7);
```

```
249 % Moles per year (volume of infow per year * concentration
      moles per litre)
250 F_U_River_In_c = [F_U_River_In_c, F_U_River_In];
251 F_U_Hydrothermal    =    Hydrothermal_Input (1) *
      Hydrothermal_Input (7);
252 F_U_Rain_In          =    Rain_Input(1) * Rain_Input(7);
253 F_U_Evaporation     =    Evaporation(1)*Evaporation(7);
254
255
256
257 River_Outflow(i,2) = Lake(i,2);
258 % River outflow Ca concentration (moles/litre)
259 River_Outflow(i,3) = Lake(i,3);
260 % River Ca 44 42 composition (per mille)
261 River_Outflow(i,4) = Lake(i,4);
262 % River outflow Mg concentration (moles/litre)
263 River_Outflow(i,5) = Lake(i,5);
264 % River outflow U concentration (moles/litre)
265
266
267
268 Total_Ca_Lake = Lake(i,2)*Lake(i,1); %moles
269 Total_Mg_Lake = Lake(i,1)*Lake(i,4); %moles
270 Total_U_Lake = Lake(i,1)*Lake(i,5);  %moles
271
272 % Water Mass Balance Equation
273
274     % Calculate new lake level for step 1+1
```

```
275     Lake(i+1,1)          =          Lake(i,1) + (Riverine_Input(1)
            + ...
276          Hydrothermal_Input(1) + Rain_Input(1) - Evaporation(1)
                )*dt;
277     % Max Lake Volume Calculated
278     River_Outflow(i,1)   =          Lake(i+1,1) - Max_Lake_Volume(
            ma);
279     % allows lake to be limited by basin size
280     % River outflow equals lake volume minus basin volume
281     if River_Outflow(i,1) < 0
282          River_Outflow(i,1) = 0;
283     end
284     %If max lake volume < basin volume there is no outflow
285     Lake(i+1,1)          =          Lake(i+1,1) - River_Outflow(i
            ,1);
286
287
288 % Calcium Mass balance equation
289
290     %Calculate New Lake Concentration after river, rain and
            hydrothermal
291     %input and evaporation and riverine outflow outputs
292      Lake_New_Conc_Ca    =          (Total_Ca_Lake + (
            F_Ca_River_In + ...
293           F_Ca_Rain + F_Ca_Hydrothermal - River_Outflow(i,1)*
                ...
294           River_Outflow(i,2) - F_Ca_Evaporation)*dt)/Lake(i
                +1,1);
```

```
295
296
297     if Lake_New_Conc_Ca > Lake_Carb_Precip(Polymorph)
298         Carbonate(i,1)    =    Lake_New_Conc_Ca*Lake(i+1,1)-Lake(
                i+1,1)...
299             * Lake_Carb_Precip(Polymorph);
300         %Moles Ca precipitated to return lake to saturation
                level
301         Lake(i+1, 2)      = Lake_Carb_Precip(Polymorph);
302         %Lake Conc returns to saturation level
303     else
304         Carbonate(i,1) = 0;
305         %Step happens if lake becomes undersaturated w.r.t
                CaCO3
306         Lake(i+1,2) = Lake_New_Conc_Ca;
307     end
308
309
310 % Mg mass balance
311
312 Carbonate(i,3)          =    ((Lake(i,4)*24.305)/(Lake(i,2)
        *40.078)...
313      *Partition_Coefficent_Mg(Polymorph)); % Carbonate Mg/Ca
            ratio
314 Total_Mg_Precipitated  =    ((Carbonate(i,1)*40.078)*Carbonate
        (i,3))/24.305;
315 % Moles mg precipitates, assuming one mole ca precipitated
        per CaCO3
```

```
316 Lake(i+1,4)          =    (Total_Mg_Lake + (F_Mg_River_In +
        F_Mg_Rain_In...
317       + F_Mg_Hydrothermal - Total_Mg_Precipitated -
              River_Outflow(i,1)*...
318       River_Outflow(i,4) - F_Mg_Evaporation)*dt)/Lake(i+1,1);
319 %Total Lake Mg accounting for inputs - outputs and new lake
        level
320
321 % U mass balance
322
323 Carbonate(i,4)           =    ((Lake(i,5)*238.0)/(Lake(i,2)
        *40.078)*...
324       Partition_Coefficent_U(Polymorph)); % Carbonate U/Ca
              mass ratio
325 Total_U_Precipitated    =    ((Carbonate(i,1)*40.078)*Carbonate
        (i,4))/238.0;
326 % Moles U precipitates, assuming one mole ca precipitated per
        CaCO3
327 Total_U_Precipitated_C = [Total_U_Precipitated_C,
        Total_U_Precipitated];
328 %Total Lake U accounting for inputs - outputs and new lake
        level
329 Lake(i+1,5)          =    (Total_U_Lake + (F_U_River_In +
        F_U_Rain_In...
330       + F_U_Hydrothermal- Total_U_Precipitated - River_Outflow(
              i,1)*...
331       River_Outflow(i,5)- F_U_Evaporation)*dt)/Lake(i+1,1);
332 Total_U_Lake_c = [Total_U_Lake_c, Total_U_Lake];
```

```
333
334 %Calcium isotope mass balance equation
335
336 %isotopic comp of carbonate precipitated from lake water
337 Carbonate(i,2) = ((1000+Lake(i,3))*Alpha(Polymorph))-1000;
338 % approximated without rayleigh model as f is essentially 1
339
340 %Lake Isotopic comp for next step
341 Lake(i+1,3) = Lake(i,3) + ((Riverine_Input(3)-Lake(i,3))*
        F_Ca_River_In...
342       + (Hydrothermal_Input(3)-Lake(i,3))*F_Ca_Hydrothermal
             +...
343       (Rain_Input(3)-Lake(i,3))*F_Ca_Rain -(Carbonate(i,2)-Lake
             (i,3))...
344       *Carbonate(i, 1) - (River_Outflow(i,3)- Lake(i,3))*...
345       (River_Outflow(i,2) * River_Outflow(i,1))-(Evaporation(3)
             -...
346       Lake(i,3))*F_Ca_Evaporation)/(Lake(i,1)*Lake(i,2));
347 end
348
349 CaCO3_Ca_isotopes = Carbonate(:,2);
350 %Ca isotope composition in Carbonates at each model step
351
352 CaCO3_Ca_isotopes = Carbonate(:,2);
353
354
355 Carbonate(:,3) = Carbonate(:,3)*10^6;
356 lake_Mg_Ca = (Lake(:,4)*24.305)./(Lake(:, 2)*40.078);
```

```
357
358 Carbonate(:,4) = Carbonate(:,4)*10^6;
359 lake_U_Ca = (Lake(:,5)*238.0)./(Lake(:, 2)*40.078)*10^6;
```

Appendix B

Chapter 3 Appendix

B.1 LakeCalc model output

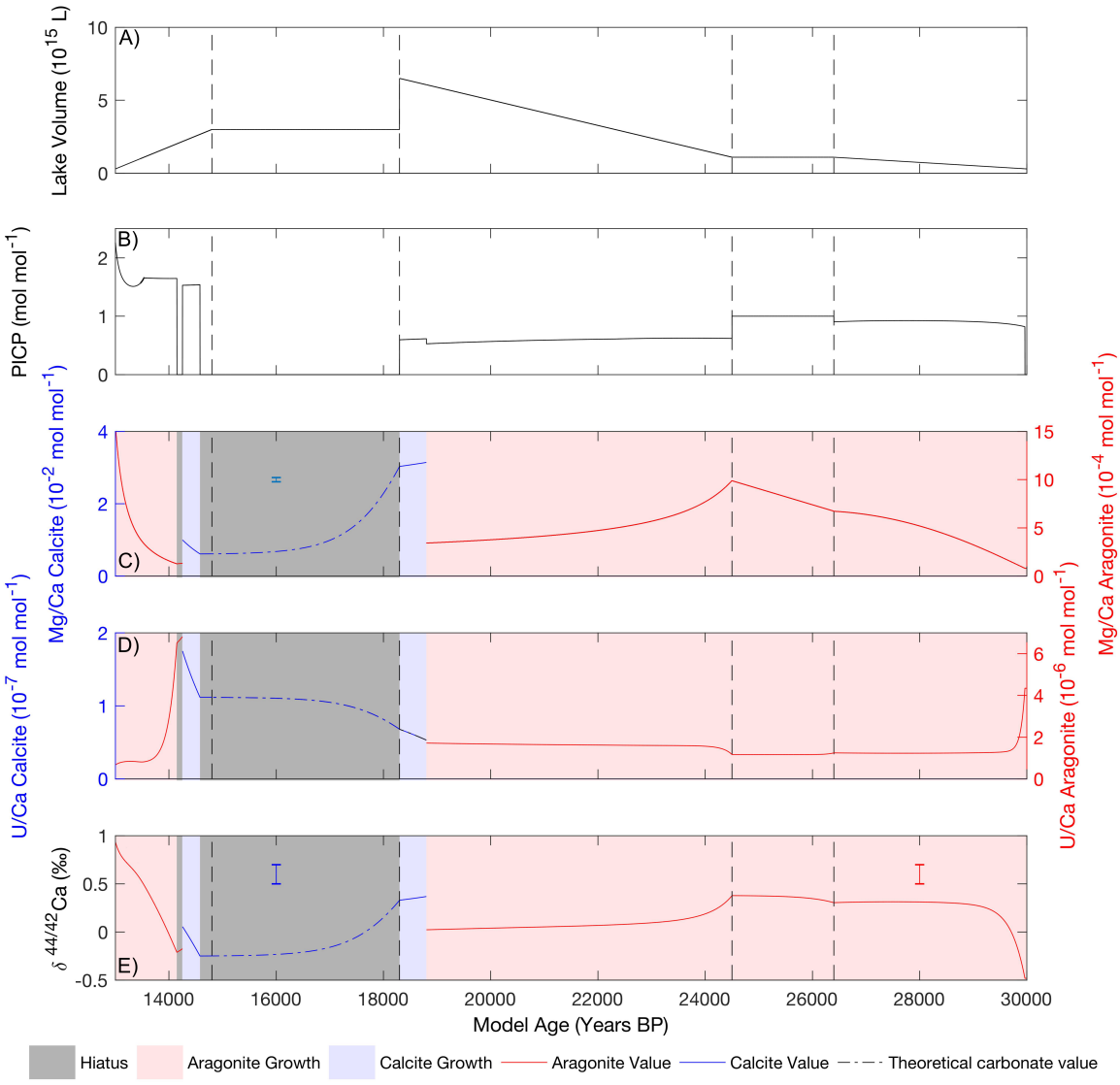


Figure B.1: The LakeCalc model output for the rise and fall of Lake Bonneville between 30 kyr (BP) - 13 kyr (BP). A) The simplified lake level reconstruction used by LakeCalc to reconstruct shifts in Lake Bonneville chemistry; B) PICP values (mol mol^{-1}); C) Mg/Ca ratios of precipitated carbonates (mol mol^{-1}); D) Ug/Ca ratios of precipitated carbonates (mol mol^{-1}); and E) $\delta^{\frac{44}{42}}$Ca of precipitated carbonates (‰). Error bars show the average 2σ uncertainties of analytical measurements of proxy values, blue are for calcite values, red for aragonite and black where they are the same for both polymorphs. Dashed lines indicate the theoretical carbonate composition during periods where LakeCalc predicts no $CaCO_3$ precipitation.

Appendix C

Chapter 4 Appendix

C.1 Radiocarbon Data

Publication Code	Sample Identifier	Depth (mm)	^{14}C Enrichment ± 1σ (% Modern)	Conventional Radiocarbon Age ± 1σ (Yr. BP)	Carbon content (%)
SUERC-97297	BA03_RC_IS_Std_ Batch_1	N.A	0.3 ± 0.01	46773 ± 198	10.08
SUERC-97298	BA03_RC_3	1.08	18.35 ± 0.11	13621 ± 46	5.57
SUERC-97300	BA03_RC_5	1.42	14.64 ± 0.11	15437 ± 62	4.73
SUERC-97304	BA03_RC_6	1.75	14.69 ± 0.09	15408 ± 49	4.89
SUERC-97305	BA03_RC_7	2.25	15.59 ± 0.09	14928 ± 47	5.21
SUERC-97306	BA03_RC_8	2.75	15.50 ± 0.09	14975 ± 46	6.86
SUERC-97307	BA03_RC_9	3.25	16.17 ± 0.09	14635± 46	11.88
UCIAMS-251350	BA03_RC_IS_Std_ Batch_2	N.A	0.2 ± 0.01	49730 ± 310	11.18
UCIAMS-251351	BA03_CT_10	0.35	18.85 ± 0.08	13405 ± 35	10.82
UCIAMS-251352	BA03_CT_11	0.85	18.86 ± 0.07	13400 ± 35	10.96
UCIAMS-251353	BA03_CT_12	1.35	17.63 ± 0.07	13945 ± 35	10.98
UCIAMS-251354	BA03_CT_14	4.10	15.16 ± 0.09	15155 ± 50	11.06
UCIAMS-251355	BA03_CT_15	5.10	13.31 ± 0.07	16205 ± 45	11.1
UCIAMS-251356	BA03_CT_16	6.10	20.97 ± 0.08	12545 ± 30	10.9
UCIAMS-251357	BA03_CT_17	195.00	14.25 ± 0.08	15655 ± 50	8.96
UCIAMS-251360	BA03_CT_18	518.50	11.02 ± 0.07	17720 ± 60	10.12

Table C.1: Radiocarbon data from speleothem BA03. The results are reported as conventional radiocarbon years BP (relative to AD 1950) and % modern ^{14}C, with ± 1σ analytical uncertainties recorded for both. The distances along the stalagmite's growth axis that sub-samples were collected from (Depth) and percentage carbon content are also listed.

C.2 Trace Element Cross Plots

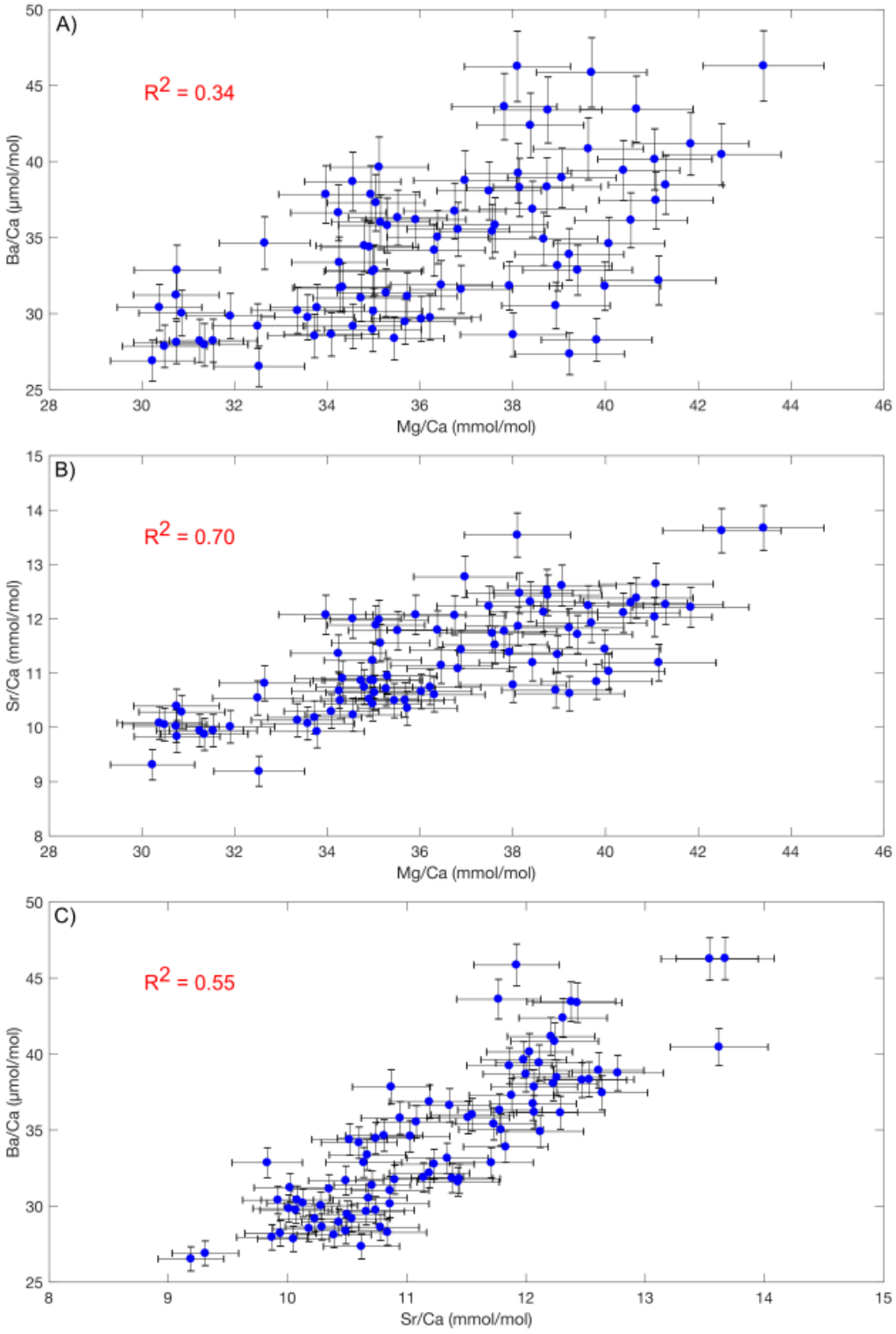


Figure C.1: Cross plots between trace elements measured in BA03. A) Ba/Ca vs Mg/Ca; B) Sr/Ca vs Mg/Ca; c) Ba/Ca vs Sr/Ca. The r-squared correlation coefficient is included for each cross plot.